Curved Carbon Materials

Strained Macrocycles
and
Photomagnetic Switches

DISSERTATION

zur Erlangung des akademischen Grades
doctor rerum naturalium
(Dr. rer. nat.)
im Fach Chemie

eingereicht an der
Mathematisch-Naturwissenschaftlichen Fakultät
der Humboldt-Universität zu Berlin

von
M. Sc. Niklas Jan Grabicki

Präsidentin der Humboldt-Universität zu Berlin
Prof. Dr. Julia von Blumenthal

Dekanin der Mathematisch-Naturwissenschaftlichen Fakultät
Prof. Dr. Caren Tischendorf.

Gutachter/innen:
1. Prof. Dr. Stefan Hecht
2. Dr. Oliver Dumele
3. Prof. Dr. Michal Juríček

Tag der mündlichen Prüfung: 08. Juni 2023

Die vorliegende Arbeit wurde in der Zeit von Januar 2019 bis März 2023 am Institut für Chemie der Humboldt-Universität zu Berlin unter der Anleitung von Dr. Oliver Dumele angefertigt.

Meiner Familie in Dankbarkeit

"You have not succeeded in science until your students are more successful than you."

Asumana Jabateh Randolph

Acknowledgements

First and foremost, I would like to thank Dr. Oliver Dumele for giving me the opportunity to start with him his newly established lab at Humboldt Universität zu Berlin. The freedom you gave me regarding my research, the people you pick and your enthusiastic guidance through the past years is acknowledged and I am deeply grateful for your support. You have influenced my scientific career so far, like no other.

I would like to thank Prof. Dr. Stefan Hecht for his support since I started my studies. Your support has opened many doors during the last six years and none of the projects presented in this thesis could have been executed without the infrastructure you are providing at our institute.

I would like to acknowledge the *Fonds der Chemischen Industrie* for a Liebig Doctoral fellowship and the Japanese Society for the Promotion of the Sciences for a short-term PhD scholarship, which was kindly hosted by Prof. Dr. Shigehiro Yamaguchi at Nagoya University.

I had the pleasure to supervise the research projects of Jeremy Maltiz, Kay Rübenstahl, Koah Nguyen, Sergey Fisher, Anna Möckel, Konstantin Günther, and Lukas Husarich, as well as Hanna Arndt during her time as an apprentice. I would like to thank all of you for your great contributions. Thereby I would like to especially thank Koah Nguyan, Sergey Fisher and Konstantin Günther. It was a pleasure to have you in the laboratory and your work had significant impact on this thesis. I would like to wish all of you the best for your future.

Even though, I have not supervised you I would like to thank Mira Müller, Tim Eppler, and Tommy Wachsmuth as I really enjoyed you as group members on a scientific and a personal basis.

I would like to thank the NMR service especially Jana Hildebrandt and Dr. André Dallmann for helpful instructions and fruitful discussions.

Further, I would like to thank Dr. Beatrice Braun-Cula for helping me with several complicated SXRD structures and in that regard as well the members of the macromolecular crystallography Beamlines at the BESSY II synchrotron.

I am really grateful to Dr. Steffen Weidner, who measured a huge amount of MALDI samples. Only due to his constant and uncomplicated help I could finish the first two projects.

I would like to thank Prof. Dr. Johannes Teichert and (soon to be Dr.) Trung Tran Ngoc for giving me the opportunity to work with them on "Photoswitching neutral homoaromatic hydrocarbons". This project was a scientific highlight during my PhD and I especially enjoyed working with you.

I would like to thank the senior scientists in the Hechtlab: Dr. Michael Pätzel, Dr. Björn Kobin, Dr. Lutz Grubert, and Jutta Schwartz. All of you helped me with your special set of skills in one way or the other during my PhD. Further, I would like to thank all past and present PhD students of the HechtLab.

Last but not least regarding our scientific work-environment I would like to thank all of the PhD students in the Dumele group. Once you joined the group I really felt like being part of a proper research group. Having started as the first PhD I was especially happy, when Josefine Sprachmann decided to join. I wish there would have been more time for our proclaimed group sports: bouldering and cycling. Further, I am really grateful to Sebastian Pallasch, I really appreciate your thorough mentality, and José Monroy Gomez por favor, disculpen mis patéticos intentos de hablar español. Josefine, Sebastian, José, Kylie, Carlos, I think shared experiences create a strong bond, please never hesitate to contact me in the future. I wish you all the best and I am without doubts that you will perform great.

I would like to thank my family and friends, who make my life most enjoyable, which at the end is what really matters. Un agradecimiento especial a ti Susana, no importa lo que quede de esta tesis, inevitablemente estará ligada a maravillosos recuerdos tuyos.

Publications

* Authors contributed equally

Peer-Reviewed Articles:

Derived from this Thesis:

N. Grabicki, S. Fisher, O. Dumele *Angew. Chem. Int. Ed.* **2023**, e202217917 https://doi.org/10.1002/anie.202217917 (open access) A Fourfold Gold(I)–Aryl Macrocycle with Hyperbolic Geometry and its Reductive Elimination to a Carbon Nanoring Host

K. Günther,* N. Grabicki,* B. Battistella, L. Grubert, O. Dumele, *J. Am. Chem. Soc.* **2022**, 144, 19, 8707–8716. https://doi.org/10.1021/jacs.2c02195 An All-Organic Photochemical Magnetic Switch with Bistable Spin States

N. Grabicki, O. Dumele *Synlett* **2022**, *33*, 1–7 https://doi.org/10.1055/s-0040-1719853 Confining the Inner Space of Strained Carbon Nanorings

N. Grabicki, K. T. D. Nguyen, S. Weidner, O. Dumele *Angew. Chem. Int. Ed.* **2021**, *60*, 14909–14914. https://doi.org/10.1002/anie.202102809 (open access) Confined Spaces in [n]Cyclo-2,7-pyrenylenes

→ Highlighted in *Nature Chemistry* **2021***, 13,* 520.

Derived from Collaborations:

Josefine Sprachmann, Tommy Wachsmuth, Manik Bhosale, David Burmeister, Glen J. Smales, Maximilian Schmidt, Zdravko Kochovski, Niklas Grabicki, Robin Wessling, Emil J. W. List-Kratochvil, Birgit Esser*, and Oliver Dumele* *J. Am. Chem. Soc.* **2023**, https://doi.org/10.1021/jacs.2c10501 Antiaromatic Covalent Organic Frameworks Based on Dibenzopentalenes

T. T. Ngoc,* N. Grabicki,* E. Irran, O. Dumele, J. F. Teichert, *Nat. Chem.* **2023** https://doi.org/10.1038/s41557-022-01121-w Photoswitching neutral homoaromatic hydrocarbons

O. Kysliak,* S. H. F. Schreiner,* N. Grabicki, P. Liebing, O. Dumele, R. Kretschmer, *Angew. Chem. Int. Ed.* **2022**, 6, e2022069, https://doi.org/10.1002/anie.202206963 (open access) A Planar Five-Membered Aromatic Ring Stabilized by Only Two π-Electrons

N. Grabicki,* O. Dumele,* H. Sai, N. E. Powers-Riggs, B. T. Phelan, M. H. Sangji, T. Chapman, J. V. Passarelli, A. J. Dannenhoffer, M. R. Wasielewski, Samuel I. Stupp *Chem.*

Mater. **2021**, *33*, 706–718 https://doi.org/10.1021/acs.chemmater.0c04123 Polymorphism and Optoelectronic Properties in Crystalline Supramolecular Polymers

Presentations

a) Oral Talks:

N. Grabicki, O. Dumele, “Functional Polycyclic Aromatic Hydrocarbons”

BASF International Summer Course, Ludwigshafen, Germany, August 2022.

N. Grabicki, K. Günther, O. Dumele, “An All-Organic Photochemical Magnetic Switch”

Contributed Lecture, International Conference for the Science and Technology of Synthetic Metals, Glasgow, Scotland, July 2022

N. Grabicki, K. Günther, O. Dumele, “Photoswitching All-Organic [5]Helicenes between Bistable Spin States”

Invited Lecture, National Institute for Materials Science, Tsukuba, Japan, May 2022.

N. Grabicki, O. Dumele, “Rim Functionalized CPPs as New Supramolecular Hosts”

Invited Lecture, Group Seminar Prof. Shigeru Yamago, Kyoto University, Kyoto, Japan, May 2022.

N. Grabicki, K. T. D. Nguyen, O. Dumele “En route to Tubular COFs: Highly functionalized Strained Macrocycles as Supramolecular Hosts”,

OpiEM3 (Organic p-Electron Molecules and Materials Meetings) Online Seminar series Organized by Prof. Mike Haley (University of Oregon), October 2020

b) Poster Presentations:

N. Grabicki, K. Günther, O. Dumele, “A Magnetic Photochemical Switch with Bistable Spin States”, International Symposium on Novel Aromatic Compounds, Warsaw, Poland, July, 2022

N. Grabicki, O. Dumele, “Functionalized CPP-Type Macrocycles as Supramolecular Hosts”, International Symposium of Macrocyclic and Supramolecular Chemistry, Eugene, Oregon, USA, June, 2022

N. Grabicki, O. Dumele, “Confined Spaces in Cyclo-2,7-Pyrenylenes”, International Symposium of Macrocyclic and Supramolecular Chemistry, Online Conference, July, 2021 → Best poster presentation award

N. Grabicki, J. Maltiz, O. Dumele, “Transimination for improved COF synthesis and 1D tubular COF’s”, GDCh Berlin Chemistry Symposium, October 2019, → Best poster presentation award

Table of Contents

Abbreviations

°	degree
[A]	concentration of species 'A'
1D	one-dimensional
2D	two-dimensional
3D	three-dimensional
Å	Ångström (1 Å = 10^{-10} m)
Ac	acetyl
aq.	aqueous
Ar	aromatic ring
ATR	attenuated total reflectance
ax	axial
br.	broad
Bu	butyl
C	Celsius
c	concentration
cal	calory (1 cal = 4.185 Joule)
calcd	calculated
CCDC	Cambridge Crystallographic Data Centre
Compd	compound
COSY	correlation spectroscopy
CPP	cyclo-*para*-phenylene
CSA	camphorsulfonic acid
Cy	cyclohexyl
CSD	Cambridge Structural Database
d	day(s); doublet (NMR)
decomp.	decomposition
DFT	density functional theory
DMF	*N*,*N*-dimethylformamide
dppf	1,1'-*bis*(diphenylphosphino)ferrocene
E	energy
ECD	electronic circular dichroism
equiv	equivalent(s);
Eq.	Equation
eq.	equatorial
ESI	electrospray ionization
Et	ethyl
Et_2O	diethyl ether
EtOAc	ethyl acetate
EtOH	ethanol
eV	electron Volt
F	structure factor (crystallography)
FT	Fourier transform
G	Gibbs energy/free enthalpy

gem	geminal
GPC	gel permeation chromatography
H	enthalpy
h	hour
H-bond	hydrogen bond
HMBC	heteronuclear multiple bond correlation
HPLC	high performance liquid chromatography
HR	high resolution
HSQC	heteronuclear single quantum coherence
Hz	Hertz
I	intensity (crystallography)
i	*iso-*
ID	identification
IR	infrared spectroscopy
IUPAC	International Union of Pure and Applied Chemistry
J	coupling constant (NMR) in Hz
K	equilibrium constant
K_a	association constant
L	liter
l	length
LC/MS	liquid chromatography/mass spectrometry
Lit.	literature
LUMO	lowest unoccupied molecular orbital
M	molar (mol/L)
m	multiplet (NMR); medium (IR), meter (SI-units)
m.p.	melting point
m/z	mass over charge ratio
MALDI	matrix assisted laser desorption/ionization
Me	methyl
MeOH	methanol
min	minute(s)
MP2	second-order Møller-Plesset perturbation theory
MPLC	medium pressure liquid chromatography
MS	mass spectroscopy
MW	molecular weight
NBS	N-bromosuccinimide
*n*Bu	*n*-butyl
NIS	N-iodosuccinimide
NMR	nuclear magnetic resonance
ORTEP	Oak Ridge Thermal Ellipsoid Plot
OTf	triflate
p	para
pH	$-\log([\mathrm{H_3O^+}]\ \mathrm{M^{-1}})$
Ph	phenyl
pin	pinacolate
ppm	parts per million

Pr	propyl
q	quartet (NMR)
quant.	quantitative
quint.	quintet
R	ideal molar gas constant (8.314 J K–1 mol–1)
R	R-factor (crystallography)
R_f	retention factor (TLC)
RMSD	root mean square deviation
RP	reversed phase
S	entropy
s	singlet (NMR); strong (IR)
sat.	saturated
SPhos	2-dicyclohexylphosphino-2',6'-dimethoxybiphenyl
T	temperature
t	tert-
t	triplet
TD-DFT	time-dependent density-functional theory
TFA	trifluoroacetic acid
THF	tetrahydrofuran
TIPS	triisopropylsilyl
TLC	thin layer chromatography
TMS	tetramethylsilane
UV	ultraviolet
V	volume
V	Volt
vis	visible
w	weak
XB	halogen bonding
Δ	difference
δ	chemical shift
ε	molar extinction coefficient (M–1 cm–1)
λ	wavelength
$\bar{\boldsymbol{\nu}}$	wavenumber

The international system of units (SI) is used.

Abstract

Curved Carbon Materials
Strained Macrocycles and
Photomagnetic Switches

The overall goal of this work was the synthesis of new one-dimensional (1D) nanotubes based exclusively on light elements (C, B, N, O, H). Inspired by carbon nanotubes, we expect that the materials envisioned herein will exhibit a variety of interesting properties. Carbon nanotubes are being explored in a wide range of materials sciences and show promising properties in terms of their tensile strength-to-density ratio, on the one hand, but also in their current-carrying capacity and thermal conductivity. Currently, the synthesis of such carbon nanotubes is only possible with comparatively complex methods. In particular, the uniform synthesis of tubes with exactly the same diameter and symmetries is still an unsolved problem.

Through this work, we hoped to establish a completely new way of synthesis for such 1D nanomaterials. For this purpose, two different types of strained aromatic macrocycles belonging to the class of cyclo-*para*-phenylenes were synthesized in *Chapters 2* and *3*. The synthesized macrocycles are display a high degree of functionalization, which will be used in the future to apply the principles of dynamic covalent chemistry in the final material synthesis. The structure of the generated macrocycles is characterized by moderate to strong shape persistence at the molecular level. The internal cavity of these cyclic compounds created by their degree of functionalization can be used to bind various molecular guests. The binding of such guests was demonstrated in an interdisciplinary approach consisting of spectroscopic methods, theoretical calculations and single crystal X-ray diffraction. The insights into the synthesis of such macrocycles obtained herein, will be instrumental in achieving the initially described goal of wet chemical synthesis of 1D organic nanotubes in the future. The additional insights gained into supramolecular binding properties will also open up new applications in the field of molecular sensing and the construction of complex synthetic structures.

Initially the methods, of macrocyclization were supposed to enable the synthesis of a chiral aromatic macrocycle based on [5]helicene subunits. However, as described in *Chapter 4* preliminary experiments showed no success with respect to macrocyclization. Instead, a by-product was isolated that proved to be a previously unknown molecular switch. This switch allows reversible generation of a paramagnetic isomer by irradiation at low temperatures. In addition to the accidentally found [5]helicene derivative, we designed and synthesized one more photoswitch, which exhibited almost the same properties. These first two examples open up a completely new class of molecular switches, of which potential applications are beyond the scope of this work.

Kurzzusammenfassung

Nicht-Planare Kohlenstoff Materialien

Gespannte Makrozyklen und Photomagnetische Schalter

Das übergeordnete Ziel dieser Arbeit war die Synthese neuer eindimensionaler (1D) Nanoröhren basierend auf leichten Elementen (C, B, N, O, H). Inspiriert von Kohlenstoff Nanoröhren erwarten wir, dass die dabei angestrebten Materialen eine Vielzahl interessanter Eigenschaften aufweisen werden. Kohlenstoff Nanoröhren werden in einem weiten Spektrum der Materialwissenschaften erforscht und zeigen vielversprechende Eigenschaften zum einen in Bezug auf ihr Verhältnis von Zugfestigkeit zu Dichte, aber auch in ihrer Strombelastbarkeit und Wärmeleitung. Aktuell ist die Synthese solcher Kohlenstoff Nanorohren nur mit vergleichsweise aufwendigen Methoden möglich. Hierbei stellt besonders die uniforme Synthese von Röhren mit exakt gleichen Durchmessern und Symmetrien ein noch ungelöstes Problem dar.

Durch diese Arbeit erhofften wir uns eine völlig neue Arte der Synthese für solche 1D Nanomaterialien zu etablieren. Dazu wurden in *Kapitel 2* und *3* zwei verschiedene Typen von gespannten aromatischen Makrozyklen synthetisiert, die der Klasse der Cyclo-*para*-phenylene zuzuordnen sind. Die synthetisierten Makrozyklen zeichnen sich durch einen Hohen Grad an Funktionalisierung aus, welcher zukünftig dazu genutzt werden soll die Prinzipien der dynamisch kovalenten Chemie in der finalen Materialsynthese anzuwenden. Die Struktur der erzeugten Makrozyklen zeichnet sich durch eine moderate bis starke Formstabilität auf molekularer Ebene aus. Der durch die Funktionalisierung erzeugte innere Hohlraum dieser zyklischen Verbindungen lässt sich nutzen, um verschiedene molekulare Gäste zu binden. Die Bindung solcher Gäste wurde in einem interdisziplinären Ansatz bestehend aus spektroskopischen Methoden, theoretischen Berechnungen und Einkristall-Röntgenbeugung bewiesen. Die Erkenntnisse in Bezug auf die Synthese solcher Makrozyklen, die hierbei erzielt wurden, werden entscheidend dazu beitragen, dass anfänglich beschriebene Ziel der nasschemischen Synthese 1D organischer Nanoröhren in Zukunft zu erreichen. Die zusätzlich Gewonnenen Einsichten in die Supramolekularen Bindungseigenschaften eröffnen zusätzlich neue Anwendungsmöglichkeiten im Bereich der molekularen Sensorik und der Konstruktion von komplexen synthetischen Strukturen.

Die Methoden, der Makrozyklisierung sollten in *Kapitel 4* dazu genutzt werden einen chiralen aromatischen Makrozyklus auf Basis von [5]Helicen-Untereinheiten zu synthetisieren. Vorläufige Versuche zeigten allerdings keinen Erfolg in Bezug auf die Makrozyklisierung. Stattdessen wurde ein Nebenprodukt isoliert, dass sich als bisher unbekannter molekulare Schalter erwies. Dieser Schalter erlaubt es durch Bestrahlung bei tiefen Temperaturen reversibel ein paramagnetisches Isomer zu erzeugen. Neben dem zufällig gefundenen Derivat wurde ein weiteres Derivat designet, welche nahezu die gleichen Eigenschaften aufwies. Dadurch eröffnet sich eine völlig neue Klasse an molekularen Schaltern, deren Anwendungspotential den Rahmen dieser Arbeit überschreitet.

Introduction

Bottom-Up Synthesis of Functional Organic Materials and Aromatic Molecules

Chapter 1: Bottom-Up Synthesis of Functional Organic Materials and Aromatic Molecules

In order to fully understand something, one needs to be able to reconstruct it from scratch. This so-called bottom-up approach is many times more labor intensive then top-down strategies. Nevertheless, it offers the most insights into the fundamental aspects that influence the properties of the novel materials. Top-down approaches are usually much more suitable to create a desired product by building on an already existing scaffold. Therefore, one of the first challenges for a synthetic chemist lies in the decision on which path to take. Herein, we illustrate a bottom-up approach for the synthesis of new functional organic materials, whose structural motif is derived from single walled carbon nanotubes (SWCN). A class of material that holds great promises for applications related to several challenges modern societies are confronted with such as energy conversion, energy storage, or information processing. We emphasize on various challenges in the bottom-up design of such materials, but as well on the plethora of opportunities that can be investigated en-route towards this exciting class of materials. Chirality is of major importance for SWCN in regard of their optical and electronic properties. Hence, we investigate the influence of chirality on a molecular basis for materials applications and encounter unexpected results.

1.1. Introduction

Carbon exists in a variety of allotropes, of which some have been known to humanity for a long time, such as diamond and graphite. Others have only been synthesized and studied in recent years. In general, the versatility of carbon allotropes and their unique macroscopic properties can be derived from the different hybridization states of carbon in combination with the topology of the resulting structure. Until today, the synthesis of carbon allotropes such as sp^3-hybridized diamond, sp^2-hybridized graphene,[1] fullerenes,[2] carbon nanotubes,[3] as well as sp-hybridized carbynes[4] and mixed sp-sp^2-hybridized graphynes[5] usually relies on unselective physical processes.[6,7] Only a limited number of procedures for their precise fabrications are reported (Figure 1.1).[5,8,9] With their unique properties the sp^2-hybridzed carbon allotropes graphene, fullerene and carbon nanotubes have been highly investigated over the last three decades due to numerous potential applications in the field of microelectronics and solar power conversion.[10–14] The bottom-up synthesis of fullerenes remains a formidable challenge for synthetic chemists with pioneering work by Larry Scott and co-workers.[15] The ongoing fascination for these molecules is well exemplified by a recent publication were high-resolution transmission electron microscopy (HR-TEM) was used to image the electron-beam-induced formation of fullerene C_{60} through cyclodehydrogenation of a tailor-made truxene derivative.[16]

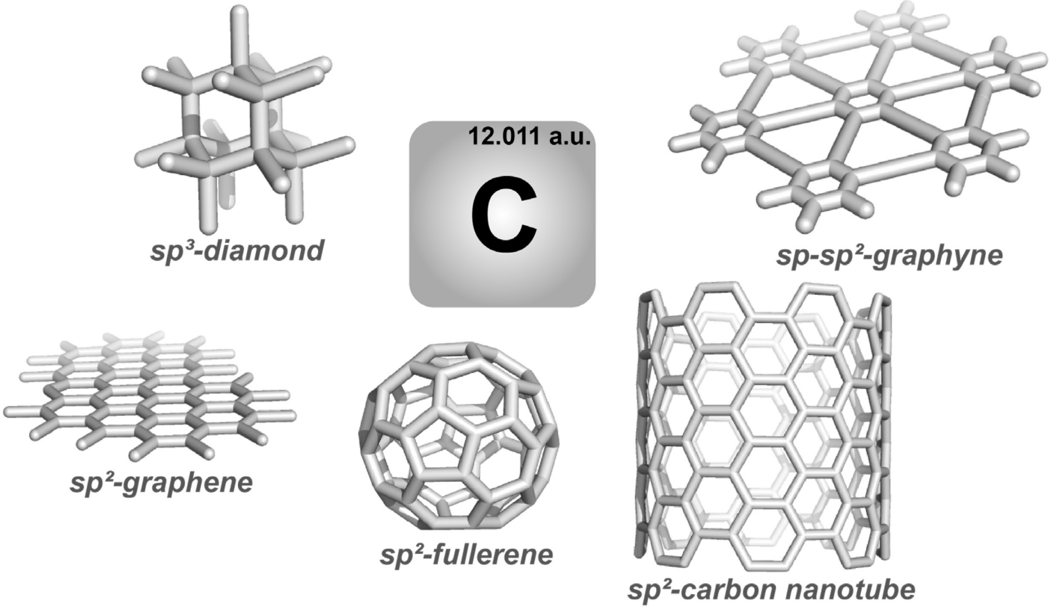

Figure 1.1: Different carbon allotropes diamond, graphene, fullerene, carbon nanotube and graphyne as well as their hybridization state. For clarity diamond, graphene, the nanotube and graphyne are shown as finite structures.

A straight forward top-down approach for the preparation of high-quality graphene crystallites is represented by micromechanical cleavage of bulk graphite. This finding allowed Andre Gaim and Konstantin Novoselov experimental characterization of the unique properties of graphene and resulted in their 2010 Noble Prize in physics.[12] Since the discovery of stable free-standing graphene, a tremendous amount of research has been dedicated to the exploration of two dimensional (2D) materials.[17–20] In that regard, covalent organic frameworks represent an exciting field for synthetic organic chemists, where extended structures are made by stitching organic molecules together through strong covalent bonds.[21] These frameworks can be made from solutions or dispersions and produce crystalline two and three dimensional nanoporous solids in batch from abundant starting materials. Depending on the preparation technique remarkable crystalline domain sizes up to several square micrometer have been obtained.[22] While the synthetic conditions maintain the integrity of the molecules used, microscopic reversibility—enabled by dynamic covalent chemistry (DCC)—leads to continuous error correction, creating defined structures (Figure 1. 2).[23]

The two most prominent motives used for the construction of COFs are imine bonds and boronic esters.[24] The two linkages are especially attractive as they are highly reversible under acidic aqueous conditions allowing for high rates of bond formation and cleavage. Boronic esters are more sensitive to hydrolysis then imines resulting in an overall limited stability of the final material.[25]

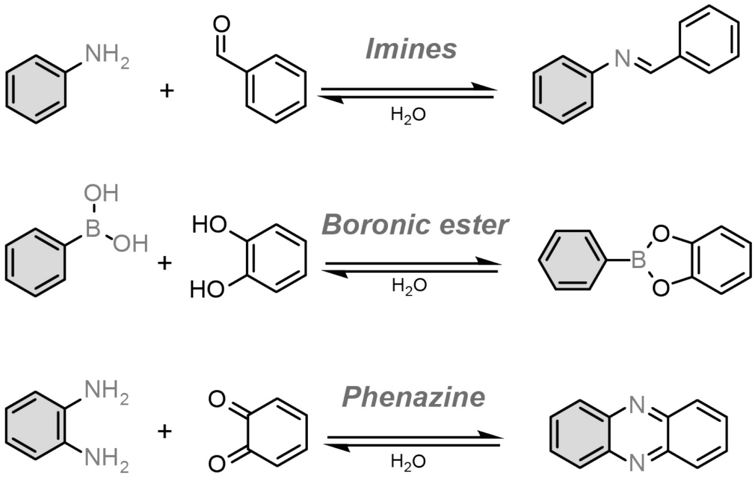

Figure 1. 2. Selection of commonly used functional groups and their respective equilibrium condensation reaction forming and cleaving covalent bonds.

The dynamic behavior of imines—routinely known as Schiff's bases—has been extensively studied since their first discovery by Hugo Schiff in 1864, which makes this motif an ideal playground for a synthetic chemist synthesizing new COFs.[26–31] Several other condensation reactions have been used such as Knoevenagel,[32,33] triazine,[34] or phenazine condensation.[35] The phenazine condensation (Figure 1. 2) is particularly appealing as it results in a rigid planar six-membered aromatic ring with a high degree of conjugation between the connected monomers.
Further importance in the design process of novel COFs is placed on the monomer's symmetry as it directly allows to predict the structure of the final scaffold (Figure 1. 3). Especially for 2D COFs the monomer units consist of (poly)cyclic aromatic cores. Therefore, a major driving force for the formation of these layered 2D materials are intermolecular non-covalent van der Waals forces between large aromatic areas that arrange within π-stacking distance to each other.[36]

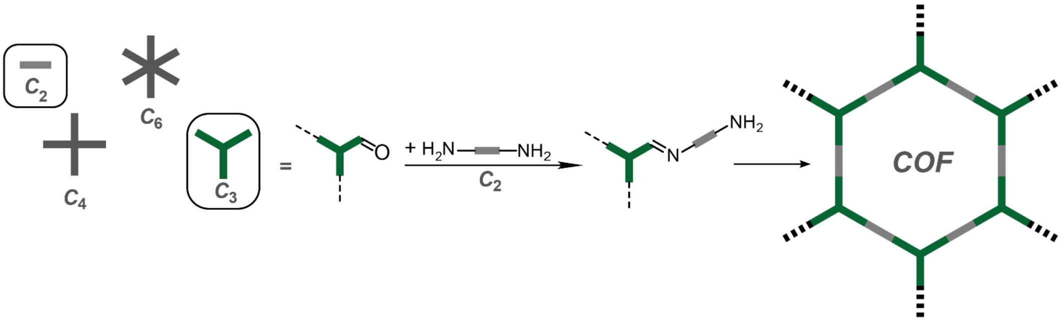

Figure 1. 3: Selection of monomer symmetries suitable to construct 2D frameworks. Resulting pore geometry derived from a C_2 and a C_3 symmetric monomer.

Opposed to the significant advances that have been achieved in this field, a comparable development is lacking in the field of synthesis of 1D tubular COFs that could be seen as covalent organic nanotubes (CONTs). A remarkable example was published by Banerjee and co-workers within the course of this thesis (Figure 1. 4, bottom).[37]

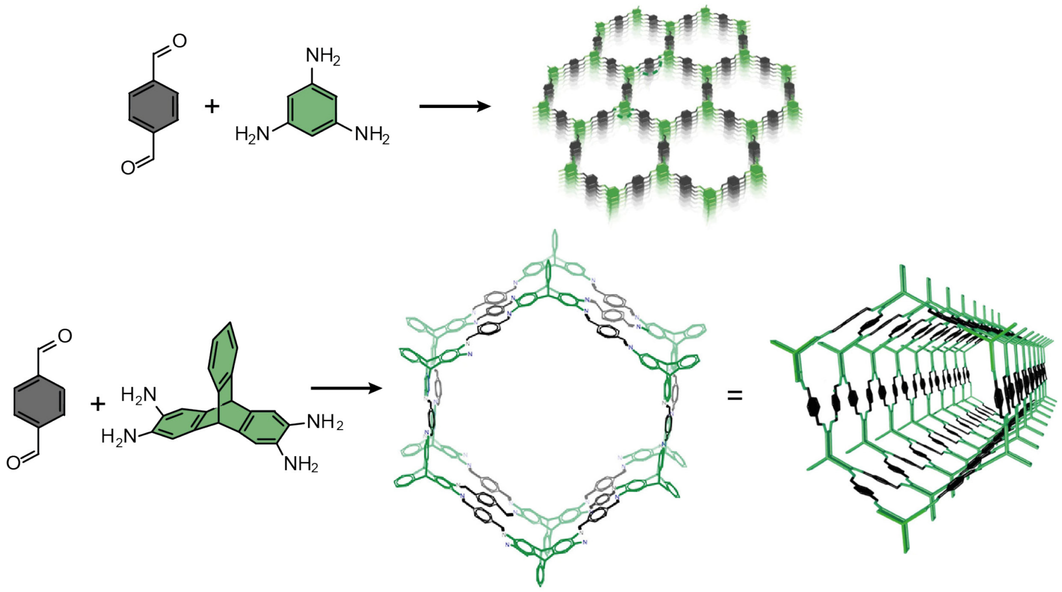

Figure 1. 4. Planar aromatic C_2 and C_3 symmetric building blocks resulting in a 2D imine COF (top) and the same C_2 symmetric terephthalic aldehyde with tetratopic triptycene tetraamine resulting in the formation of covalent organic nanotubes.[37]

While ditopic terephthalic aldehyde together with tritopic 1,3,5-triaminobenzene leads to the formation of a 2D COF with hexagonal pores under solvothermal conditions (Figure 1. 4, top), Banerjee and co-workers used terephthalic aldehyde with tetratopic triptycene, to synthesize covalent organic nanotubes. This approach is interesting from a fundamental structure-centric perspective and gives access to precisely designed tubes that are thermally stable up to 400 °C. Nevertheless, the obtained CONTs do not show properties that usually make CNTs attractive materials in electronic devices or other applications. The lack of such properties can be explained with several structural differences. First of all, the imine bond reduces the overall conjugation of the covalently connected π-systems. Further, the delocalization of the π-electrons is reduced from through bond conjugation usually present in polycyclic aromatic moieties to weaker through space conjugation due to the triptycene building block.[38] Apart from that the presented CONT do not experience any form of strain energy, which is usually the case for CNT. This bending of the otherwise planar benzene moieties, has a significant influence on the photophysical properties of CNT symbolized by the diameter dependence of the band gap.[10]

Even though, the discussed work achieved the synthesis of 1D tubular COFs using non-macrocyclic monomers, the obvious choice as a monomer to construct a 1D tube is a macrocycle (Figure 1. 5).

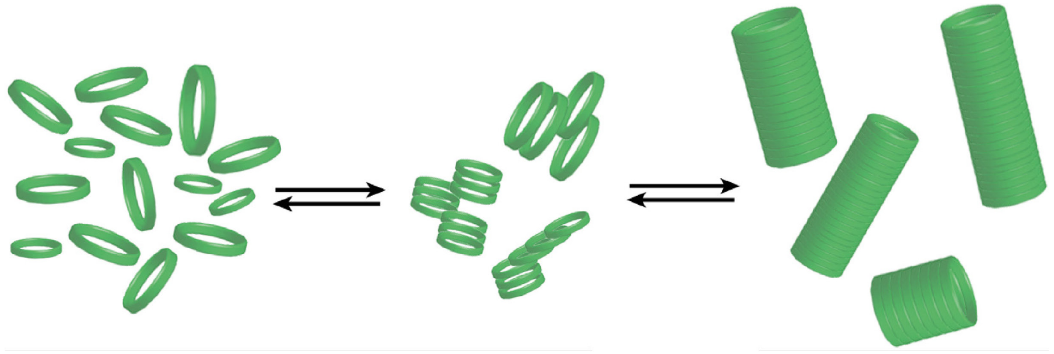

Figure 1. 5. Schematic representation of the covalent organic nanotube formation under microscopic reversibility starting from cyclic monomers leading to oligomeric structures containing several defects and the final tubes.

There are two types of CNT zig-zag nanotubes and armchair nanotubes with individual conductivity depending on their chirality.[39] While armchair nanotubes have metallic properties,[40] zig-zag nanotubes exhibit semi-conducting properties[39] which makes them potent candidates for electronic devices.[41,42] The smallest repeating unit of zig-zag nanotubes can be assigned to cyclacenes and of armchair nanotubes to cyclo-*para*-phenylenes (CPPs).[43] To develop a bottom-up synthesis and to understand the effects of curvature and strain on carbon nanotubes, these carbon nanorings represent a versatile model-compound class. Unsubstituted hydrocarbon cyclacenes show no aromatic Clar sextets, hence occur in an open-shell system independent of the ring size, which results in a biradical state.[44–46] Therefore, cyclacenes are more reactive than CPPs and only few structurally related examples are known.[47–50] On the contrary, several synthetic methodologies have been developed to synthesize various kinds of CPPs.[51–54]

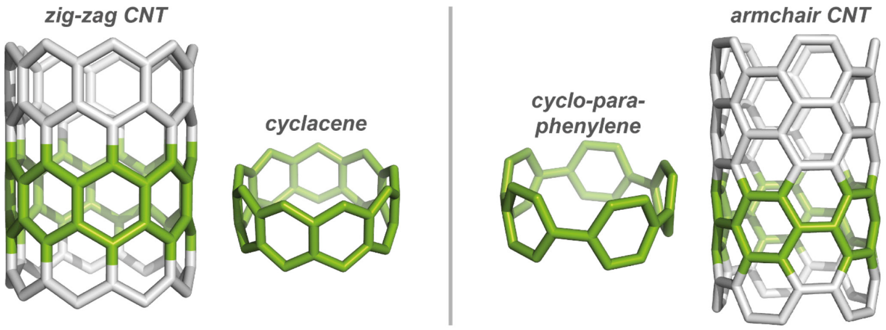

Figure 1. 6. The two classes of carbon nanotubes: zig-zag nanotube (left) and armchair nanotube (right) as well as their corresponding subunits: cyclacene (left) and cyclo-*para*-phenylene (right) highlighted in green.

The unique electronic properties of CNT arise predominantly from intralayer interactions, rather than from interlayer interactions between two different nanotubes.[55] Therefore, the symmetries of CNT are particularly important in regard of their physical properties. In general, these symmetries can be either symmorphic (armchair [*n*,*n*] and zigzag [*n*,0] CNT) or non-symmorphic. In symmorphic CNT, the translational and rotational symmetry operations can each be executed independently. Contrary, symmetry operations valid for non-symmorphic CNTs are always a combination of translation and rotation. CNT that evolve upon rolling up a 2D graphene sheet along a line that is not corresponding to the armchair or zigzag configuration are chiral CNTs (Figure 1. 7). In Figure 1. 7 only right-handed CNT can be constructed from the shown possibilities.[56] In summary, not only the diameter of the CNT is important but the plethora of different properties is majorly influenced by its symmetry thus its chirality.

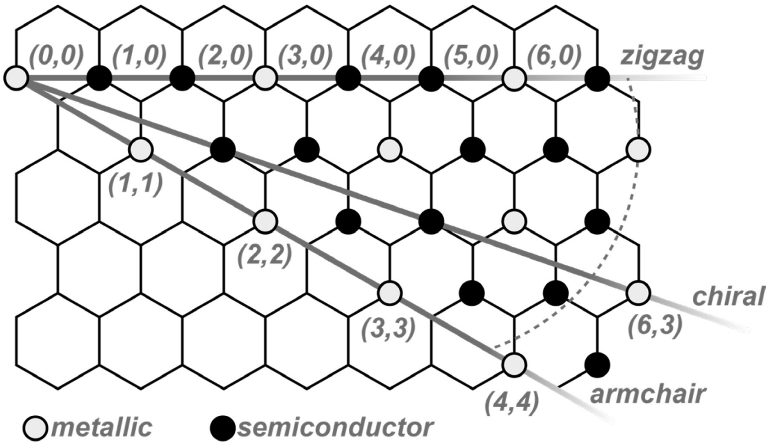

Figure 1. 7. Representation of the 2D graphene sheet with lines specifying the different types of CNT accessible, if the sheet is rolled up. CNT in between zigzag and armchair CNTs are chiral. The hollow black and full black dots denote metallic and semiconducting CNT respectively.

1.2. Synthesis of Strained and Curved Aromatic Macrocycles

The first scientific report investigating the synthesis of a CPP was published in 1934 by Parekh and Guha.[57] Unsuccessful attempts in synthesizing [2]CPP were made by desulfurization of sulfur bridged benzene units (Figure 1. 8). As [2]CPP would exhibit significant strain energy only polymeric by-products were observed.

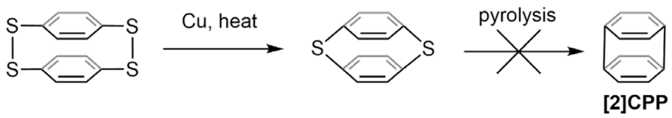

Figure 1. 8. Unsuccessful synthetic efforts from Parekh and Guha to synthesize [2]CPP by desulfurization.[57]

In 1993, the group of Vögtle attempted the synthesis of [8]CPPs following the same desulfurization approach as Parekh and Guha.[58] Their expectation that the reduction of strain energy would allow the synthesis of [8]CPP was not met. A different strategy using masked benzene rings in the form of conformationally flexible substituted cyclohexyl moieties was tried as well by the same authors. Even though they obtained an appropriate pre-organized precursor no macrocyclic structures were accessed using subsequent one-pot aryl–aryl couplings (Figure 1. 9).

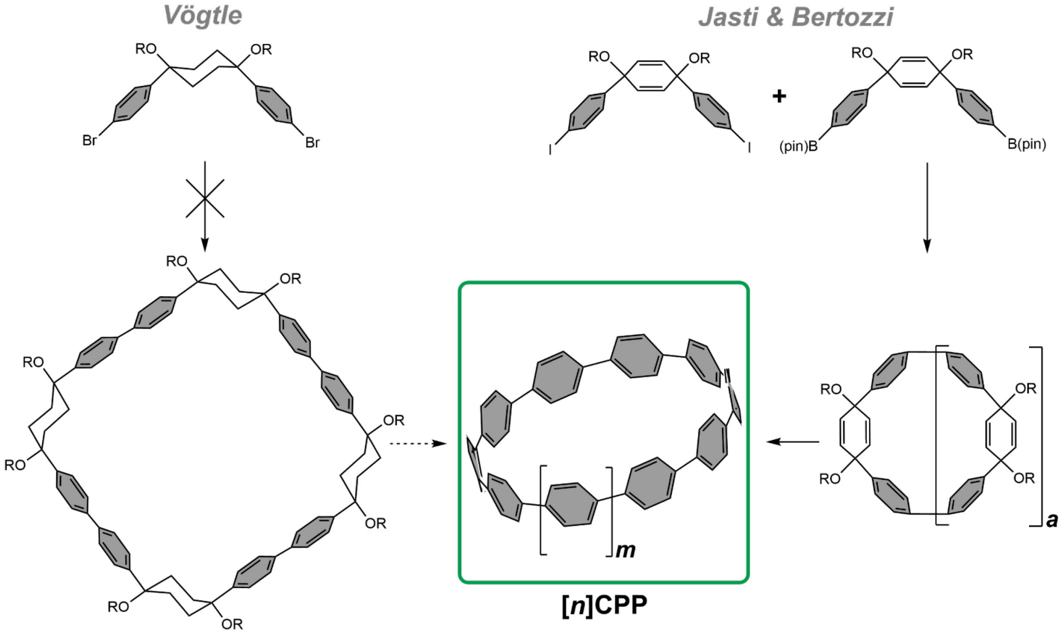

Figure 1. 9. Synthetic approach by Vögtle using 1,4-bisalkoxy-1,4-biaryl-cyclohexane to access [*n*]CPP precursor (left) and a stepwise Pd catalyzed cross-coupling for the first successful synthesis of [*n*]CPP (right, with $a = 2,3,5$ and $m = 0,4,9$). With R being either H, Me, or methoxymethyl (MOM).[58,59]

The seminal work of Vögtle inspired Jasti and Bertozzi to execute the first successful synthesis of [*n*]CPPs ($n = 9,12,18$) utilizing 1,4-cyclohexadiene units as masked benzenes that simultaneously introduce curvature and rigidity to pre-organize the macrocycle formation. Key steps within this route are an efficient method to obtain a *syn*-diol precursor and an effective aromatization with lithium naphtalenide as the final step (Figure 1. 9, right).[60,61] In the following year, the group of Itami published an alternative route, applying the 1,4-bisalkoxy-1,4-biaryl-cyclohexane motif earlier investigated by Vögtle, but this time in combination with stepwise palladium-catalyzed coupling reactions.[53] Within the last decade these modular synthetic routes were further developed to access [*n*]CPPs in various ring sizes ($n = 5–18,24$).[62–65]

In 2010, a novel synthetic approach was presented by the group of Yamago based on earlier work by the group of Beuerle, where square planar (bis)aryl Pt(II)complexes were used as corner motifs to create stable organo-platinum macrocycles.[52,66] Upon reductive elimination, novel CPP-type macrocycles are rapidly accessed in two steps from adequately borylated polycyclic aromatics.[67–72] Nevertheless, this synthetic method is not without flaws, as other shapes and therefore ring sizes can be obtained for the organo-platinum macrocycles.[71,73,74] Furthermore, *in-situ* generated $Pt(PPh_3)_{4-m}$ is known to insert into strain-activated C–C bonds. Dynamic insertion of active $Pt(PPh_3)_{4-m}$ into the C–C bond between aromatic units and subsequent ligand exchange of cyclic fragments can therefore lead to unselective formation of a variety of ring sizes.[75–79]

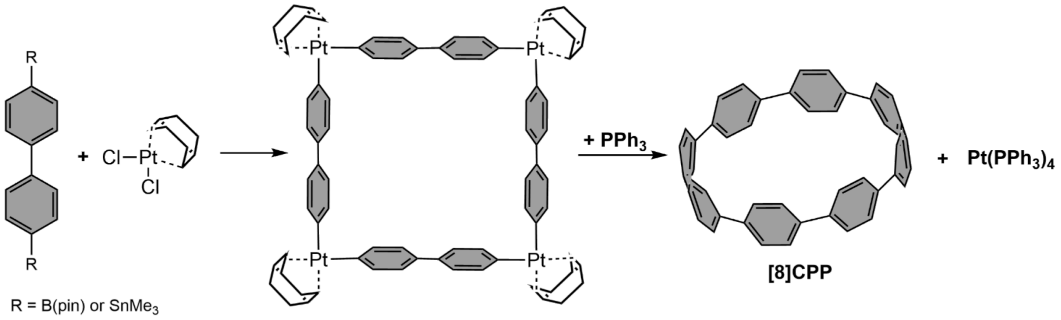

Figure 1. 10. The platinum mediated synthesis of [8]CPP by Yamago and co-workers.[52]

The most recent entry in the list of synthetic methodologies of CPPs came from Tsuchido, Osakada, and co-workers based on a stable dinuclear gold(I)-aryl complex as a corner motif followed by oxidation induced reductive elimination of [6]CPP.[54,80,81]

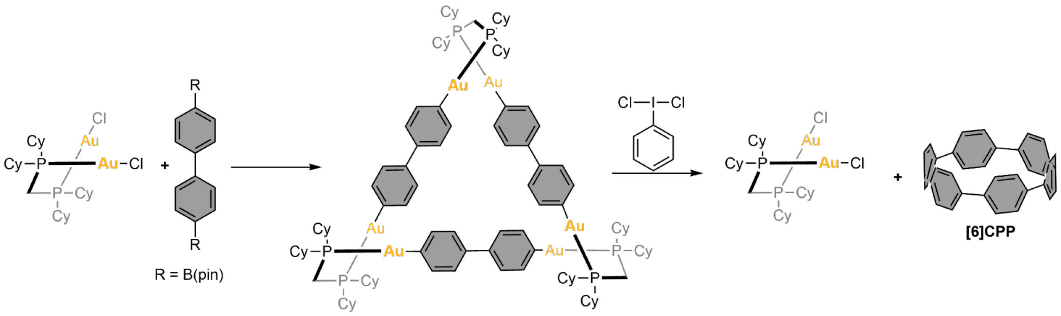

Figure 1. 11. Synthetic route for [6]CPP using dinuclear gold(I) complexes that lead to the formation of triangular organo-gold-macrocycles.[54]

Compared to the platinum mediated strategy the synthetic route utilizing the dinuclear gold(I)complex does not lead to the unselective formation of different ring-sizes. Further, the exit vector of 60° reliably produces triangular shaped organo-gold macrocycles, resulting in final [*n*]CPPs that are a multiple of three in regard of the aromatic linear linker. Additionally, the gold(I) complex is recovered at the end of the synthesis making this approach more atom economic. Current research shows that the Au–C_{Ar} bond is dynamic depending on the phosphine ligand chosen, which will allow the synthesis of a variety of exciting structures in the future.[81]

1.3. Theory and Synthetic Strategies of Macrocycles

The synthetic advances discussed in the previous section build on a strong foundation of research that has been dedicated to the synthesis of (conjugated) macrocycles, which is a delicate matter in almost any case.[82] Consequently, they require careful evaluation of the best synthetic strategy and various approaches are discussed in this chapter.

In general, the ring closure as the final macrocyclization step of an α,ω-difunctionalized oligomer is an intramolecular and unimolecular process (Figure 1. 12). In competition to the intramolecular reaction is the intermolecular coupling of two fragments that produces oligomers, polymers, and cycles of higher and lower order instead of the desired macrocycles. The reaction rate of the intramolecular ring-closure depends linearly on the concentration of the monomer ([A]) of the α,ω-difunctionalized oligomers (neglecting back reactions). In contrast the dimerization depends on $[A]^2$. Consequently, kinetic control to favor the cyclization can be achieved by lowering the concentration of the precursor. Nevertheless, dilution requires large amounts of solvent and only partially prevents oligomerization.[83]

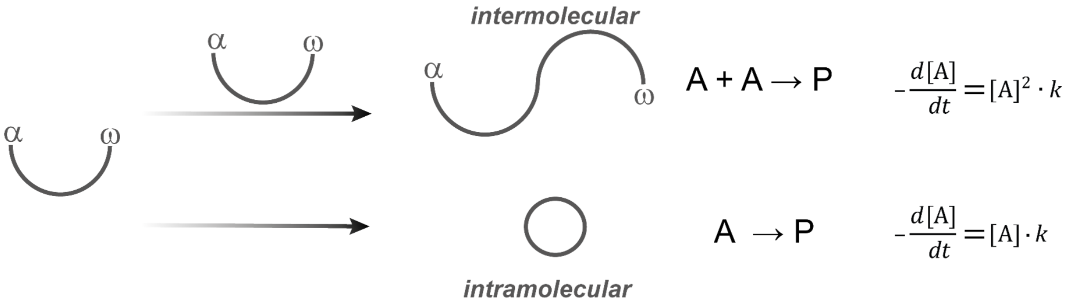

$$A + A \rightarrow P \qquad -\frac{d[A]}{dt} = [A]^2 \cdot k$$

$$A \rightarrow P \qquad -\frac{d[A]}{dt} = [A] \cdot k$$

Figure 1. 12. Oligomer formation from two monomers via an intermolecular reaction or ring closure via an intramolecular reaction. The first- and second-order kinetic rate laws of each reaction are displayed.

The amount of solvent can be reduced, following the concept of pseudo-high dilution which was first reported by Rüggli in 1912.[84] During the synthesis, Rüggli simulated a high dilution by a slow and stepwise addition of all precursors into the boiling solvent. The pace of the addition is thereby crucial. Before the addition of new precursor, all reactive intermediates must have reacted.

Even though the intramolecular ring closure is always the last step in any macrocyclization, a more refined classification of different synthetic strategies is feasible (Figure 1. 13).[85]

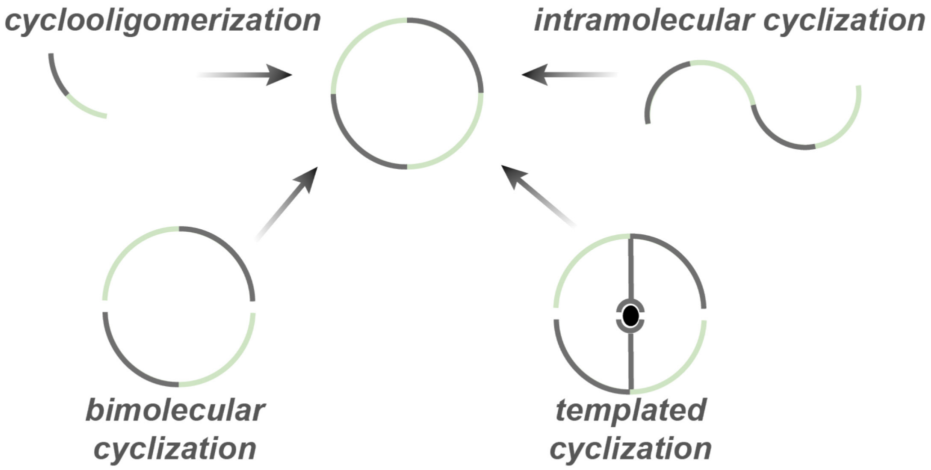

Figure 1. 13. Schematic representation of cyclization strategies: cyclooligomerization; intramolecular cyclization; bimolecular cyclization; templated cyclization.[85]

The cyclooligomerization involves a statistical combination of monomeric units and offers the most rapid access to symmetric macrocycles from simple precursors. The lack of pre-organization inevitably leads to low yields.[86] While other approaches generally give higher yields due to higher pre-organization the synthesis easily becomes excessively long. Hence, a suitable design has to be chosen for each target individually. Many reports in the literature rely on cross-coupling or homo-coupling reactions such as Suzuki–Miyaura,[87] Yamamoto,[88] Eglington,[89] and Sonogashira[85] coupling (Figure 1. 14). The irreversible nature of those metal catalyzed C—C coupling reactions and the lack of kinetic control certainly lead to higher ring-sizes and open-chain molecules.[90,91]

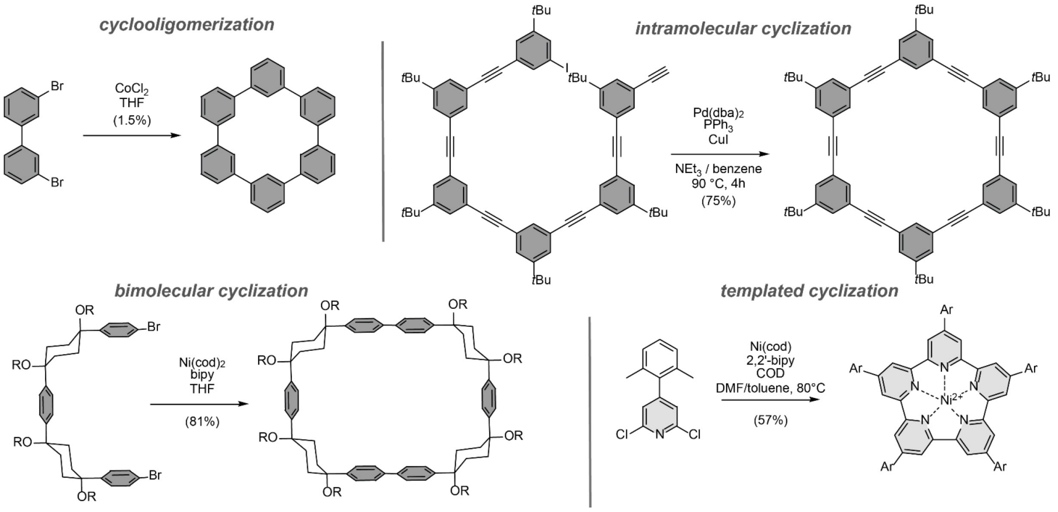

Figure 1. 14. Selected examples of different macrocyclization strategies.[86,92–94]

Another noteworthy concept for macrocyclizations is the templated cyclization of several fragments developed by Höger.[95] The templated cyclization combines low concentration of reactive compounds in the reaction mixture with a high local concentration of reactive sites. A drawback is the high degree of functionalization necessary to have an orthogonally addressable templating group. Other remarkable examples utilize perfluorophenyl−phenyl quadrupole interactions for intramolecular self-assembly,[96] covalent scaffolds,[97] solvent interactions,[98] and metal ions.[94]

The use of dynamic covalent chemistry (DCC) has proven particularly useful to circumvent the previously discussed problems regarding macrocyclizations. Nevertheless, this approach is not applicable to the construction of CPP-type macrocycles as no dynamic aryl–aryl bond formation is known up to date. DCC enables thermodynamic control of the product distribution. Prominent reactions used in such an approach are alkyne-metathesis,[99,100] imine bond formation,[31,101] and disulfide exchange.[102] The geometric prerequisites of the used monomers usually define the thermodynamically most stable cyclic structure and even more complex molecular topologies, like cages or mechanically interlocked molecules can be synthesized.[103] In this case, an additional driving force can be the precipitation of the macrocyclic structure due to reduced solubility in comparison to flexible linear oligomers.

1.4. The Concept of Strain Energy

Already in 1885 Baeyer introduced the concept of ring strain for small saturated hydrocarbons to explain the differences in the synthetic accessibility, as well as in the reactivity of cycloalkanes.[104] Geometric deviations of the ideal bond-angle of non-strained tetrahedral sp^3 carbon (109.28°) were considered as the origin of the ring strain. The theoretical approach of Baeyer included several misconceptions from the perspective of modern organic chemistry and was further improved since. Yet, to honor his pioneering work in this field angle strain is sometimes referred to as Baeyer strain. In this regard the first experimental determination of the molecular strain energy of cyclobutane and cyclopropane was of major importance, as previously articulated theoretical considerations could not be tested. In 1949 increasing accuracy of analytical instruments finally allowed to determine and compare the heat of combustion energy between the cyclic and linear non-strained analogues.[105] Since then, the concept of molecular strain energy has been expanded and nowadays includes bond-, bond angle-, and dihedral-strain as well as attractive intramolecular interactions.

An example that well exemplifies the strain induced by the deviation of the ideal tetrahedral angle of sp^3 carbon is cyclobutane. Although, all four carbons are sp^3 hybridized the square shape of the molecule does not allow a C–C–C bond angle of 109.28°. The actual angle deviates with 88° significantly from the ideal, which makes the angle strain the dominant contributor to the overall strain energy experienced by the molecule (Figure 1. 15). The torsional strain created by the eclipsed positioned hydrogen atoms is responsible for the deviation from the expected 90° bond angle, as cyclobutene has a square shape. The terms torsional strain, dihedral strain, and Pitzer strain can be used alike and define a strain energy created by atoms separated by three bonds that are placed in an eclipsed conformation instead of the more stable staggered conformation.[106,107] Further, the deviation of the C(sp^3)–C(sp^3) bond length of 1.56 Å instead of 1.54 Å adds to the molecular strain energy as bond strain. Other examples displaying the influence of strain on 3D molecular structures include the two stable isomers of cyclohexane, which exists either in the chair or twist boat conformation. Further, the dihedral angle of ca. 44° for biphenyl, is caused by contrary driving forces that balance favorable conjugation between the benzene rings and the strain created by the protons *ortho* to the interphenylene bond.[108]

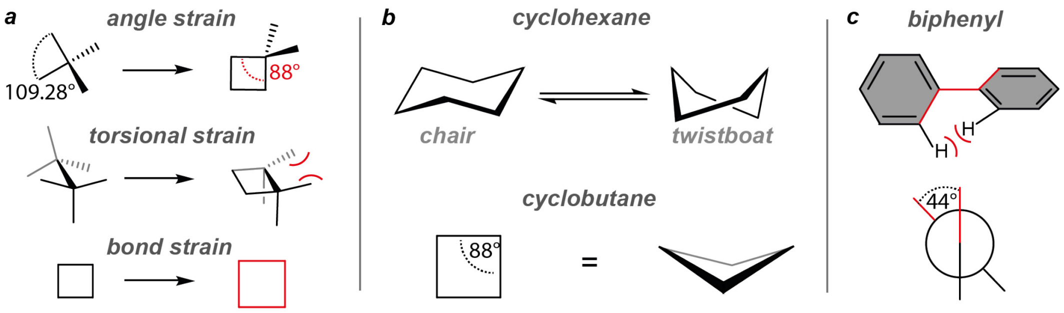

Figure 1. 15. a) Different kinds of strain exemplified on cyclobutane; b) cyclohexane in its two possible conformers (chair and twistboat) and planar 2D representation of cyclobutane as well as in the actual saddle shape; c) biphenyl with an dihedral angle of ca. 44°.

The heat of combustions naturally is an enthalpy and, as an effect, strain energy up to date is always discussed and defined as an internal energy. A refinement of this theory might be necessary in the future if more complex systems are to be compared. While the heat of combustion is probably responsible for the major energy difference between linear and cyclic molecules, this probably does not hold true if twisted cyclic structures are compared against relaxed cyclic structures. Here the differences in entropy resulting from reduction of degrees of freedom are crucial as well.

A major issue in comparing strain energies is the lack of a suitable experimental method to determine these for individual molecules, as non-strained derivatives are either synthetically inaccessible or are not entirely comparable to the parental scaffold. While cyclobutane and but-1-ene have the exact same number of atoms, their differences in heat of combustion would not only include the ring strain, but as well differences in hybridization, which bias the obtained results (Figure 1. 16a). Another well-known example is the energy difference of branched and non-branched alkanes. Even though the hybridization and the atom composition are the same the 1,3-alkyl-alkyl interaction makes the branched alkanes more stable (e.g. butane and isopropane, Figure 1. 16b).[109] Therefore, theoretical calculations are nowadays the method of choice to compare strain energies. Yet, even theoretical treatments are not flawless, but the errors obtained are systematic and allow the determination of trends if the regarded molecular structures are not too different. Of special value is the hierarchy of homodesmotic reactions classified by Wheeler, Schleyer, Houk, and Allen.[110] An excerpt of their classification is shown in the following (Figure 1. 16c).

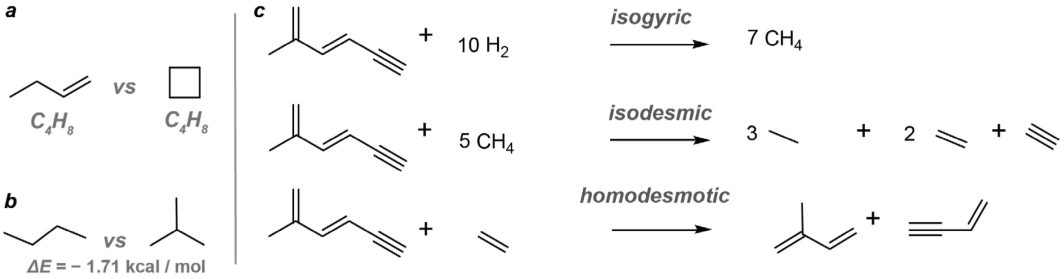

Figure 1. 16. a) Comparison cyclobut-1-ene, cyclobutene; b) comparison butane and isopropane with their corresponding energy difference taken from experimental heats of formation data at 0 K;[109] c) classification of isogyric, isodesmic, and homodesmotic reactions according to the literature.[110]

According to their approach, an isogyric reaction consists of equal numbers of atoms on both sides. An isodesmic reaction consists of an equal number of atoms, and in addition the hybridization of these atoms must be equal on both sides of the equation. Hence, these two approaches are not suitable to calculate molecular strain energies, as torsional strain of linear fragments is completely neglected. The homodesmotic reaction is feasible in the determination of strain energy and was widely applied for the determination of molecular strain energy in CPP-type macrocycles according to the reaction in Figure 1. 17.[111] The characteristics for a reaction to be classified as homodesmotic are equal numbers of carbon atoms in their various states of hybridization in reactants and products, and equal numbers of carbon atoms (regardless of the hybridization state) with zero, one, two, and three hydrogens attached in reactants and products. Many virtual concepts such as π-conjugation or hyperconjugation cannot be treated with this approach, which has to be considered in the interpretation of results created through a homodesmotic equation (Figure 1. 17).

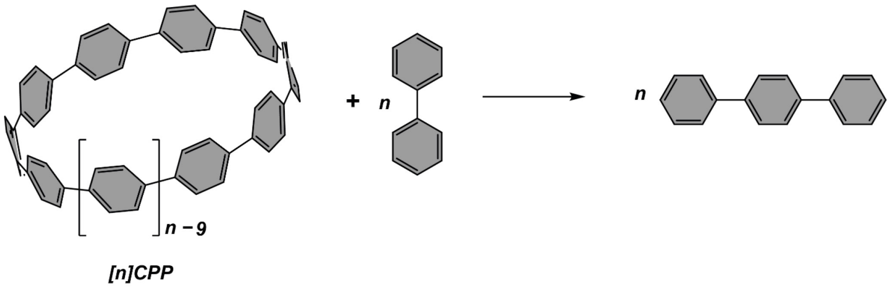

Figure 1. 17. Hypothetical homodesmotic reactions for the calculation of strain energies of [*n*]CPP.

A different approach to calculate strain energy was developed by Cowell and Jasti. Even though their major motivation was to develop a method for strained aromatic macrocycles, it can be used for non-conjugated cyclic hydrocarbons as well.[112] An issue with the use of the homodesmotic equation is that it only gives an absolute value for the molecular strain energy. Consequently, using a homodesmotic equation does not allow to determine where the strain energy is localized in the molecule, thus predictions of reactivity are not conceivable.

Their approach is based on an ideal experiment where one would calculate the trajectory of a macrocycle that undergoes ring opening and subsequent relaxation to an unstrained linear structure. With such a trajectory one could comment on how the energy of each atom changes to release strain energy as the trajectory proceeds. Unfortunately, a macrocycle cannot be broken using common quantum chemistry programs without changing the atomic environment and introducing additional strain into the system (Figure 1. 18).

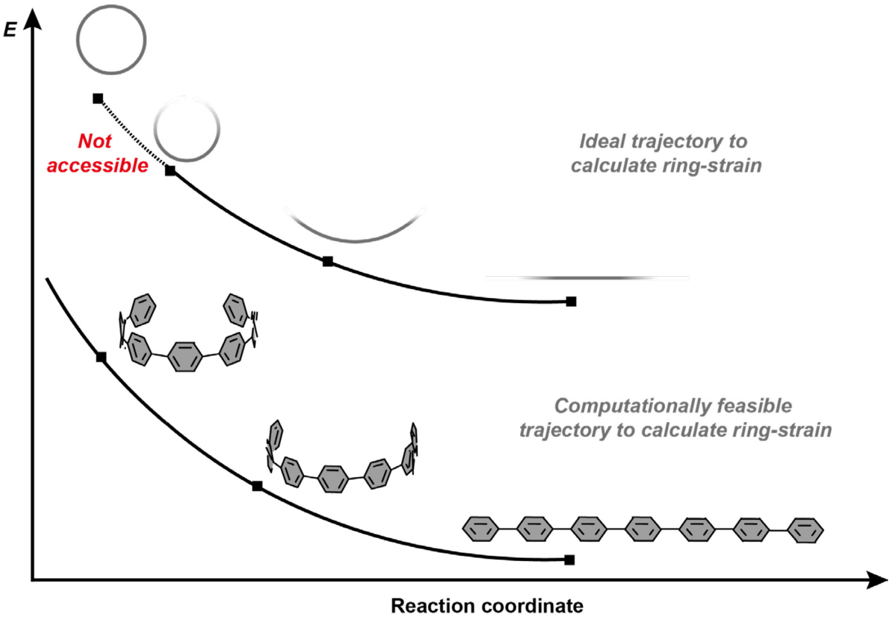

Figure 1. 18. The ideal trajectory begins with the strained macrocycle and ends with an infinite polymer where the strain has been released (top). By removing a part of the molecule, the beginning and end geometries can be connected by a strain releasing trajectory, which can be calculated. This allows the local trajectory of each atom to be determined (bottom).

Therefore, Jasti and coworkers calculate the relaxation trajectory for several equal fragments of the strained molecule. By deleting certain atoms, calculation of the trajectory becomes possible (Figure 1. 18). The trajectory of each atom in the fragment accurately describes the trajectory of each atom in the strained molecule transitioning to an unstrained state. In addition, these trajectories are averaged for multiple fragments and consequently approximate an ideal experiment to determine the strain energy. The strain energy is calculated for every coordinate in the investigated molecule and their approach allows prediction of reactivity that fits well with experimental results.

The trajectory is obtained using standard software for computational chemistry to optimize molecular structures. Within those calculations a force (F) is calculate and a displacement (Δx) is assigned for every atom coordinate. The force can be interpreted as the “strain” experienced by the atom-coordinate. Consequently, the product of force and displacement can be regarded as the strain energy. While the obtained absolute values of strain energy are in accordance with those obtained of the homodesmotic equation, the StrainViz method easily allows to visualize, where the strain is localized (Table 1. 1).[111–113]

Table 1. 1: Comparison of strain energies calculated using the homodesmotic equation and StrainViz (DFT:B3LYP/6-31-G(d) level of theory).

Molecule	Ring strain [kcal·mol^{-1}] –homodesmotic–	Ring strain [kcal·mol^{-1}] –StrainViz–	Ref.
[6]CPP	57.7	57.4	[111]
[7]CPP	65.6	64.2	[111]
[8]CPP	72.2	70.5	[111]
[9]CPP	84.0	81.0	[111]
[10]CPP	96.0	90.8	[111]
[2.2]Para-cyclophane	36.7	37.3	[113]

Molecular strain energy has a unique impact on molecular reactivity and photophysical properties, thus this method can also be applied to reactivity prediction of biorthogonal reactions in chemical biology[114] and in polymer chemistry for ring opening metathesis.[115,116]

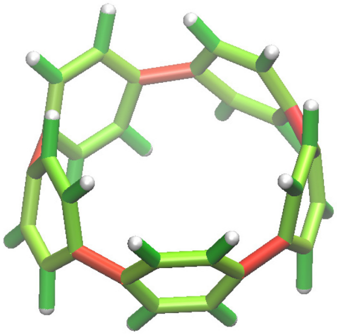

Figure 1. 19. The visualization of the strain energy of [6]CPP displaying the localization of the strain on the inter-phenylene bonds due to predominant dihedral strain. Color code: red high localization of strain energy; green: low localization of strain energy.

1.5. Unique Properties of [n]CPP-type Macrocycles

In contrast to linear poly(*para*-phenylenes) or [*n*]cyclo-*meta*-phenylenes the π-system in [*n*]CPPs is radially oriented leading to an inner and an outer π-surface (Figure 1. 20). The strain energy experienced by the molecular family of [*n*]CPPs in combination with this unusual structure leads to unique physicochemical properties.

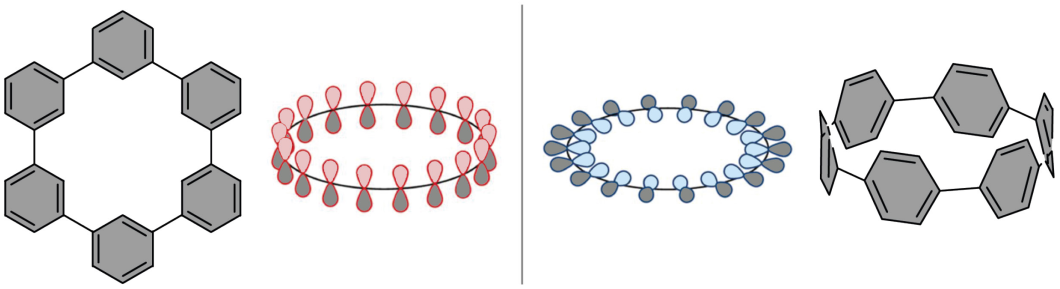

Figure 1. 20. Schematic visualization of the π-electron system of a *meta* connected hexaphenylene (left) in contrast to that of a [6]CPP (right).

Usually the HOMO and LUMO energy gap of oligophenylenes (linear and cyclic) decreases with increasing length due to an increase of conjugation. In stark contrast the HOMO and LUMO energy gap of [*n*]CPPs increases with increasing size (Figure 1. 21a). These results can be explained with the aromaticity of the phenylene units within [*n*]CPPs, which is significantly reduced due to the strain energy experienced by these molecules. The phenylene units tend to take on a quinoidal form rather than a benzenoid form when the number of phenyl units decreases.[117,118] Therefore, the smaller [*n*]CPPs have stronger polyene character compared to their larger analogues. Furthermore, the HOMO/LUMO energies of [*n*]CPPs exhibit odd–even effects. The HOMOs and LUMOs of the odd numbered [*n*]CPPs are higher and lower respectively, than those expected from even [*n*]CPPs. Conformational differences are a possible explanation for this effect, which influence the overall electronic structure. The lowest energy conformation of even numbered [*n*]CPPs generally has a $D_{(n/2)h}$ symmetry, in contrast odd numbered [*n*]CPPs have a C_2 symmetry. These point groups require the phenyl rings to be canted in alternating opposite orientations (Figure 1. 21b). However, in odd numbered CPPs this can only be achieved if one phenyl ring is perpendicular to the ring plane creating a helical twist (Figure 1. 21b, [7]CPP).

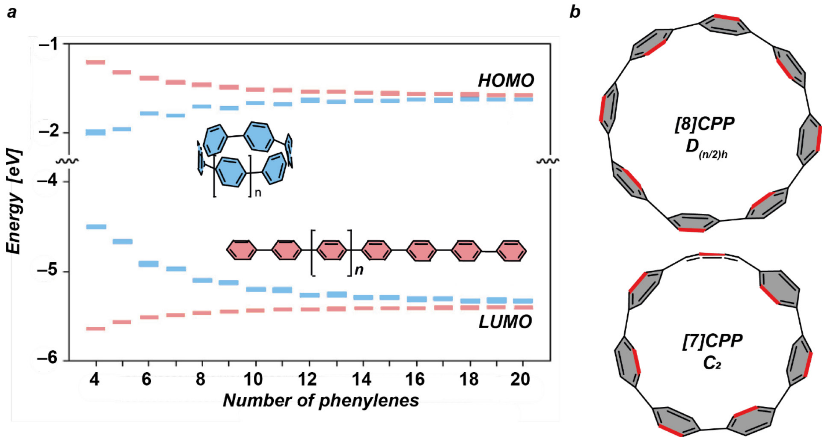

Figure 1. 21. a) Linear *para*-phenylenes and most conjugated materials have a narrowing HOMO–LUMO gap with increasing conjugation length. [*n*]CPPs on the other hand show the opposite trend. Values calculated on the B3LYP/6-31G* level of theory.[65] b) Comparison of even numbered [8]CPP with $D_{(n/2)h}$ symmetry and odd numbered [7]CPP with C_2 symmetry.

The influence of the odd–even effect and a general assimilation in regard to the electronic properties of linear oligo phenylenes occurs naturally with a decrease in strain energy. In this regard, cyclic voltammetry has provided the clearest experimental observation of the lowering LUMO and raising HOMO energy with increasing [*n*]CPP size. Although, experimental conditions vary within the electrochemical characterization [*n*]CPPs clearly become harder to reduce and oxidize as the hoops become lager. Therefore, [12]CPP has a half-wave potential of 0.85 V vs. Fc/Fc^+ while [6]CPP has a half-wave potential of 0.44 V vs. Fc/Fc^+.[65] The photophysical properties of these nano ring structures have been well characterized and a number of striking features for this homologous series are apparent (Table 1. 2).

Table 1. 2: Experimental photophysical properties of [*n*]CPPs (*n* = 5–12).

[*n*]CPP	λ_{max} [nm]	Fluorescence [nm] (quantum yield Φ)
5	335[a]	–(–)[a]
6	340[b]	–(–)[b]
7	340[c]	587 (0.007)[c]
8	340[d]	533 (0.1)[d,g]
9	340[e]	494 (0.38)[e,g]
10	338[f]	466 (0.65)[f,g]
11	340[f]	458 (0.73)[f,g]
12	339[e]	450 (0.81)[e,d]

[a]Ref.:[64] [b]Ref.:[119] [c]Ref.:[120] [d]Ref.: [52] [e]Ref.:[121] [f]Ref.:[51] [g]Ref.:[122]

The data of Table 1. 2 shows that [5]–[12]CPP have a common absorbance maximum between 335–340 nm. An explanation for this observation was postulated by Yamago and co-workers[68] using time dependent density functional theory (TD-DFT). The centrosymmetric nature of [*n*]CPPs leads to a Laporte forbidden HOMO–LUMO transition, as it would conserve the orbital symmetry. Here again, the odd–even effect is of importance as even numbered [*n*]CPPs show an oscillator strength of zero for the HOMO–LUMO transition and for odd numbered [*n*]CPPs—however very low—it is non-zero due to the inherent lower symmetry. Further, [5]–[12]CPP have degenerate HOMO−1/HOMO−2 and an almost degenerate LUMO+1/LUMO+2. Due to the different symmetries of these energy levels, transitions from HOMO−1 or HOMO−2 to the LUMO are allowed. Equally, a transition from the HOMO to the LUMO+1 or LUMO+2 is also allowed. These distinct transitions have orthogonal transition dipole moments responsible for the relatively high extinction coefficients for all [*n*]CPPs. The orbital energy trend for the HOMO−1/HOMO−2 and LUMO+1/LUMO+2 is opposite that of the HOMO and LUMO. Like linear oligophenylenes, the HOMO−1/ LUMO+1 gap narrows with increasing ring size. Figure 1. 22 illustrates that the relative magnitude of the transition is conserved across the homologous series, responsible for the common absorbance of [5]–[12]CPP.[123]

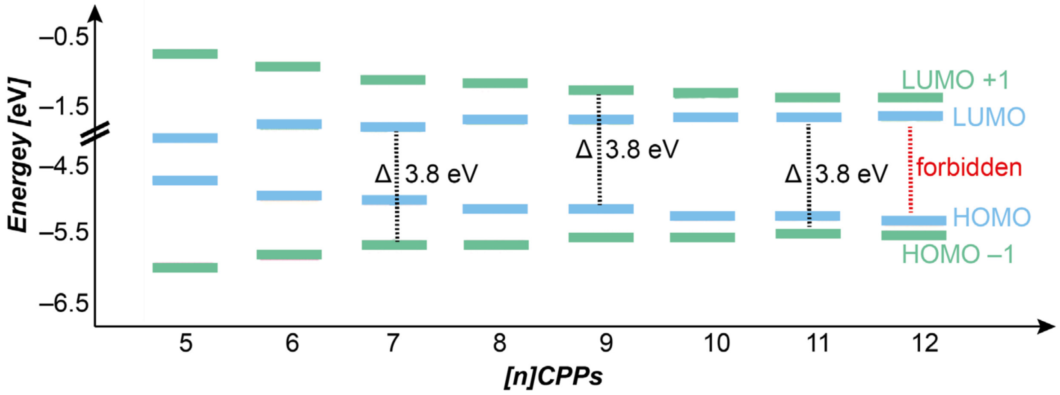

Figure 1. 22. Calculated (B3LYP/6-31G)(d) HOMO, HOMO−1, LUMO, and LUMO+1 energy levels. HOMO−1 and HOMO−2 are nearly degenerate as are LUMO+1 and LUMO+2. For clarity purposes only, HOMO−1 and LUMO+1 energies were used.[123]

In general, the trends observed within the homologous series of pure hydrocarbon [*n*]CPPs is preserved in other derivatives containing hetero atoms or polycyclic aromatic hydrocarbons as well.[70,73,74,79] These unique properties make [*n*]CPPs attractive in other areas such as fluorescence imaging.[124]

1.6. Supramolecular Chemistry of Aromatic Macrocycles

Polycyclic aromatic hydrocarbons, such as perylenediimide or hexabenzocoronene, have been well investigated in supramolecular chemistry in regard of their capability to form ordered π-stacked structures.[125,126] There, the stacking direction is vertical to the molecular plane and a plethora of possible structures have been realized. Contrary, the concave inner and convex outer π-surface of [*n*]CPPs and other strained aromatic macrocycles does not favor stacking vertical to their π-surface. These shape persistent macrocycles rather show a pronounced ability to complex suitable guest molecules with a concave π-surface; such as other macrocycles or fullerenes.[127–129] Additionally, several reports exist on the complexation of disc-like polycyclic aromatic hydrocarbons due to favorable C–H···π interactions (Figure 1. 23).[130–133]

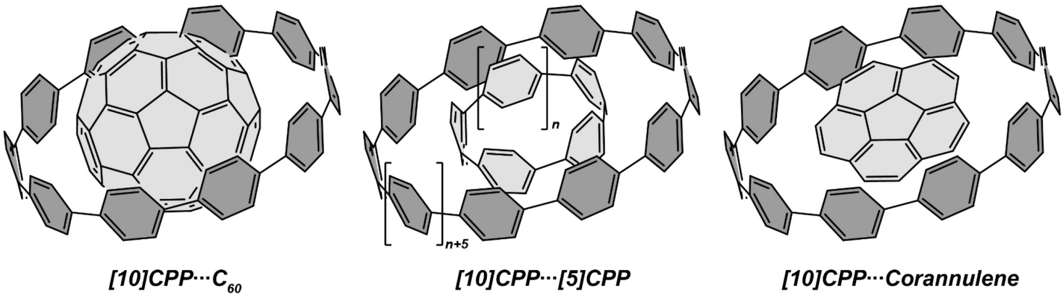

Figure 1. 23. Selection of host guest complexes displaying either a size and shape complementary π-surfaces (left, middle) or symmetry matching and attractive C–H···π interactions (right).[128,132,134]

Among these supramolecular complexes the binding constants determined for [10]CPP and C_{60} are the strongest due to the perfect match of the convex-concave π–surfaces with association constants K_a of $3.6 \cdot 10^6$ M^{-1} (determined by fluorescence quenching titration). Even a size-selective encapsulation is achievable in the presence of other [*n*]CPPs.[128] Construction of short double walled carbon nanotube analogues can also be achieved upon mixing [*n*]CPPs and [*n*+5]CPPs or other complementary shape-persistent aromatic macrocycles. Though, the binding is much weaker compared to fullerenes.[134,135] Binding of corannulene and other disc like molecules is only possible due to arrays of attractive C–H···π interactions.[136,137]

Concerning the inclusion of molecules other than fullerenes or [*n*]CPPs themselves, only a few examples are known.[138,139] This is reasoned by two structural properties of strained aromatic macrocycles. First their central cavity is not an enclosed entity but an open void space. Second the nonpolar π-surface does only offer a limited amount of attractive intermolecular interactions such as C–H···π-bonds, π–π-stacking, and van der Waals (vdW) forces in the form of London dispersion interactions. To circumvent this structural feature and facilitate supramolecular binding of strained aromatic macrocycles to novel guest molecules synthetic modifications are feasible. The introduction of heteroatoms can enable binding as shown by Gaeta and co-workers (Figure 1. 24, left).[140] Another possibility, which is elaborated within this thesis, is the implementation of a high degree of rim-functionalization of the parental [*n*]CPP scaffold to achieve confinement of the inner void volume (Figure 1. 24, right).[79,141]

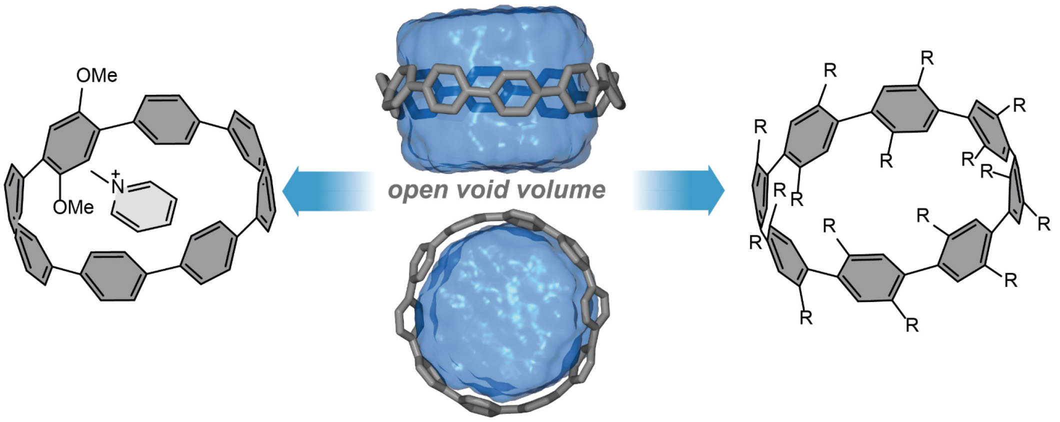

Figure 1. 24. A dimethoxy derivative of [8]CPP enabling binding of *N*-methylpyridine (left), visualization of the open void volume in the center of a [10]CPP (middle), and potential confinement strategy due to a high degree of functionalization (right).

1.7. Chiral Aromatic Macrocycles

Chirality is of major importance regarding the physical properties of CNT (as discussed in Section 1.1). In that respect several chiral [*n*]CPP-type macrocycles have been synthesized and their properties investigated. Hereby, one has to differentiate between two classes of chiral [*n*]CPP-type macrocycles. One can be seen as a true smallest repeating unit of a chiral CNT (Figure 1. 25a) which so far can only be synthesized as a racemic mixture or diastereomers.[142–146] Depending on the diameter of these macrocycles the inversion barrier can be low, resulting in rapid isomerization at ambient temperatures, which renders the chiral resolution impossible. Contrary, several chiral [*n*]CPP-type macrocycles have been synthesized and even though they do not correspond to a CNT they offer several unique features making them attractive targets. Due to greater conformational stability, their chiral separation has been successful. They can be assigned to the class of shape persistent conjugated macrocycles and their chirality is introduced by a chiral subunit as for example [6]helicene (Figure 1. 25b).[147] For the design of chiral materials, especially chiral macrocycles, the conformational stability is an essential criterion in order to maximize the chiroptical properties. A useful approach to generate conformational stability is to induce rigidity and consequently shape-persistency in the chiral macrocycle. Since the synthesis of the first carbon-rich shape-persistent macrocycle in 1964 by H. Staab (Figure 1. 14, top left) numerous rigid macrocycles are known today (Figure 1. 25c).[86,148]

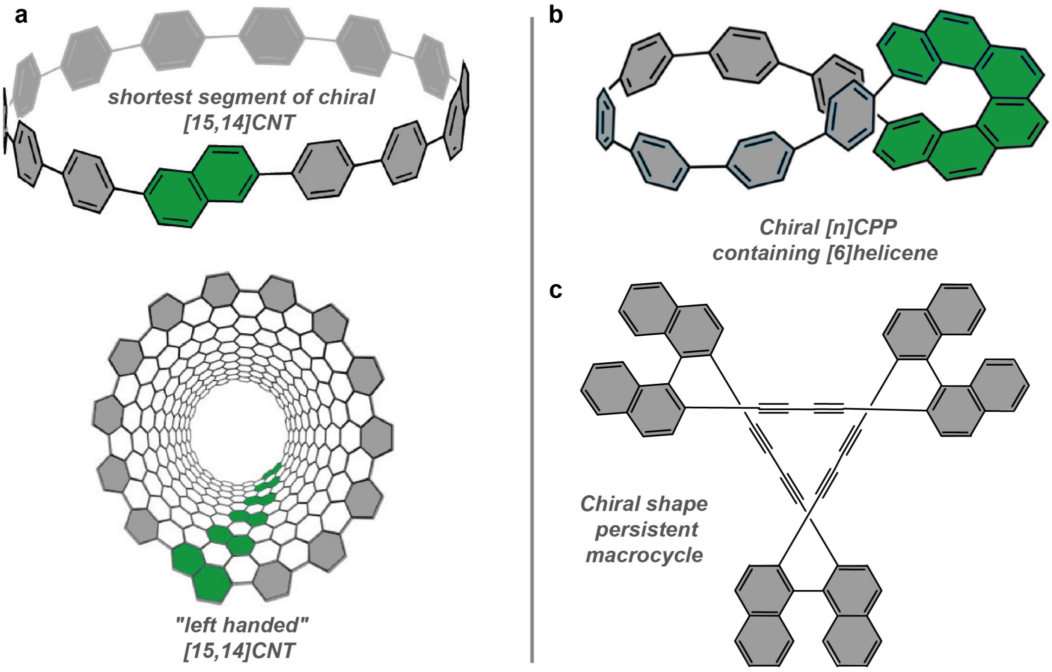

Figure 1. 25. a) A naphthalene containing [*n*]CPP as the shortest repeating unit of a chiral [15,14]CNT;[149] b) a [6]helicene containing [*n*]CPP-type macrocycle with inherent chirality (only one enantiomer displayed);[147] c) a shape persistent chiral conjugated macrocycle (only one enantiomer displayed).[150]

In the presented case the introduction of chiral [6]helicene does not only result in the synthesis of two enantiomers, but also creates a Möbius topology in regard of the delocalized π-electron system.[151] The synthesis and study of conjugated shape persistent macrocycles has been highly investigated, because of the unique performance expected from these molecules, such as circular dichroism (CD) and circularly polarized luminescence (CPL).[152] Electronic CD originates from the difference in absorptivity of intrinsically chiral chromophores for left and right circularly polarized light. Therefore, the primary observable in CD spectroscopy is the molar circular dichroism ($\Delta\varepsilon$) defined as a function of the wavelength (Equation 1.1).

$$\Delta\varepsilon(\lambda) = \varepsilon_{\mathrm{L}}(\lambda) - \varepsilon_{\mathrm{R}}(\lambda) \qquad (1.1)$$

Here, $\varepsilon_{\mathrm{L}}(\lambda)$ and $\varepsilon_{\mathrm{R}}(\lambda)$ are the molar extinction coefficients for left and right circularly polarized light. The magnitude of CD can be quantified by the absorptive dissymmetry factor (g_{abs}), which is the ratio of molar CD ($\Delta\varepsilon(\lambda)$) to molar extinction coefficient ($\varepsilon(\lambda)$) (Equation 1.2).

$$g_{\mathrm{abs}} = \frac{\varepsilon_{\mathrm{L}}(\lambda) - \varepsilon_{\mathrm{R}}(\lambda)}{1/2(\varepsilon_{\mathrm{L}}(\lambda) + \varepsilon_{\mathrm{R}}(\lambda))} \qquad (1.2)$$

In the literature the absorptive dissymmetry factor is often referred to as the anisotropy factor or simply g factor.[153]

Similarly, CPL spectroscopy measures the difference in intensity (ΔI) between the left (I_L) and right (I_R) circularly polarized emission from intrinsically chiral fluorophores (Equation 1.3).

$$\Delta I(\lambda) = I_\mathrm{L}(\lambda) - I_\mathrm{R}(\lambda) \tag{1.3}$$

Generally, the evaluation of absolute I and ΔI is difficult in a typical CPL measurement. Therefore, the relative intensity difference of left and right circularly polarized emission is used to quantify the degree of dissymmetry of CPL.[154] This luminescence dissymmetry factor is given by the following expression (Equation 1.4).

$$g_\mathrm{lum} = \frac{I_\mathrm{L}(\lambda) - I_\mathrm{R}(\lambda)}{1/2(I_\mathrm{L}(\lambda) + I_\mathrm{R}(\lambda))} \tag{1.4}$$

Optical functional materials with CPL activity have recently gained attention in various areas such as sensors, asymmetric synthesis as well as display and optical storage devices.[155–157] However, most chiral materials have very small dissymmetry factors (g_lum, < 0.01), resulting in a great bottleneck for potential applications. Therefore, it would be highly desirable to maximize g_lum. In the following it will be briefly discussed how this can be done in general, and specifically why chiral aromatic macrocycles offer exceptional opportunities to do so.

For small molecules CP emission and absorption depend on the chirality of the ground and excited electronic states, which is directly linked to the chirality of the chromophore. To describe CD and CPL quantum chemically a single electronic parameter can be used, i. e. rotational strength (R), which is the imaginary part of the scalar product of the electric ($\boldsymbol{\mu}_{ij}$) and magnetic ($\boldsymbol{m}_{ij}$) transition dipole moments of a given electronic transition between i and j states (Equation 1.5) and θ refers to the angle between the dipole moments.[158]

$$R = \mathrm{Im}\left(\boldsymbol{\mu}_{ij} \cdot \boldsymbol{m}_{ij}\right) = \left|\boldsymbol{\mu}_{ij}\right| \cdot \left|\boldsymbol{m}_{ij}\right| \cdot \cos(\theta) \tag{1.5}$$

The intensity of absorption and emission is proportional to the strength of the relevant dipole (D) given by the following equation 1.6.

$$D = \left|\boldsymbol{\mu}_{ij}\right|^2 \cdot \left|\boldsymbol{m}_{ij}\right|^2 \tag{1.6}$$

Where $|\boldsymbol{\mu}_{ij}|>>|\boldsymbol{m}_{ij}|$ is true on the molecular scale. Taking several conditions and approximation into account (described in detail elsewhere)[159–161] the dissymmetric factors g_{abs} and g_{lum} for an isotropic bulk sample are given by equation 1.7.

$$g = 4R/D \tag{1.7}$$

Equation 1.7 can be approximated to equation 1.8 as well.

$$g \approx 4\,\frac{|\boldsymbol{m}_{ij}|}{|\boldsymbol{\mu}_{ij}|}\cos(\theta) \tag{1.8}$$

According to equation 1.8 the dissymmetry is sensitive to the magnitude and relative orientations of the magnetic and electronic transition dipoles within the chromophore. Usually the magnetic dipole moment ($\boldsymbol{m}$) is much smaller than that of electronic transitions and in combination with the non-optimized spatial arrangement of these dipoles (θ) the resulting g-factors for the majority of chiral molecules are small (ca. 10^{-2}).[162] This trend is reasonable if one takes the electric dipole approximation into account, which assumes the wavelength of light is much larger than the molecule that it interacts with.[163] As a consequence the dissymmetry factor is even smaller if one tries to detect vibrational circular dichroism (VCD), where the wavelengths are about ten times longer than for the electronic transitions of CD in the UV/vis range. Here, typical VCD g-factors remain on the order of 10^{-4}.[164] A way to increase the g-factor is for example to optimize the spatial arrangement between the dipoles. A breakdown of the electric dipole approximation can be achieved either by decreasing the wavelength or by exploiting larger molecules and structures.[162,165] One thing that must always be kept in mind upon trying to increase the dissymmetry factor is that a simple increase of the chromophore's size is only feasible if it is strongly coupled to the chiral center. A very instructive example is shown in Figure 1. 26. While the g_{abs} for phenylethylammonium perchlorate is very low with $8\cdot10^{-5}$ in contrast the g_{abs} for [6]helicene is at $9\cdot10^{-3}$ because the chiral element is the chromophore itself.[153,166]

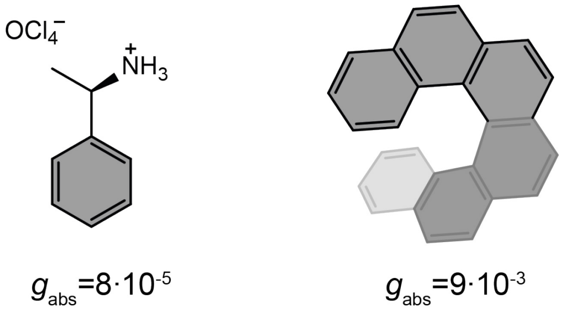

Figure 1. 26: Phenylethylammonium perchlorate and [6]helicene with their corresponding g_{abs} values. [153,166]

Even though, increasing the size of a helicene to increase its chiral responsiveness is obvious, the outcome of this procedure is discontinuous after six rings. Interestingly, this correlates to the length at which the molecule achieves one full helical turn. This leads to the conclusion that a pure assessment of size versus chiroptical response is neither trivial nor appropriate in many of these cases, as other mechanisms such as chromophore coupling play a role.[167]

Another way to increase the intrinsic chiroptical activity is to exploit forbidden transitions. The strength of an electronic transition is determined by the magnitude of its transition dipole moment ($\boldsymbol{\mu}$), which can be assessed using a set of selection rules. The spin must be conserved (spin selection rule) and the transition must involve a change in parity of the wavefunctions. In contrast, for an allowed magnetic dipole transition, the parity of the initial and final state of the transition must be conserved. Consequently, the electric transition dipole moment involves the translation of charge density and the magnetic transition dipole requires a rotation of charge density. The combination of translation and rotation is responsible for the helical interaction with the light. The difference in the selection rules means that in magnetically allowed transitions the ratio of $|\boldsymbol{m}|$ and $|\boldsymbol{\mu}|$ can amplify the dissymmetry according to equation 1.8, but often to the detriment of the overall emission intensity.[168] In 1967, the very first example of CPL from a small organic molecule was reported for trans-β-hydrindanone (*trans*-bicyclo[4.3.0]nonan-8-one), a cyclic chiral ketone (Figure 1. 27).[169]

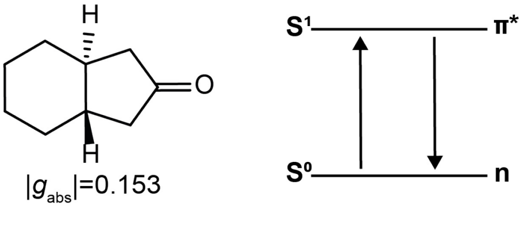

Figure 1. 27. Trans-bicyclo[4.3.0]nonan-8-one, its g_{abs} and a simplified diagram of the involved transitions.

Later on, similar behavior was found for other cyclic chiral ketones and it was reasoned that the large dissymmetric factors occur due to the magnetically allowed, but electronically forbidden, n→π* transition of the locally C_{2v}-symmetric carbonyl group. Yet, most ketones are not suitable for CPL emissive applications due to their low luminescence quantum yields (the electronic transition is forbidden) together with the limited tuneability of their emission wavelengths. Furthermore, their $|g_{\mathrm{lum}}|$ values are often considerably lower than $|g_{\mathrm{abs}}|$ (0.025 for *trans*-bicyclo[4.3.0]nonan-8-one). This discrepancy in the *g*-factor of absorption and emission is a consequence of geometric changes of the C=O bond in the excited state.[168]

An alternative approach is to design the molecule to better balance the contributions of $|\boldsymbol{\mu}|$ and $|\boldsymbol{m}|$ and to optimize the angle θ between them. An elegant way to achieve this for π→π* transitions was demonstrated by Isobe and co-workers using a cylindrical molecule (Figure 1. 28).[68] In this example, the chiral chromophore extends over the entire [*n*]CPP-type macrocycle, in a way that the sum of the $\boldsymbol{\mu}$ of individual electrons cancel out in the *xy*-plane ($\boldsymbol{\mu}_x = \boldsymbol{\mu}_y = 0, \boldsymbol{\mu}_z \neq 0$). The magnetic dipole $\boldsymbol{m}$ originates from the change in angular momentum due to the movement of an individual electron during an electronic transition and is proportional to the vector product of $\boldsymbol{\mu}$ and the displacement vector $\boldsymbol{r}$. Since $\boldsymbol{\mu}_x = \boldsymbol{\mu}_y = 0$, and $\boldsymbol{r}$ radiates towards the outside of the macrocycle, the overall $\boldsymbol{m}$ is orientated antiparallel to the z-direction. The resulting $\boldsymbol{\mu}$ is parallel to the C_2 axis that is orthogonal to the xy-ring plane. The resulting angle θ equals 180°, which gives a value of −1 for cos(θ) and consequently the dissymmetry is comparatively large, with a solution $|g_{\mathrm{lum}}|$ of 0.15 at 443 nm and a fluorescence quantum yield of 80%.

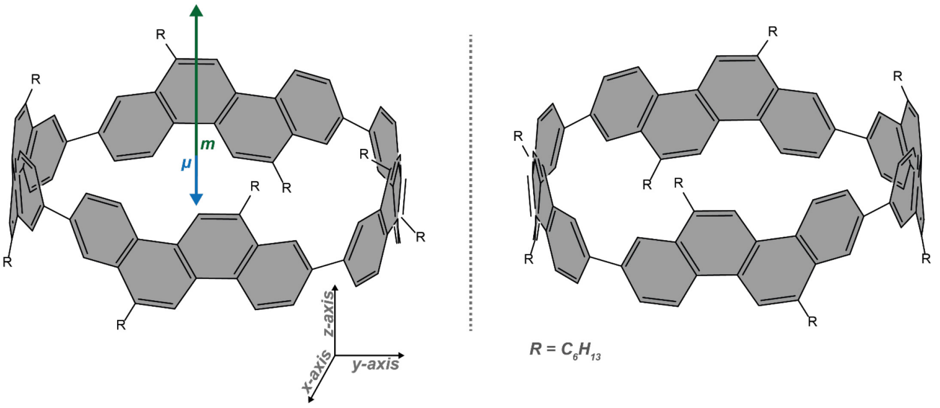

Figure 1. 28. The two enantiomers of the chrysene macrocycle with the orientation of the transition dipole moments $\boldsymbol{\mu}$ and $\boldsymbol{m}$.

This example shows that careful molecular design allows to create rigid conjugated macrocycles with CPL properties unusual for pure hydrocarbons.

1.8. Motivation and Aim of the Thesis

In this thesis, several molecular designs of [*n*]CPP-type macrocycles are investigated with the final goal to use them as monomers for the bottom-up synthesis of heteroatom-doped CONTs. The synthesized macrocycles are studied as supramolecular host for a variety of guests. Further the introduction of *pseudo*-linear chiral building blocks into macrocyclic molecules was explored, as they are attractive models to study the design rules for chiroptical activity.

In c*hapter 2*, we report on a set of strained aromatic macrocycles based on highly functionalized pyrene with size-dependent photophysical properties. The *K*-region of pyrene was functionalized to access highly functionalized [*n*]CPP-type macrocycles that could function as monomers for the bottom-up construction of CONTs. Furthermore, the ethylene glycol groups decorate the outer rim and thereby confine the space inside the macrocycles. This confined space is especially pronounced for *n*= 4, 5, which leads to an internal binding between the ether-decorated [5]cyclo-2,7-pyrenylene and shape-complementary crown ether–cation complexes. Unambiguous structural characterization of the ether-decorated [*n*]cyclo-pyrenylenes as well as one of their host–guest complexes has been achieved by single-crystal X-ray analysis. The presented rim functionalization does not allow further investigation towards the synthesis of CONTs due to ineffective deprotection, but the confinement strategy makes these macrocycles an attractive supramolecular host family with a favorable, size-independent read-out signature and binding capabilities extending beyond fullerene guests.

In c*hapter 3*, we report on a macrocycle design that is overall less strained and bears a large cavity with a concave π-surface. The reason for the overall reduction of strain energy is the use of an ethylene glycol-decorated [6]cyclo-meta-phenylene (CMP) as a subunit for the final nanoring. The preassembly is achieved via a four-fold $Au(I)_2$–aryl metallacycle with an overall square arrangement. The corners consist of rigid dinuclear gold(I) complexes previously known to form triangular metallacycles. The interplay between the conformational flexibility of the [6]CMP macrocycle—that can adopt a “chair” or “boat” conformation—and the rigid dinuclear gold(I) moieties enable the square geometry, which is revealed by single-crystal X-ray diffraction. The formation of the gold complex shows size-selectivity compared to an established alternative route using platinum(II) complexes as corner motifs. Upon oxidation-induced reductive elimination an all-organic ether-decorated carbon nanoring is synthesized and investigated as a host for the complexation of large guest molecules with a suitable convex π-surfaces. Isothermal NMR binding titration reveals binding of [6]cycloparaphenylene ([6]CPP), [7]CPP, C_{60}, and C_{70}.

In c*hapter 4*, a 1,14-dimethyl-[5]helicene is used as a pseudo linear building block to be implemented into a [*n*]CPP-type macrocycle. While the formation of a metallacycle using platinum(II) complexes as corner motifs cannot be observed a side product formation was detected. This finding led to the investigation of two 1,14-dimethyl-[5]helicene derivatives bearing radical stabilizing groups at the 4,11-positions to afford two spin-state switches. Irradiation of these diamagnetic molecules with an LED light source at cryogenic temperatures leads to the formation of a stable paramagnetic state, which is confirmed by EPR spectroscopy. The underlying mechanism is a 6π retroelectrocyclization. Through a thermal stimulus the paramagnetic forms react back to the diamagnetic form. The switching can be monitored with UV/vis- and EPR spectroscopy. These studies are accompanied by electrochemical investigations.

Chapter 2

Confining the Inner Space of [*n*]Cyclo-2,7-pyrenylenes

Parts of this chapter are already published in:

Angew. Chem. Int. Ed. **2021**, *60*, 14909–14914
DOI: https://doi.org/10.1002/anie.202102809

Authors: Niklas Grabicki, Khoa T. D. Nguyen, Steffen Weidner, Oliver Dumele

and

Synlett **2022**, *33*, 1–7
DOI: https://doi.org/10.1055/s-0040-1719853

Authors: Niklas Grabicki, Oliver Dumele

Chapter 2: Confining the Inner Space of [*n*]Cyclo-2,7-pyrenylenes

---

Strained aromatic macrocycles have distinct properties compared to their linear counterparts such as shape persistence, enhanced solubility, and the ability to complex guests.[170–172] *Among them, conjugated aromatic cyclo-para-phenylenes (CPPs) offer several unique features such as size independent UV/vis absorption, size dependent fluorescence and radially oriented π-systems leading to an inner and outer π-surface.*[123,173–175] *They represent the smallest repeating unit of arm-chair carbon nanotubes and thus have been investigated as a molecular model system that allows to study effects such as strain, curvature, diameter size and chirality on a defined and soluble entity.*

2.1. Design of Highly Functionalized [*n*]CPP-type Macrocycles

There are several prerequisites that need to be met to make a monomer suitable for the bottom-up synthesis of CONTs. First of all it is of major importance that the CONT is the most stable product from a thermodynamic point of view because otherwise the principles of reticular chemistry cannot be applied efficiently.[25] To achieve this requirement the monomer should be shape persistent and express a high degree of symmetry because otherwise the preorganization might be too diminutive and multiple orientations may limit the conversion towards a defined nanostructure.[176] Further, the macrocycle needs to be accessible in larger quantities, as the efficient synthesis of COFs still relies on empirical reaction screening requiring several 100 milligrams of monomer even for well-established 2D and 3D COFs. The rich chemistry developed on pyrene itself and the already reported [4]cyclo-2,7-pyrenylene[67] **1** make this polycyclic aromatic hydrocarbon a feasible starting point to devise a highly functionalized aromatic macrocycle.[177] Symmetrically substituted pyrene-4,5,9,10-tetrone (**2**) is an excellent starting point to develop a shape persistent, highly functionalized CPP-type macrocycle. The high number of electron-withdrawing groups turn **3** not only into an attractive molecular target but in theory enable phenazine condensation with suitable diamines (Figure 2. 1).

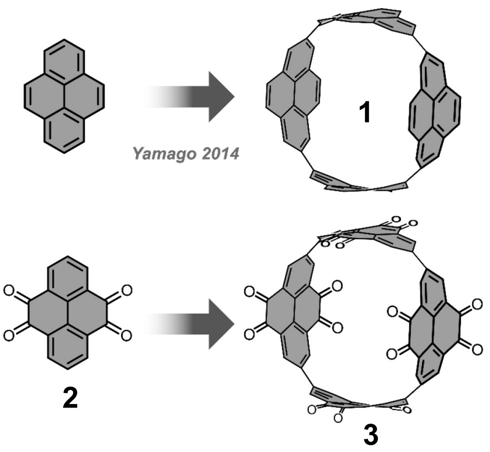

Figure 2. 1. Reported pyrene based macrocycle (top) and an adapted molecular design to fulfil the requirements for a CONT monomer.[67]

The molecular shape of the pyrene subunit leads to an extended π-conjugated surface –compared to parental [*n*]CPP– , which further creates an accessible volume that might prove interesting for host–guest interactions. The oxidation of the *K*-region of pyrene to pyrene-4,5,9,10-tetrone (**2**) has been reported previously and leads to the introduction of reactive diketone functionalities.[178] As earlier discussed (Figure 1. 2.), these diketones have been shown to undergo phenazine condensation in a dynamic reversible fashion under solvothermal conditions. Therefore, pyrene-4,5,9,10-tetrone has been reported to form porous and crystalline COFs with triphenylene hexamine as the C_3-symmetric tritopic linker.[179] Initially the mixing of [4]cyclo-2,7-pyrenylene macrocycle **3** and 1,2,4,5-tetraaminobenzene will lead to the formation of various oligomers with defects, but reversible bond formation and cleavage should favor the tube growth (Figure 2. 2).

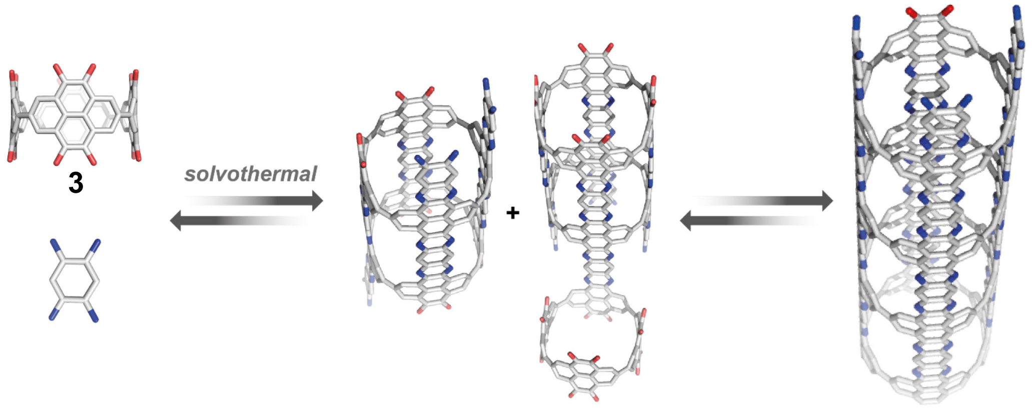

Figure 2. 2. Schematic representation of a bottom up CONT from a [4]cyclo-2,7-pyrenylene bearing diketone functionalities (red) and 1,2,4,5-tetraaminobenzene (color code: carbon = grey, oxygen = red, nitrogen = blue).

The rigid geometry of the macrocycle only allows a maximum of covalent bonds formed upon 1D lateral growth. The synthesized tubes would form diameter selective single walled CONTs, which is so far not possible using currently established methods of CNT manufacturing.[180]

2.1.1. Retrosynthetic Analysis of Highly Functionalized [4]cyclo-2,7-pyrenylene

The diketone functionality is known to be redox active, which makes the protection with ethylene glycol groups necessary throughout the synthesis. Another advantage of the introduction of the protecting groups is the confinement of the inner space of the macrocycle **4[4]**, opening up potential applications for this molecule as a supramolecular host ([4] denoting the amount of repeating units *n* within the macrocycle). Synthesizing [*n*]CPP-type macrocycles consisting of a multiple of four polycyclic aromatic moieties has been achieved multiple times using Pt(II) complexes as corner motives.

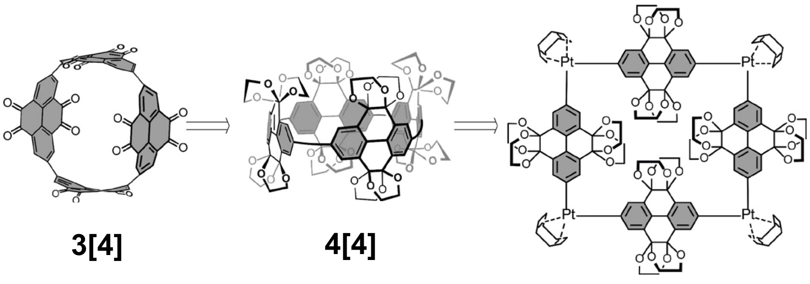

Figure 2. 3. Retrosynthetic analysis of **3[4]** to the metallacycle **5[4]**.

The synthesis of metallacycles such as **5[4]** (Figure 2. 4) can be achieved either from a corresponding diboronic ester **6** or from (bis)trimethyl-tin derivative **8**.[52,142] Diboronic ester **6** can be synthesized via Ir-catalyzed C–H borylation from protected pyrene-4,5,9,10-tetrone **7**. The organostannane **8** can be synthesized from the protected and brominated pyrene-4,5,9,10-tetrone **9**, which makes the overall step count longer for this route.[181,182] Ethylene glycol protection of **2** or **10**, as well as oxidation of pyrene using $RuCl_3$ were previously reported in the literature.[178,183–185]

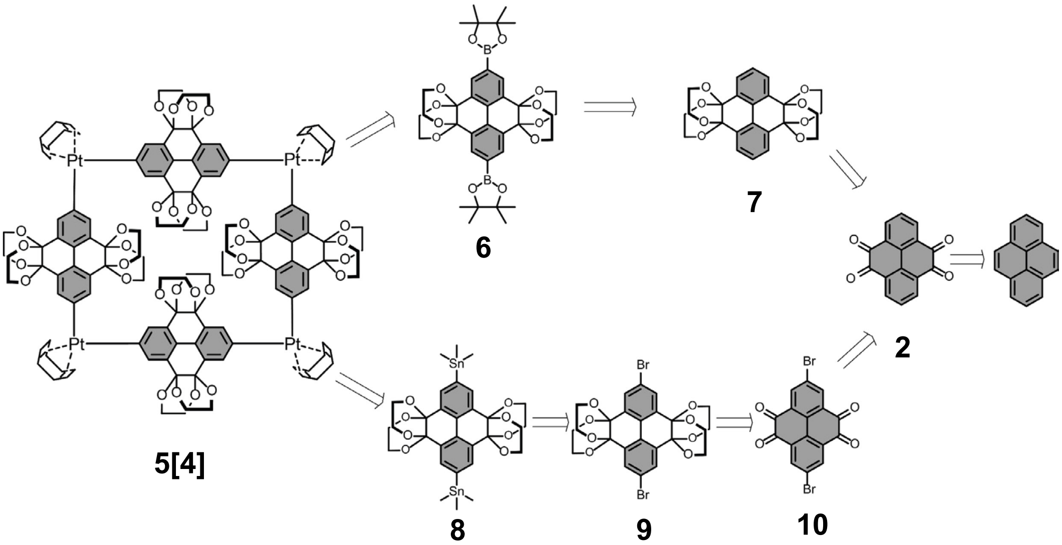

Figure 2. 4 Retrosynthetic analysis of metallacycle **5[4]** to commercially available pyrene.

2.2. Synthesis of [*n*]Cyclo-2,7-pyrenylene Derivatives

First the shorter synthetic route targeting (di)boronic ester **6** was established. Oxidation of pyrene to pyrene-4,5,9,10-tetrone and ethylene glycol protection was achieved based on reported literature procedures.[178,186,187] Iridium catalyzed CH-borylation yields the desired metallacycle precursor **6** in gram scale. This chemical transformation from **7** to **6** was previously unknown but published during the course of this thesis with a similar synthetic procedure as the one developed by us (Figure 2. 5).[182]

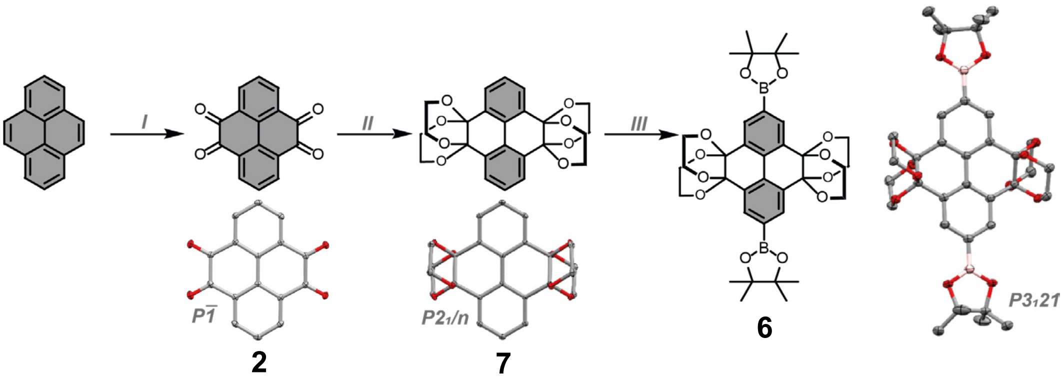

Figure 2. 5. Synthetic procedures I) $RuCl_3$, $NaIO_4$, $CH_3CN/CH_2Cl_2/H_2O$, 0 °C, 30 min, then 25 °C, 2 h, 25% yield; II) ethylene glycol, camphorsulfonic acid, MeOH, 120 °C, 24 h, 73%; III) 4,4′-di-*tert*-butyl-2,2′-bipyridine, [Ir(OMe)(COD)]$_2$, bis(pinacolato)diboron, 1,4-dioxane, 120 °C, 18 h, 84%; towards borylated building block **6** and corresponding single crystal X-ray structures.

The synthesized compound **6** can be readily transformed into metallacycle **5[*n*]** according to a procedure reported originally by Yamago for arylstannanes and by Isobe for aryl boronic esters (Figure 2. 6).

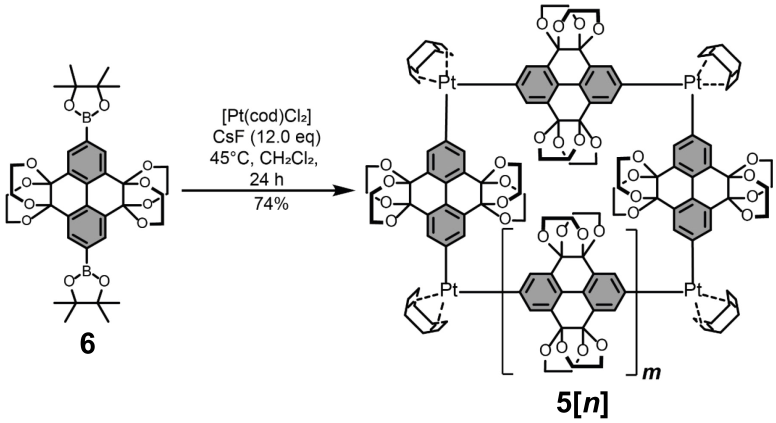

Figure 2. 6. Synthesis of platinum metallacycle **5[*n*]**.

The platinum-mediated macrocyclization with subsequent reductive elimination is known to result in several ring sizes of the final all-organic macrocycles.[69,71,73,74,76,188] Two effects are known to be responsible for this lack of selectivity. In theory, the platinum macrocycle with equally long subunits should always result in an overall square shaped complex due to the 90° angle of the square planar coordination of platinum(II). Nevertheless, deviations of this ideal angle enable other shapes for the synthesized metallacycles, resulting in a mixture of differently sized congeners of **5[*n*]**.[75,189,190] Further, the formation of $Pt(PPh_3)_{4-x}$, which evolves upon addition of PPh_3 and reductive elimination. The reactive $Pt(PPh_3)_{4-x}$ has been experimentally shown to insert into strain-activated C–C bonds.[75,191] Subsequent ligand exchange of cyclic fragments results in a variety of ring-sizes that can emerge even from one single-sized metallacycle (*vide infra*).

Recycling gel permeation chromatography (*r*GPC) revealed such behavior for the displayed metallacycle synthesis as well. Higher selectivity has been reported in the literature upon screening different solvents, yet the underlying rational to these observations has not been revealed up to date.[192] In our case a screening of different solvents did not lead to an improvement regarding the size-selective synthesis of metallacycles **5[*n*]**. The obtained chromatogram using $C_2H_2Cl_4$ as reaction solvent seems to contain the least number of linear oligomers (broad shoulder at the beginning) and only two defined macrocyclic species (Figure 2. 7).

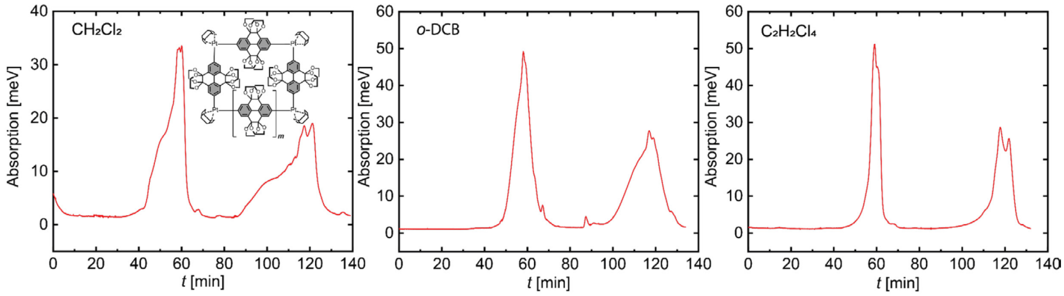

Figure 2. 7. Chromatograms of the first two cycles of the *r*GPC (eluent chloroform) separation from platinum mediated macrocyclization reactions obtained from individual experiments, where all parameters were kept constant except for the solvent (denoted in each spectra).

Nevertheless, *r*GPC analysis of the following reaction step (Figure 2. 8 top) reveals the formation of **4[*n*]**, as a mixture of different sized cyclic congeners and linear oligomers (Figure 2. 8 bottom) regardless of the solvent used for the platinum mediated macrocyclization.

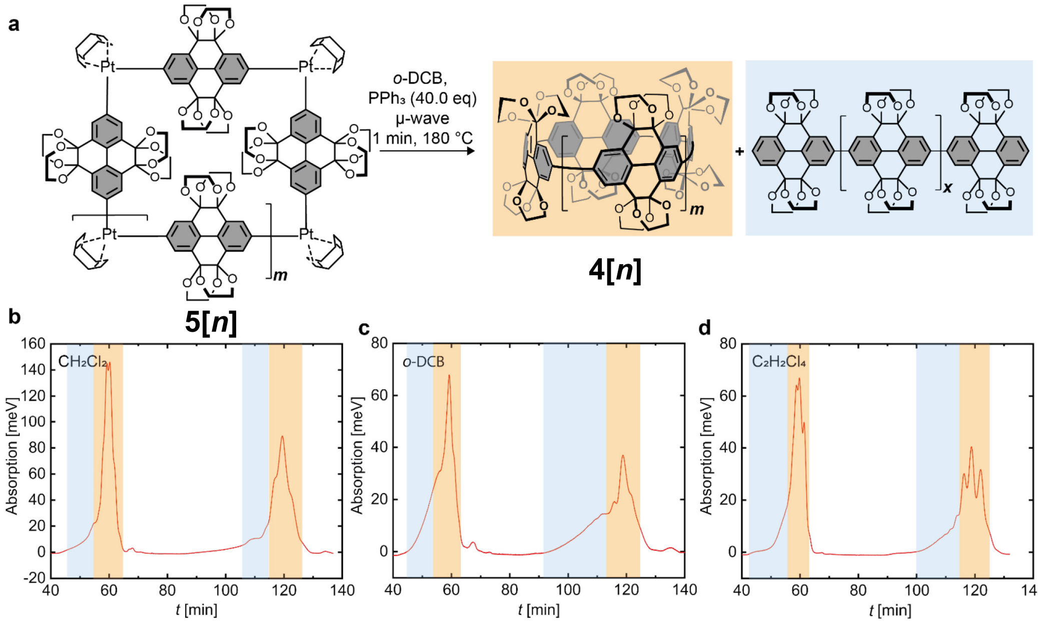

Figure 2. 8. a) Reductive elimination of metallacycle mixture **4[*n*]** in *o*-DCB. The first two cycles of *r*GPC purification (eluent chloroform) of the crude reaction mixture of the reductive elimination, where metallacycles were previously prepared in b) CH_2Cl_2, c) *o*-DCB, d) $C_2H_2Cl_4$ as the solvent.

MALDI-TOF MS analysis (Figure 2. 9) of the crude reaction mixtures confirmed the occurrence of five different ring sizes with the smallest congener consisting of four pyrenylene subunits and the largest detectable consisting of eight subunits. Isolation of the individual congeners was accomplished by *r*GPC.

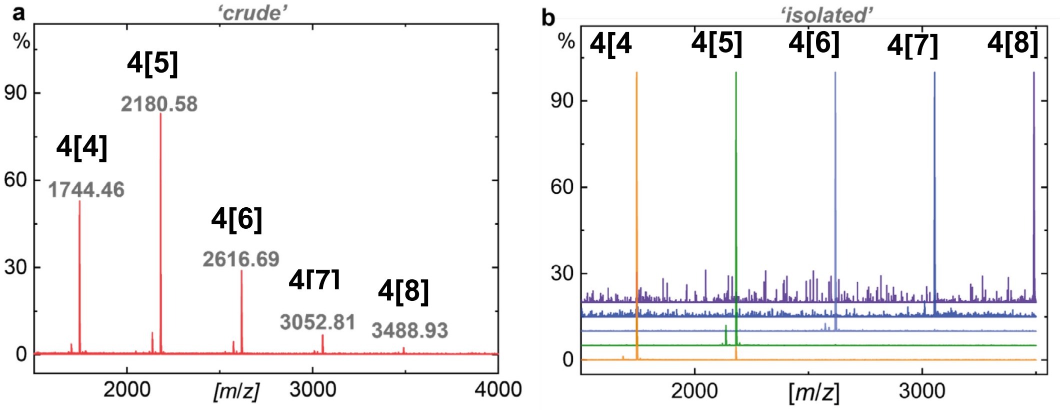

Figure 2. 9. MALDI-TOF mass-spectra of a) the crude reaction mixture of the reductive elimination performed on the Pt-metallacycles and b) stacked MALDI-TOF mass-spectra of the individual ring sizes after isolation using *r*GPC.

The ^1H NMR spectra show a single signal in the aromatic region for each macrocycle **4[*n*]** owing to their average D_{nh} (n = 4–8) symmetry.[193] The tedious separation to obtain pure samples of the individual congeners results in larger discrepancies regarding the isolated yields, even for the same reaction set-up. Therefore, the yields are given as an average over three individually performed reactions.

Table 2. 1. Scale and yields for **4[4–8]** of three independently performed reactions.

Scale	**Yield 4[4]**	**Yield 4[5]**	**Yield 4[6]**	**Yield 4[7]**	**Yield 4[8]**
100 mg	3.8%	4.1%	2.6%	1.6%	0.7%
150 mg	6.2%	8.7%	7.3%	10.3%	4.3%
100 mg	7.3%	12.3%	8.7%	8.8%	3.1%
Average	5.8%	8.4%	6.2%	6.9%	2.7%

Due to the limited solubility of **4[8]** full characterization by NMR spectroscopy was not successful, pointing towards the feasible limitations in terms of larger ring sizes for the presented macrocycles. Unambiguous structural proof was obtained by single-crystal X-ray diffraction for **4[4–6]** of which **4[5]** could only be crystallized as a host–guest complex, which will be discussed later.

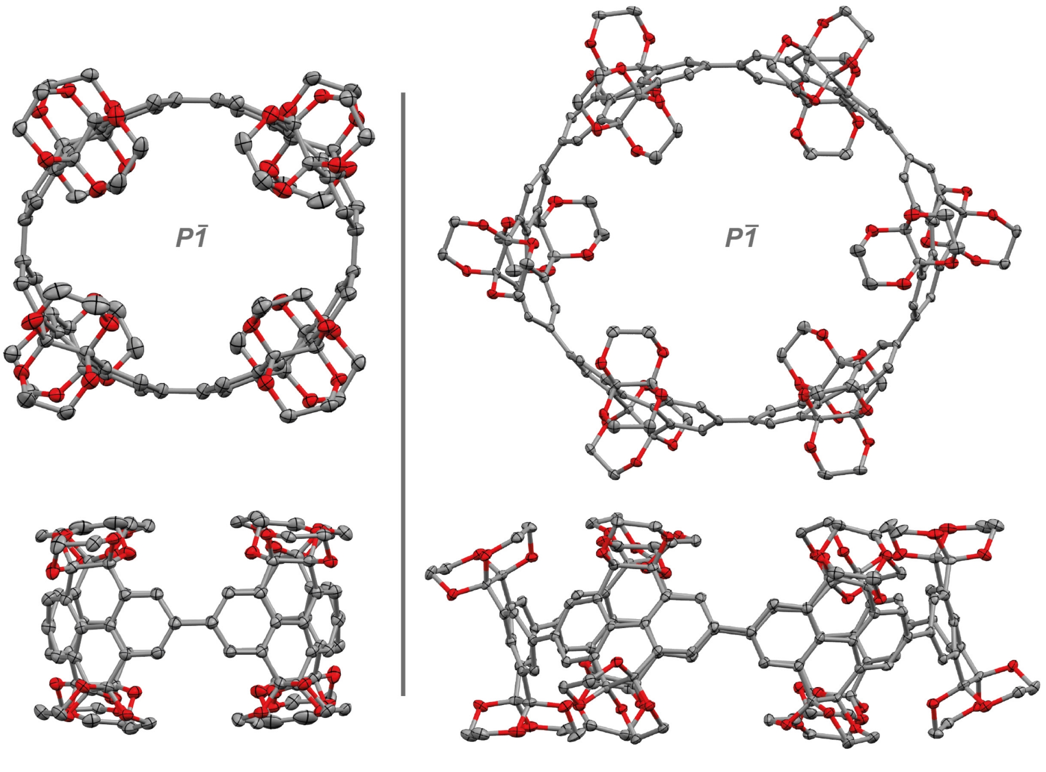

Figure 2. 10. X-ray structure and space group of **4[4]** (left) and **4[6]** (right) at 100 K. Ellipsoids are shown at 50% probability, hydrogen atoms and solvent molecules are omitted for clarity. Color code: carbon, grey; oxygen; red

2.3. Spectroscopic and Computational Characterization of [*n*]Cyclo-2,7-pyrenylene Derivatives

The UV/Vis absorption of the series **4[4–8]** show similar absorption maxima λ_{max} for all macrocycle sizes (4–8), which is a typical property for this class of molecules originating from a formally Laporte forbidden optical HOMO–LUMO transition.[65,123,194] Exceptions to this forbidden transition lead to a red-shifted shoulder of all absorption maxima (400–450 nm). While the entire series of **4[4–8]** shows rather large apparent Stokes shifts, considering the forbidden HOMO–LUMO transition the genuine Stokes shifts are 28–45 nm (0.20–0.31 eV).

Table 2. 2. Photophysical data of the series **4[4–8]** in $CHCl_3$ solution.

	4[4]	**4[5]**	**4[6]**	**4[7]**	**4[8]**
λ_{max} [nm]	374	375	371	375	378
$\lambda_{emission}$ [nm][a]	468	468	448	440	435
stokes shift [eV]	0.28	0.27	0.31	0.24	0.20

[a]Excitation at 375 nm

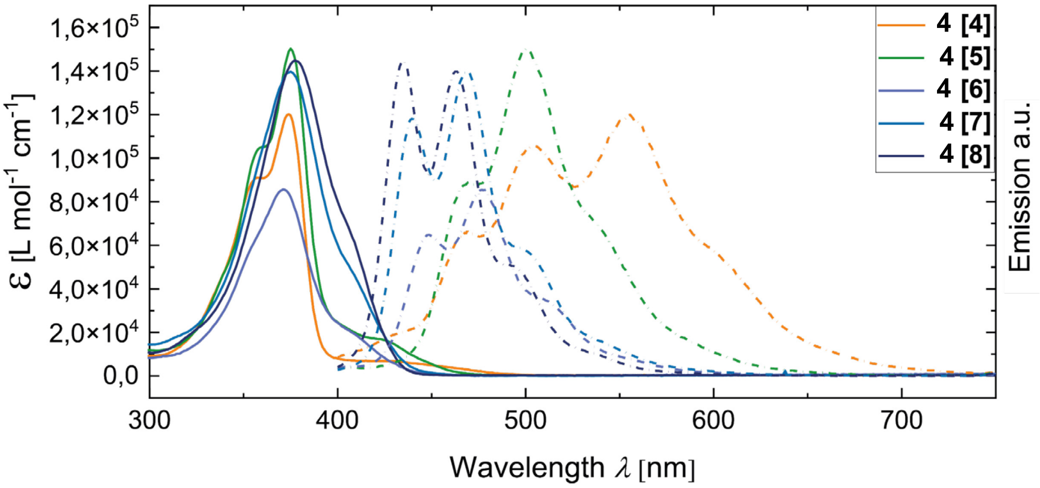

Figure 2. 11. UV/Vis absorption (solid lines) and normalized emission (dashed lines) spectra of **4[4–8]** ($CHCl_3$, 25 °C).

Using time-dependent density functional theory (TD-DFT, level of theory: CAM-B3LYP/6-31G(d,p)) the calculated oscillator strengths for the HOMO–LUMO transitions of **4[4–8]** were rather low ($f < 0.2$) verifying the forbidden nature of the HOMO–LUMO transition.

The unique photophysical properties of these CPP-type macrocycles are assigned to their cyclic symmetric structure in combination with the strain necessary to bend their otherwise planar aromatic repeating units.

We calculated the strain energy of **4[4–8]** using homodesmotic equations and also assessed the ring strain energy with StrainViz (Figure 2. 12).[112,195] The results of these calculations generally follow the same trend for the series **4[5–8]** except for the shortest, most strained tetramer **4[4]**, for which the homodesmotic equation calculates a higher strain energy than the results obtained from the StrainViz analysis (Figure 2. 12). Strain energies cannot be determined experimentally, yet the calculated results allow for comparison within this set of macrocycles. A great advantage of StrainViz is the visualization of the strain energy on all bonds, while classifying it into bond-, angle-, and dihedral strain energy. For [*n*]CPPs in general, dihedral strain has the highest impact because an average biphenyl angle of circa 44° cannot be fulfilled between all Clar-sextet units.[108] This holds true for the investigated series of macrocycles as well. Similar to [*n*]CPPs where the highest strain energy is localized on the bonds between the individual phenyl rings the highest strain for **4[4–8]** is localized at the bond connecting the individual pyrene subunits. Figure 2. 12 and Table 2. 3 show that the total strain and the subsets of bond-, angle-, and dihedral strain depend on the executed fragmentation. In conclusion, this information is crucial if one wants to compare different congeners. The results presented in Figure 2. 12 were all obtained using the fragmentation going through the bond connecting the individual pyrene units. In general, one can say, that the homodesmotic equation and StrainViz are valuable tools to compare individual macrocycles and elaborate trends regarding the strain energy experienced by these molecules. Nevertheless, the methods incorporate several approximations and therefore the obtained values should not be compared without care, especially when molecules with different structural features are examined.

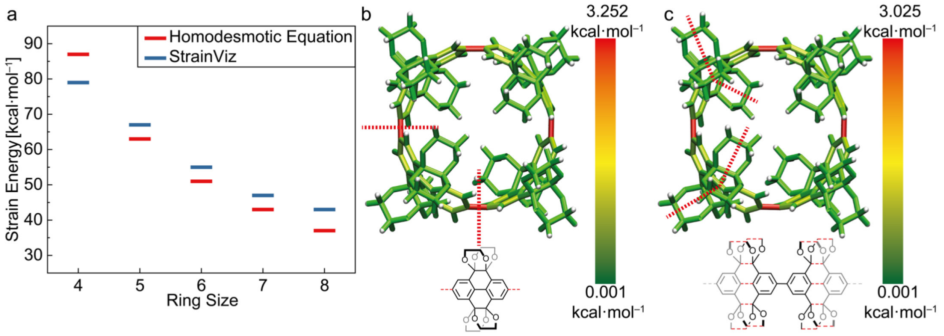

Figure 2. 12. a) Graph showing the molecular strain energies for **4[*n*]** calculated using the homodesmotic model and StrainViz (B3LYP/6-31G(d)). b) Graphical representation of the strain distribution with scale bar for **4[4]** given by StrainViz displaying the bonds that were cut (dashed red lines) to prepare the necessary molecular fragments. c) Graphical representation of the strain distribution for **4[4]** given by StrainViz with scale bar displaying an alternative set of bonds that were cut (dashed red lines) to prepare the necessary molecular fragments.

Table 2. 3. Strain energies calculated using StrainViz (B3LYP/6-31G(d)) comparing the obtained results with differently constructed fragments of Figure 2. 12 b) and c).

Fragmentation	Total [kcal· mol^{-1}]	Dihedral [kcal· mol^{-1}]	Bond [kcal· mol^{-1}]	Angle [kcal· mol^{-1}]
b)	79.2	71.7	2.6	5.0
c)	84.8	73.5	3.1	8.3

2.4. Supramolecular Host-Guest Studies of Highly Functionalized [*n*]Cyclo-2,7-pyrenylene

The strain that bends the otherwise linear pyrene subunits of **4[4–8]** also leads to a rather rigid and shape persistent molecular structure. As the yields are generally too low to synthesize large enough quantities to further test the bottom-up synthesis of CONTs this shape persistence let us to investigate these molecules as a new class of fluorescent supramolecular hosts. With the radially into the center converging ethylene glycol groups a confined space is created that can be used as a cavity for host-guest chemistry. A crucial parameter in this concept is the ratio of the gate diameter formed by the ethylene glycol groups to the cavity diameter in the center of the macrocycle. For unsubstituted [*n*]CPPs this ratio is 1 (Figure 2. 13).

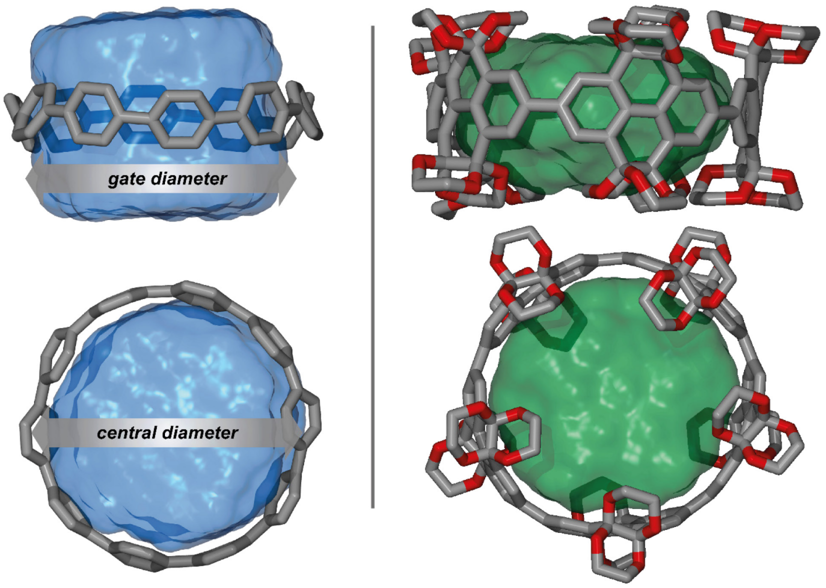

Figure 2. 13. Comparison of the accessible inner space between a non-functionalized [10]CPP and a highly functionalized [5]cyclo-2,7-(4,5,9,10-tetrahydro)pyrenylene derivative.

For the functionalized macrocycles presented herein this ratio depends on the ring size, with larger ring size the degree of confinement decreases. Contrary, for **4[4]** the opening of the average gate diameter was calculated to be 3.65 Å at the van der Waals surface. Therefore, it is too small to incorporate anything but small solvent molecules.

If the gate diameter becomes very small the energetic barrier to pass the gate of the cavity is too high, whereas for a large opening the effect of tight binding due to confined space vanishes.[196–198]

These considerations guided us to investigate the host properties of **4[5]** as it bears a cavity volume large enough to host a variety of molecular guest and a defined cavity resulting from a ratio of 0.67 between central cavity diameter and gate diameter.

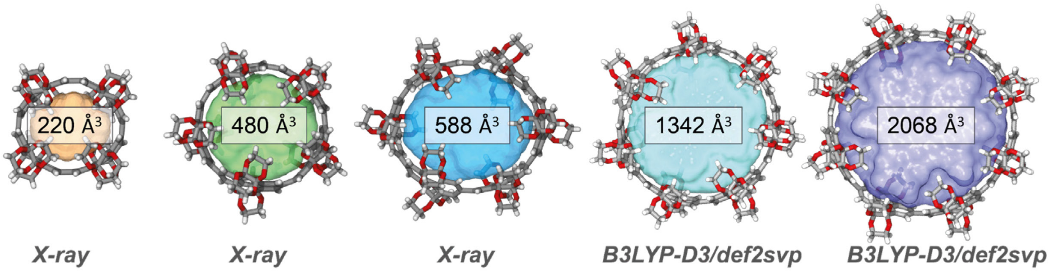

Figure 2. 14. Ball-and-stick representation of the X-ray (**4[4–6]**) and the geometry-optimized (DFT) structures **4[7–8]** containing the calculated cavity volume using the MS Roll suite implemented in X-Seed.[199,200]

Inspired by the strong binding of [10]CPP towards fullerene C_{60} we first investigated the binding of **4[5]**, which also consists of ten circularly arranged phenyl rings. No binding of **4[5]**, towards C_{60} can be determined using ^1H NMR spectroscopy (see Appendix Figure A. 6). While the same technique allowed Yamago and co-workers to determine that equally sized [10]CPP selectively binds C_{60} in the presence of other [*n*]CPPs this exemplifies the strong influence the ethylene glycol groups have on the here presented series of macrocycles.[128]

Host-in-host complexes have been an intriguing starting point in the construction of more complex superstructures.[201–203] A well-studied example is the encapsulation of crown ethers (or their nitrogen-containing equivalents) into larger cages or molecular capsules.[204–208] We selected crown ethers as guests because they are conformationally flexible allowing them to pass the gate of the macrocycle, and being commercially available in various sizes, which allows to explore the binding properties in great detail. We first studied the binding of several crown ether metal cation complexes to **4[5]** using UV/Vis absorption spectroscopy at 25 °C. Therefore, a solution of the host and a guest solution were prepared in $CHCl_3$. The guest solution has the same concentration as the host solution in regard of **4[5]** and a defined amount of crown ether. The prepared solutions were then saturated with ion-size matching salts and filtered prior to their subsequent addition towards the host solution. Addition of a 12-crown-4·LiCl guest solution did not lead to a change in absorption (Figure 2. 15a). Similar, the addition of dibenzo-18-crown-6·$K(BF_4)$ does not lead to a change in absorption (Figure 2. 15b).

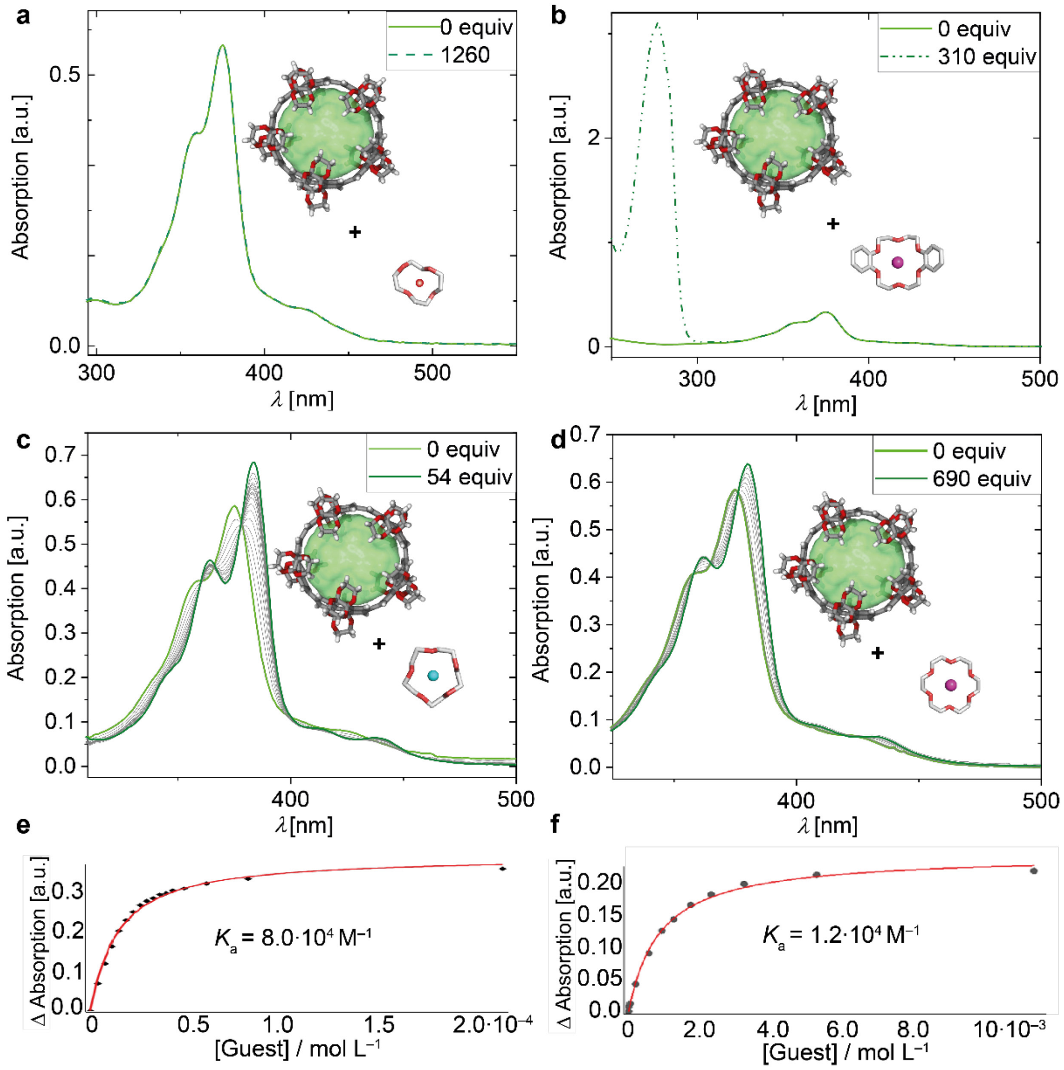

Figure 2. 15 Isothermal UV/vis absorption binding titration Spectra of **4[5]** at 25 °C, in $CHCl_3$, (c(**4[5]**) = $3.8 \cdot 10^{-6}$ mol L^{-1}) upon subsequent addition of a) 12-crown-4·LiCl; b) dibenzo-18-crown-6·K(BF_4) c) 15-crown-5·Na(BF_4) d) 18-crown-6·K(BF_4) and the corresponding non-linear curve fitting plots for the data respectively in e) and f).

In contrast, upon addition of 15-crown-5·Na(BF_4) a bathochromic shift combined with a narrowing of the absorption bands of **4[5]** and multiple distinct isosbestic points were observed. The new absorption maximum λ_{max} of the complex **4[5]**···[15-crown-5·Na(BF_4)] is red-shifted by 9 nm as compared to pure **4[5]** as extracted from the data of isothermal UV/Vis absorption titration with addition of up to 54 equivalents of 15-crown-5·Na(BF_4). The obtained data can be used to perform non-linear least-square curve fitting according to the Benesi–Hildebrand method.[209] The fitting curves were obtained by plotting the absorbance changes at a selected wavelength (ΔA) versus the concentration of the guest ([guest]) . While the host concentration is known as well ($[\text{host}]_{Tot}$) the unknown parameters are: $\varepsilon_{\text{host·guest}}$ as the absorption of the complex and K_a as the association constant. An error of 20% was estimated for these values. Regarding the limited space within the cavity, a 1:1 stoichiometry for the complexation was assumed, using the following equation 2.1 for the determination of K_a.[209,210]

$$\Delta A = \frac{\varepsilon_{host \cdot guest}}{2} \cdot \left[\left([\text{host}]_{Tot} \cdot [\text{guest}] + \frac{1}{K_a} \right) - \sqrt{\left([\text{host}]_{Tot} + [\text{guest}] + \frac{1}{K_a} \right)^2 - \left(4 \cdot [\text{host}]_{Tot} \cdot [\text{guest}] \right)} \right] \quad (2.1)$$

An association constant of $K_a = 8.0 \cdot 10^4$ M^{-1} was obtained for the complex **4[5]**···[15-crown-5·Na(BF_4)]. This is among the strongest binding observed for a non-fullerene guest to any [*n*]CPP-related macrocycle. Isothermal UV/Vis absorption titration upon addition of 18-crown-6·K(BF_4) gave a bathochromic shift of 5 nm for λ_{max}, accompanied by a narrowing of the absorption, and several distinct isosbestic points. Non-linear least-square curve fitting of the absorption titration data (Figure 2. 15f) afforded an association constant of $K_a = 1.2 \cdot 10^4$ M^{-1}.

To gain more structural information on the binding we turned to isothermal ^{1}H NMR binding titration, but the necessity for higher concentrations compared to UV/Vis experiments led to peak broadening and precipitation upon addition of 15-crown-5·Na(BF_4) to a solution of **4[5]** in $CDCl_3$ (Figure 2. 16).

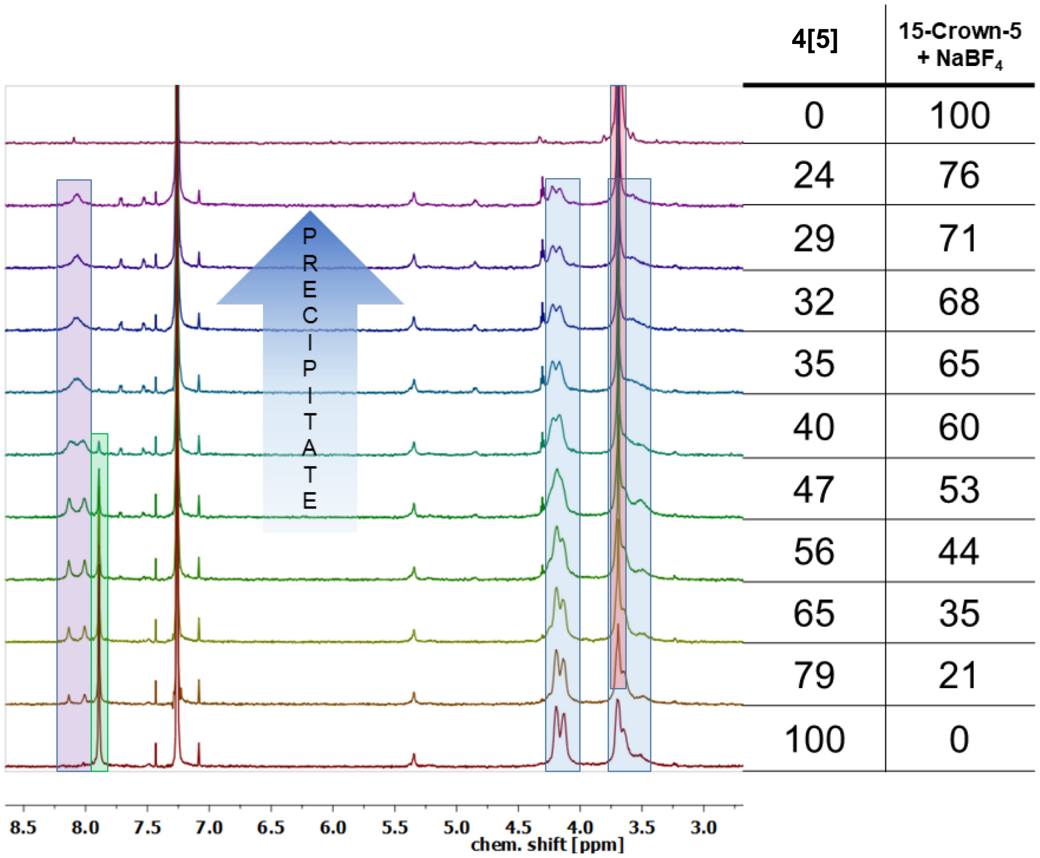

4[5]	15-Crown-5 + $NaBF_4$
0	100
24	76
29	71
32	68
35	65
40	60
47	53
56	44
65	35
79	21
100	0

Figure 2. 16. Isothermal ^{1}H NMR binding titration (600 MHz, 25 °C, in $CDCl_3$) *c*(**4[5]**) = $1.3 \cdot 10^{-3}$ M; The table on the right shows the molar distribution between [**4[5]**] and 15-crown-5/$NaBF_4$. At a molar ratio of 35:65 precipitation within the NMR tube was observed by eye (as indicated by the blue arrow). Highlighted in blue are the proton signals of the ethylene glycol groups, green is the proton signal of free host, purple are the new signals.

Nevertheless, we examined the spectra and two distinct peaks evolve upon addition of 15-crown-5·$NaBF_4$ (Figure 2. 16), assuming that these result from slow exchange, allows to determine the binding constant using the following equation

$$K_a = \frac{[HG]}{([H]_0 - a \cdot [HG])^a - ([G]_0 - b \cdot [HG])^b} \tag{2.2}$$

, where $[H]_0$ is the host concentration, $[HG]$ is the concentration of the host-guest complex, $[G]$ is the concentration of the guest, a is the stoichiometry of the host and b is the stoichiometry of the guest. The concentration of the host-guest complex can be determined with the following equation

$$[HG] = \frac{n}{n+m}\frac{[H]_0}{a} \tag{2.3}$$

, where n is the integral of the host-guest and m is the integral of the free host complex.

Three values are obtained for different ratios of [host]/[guest], which are displayed in Table 2. 4. The obtained values are prone to error due to the observed precipitation, yet are roughly in agreement with the binding obtained from UV/vis binding titrations.

Table 2. 4 Calculated binding constants K_a at different host/guest ratios using the integrals n, m of Figure 2. 16. Guest: 15-crown-5·$NaBF_4$.

ratio (**4[5]**/guest)	65:35	56:44	47:53	**Average**
$\frac{n}{m}$	0.35	1.00	0.74	–
K_a	$1.3 \cdot 10^3$ M^{-1}	$1.5 \cdot 10^3$ M^{-1}	$3.13 \cdot 10^4$ M^{-1}	**$1.1 \cdot 10^4$ M^{-1}**

As other combinations of **4[5]** and the different crown-ethers were tested no binding could be observed. Isothermal titration experiments for **4[6]** towards crown ethers, showed no pronounced binding for the addition of neither 15-crown-5·$Na(BF_4)$ (K_a = 28 M^{-1}) nor 18-crown-6·$K(BF_4)$(K_a too weak to be detected, Appendix Figure A. 3). We assign these results to the drastic increase of the cavity volume by 23% from **4[5]** to **4[6]**. The latter therefore requires much larger guests for reasonable strong binding. Further, no binding event is observed for **4[4]** with the smallest crown ether 12-crown-4·LiCl (Appendix Figure A. 1). The already mentioned very small gate opening does presumably not allow guest-binding.

Crystals suitable for synchrotron-based X-ray crystallography were obtained for the complex **4[5]**···[18-crown-6·K-(BF_4)] (Figure 2. 17). The cationic 18-crown-6·K^+ is located in the center of the cavity of **4[5]** embraced by the ethylene glycol groups of

4[5] as a secondary coordination sphere.[208] The guest 18-crown-6·K$^+$ is bound in an unexpected non-planar conformation with one ethylene glycol unit twisted out-of-plane.

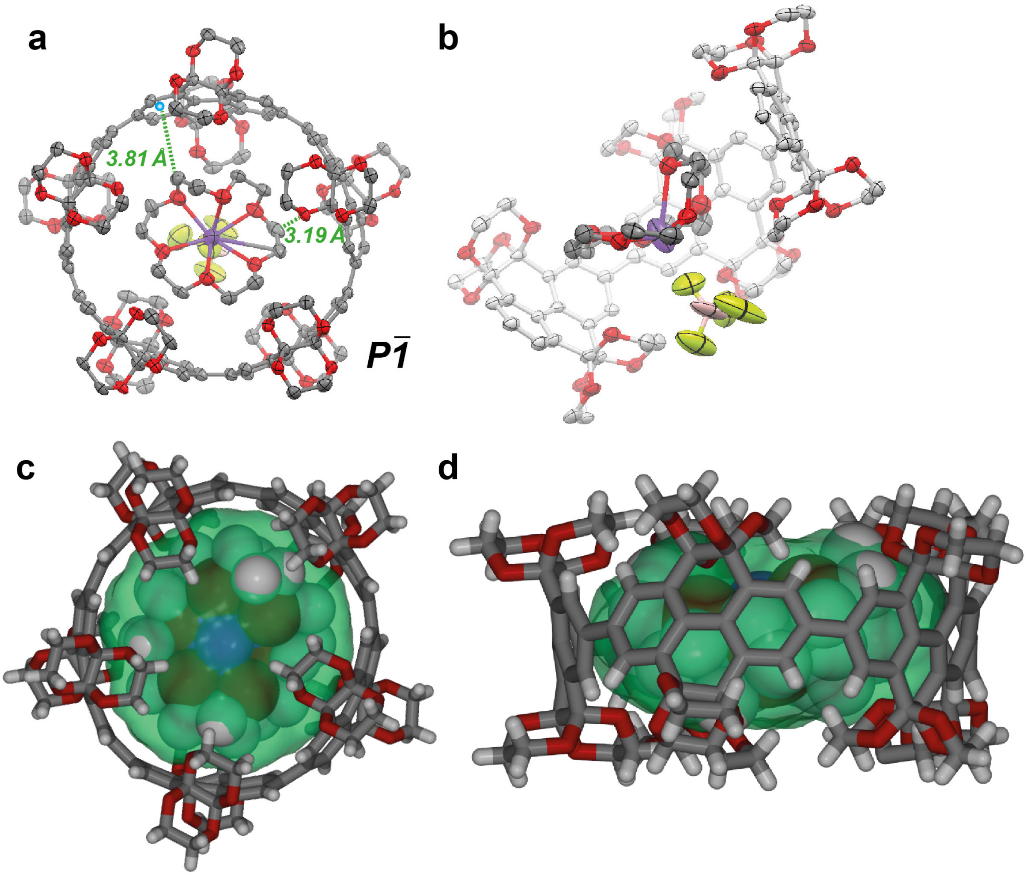

Figure 2. 17. a) Single-crystal X-ray structure of **4[5]**···[18-crown-6·K(BF4)], H-atoms, solvent molecules and disorder are omitted for clarity, thermal ellipsoids shown at 50% probability showing two exemplary heavy atom distances; b) twisted structure of a) to better show the conformational distortion of the 18-crown-6 ether; c) Top and d) side view of X-ray structure of **4[5]**···[18-crown-6·K(BF_4)], where **4[5]** is shown as sticks, 18-crown-6·K$^+$ as van der Waals spheres, and the green surface represents the calculated cavity volume visualized using X-seed.

Measuring the distance between centroids of the phenyl subunits of **4[5]** and the C-atoms of the crown ether shows ten close contacts (3.5–4.0 Å) assigned to C–H···π interactions. An exemplary distance of 3.8 Å is shown in Figure 2. 17a. Several further C–H···O hydrogen bonds were determined between the strongly polarized C–H groups of the crown ether as hydrogen bond donors and the oxygens of the ethylene glycol groups of **4[5]** acting as hydrogen bond acceptors. An example of this hydrogen bond is highlighted in Figure 2. 17a having a length of 3.18 Å.

The energetic difference in vacuum of the bent conformation compared to its optimized planar conformation of cationic 18-crown-6·K$^+$ was calculated to be 2.0 kcal·mol^{-1} (DFT:B3LYP-D3/def2QZVP), which in the complex is well compensated by a non-covalent interaction free enthalpy (Figure 2. 18).

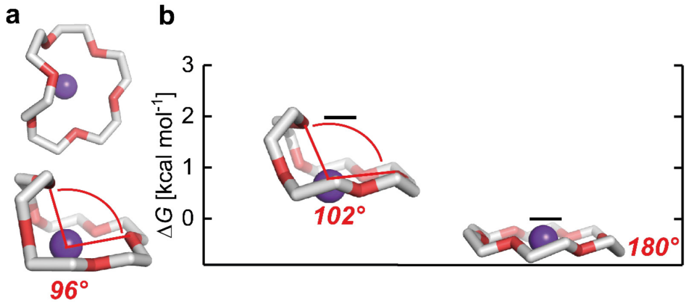

Figure 2. 18. a) Top and side view of cationic 18-crown-6·K+ as extracted from the X-ray structure of the **4[5]**···18-crown-6·K(BF_4) complex, b) Energy diagram comparing the geometry optimized structure of the X-ray excerpt to the planar geometry-optimized structure at the B3LYP-D3/def2QZVP level of theory Angles O–M–O of opposite O-ether fragments are depicted in red. The relative calculated Gibbs energies are plotted. The bent structure in b) is 2.0 kcal·mol⁻¹ higher in energy than the planar structure.

As an unambiguous prove that the binding is depending on the confinement of the inner cavity by the ethylene glycol groups we performed control experiments on [10]CPP, which has an almost identical central diameter. The equally sized but unconfined parent [10]CPP shows significantly smaller binding constants of $K_a = 103\ M^{-1}$ and $K_a = 24\ M^{-1}$ for 15-crown-5·Na(BF_4) and 18-crown-6·K(BF_4), respectively (25 °C, $CHCl_3$).

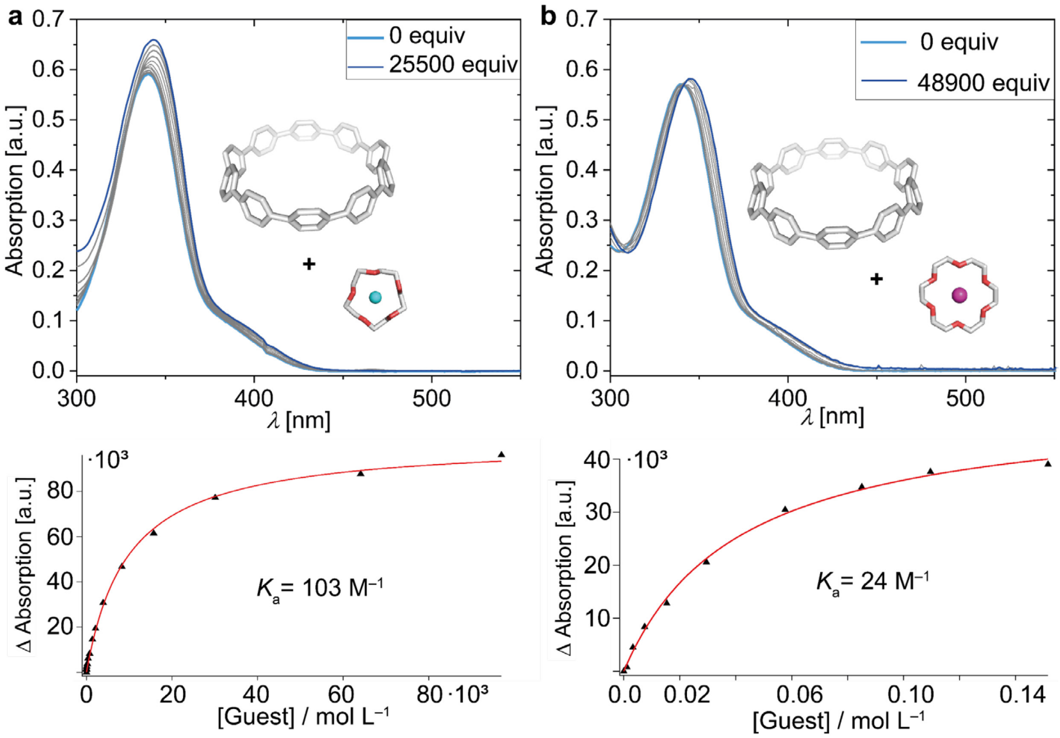

Figure 2. 19. Isothermal UV/vis absorption binding titration Spectra of [10]CPP at 25 °C, in $CHCl_3$, ($c([10]CPP) = 3.8\cdot10^{-6}\ mol\ L^{-1}$) upon subsequent addition of a) 15-crown-5·Na(BF_4) and the corresponding non-linear curve fitting plot below; and b) 18-crown-6·K(BF_4) and the corresponding non-linear curve fitting plot for the data below.

2.5. Alternative Synthetic Route of Highly Functionalized [*n*]Cyclo-2,7-pyrenylene

The unselective formation of different ring sizes evaluated in the previous part was advantageous in regard of supramolecular host-guest studies and allowed to investigate a whole set of new [*n*]CPP-type macrocycles. Nevertheless, to perform more studies or try different protocols for the deprotection of the obtained macrocycles and subsequent bottom-up synthesis of CONTs a more selective synthesis eliminating the labor-intensive purification is highly desirable. Therefore, we tested the platinum macrocyclization route from the organostannane **8**. Dibromo compound was prepared according to literature procedures.[183,186] Palladium-catalyzed stannylation of **8** was achieved with a procedure adapted from the literature.

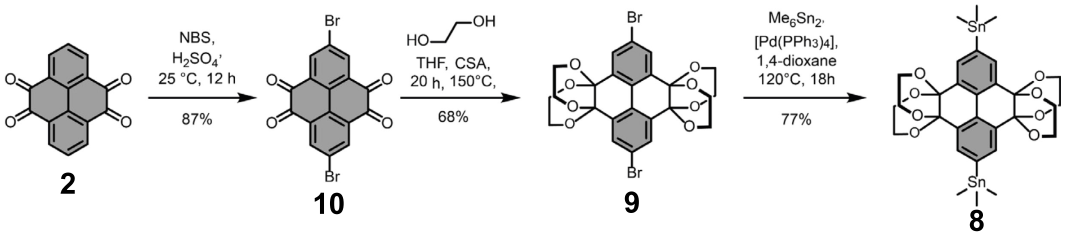

Figure 2. 20. Synthetic procedures for stannylated building block **8**.

The formation of platinum metallacycle **5[*n*]** was performed in dry THF as reported for the non-functionalized pyrene macrocycle.[67]

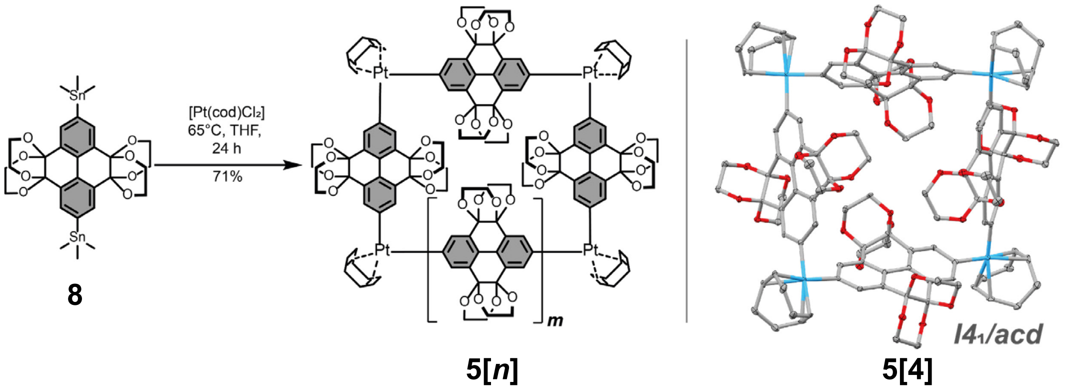

Figure 2. 21. Synthesis of platinum metallacycle **5[*n*]**.

Even though the four membered platinum macrocycle crystallized readily from a NMR solution in CD_2Cl_2 of the isolate solid, *r*GPC analysis showed that several ring sizes were formed during this reaction. The NMR spectra of solids of the metallacycles isolated from the stannylated or the borylated precursor appear to be almost identical. The reason for an absence of single-crystalline material in the borylated route must therefore depend on a minor impurity. Among two other reports,[67,189] this is one of the few cases were the platinum intermediate could be isolated. Surprisingly the crystal structure of **5[4]** displays a non-planar molecular structure (Figure 2. 22d) in contrast to the other reported examples. The non-planar structure becomes feasible due to the slightly more acute angle of C_{Ar}–Pt–C_{Ar} with 86.4°. Where the tetrahydropyrenylene of Yamago and co-workers shows a mix of a slightly more acute and obtuse angles.[67]

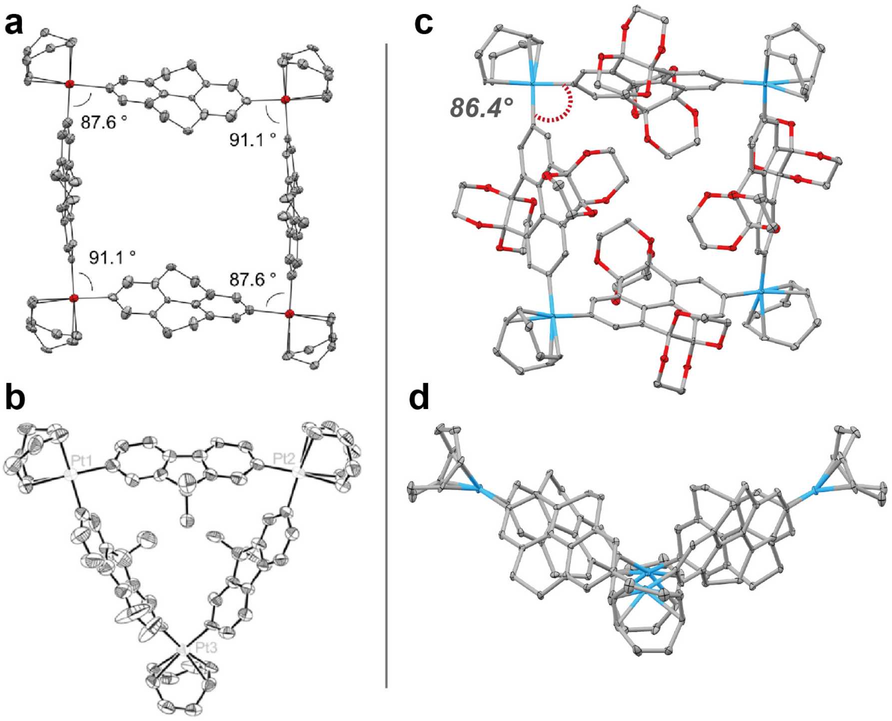

Figure 2. 22. Single crystal X-ray structures of reported platinum macrocycles that function as precursors for all-organic nanorings with a) tetrahydropyrenylene[67] b) diemethylfluorene as a subunit[189] c) ethylene glycol protected pyrenetetrone top view and d) side view displaying the non-planar molecular structure.

The successful isolation of a larger set of single crystals, which appeared homogeneous in shape and size, in combination with the exemplary structure determination on one of these crystals, allowed us to perform reductive elimination on a presumably pure sample of four membered platinum-macrocycles. The subsequent *r*GPC analysis showed the formation of different sized nanorings, but a significant increase in formation of **5[4]** (Figure 2. 23, highlighted in orange). The formation of larger ring sizes in comparison is reduced and **4[7–8]** are not detectable in the *r*GPC chromatogram. Which of the two options—either reinsertion of $Pt(PPh_3)_{4-x}$ into the strain activated bond or small amounts of the corresponding metallacycle as impurity—are the cause for the occurrence of **5[5–6]** cannot be clarified.

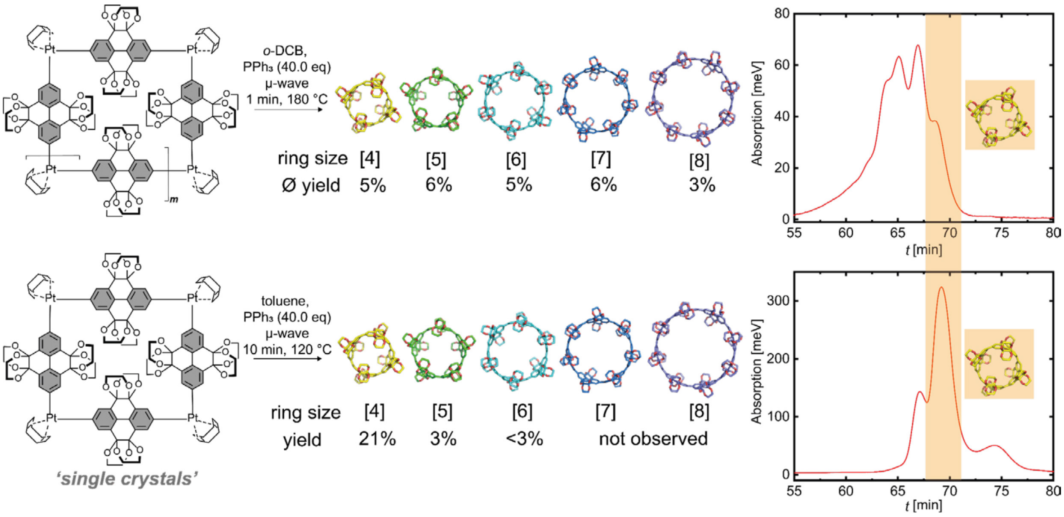

Figure 2. 23. Comparison of the reductive elimination from a solid containing different ring sizes of the platinum metallacycle and a sample of single crystals of the four membered molecule, with corresponding yields and the *r*GPC chromatograms of the crude reaction mixture.

This result shows that the applied route offers improvement in regard of the selectivity within the synthesis. This encouraged us to investigate the deprotection of the obtained macrocycles as this step represents the crucial last one before attempts towards the synthesis of CONTs can be conducted. Several deprotection methods are known from the literature to transform the ethylene glycol protected pyrene-4,5,9,10-tetrone into the unprotected version (Table 2. 5).

Table 2. 5. Evaluation of reported literature conditions for removal of ethylene glycol groups.

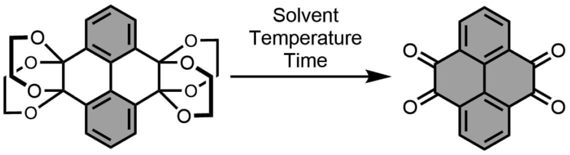

Compound [Lit.]	Scale [mg]	Solvent [ratio]	Temp	Time	Yield
7[185]	53.0	TFA/H_2O [9/1]	25 °C	6 h	75% of **2**
7[211]	10.2	CH_2Cl_2/$HClO_4$ [8/1.2]	0 °C – 25 °C	5 h	75% of **2**
7[212]	10.6	H_2SO_4 / H_2O [10/1]	25 °C	0 h	0%

As the strain energy of the macrocycles correlates to their reactivity and the separation of the different sizes is labor intensive deprotection protocols were attempted on the mixture containing **4[4–8]** (Table 2. 6).

Table 2. 6 Evaluation of reported literature conditions for removal of ethylene glycol groups applied to the mixture containing **4[4–8]**.

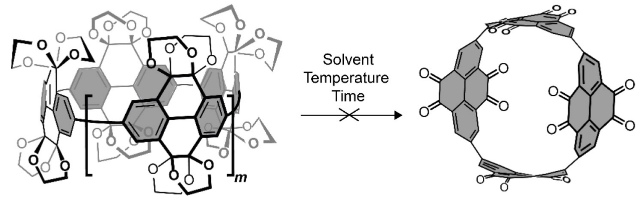

Compound	Scale [mg]	Reactant	Solvent [ratio]	Temp	Time	Yield
4[4–8]	5.6	-	TFA/H_2O (9/1)	25 °C	3 h	0%
4[4–8]	4.2		CH_2Cl_2/$HClO_4$ (8/1.2)	0°C–25 °C	5 h	0%

In contrast to the deprotection of the monomeric subunit the addition of acid to the reaction mixture always led to a drastic color change from orange to black. Subsequent analysis always showed that the signals of the ring mixture disappeared and no signals that could be assigned to a macrocyclic product could be obtained.

2.6. Conclusion

Within this chapter we outlined a novel approach for the bottom-up synthesis of CONTs. The investigated molecular design of a potential monomer was synthetically realized, except for the last deprotection step. Nevertheless, the obtained macrocycles were investigated on their host capabilities for molecular guests including fullerenes and several different cationic crown-ether complexes. For congener **4[5]** we determined the strongest binding to a non-fullerene guest up to today. While a significant increase in size-selectivity was observed if single crystalline metallacycle was used for the reductive elimination, the resulting four membered congener, could not be used as a supramolecular host, due to a small gate opening. Application of deprotection protocols to obtain **3[*n*]** was unsuccessful.

We anticipate that our approach to synthesize monomers for the diameter selective bottom-up synthesis of CONT will contribute to the development of other macrocyclic structures that will ultimately allow the controlled synthesis of new 1D nanostructures. Further our findings bear valuable insights into the development of novel fluorescent CPP-type macrocycles that could as well function as sensors or be implemented into artificial membranes to create artificial membrane channels.

Chapter 3

A Fourfold Gold(I)–Aryl Macrocycle and its Corresponding Carbon Nanoring Host

Parts of this chapter contain contributions of the master thesis of Sergey Fisher and are already published in:

Angew. Chem. Int. Ed. **2023**, e202217917

DOI:https://doi.org/10.1002/anie.202217917

Authors: Niklas Grabicki, Sergey Fisher, Oliver Dumele

Chapter 3: A Fourfold Gold(I)–Aryl Macrocycle and its Corresponding Carbon Nanoring Host

In Chapter 2, our first design approach was investigated to synthesize a potential monomer for the bottom-up synthesis of a CONT. Despite different synthetic routes and significant knowledge gain on the undergoing processes it was not possible to obtain suitable amounts of isolated cyclic conformers bearing multiple diketone functional groups on each site that would enable subsequent material synthesis. Therefore, another approach will be investigated in this chapter based on a different monomer design that has inherently less strain energy. We expected that a reduction in strain energy will allow a more size selective synthesis and render the resulting cyclic carbon nanorings less reactive. In addition, they might offer unique host capabilities due to a much larger inner void volume. To achieve this, we based our molecular design on an already published scaffold consisting of [6]cyclo-meta-phenylene units that are circularly arranged.[86,213] *This reported motif is synthetically accessed via a completely new synthetic method that uses bidentate gold(I) complexes.*[191,214]

3.1. Design of Highly Functionalized Extended Aromatic Macrocycles

With the earlier mentioned prerequisites that need to be met to make a monomer suitable for the bottom-up synthesis of CONTs in mind, we devised another molecular design in this chapter. From our previous findings we concluded that the required shape persistence must not be a result of too high molecular strain energy, because this inherently leads to reduced yields and makes the resulting macrocycles prone to degradation in any kind of follow-up reaction.

In an urge to synthesize CPP-type macrocycles with large π-surfaces that resemble their parental nanostructures, the group of Du synthesized a nanoring consisting of hexabenzocoronene.[215] Based on this work Isobe and co-workers utilized [6]cyclo-*meta*-phenylene (CMP) units, first synthesized by Staab in 1964,[86,216] to create nanoring derivatives with significantly reduced molecular strain due to the missing central benzene ring (blue in Figure 3. 1).[213] The implementation of a [6]CMP subunit into a CPP scaffold combines rigidity with sufficient flexibility. This molecular subunit represents an almost linear linker necessary in the pre-organization of the macrocycle and in addition displays sufficient degrees of freedom produced by multiple *meta*-linked phenine units to compensate the induced strain. Torsion along the biphenyl bonds at the phenine moieties in each macrocyclic sub-panel allow a non-planar substructure and possibly releases strain energy in the final CPP (Figure 3. 1). The synthesized nanoring was defined as a cyclo-*para*-phenylene geodesic framework ([*n*]CPP GPF) by Isobe and co-workers.[217]

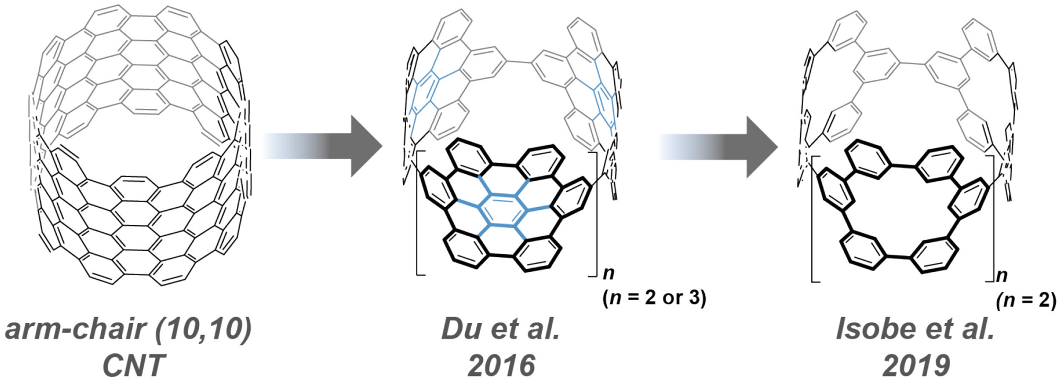

Figure 3. 1. An arm-chair (10,10) CNT segment of which a [*n*]cyclo-hexabenzocoronene can be cut out first synthesized by Pingwu Du et al. and the corresponding phenine macrocycle containing one central benzene ring. Drastically reducing the molecular strain energy of the final macrocycle.[213,215]

Intrigued by these studies we envisioned to expand our previous pyrenylene subunits **7** to synthesize an interphenylene bridged [6]CMP derivative **11**. This should be a useful building block to create a highly functionalized nanoring that shows significantly less molecular strain energy. Therefore, nanoring **12[4]** should tolerate follow-up reaction sequences such as removal of the ethylene glycol groups. Isobe and co-workers reported a remarkable yield of 20% over two steps for the platinum-mediated macrocyclization of **13[4]**. Combined with the reported size-selectivity they obtained in this case, this molecular design appears to be a good starting point. Interestingly the group reported that a minor change from TMS groups of **13[4]** (Figure 3. 2) to *tert*-butyl groups resulted in the formation of three different ring sizes with all of them in a single digit percentage yield ([3]CPP GFP = 3%, [4]CPP GFP = 6%, [5]CPP GFP = 3%). A reason for this change in selectivity could not be revealed.[188]

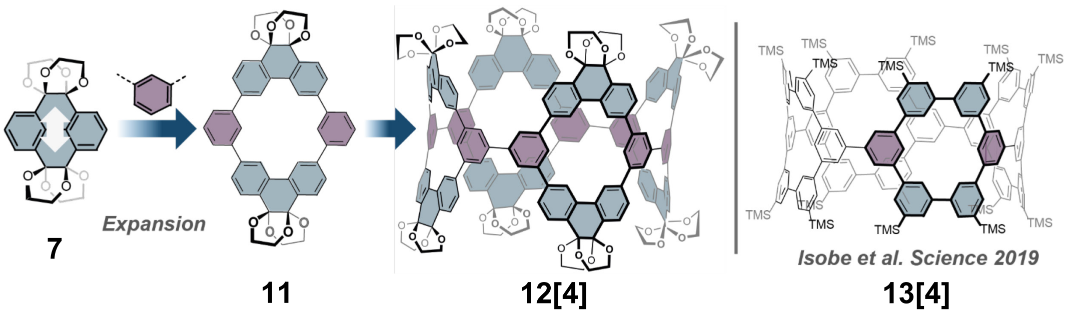

Figure 3. 2. Expansion of the pyrenylene core utilized in the last chapter towards interphenylene bridged [6]CMP and the resulting carbon nanoring host including a similar *meta*-phenylene core as reported by Isobe and co-workers (TMS = trimethylsilyl).[213]

As such minor structural changes in the molecular design can already lead to significant experimental changes regarding the synthetic outcome we first wanted to quantitatively analyze and compare our [6]CMP derivative to that of Isobe and co-workers using DFT calculations.

3.2. Conformational Analysis of [6]CMP Derivatives

To discuss the influence an introduction of two phenanthrene units has on TMS substituted [6]CMP **14** the following structures were optimized by DFT calculations at B3LYP-D3/6 31G(d,p) level of theory (Figure 3. 3).

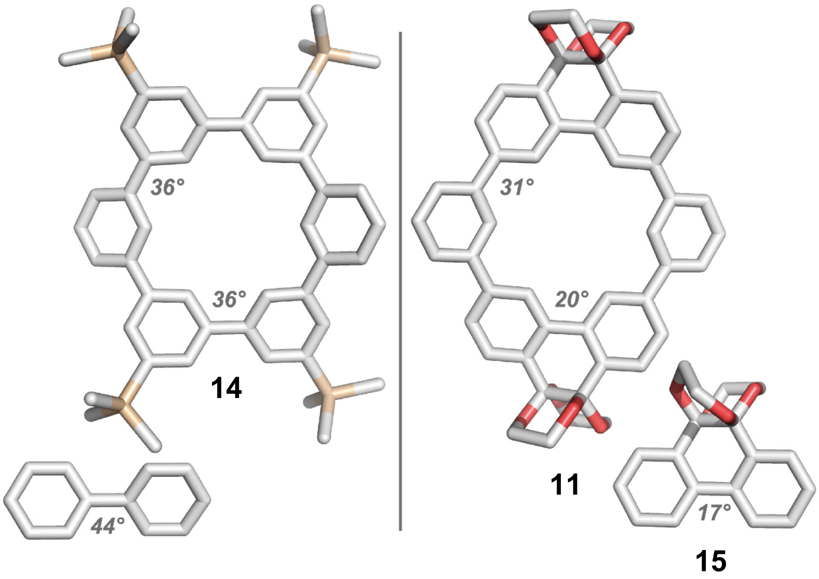

Figure 3. 3. The calculated dihedral angles by DFT calculations at the B3LYP-D3/6-31G(d,p) level of theory for TMS macrocycle **14**, interphenylene bridged macrocycle **11**, biphenyl, and phenanthrene-9,10-di(ethylene glycol)ketal (**15**). Color code: C, gray; O, red; Si, beige.

The DFT-optimized dihedral angle of plain biphenyl is 44° where the torsional angle is balanced between a steric repulsion of hydrogens and favorable π conjugation.[218] Implementation of an interphenylene bridge in ortho position to the connecting carbon–carbon bond strongly influences this torsion angle. In our case a sp^3-hybridized bridge reduces the parental dihedral angle in biphenyl to 17° in **15** caused by the elongated single bond that is incorporated into the chair-puckered 1,4 dioxanyl moieties. The structural influence of a phenanthrene moiety is immediately visible, when comparing **14** and **11**, where the [6]CMP scaffold of **14** arranges itself in six torsion angles of ca. 36°. A torsion of 44° is not observed due to the macrocyclic fixation of the phenylene units. In case of **11**, the protected phenanthrene fragments exhibit a torsion angle of 20° and consequently limit the total flexibility of the scaffold. As a result, the biphenyl angle of the phenanthrene–phenylene bonds are 31°, deviating from an equilibrated dihedral angle of 44°.

The presence of dihedral angles within [6]CMP cause a non-planar structure for both subunits **14** and **11**. In analogy to the non-planar hexagon structure of cyclohexane, [6]CMP can arrange into different isomers, too. Therefore, the (twist)boat and chair conformation in cyclohexane can be used to classify the structure of [6]CMP as well (Figure 3. 4).

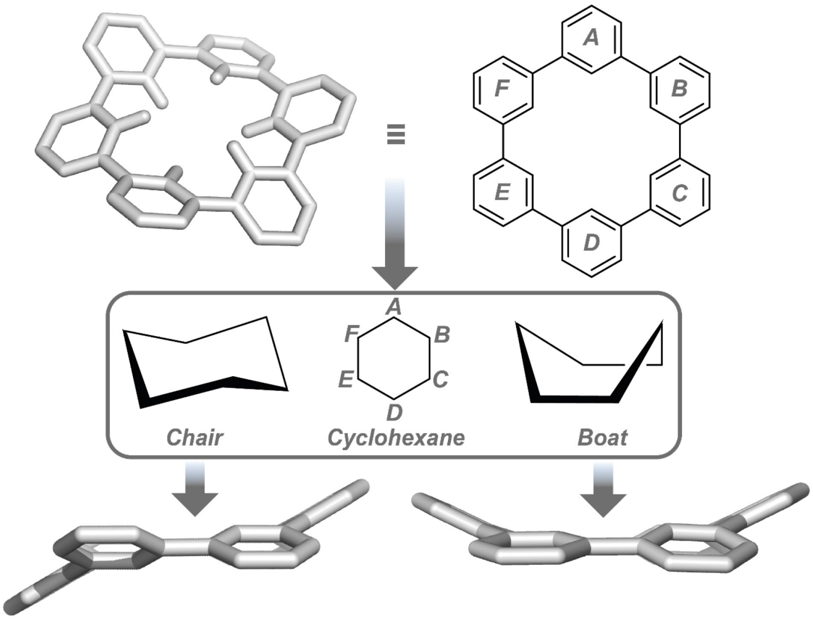

Figure 3. 4. A 3D structure of [6]CMP displaying the central protons which result in the conformational diversity. Each phenylene unit can be seen as a carbon atom in cyclohexane. The structures of [6]CMP can be derived from the chair and boat conformations of cyclohexane and are assigned accordingly.

We expected the chair isomer of [6]CMP to have a lower energy compared to the boat due to alternating inner hydrogen atoms within the [6]CMP. A boat conformer has two preorganized rings for example A and D (Figure 3. 4) directing the hydrogen atoms into the same direction. The remaining hydrogens of the rings B, C, E, and F have to organize in between the remaining space which is predefined by the dihedral angles connecting each phenylene unit.

Despite the expected higher energy of the boat conformer compared to the chair conformer, the curvature of CPP-type macrocycle **12[4]** requires a boat arrangement for each of the subunits (Figure 3. 5).

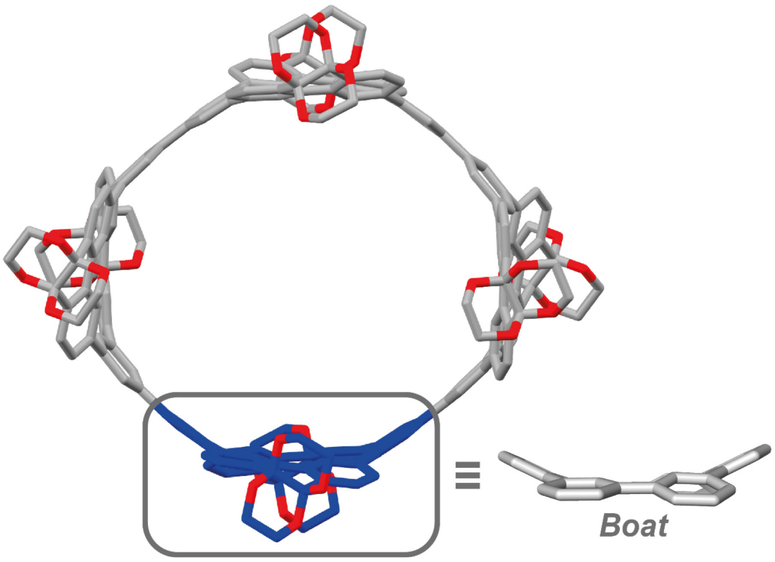

12[4]

Figure 3. 5. Structure of the targeted nanoring **12[4]**. The chair conformation of the monomeric subunit is highlighted in blue.

Considering the high synthetic effort for **12[4]**, we aimed to exclude any unexpected conceptional error caused by conformational restrictions of the monomeric unit. A ring-flip must be energetically feasible during the final macrocyclization, switching from the favored chair conformer to the boat conformer. To quantify the influence of the phenanthrene units on this overall ring-flip — in analogy to cyclohexane's pseudo rotation — the energy barrier was calculated by a dihedral scan and subsequent transition state optimization to a saddle point using DFT (level of theory B3LYP-D3/6-31G(d,p)). The scan was performed on the geometry-optimized structures around the dihedral angle between the sole phenyl moiety and the phenanthrene moiety within **11** (corresponding atoms highlighted in purple, Figure 3. 6). This procedure allows to estimate the geometry of the transition state, which was further optimized to a saddle point (structure **TS** in Figure 3. 6) after the initial scan.

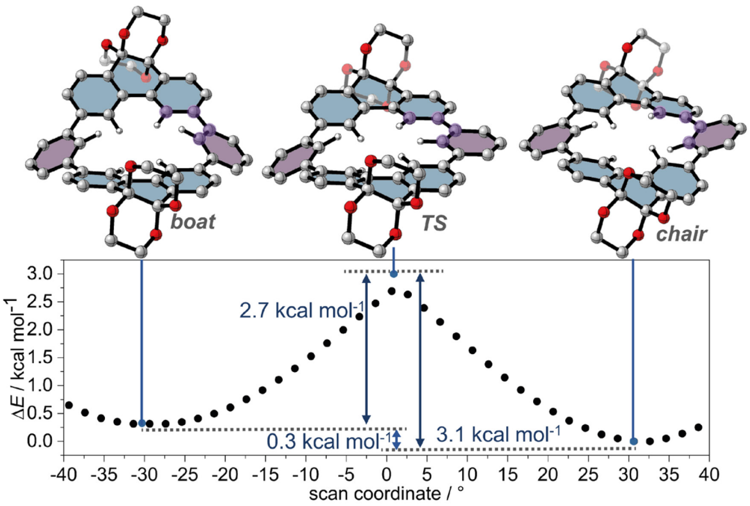

Figure 3. 6. The optimized structures of **11** in the boat, transition state, and chair conformation by DFT calculations at the B3LYP-D3/6-31G(d,p) level of theory. Initial dihedral scan coordinate (black dots) with energetic positions of unrestricted optimized structures of boat, TS, and chair (blue dots). The scan was performed on the purple highlighted dihedral bond. All hydrogen atoms, except the inner ones of [6]CMP, are omitted for clarity. Color code: H, white; C, gray; O, red.

From the relative energies of the conformers and the transition state (TS), the energetic barrier of the ring-flip and the total energy difference were calculated. The structures of the boat and the chair conformation have the expected arrangement of inner hydrogen atoms within the [6]CMP unit (Figure 3. 6). The calculated geometry is verified to be a transition state by one imaginary frequency at –81 cm^{-1} corresponding to a torsional twisting mode of the three in-plane hydrogens. The energetic barrier for the chair-to-boat isomerization is 3.1 kcal mol^{-1} and 2.7 kcal mol^{-1} vice versa. The total difference of both conformers is 0.3 kcal mol^{-1}. To put the value for the chair boat isomerization of **11** into perspective the chair→twist-boat isomerization of deuterated cyclohexane (C_6HD_{11}) at 25 °C in solution is too fast to be detected on the NMR time scale and has a barrier of ca. 10 kcal mol^{-1}.[219]

The total distribution of chair to boat of **11** at 25 °C *in vacuo* is calculated to be 1.7:1. Therefore it can be concluded that introduction of the phenanthrene subunits should not have a drastic influence on the macrocyclization to obtain nanoring **12[4]**.

3.3. Synthesis of a Carbon Nanoring Consisting of Four Highly Functionalized [6]CMP Subunits

Constructing phenyl-containing macrocycles, such as **11**, is challenging because they typically suffer from low yielding macrocyclization steps. Further, the necessity for high dilution limits the up-scaling and the undesired side products express similar polarity hampering purification.[90,220,221] Structurally similar macrocycles to **11** were reported by Isobe and co-workers, which were prepared using nickel catalyzed Yamamoto coupling.[221] The difficulty in our design lies in the lack of a C_3 symmetry axis, which does not allow a straightforward cyclooligomerization using 3,6-dibromo phenanthrene **16**.[83] In contrast, it would be necessary to prepare the unsymmetrical *meta*-terphenylene precursor **17** first, requiring significant synthetic effort including protection and deprotection steps to avoid terphenylene formation (Figure 3. 7). Therefore, stepwise or one-pot macrocyclizations under Suzuki–Miyaura conditions appears to be more suitable.[222,223]

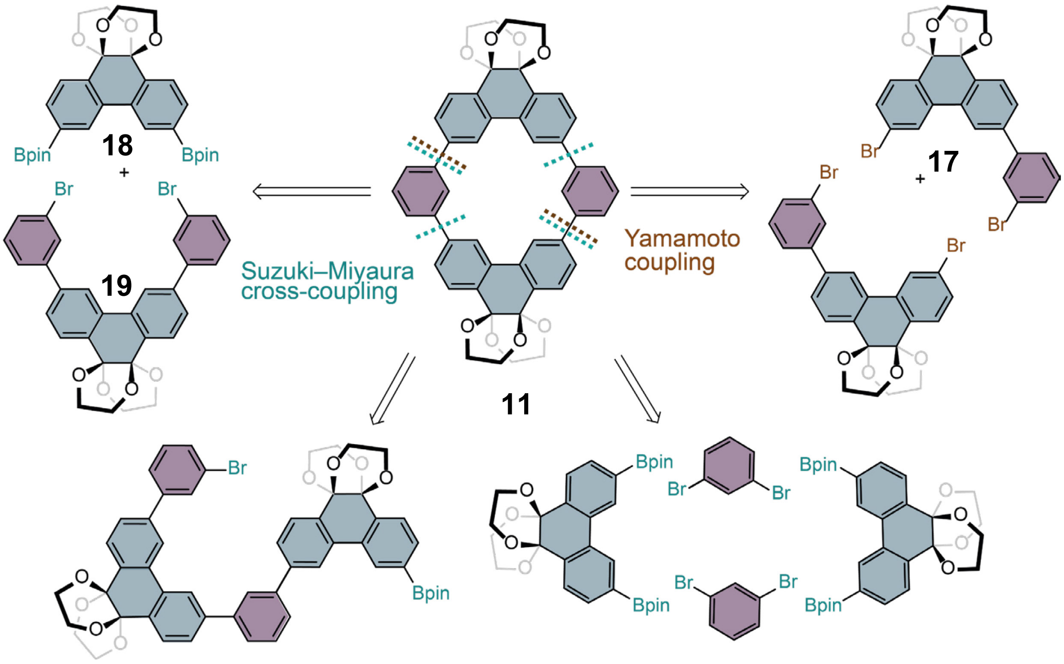

Figure 3. 7. Retrosynthetic approaches to obtain the C_{2h} symmetric **11** via Suzuki–Miyaura cross-coupling or Yamamoto coupling.

We decided to investigate several synthetic routes to access diboronic ester **20**. Diboronic ester **18** was synthesized on a multi-gram scale within three steps starting from commercially available 9,10-phenanthrenequinone (Figure 3. 8).[224] One-pot macrocyclization of diboronic ester **18** and 1,3-dibromobenzene led to the formation of bisacetal interphenylene-bridged [6]CMP derivative **11**. Due to the reduced symmetry of **11**, the one-pot macrocyclization of the unequal building blocks **18** and 1,3-dibromobenzene is impeded compared to parental [6]CMP.[223] Due to the low yield of 7% in this step of route A we explored a stepwise protocol termed route B as well. Nevertheless, the combined yields over two steps are in a similar range as for the one-pot procedure. We reasoned that a sterically bulky substituent on the five position of the 1,3-dibromobenzene might increase the pre-organization in the final macrocyclization step from terphenyl to functionalized [6]CMP. To test this hypothesis 1,3-dibromo-5-(trimethylsilyl)benzene was cross-coupled to diboronic ester **18** in route C (Figure 3. 8).[222] Even though the yield could be increased for the macrocyclization the overall increased number of synthetic steps from five linear for route A to seven linear steps did not represent an overall improvement.

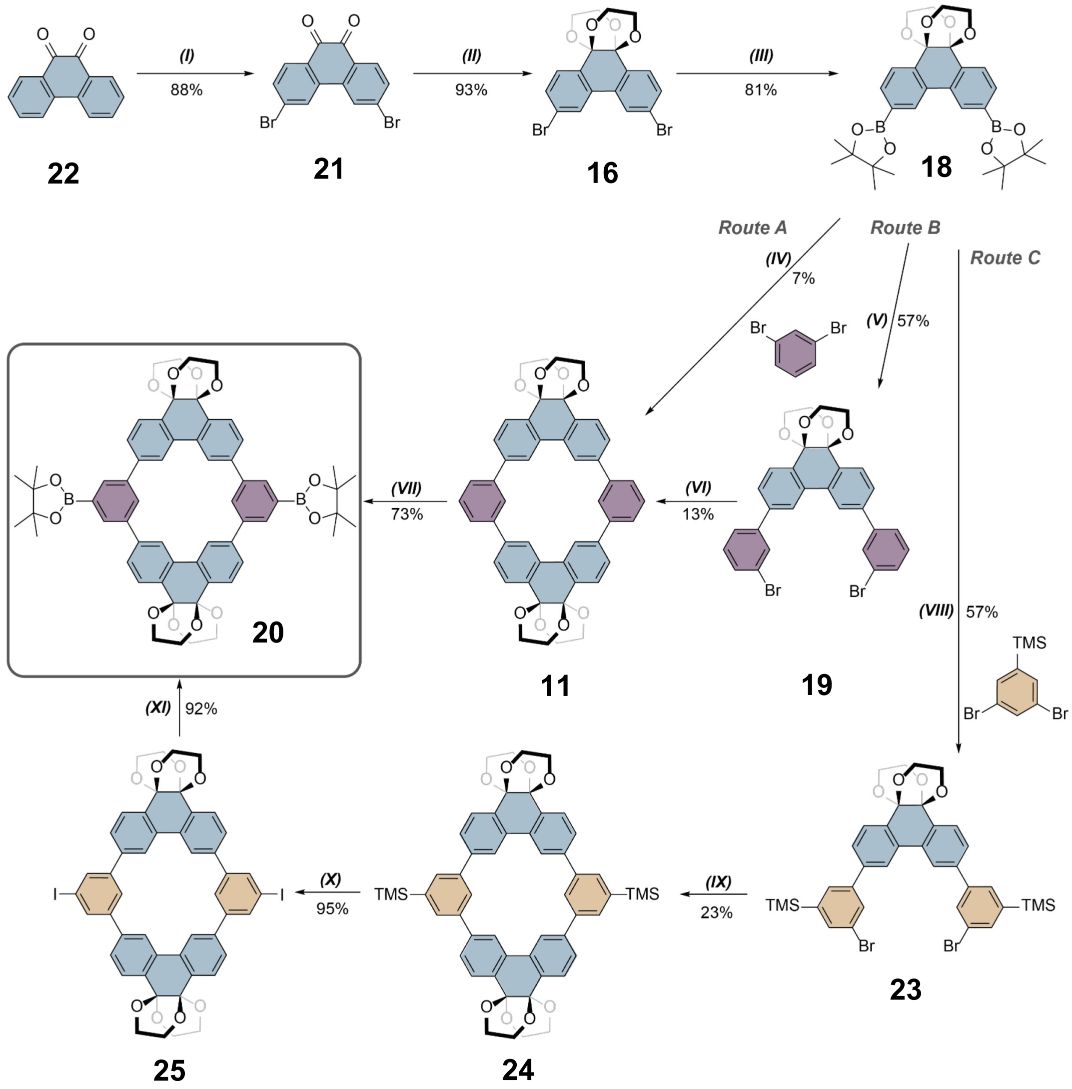

Figure 3. 8. Synthetic routes towards macrocycle **11**. Reagents and conditions: (I) DBPO, Br_2, nitrobenzene, 140 °C, 3 h; (II) ethylene glycol, CSA, methanol, 120 °C, 16 h; (III) bis(pinacolato)diboron, Pd(dppf)Cl_2, KOAc, 1,4-dioxane, 80 °C, 16 h; (IV) 1,3-dibromobenzene, Pd(OAc)$_2$, SPhos, K_3PO_4, 1,4-dioxane, 60 °C, 3 h; (V) 1,3-dibromobenzene, Pd(dppf)Cl_2, K_2CO_3, DMSO, 80 °C, 4 h; (VI) borylated phenanthrene **18**, Pd(OAc)$_2$, SPhos, K_3PO_4, 1,4-dioxane, 60 °C, 24 h; (VII) bis(pinacolato)diboron, [Ir(COD)(OMe)]$_2$, 4,4′-di-*tert*-butyl-2,2′-dipyridyl, 1,4-dioxane, 120 °C, 36 h; (VIII) Pd(dppf)Cl_2, K_2CO_3, DMSO, 80 °C, 2 h; (IX) borylated phenanthrene **18**, Pd(OAc)$_2$, SPhos, K_3PO_4, 1,4-dioxane, 60 °C, 24 h; (X) iodine monochloride, dichloromethane, 25 °C, 30 min; (XI) bis(pinacolato)diboron, Pd(dppf)Cl_2, KOAc, DMF, 100 °C, 1 h.

The discussed flexibility in [6]CMP derivative **11** is well displayed in its solid state crystal packing. In analogy to cyclohexane only the chair confirmation is observed for **11** (Figure 3. 9).

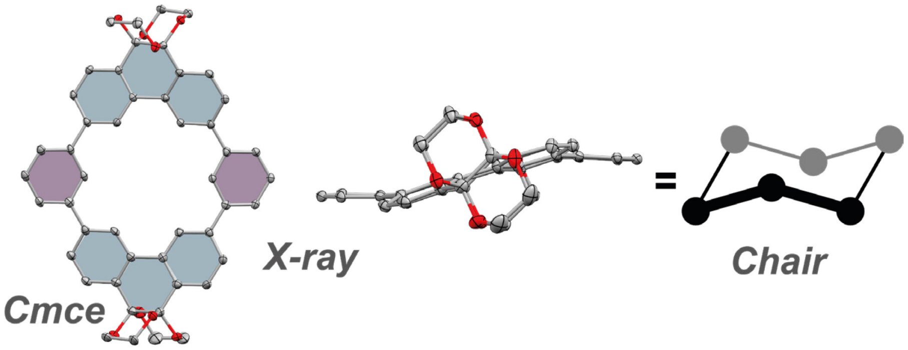

Figure 3. 9. Single-crystal X-ray structure of **11** (top view and side view) that has a chair conformation in the solid state. H-atoms are omitted for clarity, thermal ellipsoids are shown at 50% probability at 100 K.

Iridium-catalyzed C–H borylation of **11** resulted in borylated subunit **20**, which was utilized to investigate platinum and gold mediated macrocyclizations. Based on earlier reports we presumed that the platinum mediated macrocyclization is likely to be size unselective.[69,73,188,225] While the gold-mediated macrocyclization has been size-selective in earlier reports, so far it only gave trigonal metallacycle structures for rigid rod shaped aromatic subunits (Figure 3. 10a).[81,191]

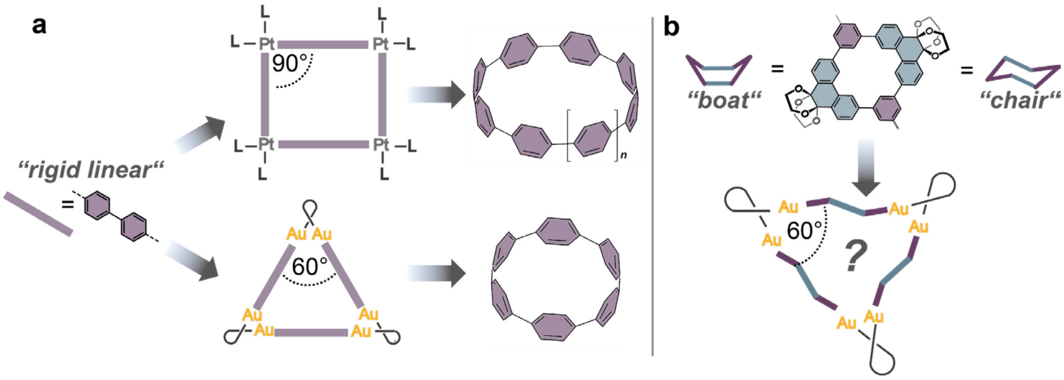

Figure 3. 10. a) Schematic representation of the favored geometrical shapes for the platinum and the gold mediated macrocyclization utilizing rigid rod shaped aromatic subunits. b) Expected trigonal geometry using a flexible macrocyclic subunit based on macrocycle **11**.

Initial exploration of established platination methods[52,142,213] to form Pt-macrocycle **26[*n*]** and reductive elimination gave a mixture of various ring sizes (Figure 3. 11). Isolation of the fourfold nanoring **12[4]** and the fivefold nanoring **12[5]** was achieved by tedious recycling gel permeation chromatography (*r*GPC) in < 1% yield, each.

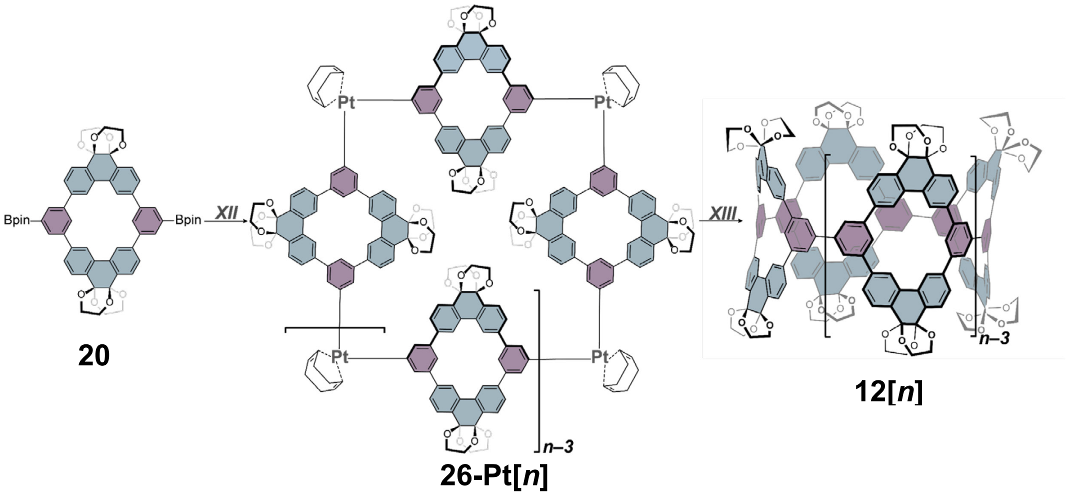

Figure 3. 11. Synthetic scheme for the platinum mediated macrocyclization XII) [PtCl$_2$(COD)], CsF, THF, 66 °C, 24 h; XIII) P(Ph$_3$) toluene, 100 °C, 22 h, <1% yield each over two steps for isolated nanorings **12[4–5]**; COD=cyclooctadiene.

Formation of several ring sizes and low yields are common features observed in other examples following the platinum-mediated macrocyclization, including the reported synthesis in the previous chapter.[69,71,73,74,188,225] Even though Poriel and co-workers reported an improve of size-selectivity, screening different solvents this could not be achieved in our system.[192]

Running into a similar problem as reported in the last chapter, we turned to a completely new macrocyclization method utilizing dinuclear gold(I)-complexes. As there are exclusively reports on triangular metallacycles in the literature we expected a cyclotrimerization leading to an equally-shaped macrocycle as in Figure 3. 10b.[81,191] Reaction of [6]CMP diboronic ester **20** with [Au$_2$Cl$_2$(dcpm)] (dcpm=bis(dicyclohexylphosphino)methane) produced an unexpected fourfold gold macrocycle **26[4]** in 33% yield after *r*GPC.

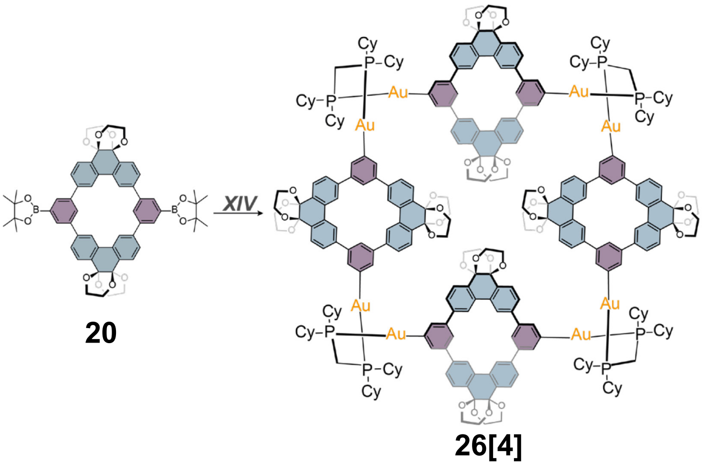

Figure 3. 12. Synthetic scheme for the gold mediated macrocyclization XIV) [Au$_2$Cl$_2$(dcpm)], Cs$_2$CO$_3$, toluene/EtOH/H$_2$O (4:1:1), 50 °C, 20 h; XV) PhICl$_2$, DMF, –50 °C to 25 °C, 20 h, 35% yield.

Defined fractions of larger ring sizes were not detected during preparative *r*GPC resulting in a straight forward separation. Nevertheless, comprehensive characterization of **26[4]** by NMR spectroscopy was not possible due to broad signals and limited solubility. As we presumed that an increase of the dynamics of the system might lead to a sharpening of the NMR signals we performed variable temperature (VT) ^{1}H NMR experiments, yet did only observe degradation of **26[4]** at above 65 °C to subunit **11** (Figure 3. 13).

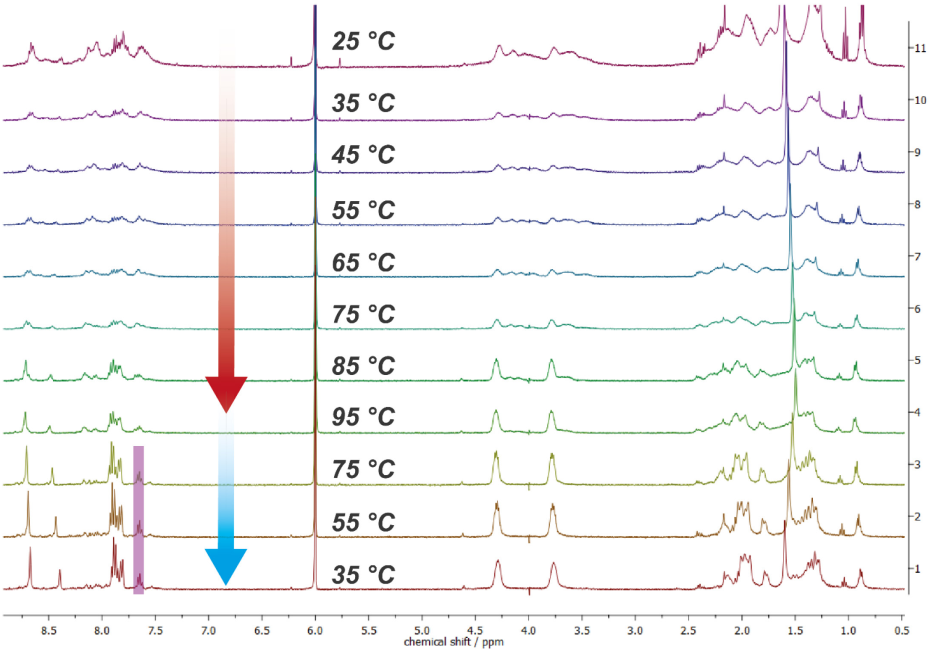

Figure 3. 13. ^{1}H NMR variable temperature (VT) spectra (400 MHz, $C_2D_2Cl_4$, 25–95 °C and 95–35 °C) of Au-macrocycle **26[4]**.

Comparing the ^{1}H NMR spectrum of **26[4]** after cooling down again to 25 °C to the ^{1}H NMR spectrum of [6]CMP derivative **11** shows signals in agreement with each other, especially in regard of the newly formed triplet. This signal must correspond to the signal for the proton attached to the carbon atom, which was previously bound to a gold atom (highlighted in purple, Figure 3. 13).

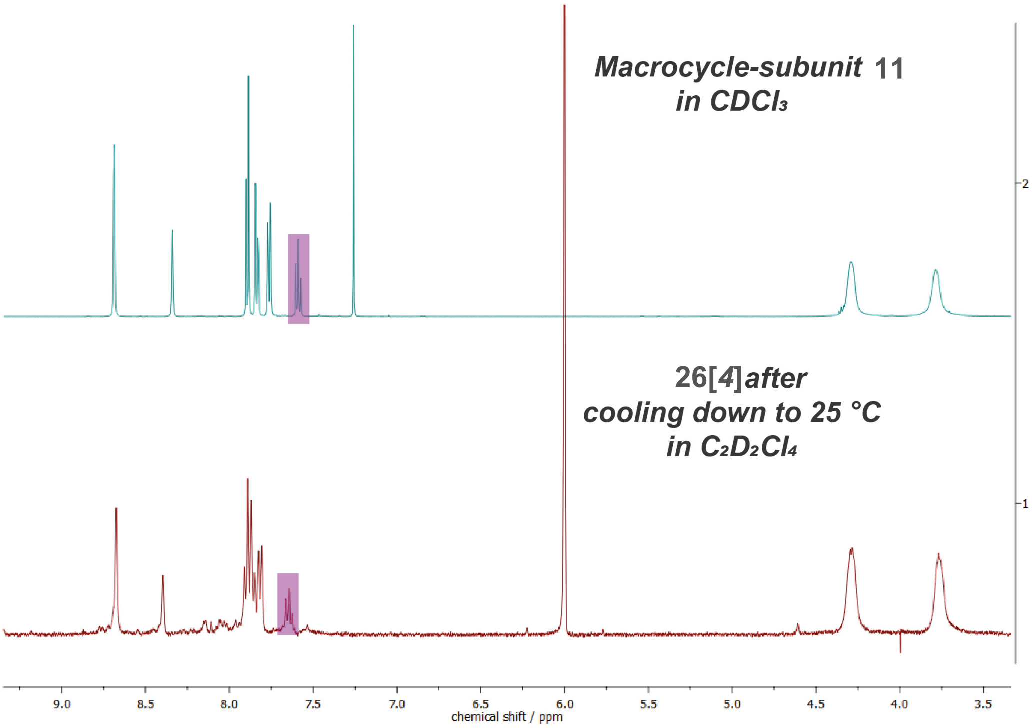

Figure 3. 14. ^{1}H NMR spectra of [6]CMP derivative **11** (500 MHz, $CDCl_3$, 25 °C) (top) and the ^{1}H NMR spectra (400 MHz, $C_2D_2Cl_4$, 25 °C) of the degradation product after VT-NMR experiment of Au-macrocycle **26[4]**.

Fortunately, crystal formation was repeatedly observed in $CDCl_3$ after *r*GPC purification, where several different crystals exhibited uniform unit cell parameters (Figure 3. 15). As a result, unambiguous structural prove for **26[4]** was obtained from single-crystal X-ray diffraction data. Macrocycle **26[4]** displays an unusual structure in which two [6]CMP moieties are in a chair conformation and two [6]CMP moieties are in a boat conformation (Figure 3. 16). This arrangement produces hyperbolic edges of the complex in the solid state. The sum of the angles deviates from 360° usually expressed by Euclidian geometries, which is characteristic for hyperbolic geometries. In addition, complex **26[4]** has two chirality axes formed by the twisted Au_2P_2C five-membered rings of the two corners in the asymmetric unit. We determined these axis to be of *M* and *P* chirality (Figure 3. 15).

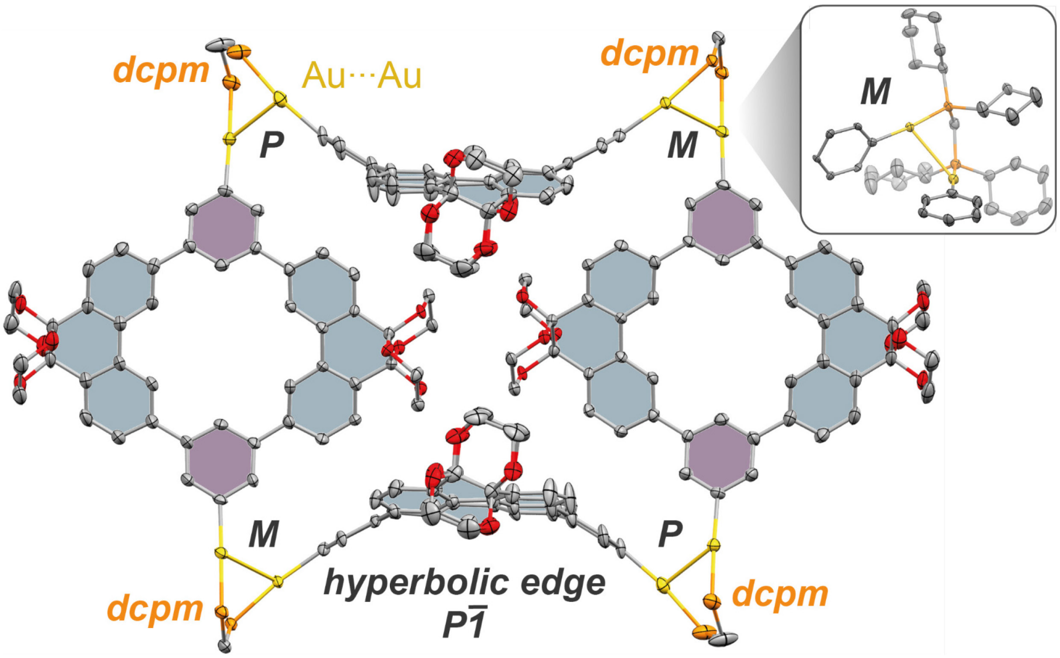

Figure 3. 15. Single-crystal X-ray structure of gold macrocycle **26[4]** with an inset showing the dcpm ligand and the chirality of the gold-corner. H-atoms, dcpm ligands (including non-refined atoms) and solvent molecules are omitted for clarity, thermal ellipsoids are shown at 50% probability, data obtained at 100 K. (dcpm = bis(dicyclohexylphosphino)methane).

In summary the crystal structure of **26[4]** displays several unique features, yet they are in accordance with those reported earlier in the literature for triangular gold(I)macrocycles.[81] The four Au_2(dcpm) corners show torsion angles along the C–Au···Au–C bonds of 53° and 48° (Figure 3. 15), while aurophilic interactions between the Au(I)···Au(I) centers, bridged by a dcpm ligand, are present with distances of 3.124 Å and 3.150 Å (Figure 3. 16).

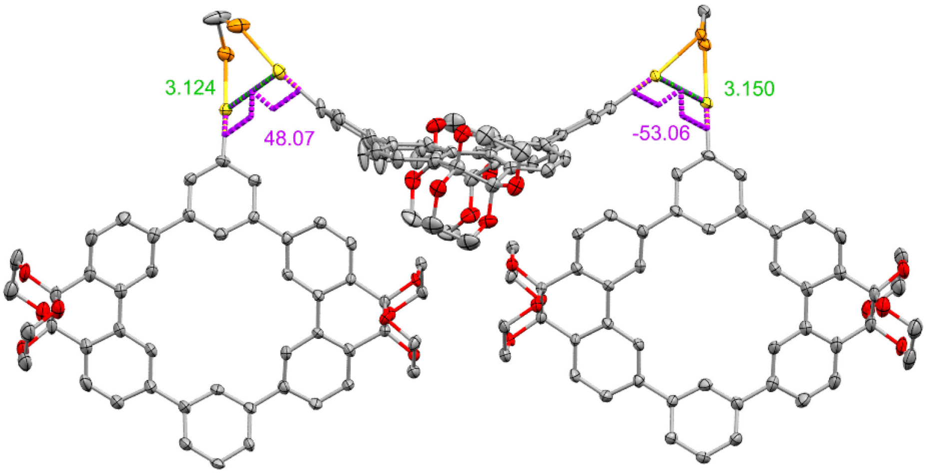

Figure 3. 16 Excerpt of the X-ray structure of **26[4]** showing the Au···Au distances in Å (green) and the torsion angles along the C–Au···Au–C bonds in degrees (purple).

This demonstrates the rigidity of the dinuclear Au(I) complex imposed through aurophilic interactions. Flexibility originates from the [6]CMP subunits due to torsional freedom around the phenyl—phenanthrenyl bonds. The polarized C–H bonds of the ethylene glycol groups in the center of **26[4]** engage in several C–H···O hydrogen bonds with heavy atom distances between 3.126 Å and 3.409 Å (Appendix Figure A. 68). We assume that this cooperative interaction network stabilizes the overall structure of **26[4]** while preventing inner void space. Only the interplay of the above mentioned effects leads to such an unexpected geometry in the solid state.

To proceed to the all-organic carbon nanoring **12[4]** eight Au–C_{Ar} need to be cleaved and four new C_{Ar}–C_{Ar} need to be formed. Furthermore two [6]CMP subunits need to transform from the chair conformation into the boat conformation and the other two [6]CMP units in metallacycle **12[4]** need to invert in regard of their boat conformation. All of this happens upon oxidative chlorination of complex **26[4]**. The oxidation of Au(I) to Au(III) induces the reductive elimination, which finally yield nanoring **12[4]** in 20% yield. As reported in the literature the precursor complex $[Au_2Cl_2(dcpm)]$ can be recovered using silica gel column chromatography (Figure 3. 17).

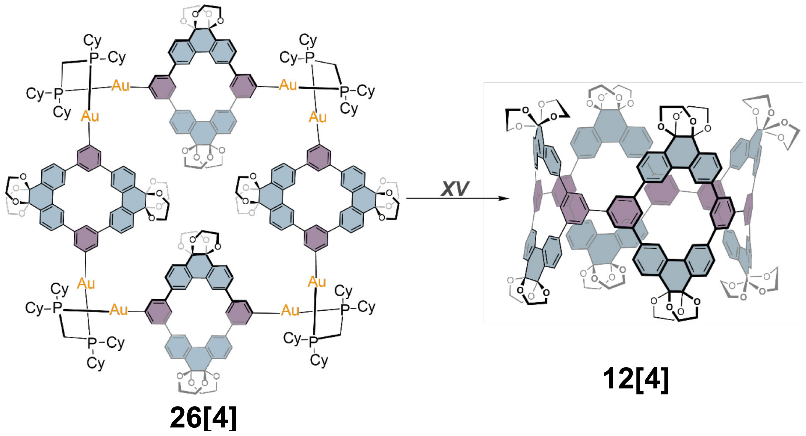

Figure 3. 17. Synthetic scheme for the gold mediated macrocyclization XV) $PhICl_2$, DMF, –50 °C to 25 °C, 20 h, 20% yield.

To obtain analytically pure samples silica gel column chromatography was performed followed by *r*GPC showing a size-selective formation of one ring-size (Figure 3. 18).

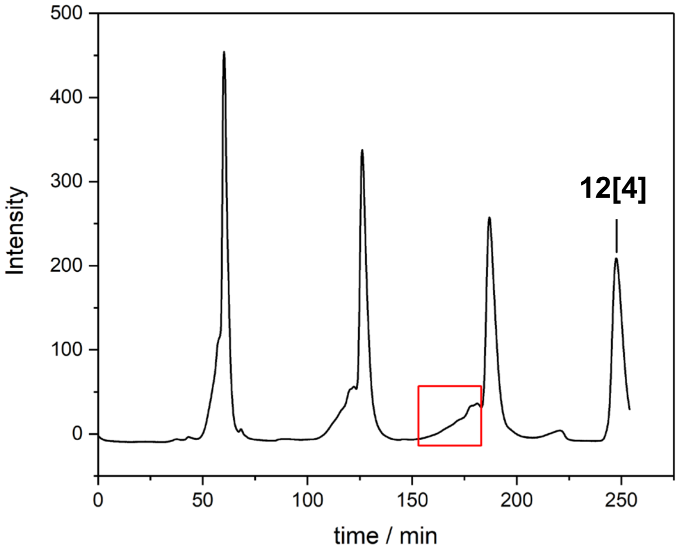

Figure 3. 18. Recycling GPC chromatogram of **12[4]** obtained synthetically from Au-macrocycle **26[4]**. Using $CHCl_3$ with 4% ethanol as a stabilizer. Highlighted in a red rectangle is assumingly linear oligomer, even though no masses were detected via MALDI-MS. The major signal collected at the end corresponds to macrocycle **12[4]**.

In summary, this synthetic route is clearly superior for our synthesis of nanorings in the form of **12[*n*]**. The size-selectivity reported in the literature can be well reproduced in our case. Even tough, ^{1}H NMR spectra does not allow the differentiation between different ring-sizes the unambiguous structural proof was obtained again by single-crystal X-ray analysis of **12[4]** (data obtained from the MX14.2 beamline at the synchrotron BESSY2).[226,227] Regarding the size of this macrocycle the central diameter of ca. 16 Å is comparable to that of [12]CPP.[228]

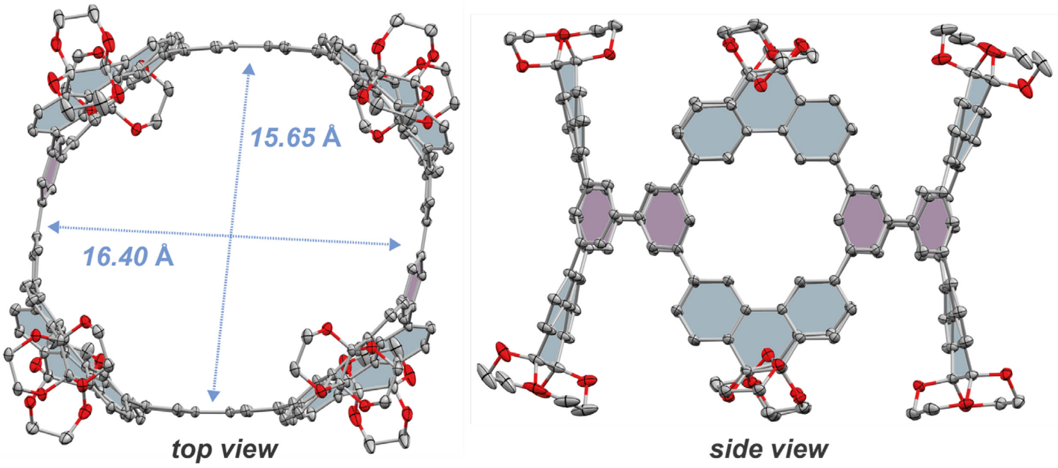

Figure 3. 19. All-organic nanoring **12[4]**. H-atoms, dcpm ligands and solvent molecules are omitted for clarity, thermal ellipsoids are shown at 50% probability, data obtained at 100 K. dcpm (=bis(dicyclohexylphosphino)methane).

Further, the data revealed a porous molecular crystal structure with several resolved $CHCl_3$ and benzene solvent molecules that show $Cl_3C{-}H\cdots O_{host}$ hydrogen bonds (3.2–3.5 Å heavy atom distance) and $C{-}Cl\cdots O_{host}$ halogen bonds (3.0 Å) (Figure 3. 20).

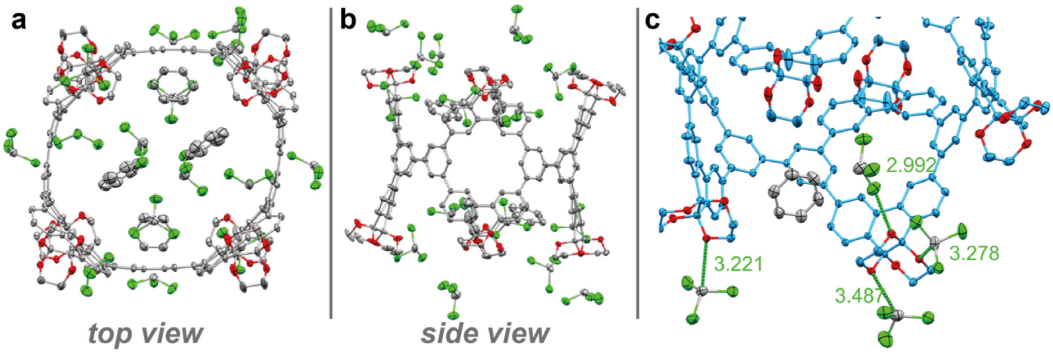

Figure 3. 20. a) top view of **12[4]** displaying the resolved solvent molecules b) side view c) excerpt of the X-ray structure of **12[4]** showing the solvent interactions (1 x halogen bond: $Cl\cdots O_{host}$ = 2.992 Å, 3 x H-bond ($Cl_3C{-}H\cdots O_{host}$= 3.221–3.487 Å) between the $CHCl_3$ and the ethylene glycol groups. Color code: C_{host} = blue, $C_{solvent}$ = grey, O = red, Cl = green. thermal ellipsoids are shown at 50% probability, data obtained at 100 K.

The packing shows a slipped-stacked tubular arrangement, presumably due to the sterically demanding ethylene glycol groups that prevent a self-filling herringbone assembly (Figure 3. 21).

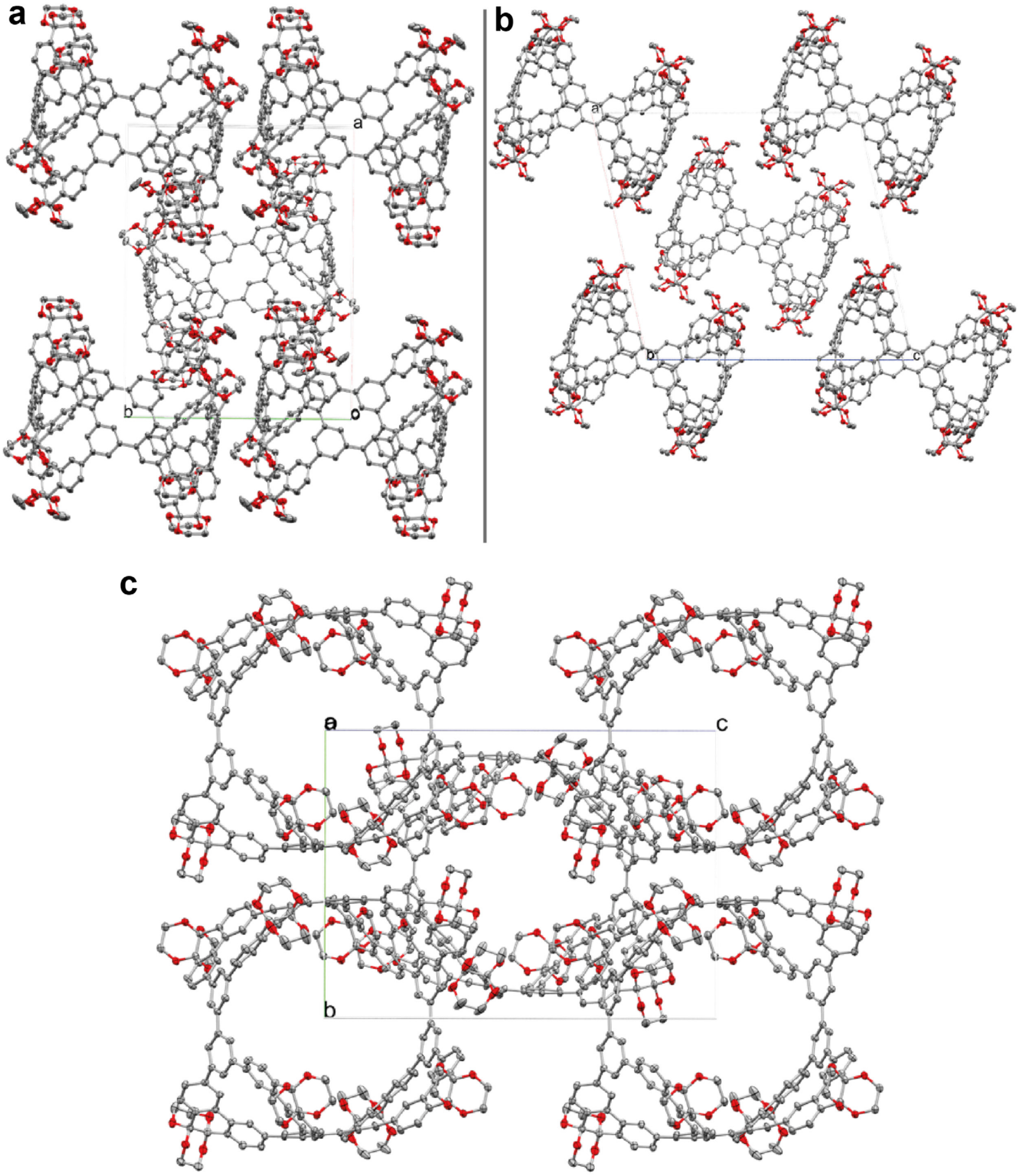

Figure 3. 21. X-ray structure of **12[4]** showing the crystal packing viewed along a) the c-axis, b) the b-axis, c) the c-axis.

3.4. Photophysical Properties and Strain Analysis of 12[*n*]

The UV/vis absorption maximum $\lambda_{\max}$ of **12[4]** at 261 nm shows only a small red shift compared to its subunit **11** at 259 nm due to the poorly conjugated meta-connectivity between the individual [6]CMP-panels. Similar to [*n*]CPP-type macrocycles, a small red-shifted shoulder can be observed for **12[4]** (Figure 3. 22).

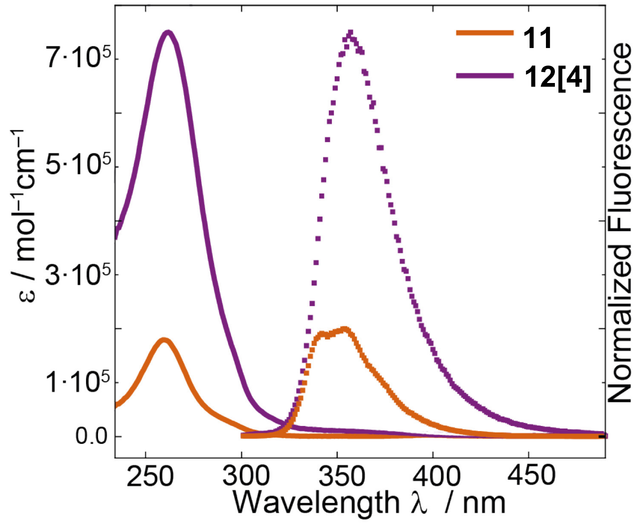

Figure 3. 22. UV/vis absorption (solid lines) and emission (dashed lines) spectra of **11** and **12[4]** (CH_2Cl_2, 25 °C, excitation wavelength 250 nm).

To explain this behavior, we turn to the same explanations as introduced in *Chapter 2.* Considering the oscillator strengths (f_{os}) of the calculated transitions, the shoulder at 292 nm is assigned to a Laporte forbidden HOMO–LUMO transition (Table 2. 7).[65,123,229] This property was observed by us for the class of [*n*]cyclo-2,7-pyrenylenes in *Chapter 2* as well and is a common feature observed for CPPs. It originates from the high molecular symmetry of these macrocycles, which is retained in their molecular orbital structure (Figure 3. 23).[173]

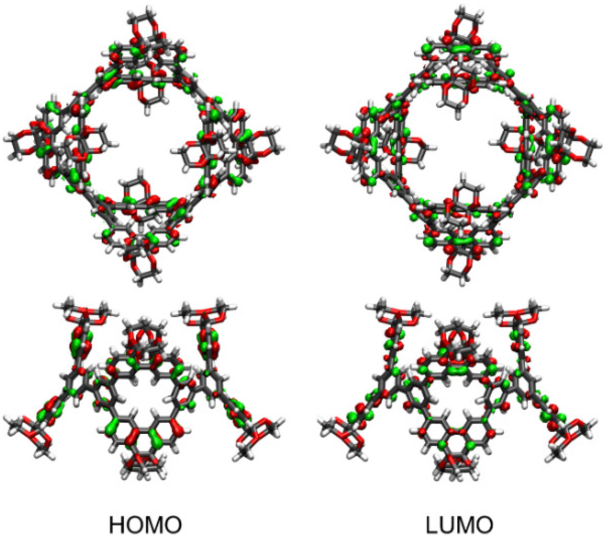

Figure 3. 23. HOMO, LUMO, representation on the geometry optimized structure of **12[4]** from top and side view (level of theory: B3LYP-D3/6-31G(d)).

Interestingly, the main absorption band at 261 nm of **12[4]** does not correspond to the HOMO→LUMO+1 or HOMO→LUMO+2 transition as it is typically observed for [*n*]CPPs, but is composed of multiple transitions between various energy levels (Table 2. 7, here the main absorption is calculated to 265 nm).

Table 2. 7. Calculated transitions of **12[4]** (level of theory: TD-DFT/cam-B3LYP/6-31G(d,p), PCM (CH_2Cl_2, as implicit solvent).

Excited State	λ / nm	Oscillator Strength	Transition Contribution (first 5 transitions)		Orbital Assignment
1	266.1	0.000	768 → 777	10%	770 = HOMO–2 771 = HOMO–1 772 = HOMO 773= LUMO 774 = LUMO+1 775 = LUMO+2
			769 → 773	12%	
			769 → 777	16%	
			770 → 776	19%	
			771 → 775	19%	
			772 → 774	19%	
2	265.4	0.005	767 → 775	12%	
			769 → 774	12%	
			769 → 780	16%	
			770 → 778	16%	
			771 → 779	16%	
			772 → 773	17%	
3	265.2	0.395	771 → 773	13%	
			771 → 774	15%	
			771 → 777	16%	
			771 → 780	12%	
			772 → 775	15%	
			772 → 779	11%	
4	265.2	0.395	770 → 773	11%	
			770 → 774	17%	
			770 → 777	16%	
			770 → 780	12%	
			772 → 776	14%	
			772 → 778	11%	
5	265.1	0.3067	768 → 779	15%	
			771 → 773	12%	
			771 → 774	13%	
			772 → 775	13%	
			772 → 779	12%	

The photophysical properties of these CPP-type macrocycles cannot only be derived from the symmetrically curved structure, but as well from the molecular strain energy necessary to create this circular arrangement. To calculate the strain energy of **12[*n*]** (*n* = 3–5), either the homodesmotic equation or StrainViz[112] can be used (Table 2. 8).[110] The requirements to construct a homodesmotic reaction were introduced in detail in *Chapter 1 (*Figure 1.17*)*. Following these rules, the homodesmotic equation to calculate the ring strain of **12[*n*]**, was put together. The structures of **12[*n*]** as well as their subunit **11** and the corresponding dimer were optimized by DFT calculations at the B3LYP-D3/6-31G(d) level. Since the [6]CMP subunit takes up a boat conformation within the macrocyclic structures, it is particularly important to optimize the geometry of subunit **11** and the dimer to this conformation, too.

By comparing the values for **12[*n*]** (Table 2. 8, last column, entry 1–3), it is noticeable that the strain energies differ from the expected results. The strain energy of trimer **12[3]** is 60.7 kcal mol^{-1}. With an increasing diameter we expected that pentamer **12[5]** has a lower strain energy than **12[3]**, however the calculated energy is 70.5 kcal mol^{-1} (Table 2. 8, last column, entry 1 and 3). This high strain energy experienced by **12[5]** is unrealistic if compared to [12]CPP (Table 2. 8, last column, entry 4), since [12]CPP is smaller in diameter and does not display the conformational degrees of freedom to compensate the strain energy. In sharp contrast to the high energies of **12[3]** and **12[5]**, the tetramer **12[4]** has a calculated strain energy of 4.0 kcal mol^{-1} (Table 2. 8, last column, entry 2), which is significantly lower. Overall, we expected that the strain energy gets smaller with an increase in ring-size which is not observable. A counterintuitive trend is visible where pentamer **12[5]** has the highest and tetramer **12[4]** the lowest strain energy. We reason that the deviation of the calculated values from the estimated trend is due to the flexibility of the phenine framework. Multiple, flexible dihedral angles favor numerous local minima which complicates the calculation involving the subunit **11** and its dimer.

Table 2. 8. The strain energies calculated by StrainViz[112] and classified in total strain, bond strain, angle strain and torsion strain as well as the calculated strain from the homodesmotic equation for **12[*n*]**. Calculations were performed by DFT calculations at the B3LYP-D3/6-31G(d) level.

	StrainViz				homodesmotic eq.
	total strain	bond strain	angle strain	torsion strain	total strain
	[kcal mol^{-1}]				
12[3]	30.1	5.6	3.2	21.3	60.7
12[4]	10.7	0.4	1.0	9.3	4.0
12[5]	6.7	1.2	0.8	4.2	70.5
[12]CPP	–	–	–	–	48.1[111]

Based on the complexity of this system, the StrainViz approach seems to be more suitable. As explained in the previous chapter this approach tries to approximate the calculation of an ideal strain release trajectory without the need to calculate differences between **12[*n*]** and its subunits (Figure 3. 24).

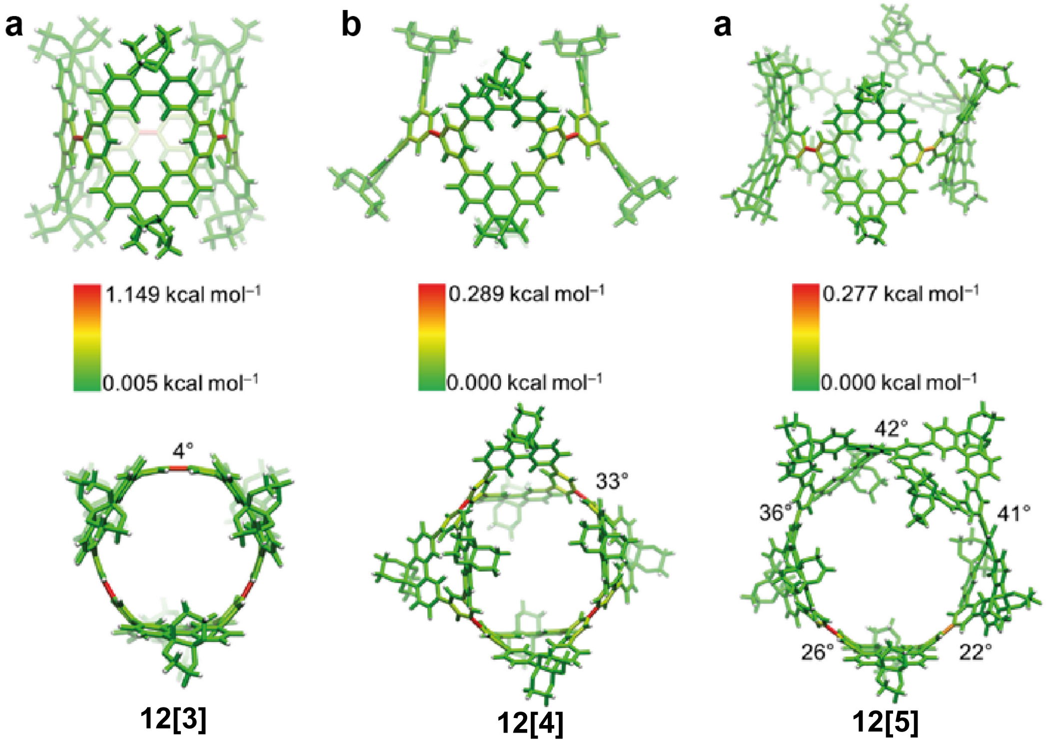

Figure 3. 24. The torsion strain energies calculated and visualized by StrainViz for a) **12[3]**, b) **12[4]**, and c) **12[5]**, from side and top view are shown. The top view of each cycle has additionally the torsion angle for each strained bond implemented. The color code represents the torsion on each bond and carbon atom and should be considered independently for each molecule. Calculations were performed by DFT calculations at the B3LYP-D3/6-31G(d) level.

The strain energy of **12[4]**, calculated using StrainViz, revealed an evenly distributed dihedral strain energy on all twelve biphenyl units within the [6]CMP-panels, but a localized strain energy on the bonds connecting the [6]CMP moieties (red bonds Figure 3. 24). As expected, the overall strain for **12[4]** is with 9.3 kcal mol^{-1} significantly smaller compared to 48.3 kcal mol^{-1} for equally sized [12]CPP. [111]

This is explained by multiple flexible *meta* connections (additional degrees of freedom) in **12[4]** compared to [12]CPP, which efficiently reduces the strain energy. Further, the expected trend of reduced strain energy upon an increase of molecule size is well reproduced in the StrainViz approach.

The highest observed ring-strain energy was calculated for the trimer with 21.3 kcal mol^{-1}. In the case of **12[3]** and **12[4]**, the strain is located equally distributed on the bonds connecting each [6]CMP panel which is also reflected in the equal dihedral angles of these bonds. However, for the pentamer **12[5]** a localized strain on two bonds is observed which is also in agreement with the varying dihedral angles of each bond linking the monomers. This irregularity can be explained by the odd number of monomeric subunits. Each monomer can either flip the top or the bottom phenanthrene towards the center of the ring. Due to steric repulsion, the flip is ideally alternating, as it can be seen for **12[4]**. Yet, the alternation can only be achieved by an even number of fragments within a cyclic structure. Small molecules with an odd number of fragments such as **12[3]** are too rigid to allow any additional flexibility and are forced into shape-persistent structures. Larger macrocycles such as **12[5]** rotate one monomeric unit into the void of the cycle which influences the arrangement of the other monomers resulting in the release of steric repulsion. However, the rotations break the symmetry and inducing strain on the opposite bond of the most tilted fragment.[230,231]

3.5. Supramolecular Binding of Aromatic Guests with 12[4]

The strain-energy experienced by **12[4]** induces a certain degree of shape persistence that leads to an unusually large void volume for a single small molecule. Inspired by the successful construction of host-in-host complexes in the previous *Chapter 2* we turned again to isothermal titration techniques to study the host properties of **12[4].** The central void volume of **12[4]** has its largest extension in the center were the heavy atom distances show a diameter of the cavity (d_{cavity}) averaged to 16.6 Å (Figure 3. 25a). The opening is defined by the heavy atom distance between the closest atoms of the ethylene glycol groups with an average (d_{gate}) of 14.2 Å (Figure 3. 25b). The ratio between d_{gate} and d_{cavity} calculates to 0.86. This value means only a medium degree of confinement compared to that of the four and five membered pyrene nanorings investigated in the last chapter. The void volume was determined using the MS Roll algorithm implemented in X-Seed giving a size of 5500 Å^3 (Figure 3. 25b, c, blue volume, calculated and visualized using the MS Roll suite implemented in X-Seed Version 4.04[42]). These initial findings regarding macrocycle **12[4]** motivated us, to explore the guest uptake into this confined space.[197,198,225,232]

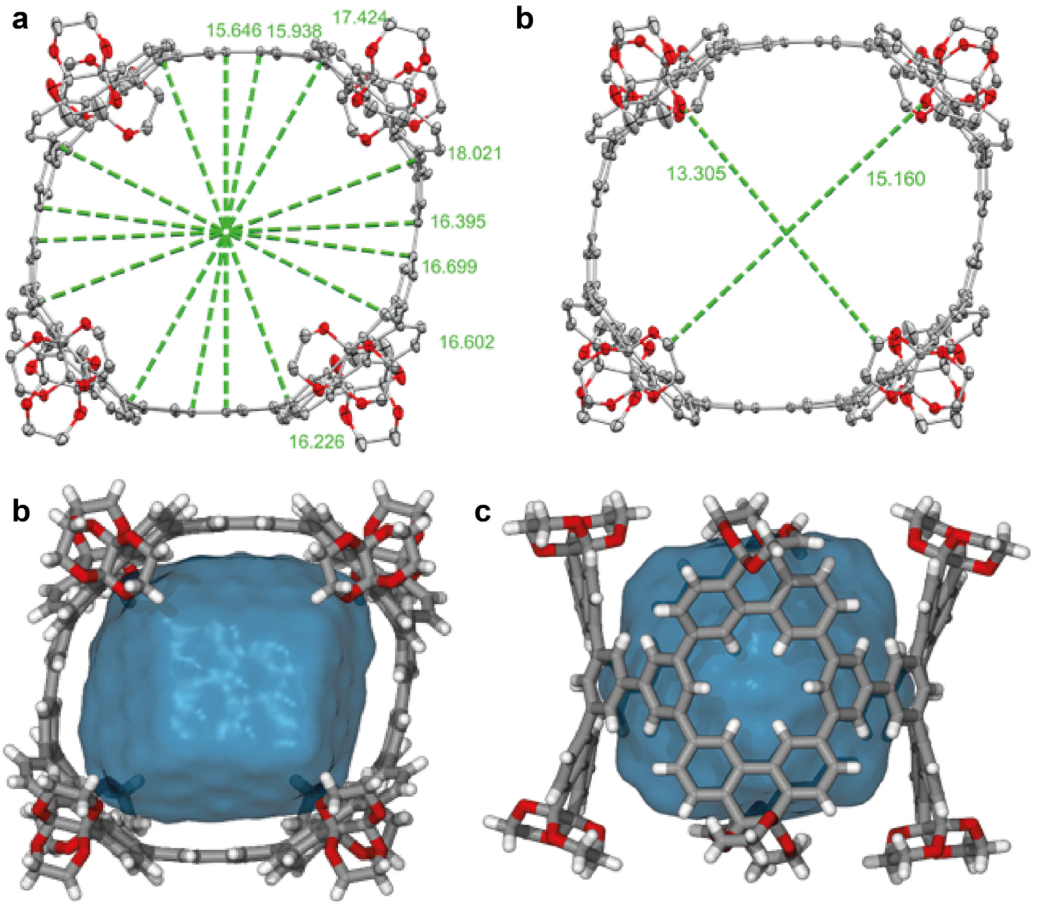

Figure 3. 25. X-ray structure of macrocycle **12[4]** a) (top view) with heavy atom distances representing the central diameter of the inner macrocycle (d_{cavity}) in Å), b) the diameter of the ethylene glycol decorated opening (d_{gate},)in Å, c) top view of the calculated and visualized inner void volume (5500 Å^3) using MS Roll, and d) side view.

Previous studies have shown that shape-persistent [*n*]CPPs bind [*n*–5]CPPs and fullerenes selectively.[70,128,129,188,213] The similarity of **12[4]** to [12]CPP, in regard of their central diameter, directed us to investigate the binding of [7]CPP through ^{1}H NMR isothermal binding titrations. Upon addition of [7]CPP to **12[4]** in CDCl$_3$ at 25 °C, three sets of protons (H$_a$, H$_d$, H$_e$,) showed a significant change in chemical shift ($\Delta\delta$) at fast exchange (Figure 3. 26a, b).

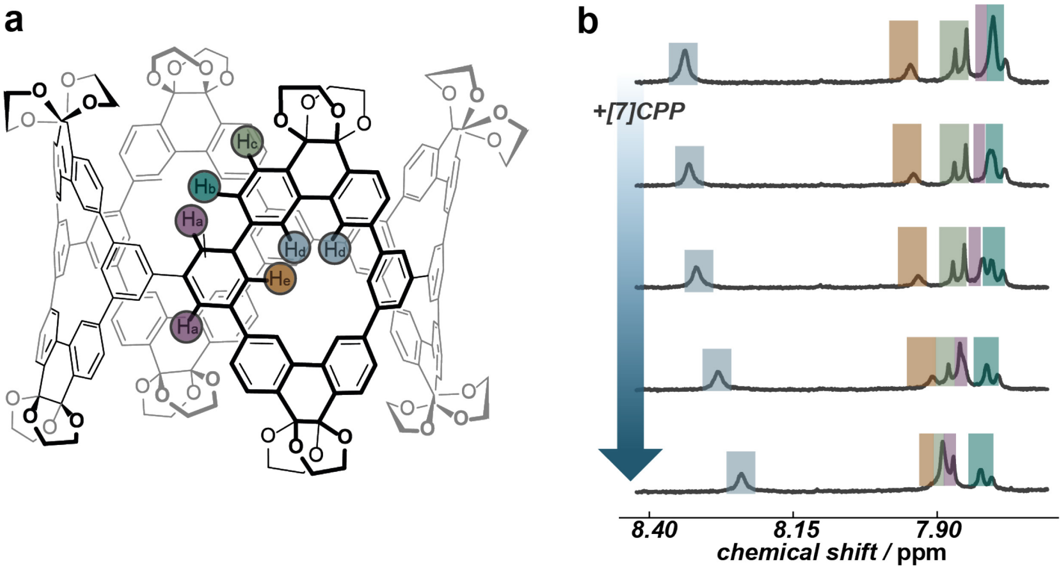

Figure 3. 26. a) Molecular structure of **12[4]** with the protons responsible for the observed signals highlighted in color b) ^{1}H NMR spectrum of **12[4]** upon addition of [7]CPP in the range of 8.40–7.80 ppm in $CDCl_3$ at 25 °C;

With the obtained spectra it is possible to calculate an association constant. Therefore, non-linear curve fitting (using Origin 2019b) of the titration data was performed according to the Benesi–Hildebrand method. The fitting curves were obtained by plotting the change of chemical shift ($\Delta\delta$) of the host signals against the concentration of the guest and using the following equation:[209,210]

$$\Delta\delta = \delta_{\Delta(\mathrm{HG})} \frac{\frac{1}{2}\cdot\left[\left([\mathrm{host}]_{Tot}\cdot[\mathrm{guest}]+\frac{1}{K_\mathrm{a}}\right)-\sqrt{\left([\mathrm{host}]_{Tot}+[\mathrm{guest}]+\frac{1}{K_\mathrm{a}}\right)^2-\left(4\cdot[\mathrm{host}]_{Tot}\cdot[\mathrm{guest}]\right)}\right]}{[\mathrm{host}]_{Tot}} \tag{3.1}$$

In Eq. 3.1 the unknown parameters are: $\delta_{\Delta(\mathrm{HG})}$ as the chemical shift of the host–guest complex and K_a as the association constant. An error of 20% is estimated for these values.

Using the change in chemical shift of proton H_a is not reasonable, as this signal overlaps with the signal of other protons. Thus, we only executed the curve fitting for the ^{1}H NMR chemical shifts of protons H_d and H_e (Figure 3. 27). In Addition, these signals are singlets allowing for an easier determination of the chemical shift, as all of the signals broaden upon guest addition. The downfield shift of proton H_d can be rationalized with the increased magnetic shielding experienced by these protons due to the exposition towards the π-surface of [7]CPP, which therefore must align parallel to the walls of **12[4]** in its center. The association constant of **12[4]**···[7]CPP is in the same range as that of [12]CPP···[7]CPP determined by Yamago and co-workers (K_a = 93 M^{-1} in TCE-d_2 at 50 °C).[134]

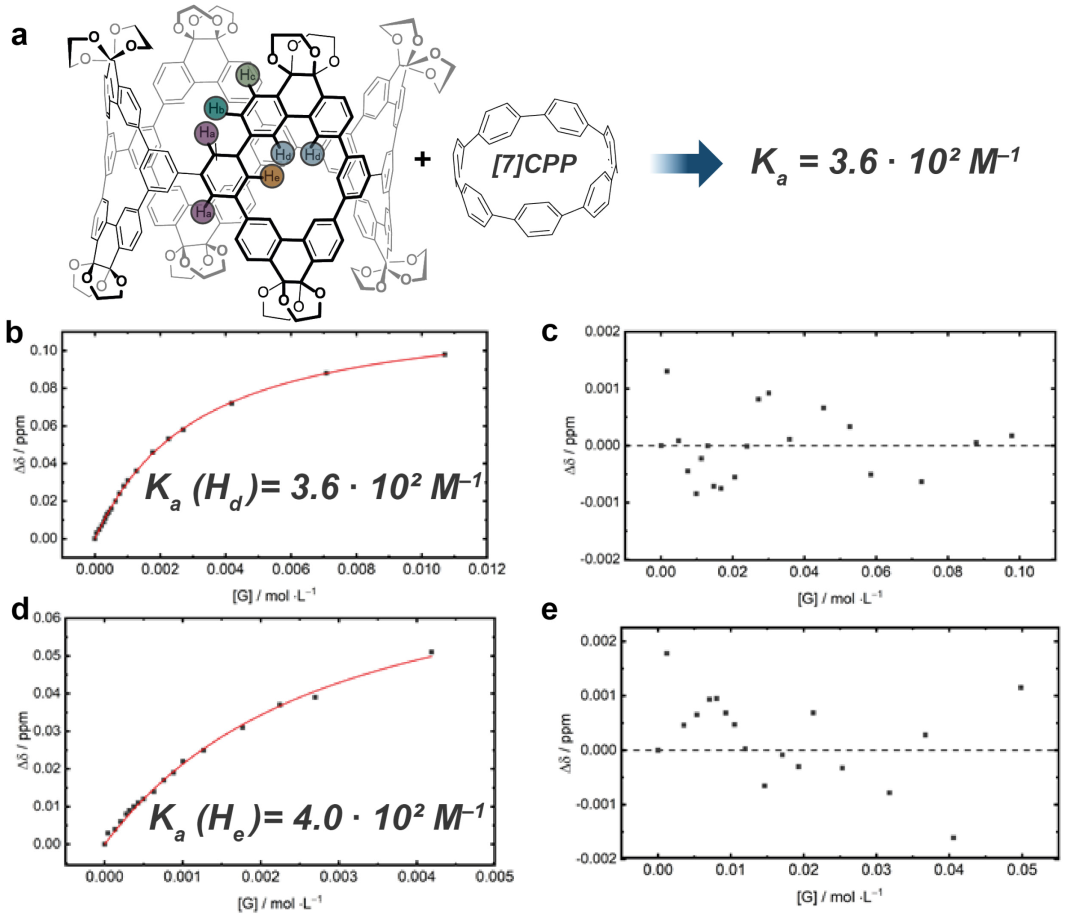

Figure 3. 27. a) Scheme for the investigated binding. b) Non-linear least-square curve fitting analysis obtained from the isothermal binding titration (c(**12[4]**) = $4.93 \cdot 10^{-4}$ mol L^{-1}, in $CDCl_3$ at 298 K) with 1:1 stoichiometry upon addition of [7]CPP. $\Delta\delta$ taken for proton H_d. The association constant K_a was determined to be: $K_a = 3.6 \cdot 10^2$ M^{-1} with an R^2 of 0.9996 c) corresponding residual difference plot of the predicted values of the fit vs experimental values. d) $\Delta\delta$ taken for proton H_e The association constant K_a was determined to be: $K_a = 4.0 \cdot 10^2$ M^{-1} with an R^2 of 0.9964. The last two additions could not be considered due to an overlap of the signals; hence the K_a of this fit is rather erroneous, and thus neglected and e) corresponding residual difference plot of the predicted values of the fit vs experimental values.

We show not only the titration data with its fit, but as well the corresponding residual distribution (Figure 3. 27c, e). It used to be common practice to determine stoichiometry of the host–guest complex in a given solvent at a given temperature by employing Job's method of continuous variation.[209,210] Nevertheless, recent reports in the literature suggest to confirm the choice of an appropriate stoichiometry by plotting the residuals of the non-linear curve-fit.[233,234] Hereby a stochastic distribution of the residuals confirms the choice of the used 1:1 stoichiometry. In contrast, a sinusoidal distribution of the residuals usually indicates that the wrong stoichiometry model was chosen. With the first successful binding we aimed to investigate other guests that show a suitable convex π-surface. In the following we only show the data of proton H_d, as it is based on 16 protons compared to 8 protons for H_e making it easier to determine the $\Delta\delta$ at challenging low concentrations. In general, the association constants determined with either proton are in the same range. The data for proton H_e is displayed in the appendix.

While earlier investigations found no binding of [*n*]CPPs with [*n*–6]CPPs, we wanted to test the binding of **12[4]** towards this [6]CPP as a guest. A small change in the chemical shift occurs upon addition of [6]CPP (Figure 3. 28)

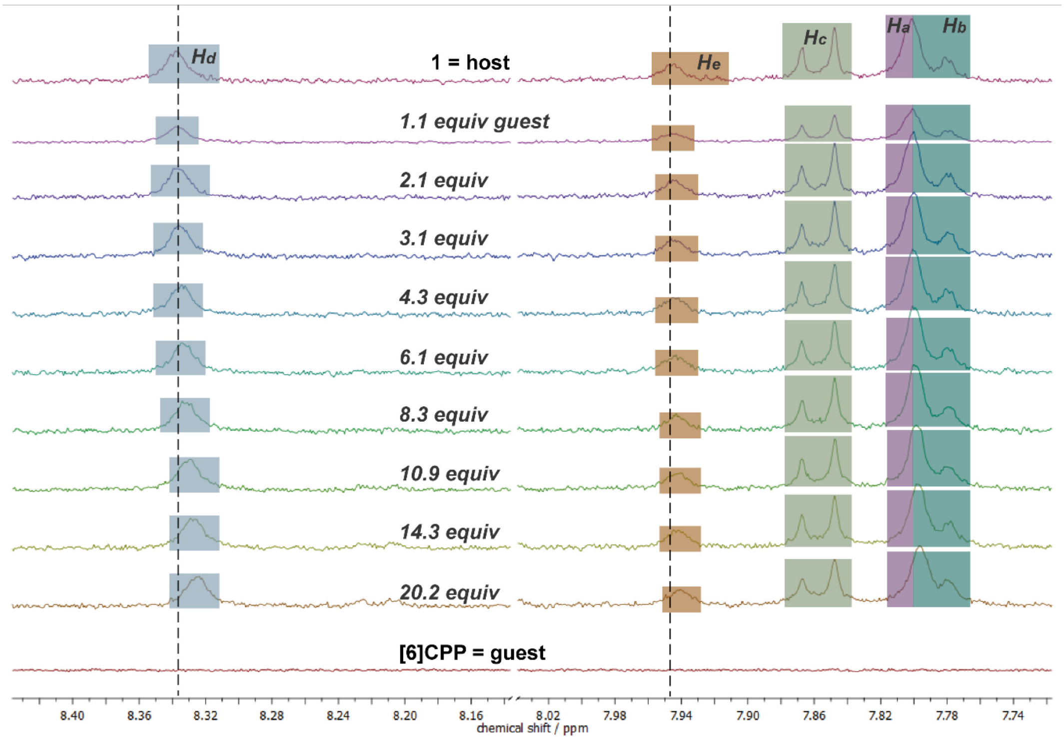

Figure 3. 28. Isothermal NMR binding titration, zoom into the chemical shift region where the host protons change. Dashed lines as a guidance for the small $\Delta\delta$. Spectra of **12[4]** at 25 °C, in $CDCl_3$, (c(**12[4]**) = $1.9\cdot10^{-4}$ mol L^{-1}) upon subsequent addition of [6]CPP as stock-solution in $CDCl_3$.

We could fit the obtained ^1H NMR binding data of proton H_d to obtain an association constant of K_a = 110 M^{-1}, resulting in a weaker binding than in the association of **12[4]**···[7]CPP (Figure 3. 29). The size mismatch of **12[4]** and [6]CPP clearly effects this result. In accordance to that non-linear curve fitting was unsuccessful for the data of proton H_e as the data remained in the linear regime (Appendix Figure A. 18 and Figure A. 19).

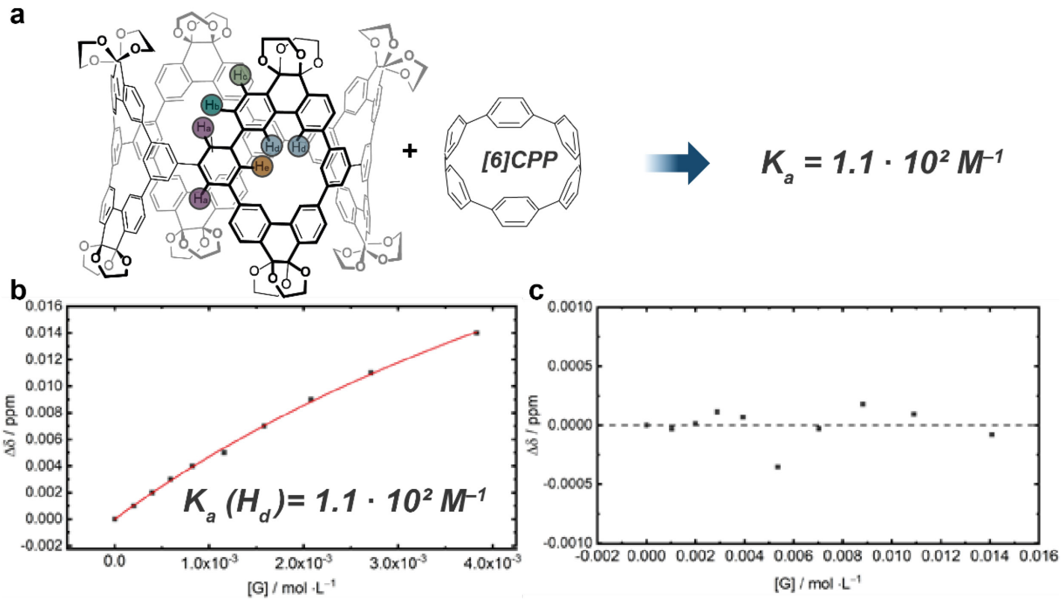

Figure 3. 29 a) Scheme for the investigated binding. b) Non-linear least-square curve fitting analysis obtained from the isothermal binding titration (c(**12[4]**) = 4.93·10^{-4} mol L^{-1}, in $CDCl_3$ at 298 K) upon addition of [6]CPP. $\Delta\delta$ taken for proton H_d. The association constant K_a was determined to be: K_a = 1.1·10^2 M^{-1} with an R^2 of 0.9989. c) Residual difference plot of the predicted values of the fit vs experimental values.

Fullerenes are known to be among the strongest binding guests for [*n*]CPPs, which guided us to investigate their association with nanoring **12[4]**. The reason for their strong binding towards [*n*]CPPs results from their large shape-complementary convex π-surface. Thereby it must be noted, that efficient binding is only reported for [10]CPP and C_{60}.[128,129] Regarding the size of macrocycle **12[4]** it has a central diameter of 16 Å—slightly too large to efficiently host C_{60} with its mean diameter of 7.1 Å—yet we could observe significant shifts for protons H_d and H_e (Figure 3. 30). The obtained data allowed us to determine an association constant of 7.2·10^3 M^{-1} for **12[4]**···C_{60} at 25 °C in *o*-dichlorobenzene-d_4 (DCB-d_4) (Figure 3. 31).

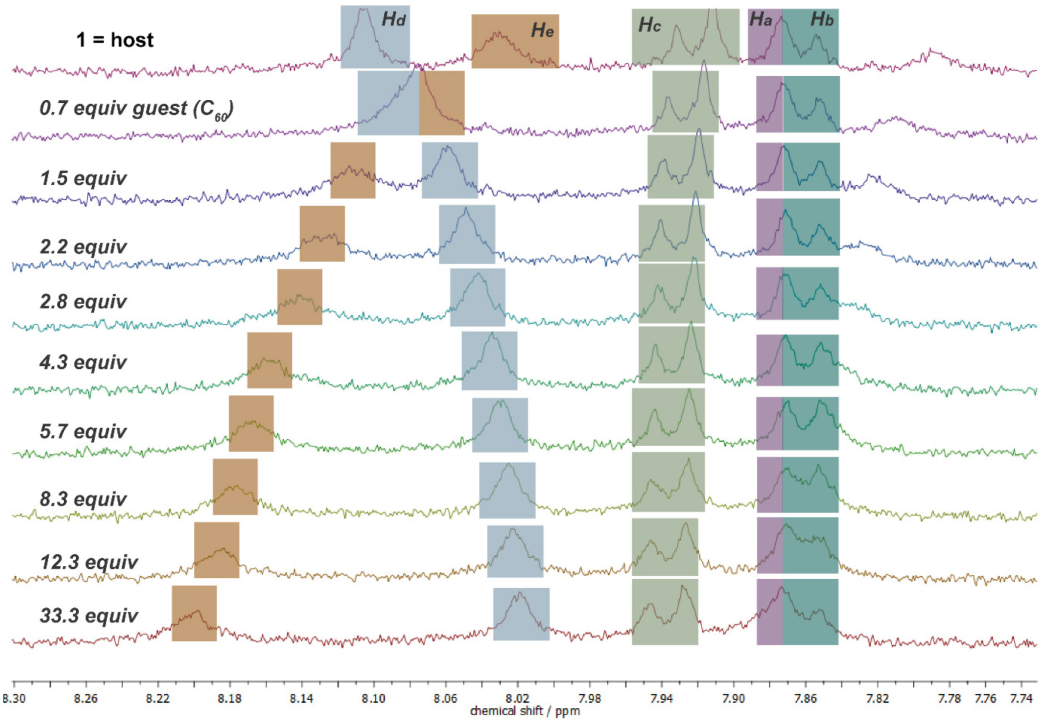

Figure 3. 30. Isothermal NMR binding titration, zoom into the chemical shift region where the host protons change. ^{1}H NMR spectra of **12[4]** at 25 °C, in *o*-DCB(*d*$_4$), (*c*(**12[4]**) = $2.79\cdot10^{-4}$ mol L^{-1}) upon subsequent addition of C$_{60}$ as a stock-solution in *o*-DCB(*d*$_4$) and as solid (last two additions).

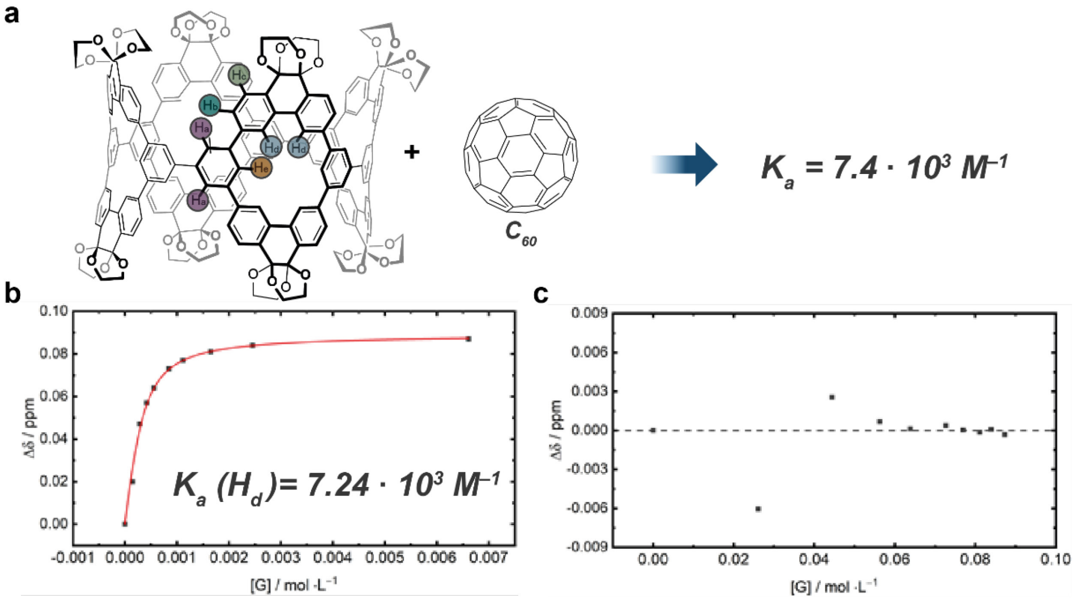

Figure 3. 31. a) Scheme for the investigated binding. b) Non-linear least-square curve fitting analysis obtained from the isothermal binding titration with 1:1 stoichiometry (*c*(**12[4]**) = $2.79\cdot10^{-4}$ mol L^{-1}, in *o*-DCB(*d*$_4$) at 298 K) upon addition of C$_{60}$. $\Delta\delta$ taken for proton H$_d$. The association constant K_a was determined to be: $K_a = 7.24\cdot10^3$ M^{-1} with an R^2 of 0.9942. c) Residual difference plot of the predicted values of the fit vs experimental values. Data acquired by isothermal binding titration with 1:1 stoichiometry.

Compared to the spherical shape of C_{60}, the shape of C_{70} is reminiscent of a rugby football with a short axis of 7.12 Å and a long axis of 7.96 Å.[235] As expected, the larger C_{70} can fill more of the void volume of host **12[4]** leading to an increased π–π interaction surface, which leads to a strong shift of the proton signals in the ^1H NMR spectra upon addition of C_{70} to nanoring **12[4]** (Figure 3. 32). that is reflected in a K_a of $1.0 \cdot 10^4$ M^{-1} (Figure 3. 32).

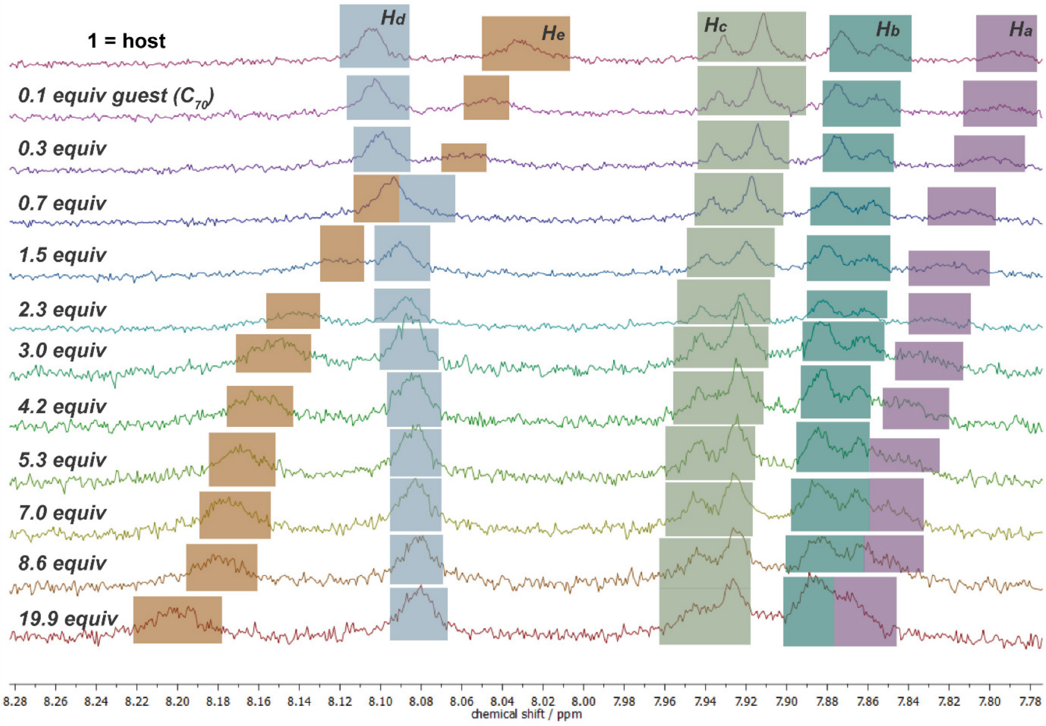

Figure 3. 32. Isothermal NMR binding titration, zoom into the chemical shift region where the host protons change. Spectra of **12[4]** at 25 °C, in *o*-DCB(d_4), (c(**12[4]**) = $2.92 \cdot 10^{-4}$ mol L^{-1}) upon subsequent addition of C_{70} as a stock-solution in *o*-DCB(d_4) and as solid (last addition).

In accordance to this change we were able to determine the strongest association of all our investigated host-guest systems a constants of K_a of $1.0 \cdot 10^4$ M^{-1} (Figure 3. 33).

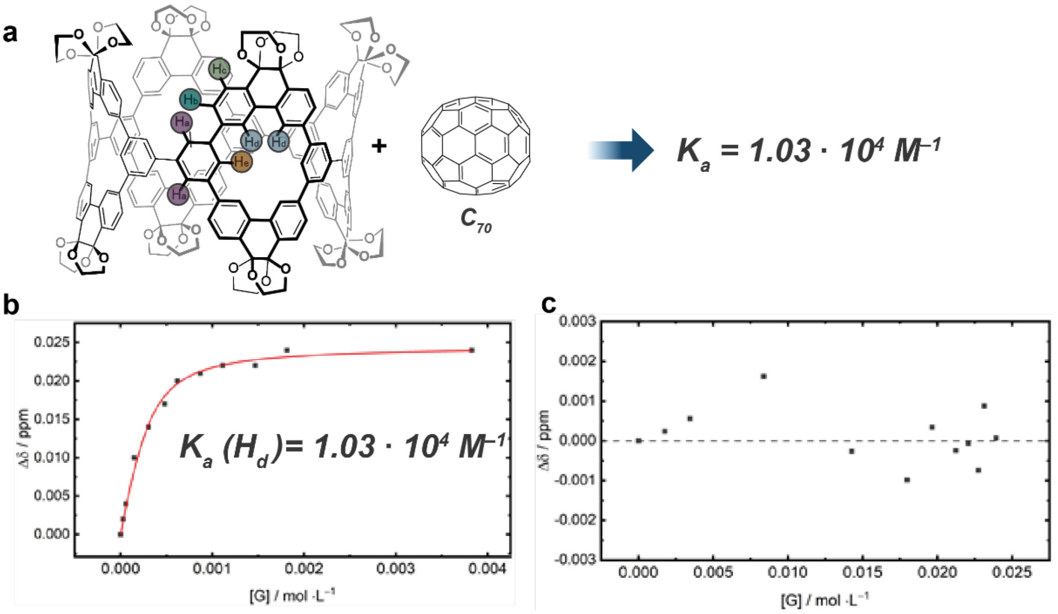

Figure 3. 33 a) Scheme for the investigated binding. b) Non-linear least-square curve fitting analysis obtained from the isothermal binding titration (c(**12[4]**) = $2.92 \cdot 10^{-4}$ mol L^{-1}, in *o*-DCB(d_4) at 298 K) upon addition of C_{70}. $\Delta\delta$ taken for proton H_d. The association constant K_a was determined to be: $K_a = 1.03 \cdot 10^4$ M^{-1} with an R^2 of 0.9936. c) Residual difference plot of the predicted values of the fit vs experimental values. Data acquired by isothermal binding titration with 1:1 stoichiometry.

In comparison, structurally similar [4]CPP geodesic phenine framework ([4]CPP-GPF) shows binding to C_{70} in the less competitive solvent toluene-d_8 of $K_a = 4.7 \cdot 10^4$ M^{-1}.[188] Of course, this result is somewhat expected, as both molecules have the exact same amount of phenyl rings. Possible structures of the investigated complexes of **12[4]** were disclosed by density functional theory (B3LYP/3-21G level of theory). Even though, this approach and the level of theory are not sufficient to accurately calculate the structure of a potential host-guest complex or determine energetically reasonable values for the host-guest binding it visualizes the ability of **12[4]** to bind a variety of guests with large curved π-surfaces. Albeit they are not perfectly complementary in size and shape (Figure 3. 34).

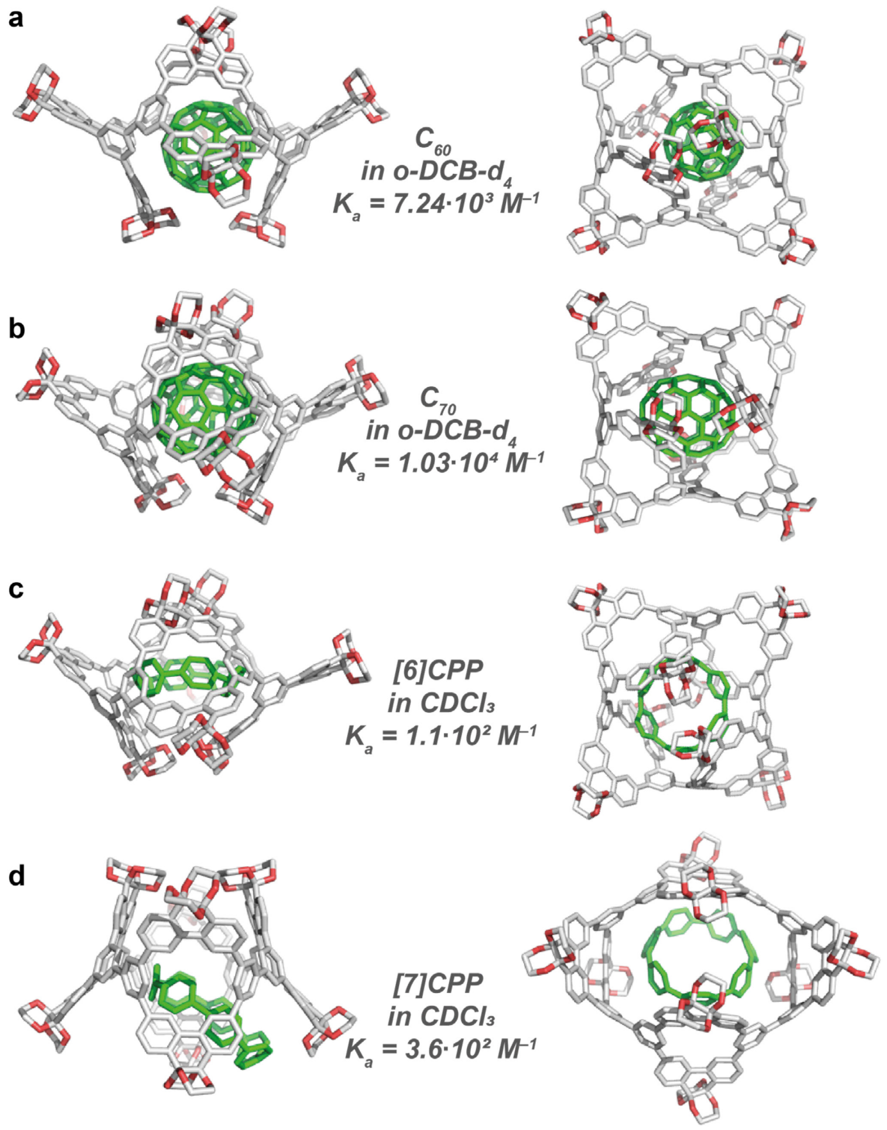

Figure 3. 34. Side and top view of the geometry optimized structures of **12[4]** with the investigated guests placed inside the void volume at the B3LYP/3-21G level of theory and the investigated guests with their corresponding association constants (K_a) determined by ^1H NMR isothermal binding titration in the respective solvent.

To pave the way for future assembly studies we wanted to determine, if **12[4]** really differentiates between aromatic molecules with a convex π-surface and guests which bear a flat aromatic π-surface. In general, planar π-aromatic molecules are already reported to bind to the inner π-surface of CPP-type macrocycles upon CH···π interactions.[133,236] Our titration studies though did not show binding of rigid planar π-aromatic molecules such as pyrene, perylene, or coronene (Figure 3. 35, experimental data in the Appendix Figure A. 8 and following).

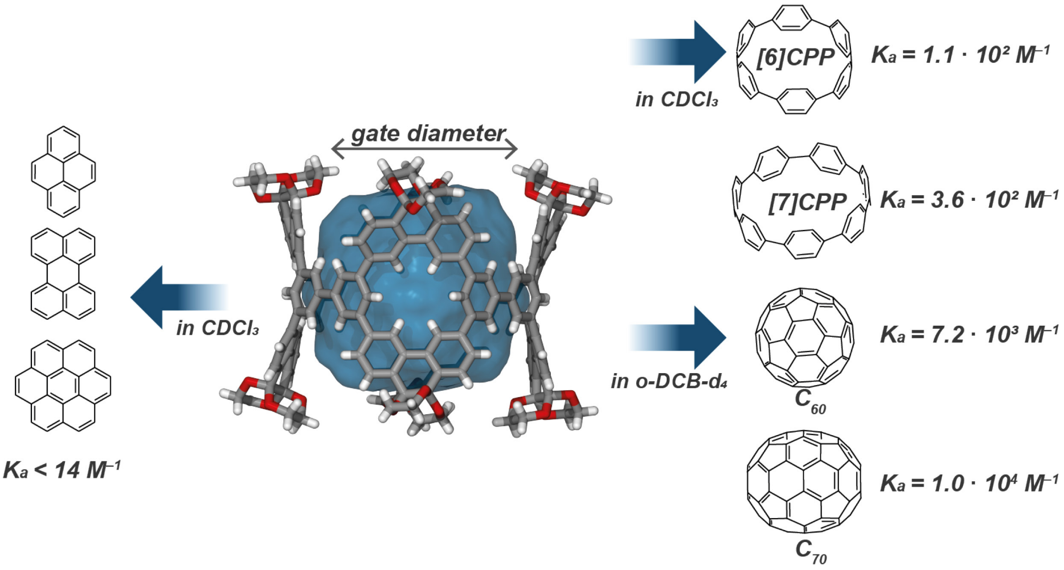

Figure 3. 35. Single-crystal X-ray structure of **12[4]** with the visualized void volume (calculated using the MS Roll suite implemented in X-Seed) and the investigated guests with their corresponding association constants (K_a) determined by ^{1}H NMR isothermal binding titration.

The presented data gives an overview of guests binding strongly inside the void volume and we envision **12[4]** as a promising host molecule for future assembly studies with more elaborated guests bearing the potential to achieve large multi-component supramolecular structures.

3.6. Conclusion

We investigated the synthesis of large almost strain free carbon nanorings with a high degree of rim-functionalization. The newly developed gold macrocyclization strategy appears to be superior in our case compared to the platinum mediated approach. A metal-organic macrocycle was synthesized and characterized consisting of hyperbolic geometric features that evolved from the unique conformational flexibility of the macrocyclic subunits leading to an unprecedented fourfold Au(I)–aryl macrocycle. The reductive elimination to carbon nanoring **12[4]** proceeds with size-selectivity and a remarkable yield of 20%. The investigated molecular design of a potential monomer for the bottom-up synthesis of CONTs was synthetically realized, except for the last deprotection step. The deprotection was not tested yet, since nanoring **12[4]** was first investigated on its host capabilities. The final macrocycle shows binding towards multiple guests with suitable convex π-surfaces including fullerenes (C_{60} and C_{70}) and [6–7]CPP. Binding to such large and confined cavities will be of high interest for the sensing of guests with biological relevance, as well as for constructing interlocked molecular topologies. We are confident that our findings bear importance for the design of metal- and all-organic macrocycles and cages.[237–239]

Chapter 4

An All-Organic Photochemical Magnetic Switch with Bistable Spin States

Parts of this chapter are already published in:

J. Am. Chem. Soc. **2022**, *144*, 8707–8716.

DOI:https://doi.org/10.1021/jacs.2c02195

Authors: Niklas Grabicki,* Konstantin Günther,* Beatrice Battistella, Lutz Grubert, Oliver Dumele

*these authors contributed equally and either has the right to list himself first in bibliographic documents.

Chapter 4: An All-Organic Photomagnetic Switch with Bistable Spin States

With the established methods to synthesize strained aromatic macrocycles in hand we aimed to explore cyclic chiral structures as well. Chirality is especially important for carbon nanotubes and chiral macrocycles are appealing in regard of their chiral response due to the unique interplay of magnetic- and transition dipole moment in cyclic molecules. We therefore aimed towards the synthesis of chiral CPP-type macrocycles based on [5]helicenes. Nevertheless, during our investigations we encountered an unprecedented way to functionalize [5]helicenes transforming them into all-organic photoswitches with bistable spin states. The switching is based on a reversible electrocyclic reaction of its carbon skeleton and can be monitored with UV/vis spectroscopy and EPR spectroscopy or induced by electrochemical reduction and re-oxidation. Variable-temperature EPR spectroscopy of the paramagnetic species revealed an open-shell triplet ground state with an experimentally determined triplet–singlet energy gap.

4.1. Introduction to the Design of a [5]Helicene-Based CPP-type Macrocycle

Conformational rigidity and shape-persistency are prerequisites for outstanding chiroptical properties in all-organic molecules.[240] Outstanding in this context is the non-linear amplification of the absorption intensities in the electronic circular dichroism (ECD) spectra of a macrocycle compared to its monomer units.[241] Macrocycles that are shape-persistent but not conformationally rigid do not show this non-linear amplification in ECD spectra.[242] Conformational rigidity of a molecule describes shape-persistence in combination with no free torsional rotation. Due to the development and the progress in CPP synthesis, the introduction of strain into a macrocycle represents a new and powerful method to implement conformational rigidity and stability. Therefore, these methods represent strategies enabling the synthesis of unique strained chiral macrocycles.[243]

A straightforward approach to design a chiral conjugated CPP-type macrocycle is based on the use of chiral subunits. In this regard only helical or axial chiral building blocks are suitable, since a stereogenic carbon center would break the conjugation. Within several feasible molecules the implementation of [*n*]helicenes represents a formidable challenge (Figure 4. 1). The structurally rigid compound class is ideal to investigate the effects of strain and macrocyclization on axial chirality.

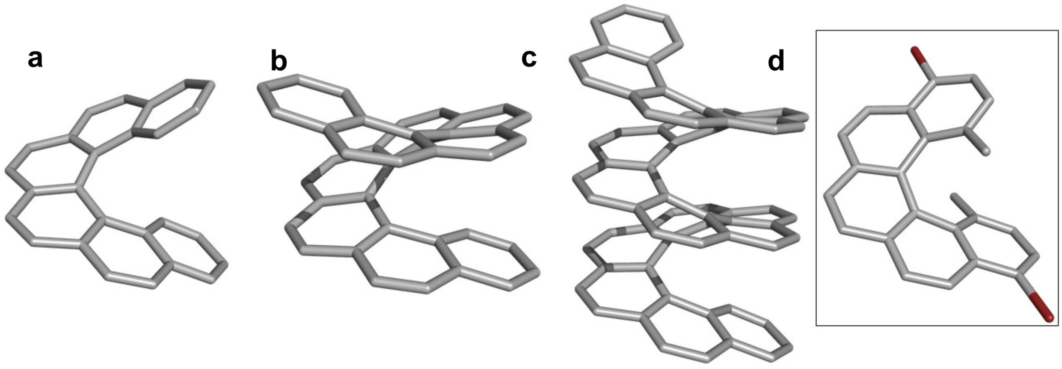

[6]helicen [9]helicen [16]helicene 27

Figure 4. 1. Examples of [*n*]helicenes with a) [6]helicene, b) [9]helicene, c) [16]helicene and d) 4,11-dibromo-1,14-dimethyl-[5]helicene. Only the (*M*)-enantiomer of each helicene is displayed, hydrogens are omitted for clarity. Color code: bromine, red; carbon, grey.

On first sight the introduction of these molecules into a macrocycle does not seem suitable, since general synthetic approaches for CPPs need linear connection points. Only recently a conformationally stable yet *pseudo*-linearly extended [5]helicene bearing substituents in the 4,11-positions has been reported (Figure 4. 1d).[244] [*n*]Helicenes with *n* > 3 adopt helically twisted geometries that are axially chiral[245] and possess electronic properties that are distinctly different[246] from those of the linear meta-fused acenes. They have been investigated in the context of [*n*]helicene-based nanographenes[247,248] and open-shell molecules[249] sought for their potential applications in materials chemistry and organic electronics.

In regard of the previously discussed metal-mediated macrocyclization strategies, the synthetic approach to realize a [5]helicene-based CPP-type macrocycle appears challenging, due to several reasons. First, the platinum macrocyclization from diboronic ester (±)-**28** to Pt-macrocycle *rac*-**29** is rather unpredictable regarding potential ring-sizes. In addition, the chirality of the [5]helicene subunit enables in theory a variety of possible isomers, depending on the ratio of enantiomers implemented per macrocycle. Finally, subsequent reductive elimination giving an all-organic molecule will most probable result in a high amount of strain energy for **30** (Figure 4. 2).

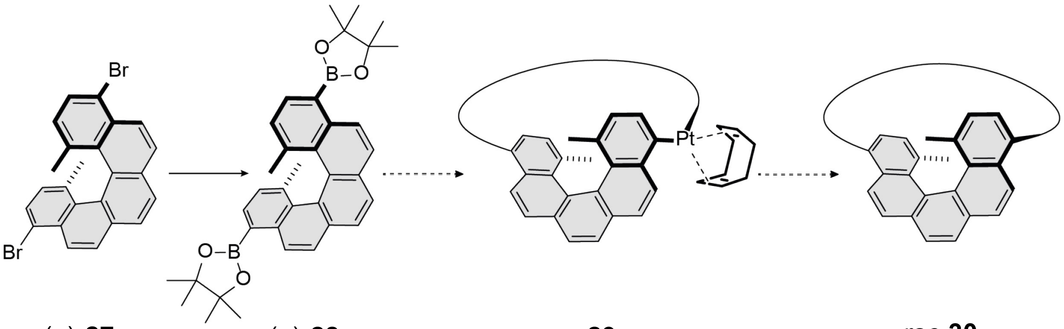

(±)-**27** (±)-**28** *rac*-**29** *rac*-**30**

Figure 4. 2. Synthetic strategy towards [5]helicene based CPP-type macrocycles.

Within the course of this thesis the transformation of dibromide (±)-**27** into boronic ester (±)-**28** was achieved. Nevertheless, upon attempted platinum mediated macrocyclization, only the diketone side product (±)-**31-C** was isolated (Figure 4. 3).

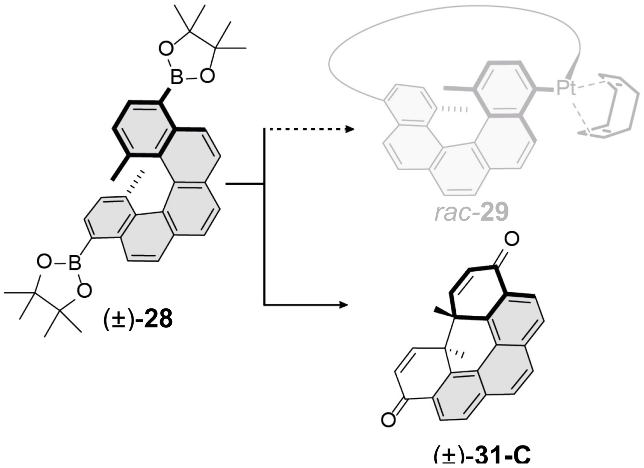

Figure 4. 3. Attempted Pt-mediated macrocyclization and unprecedented side-product.

The structure of the side product is interesting in regard of its formation. Scaffolds derived from [5]helicene are known to undergo 6π electrocyclization upon irradiation. The theoretically precursor that could undergo 6π electrocyclization to form (±)-**31-C** has two mesomeric structures an all quinoidal and an aromatic diradical form (Figure 4. 4, (±)-**31-O**).

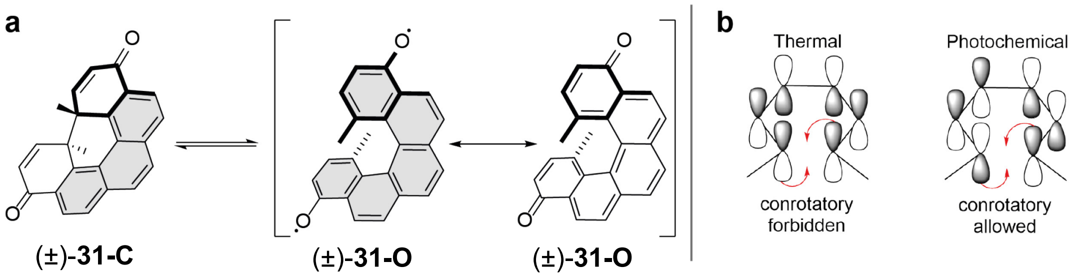

Figure 4. 4. a) Potential switching of diketone to the open helical form in its two mesomeric structures. b) Conservation of orbital symmetry according to Woodward-Hoffmann rules for a formal 6-π electrocyclization.[250]

According to the Woodward–Hoffmann (WH) rules for the conservation of orbital symmetry a conrotatory 6π electrocyclization is not allowed thermally. In the [5]helicene scaffold the electrocyclization must occur conrotatory. As we performed the platinum macrocyclization without an additional irradiation source, it is obvious to propose the contribution of a diradical species, because the WH rules do not apply as strict for radicals. Since the switching between spin states is rarely possible for organic molecules we focused on the investigation of this unprecedented side product in the last chapter of this thesis.

4.2. Introduction to Molecular Spin State Switches

While bulk materials can exhibit magnetic properties, these are fundamentally different from those of isolated atoms or molecules. On the macroscopic scale magnetism is a collective phenomenon involving the mutual cooperation of large numbers of microscopic magnetic moments.[251] Magnetic bistability is mentioned hereby as particularly important in regard of applications and can be found in the magnetization of ferromagnetic materials. The stability decreases with decreasing number of interacting atoms or molecules. As a results technical applications at room temperature generally need nanoparticles of at least 7 to 10 nm. In ferromagnetic systems the magnetically interacting spins are located on adjacent atoms. In contrast, spin crossover (SCO) complexes can have varying interaction of electron spins within the same atom.[251]

Such complexes are known from first row transition metals (d^4 to d^7 orbital occupancy), where the metal ion can exist either in a low spin or a high spin configuration, depending on the ligand field strength. Since both configurations are energetically similar an external stimulus such as temperature, light, or pressure can be used to switch between these two magnetic states.[252]

In the solid state, which at least compromises of a few thousand molecules, cooperative effects can lead to a preservation of one state, once such an external stimulus was applied to populate it.[253] Therefore, these SCO complexes can exhibit bistability in the solid state. In solution gradual spin crossover according to a Boltzmann distribution inevitably leads to an immediate reversal once the external stimulus is ended (e.g. irradiation with light versus no irradiation).

Pioneering work in the field of molecular spin state switches has been performed by Herges and co-workers.[251,254,255] They achieved visible light mediated reversible ligand and coordination resulting in the switching of magnetic properties at room temperature and in solution for magnetically noninteracting molecules. Hysteresis was achieved without cooperative effects, such as magnetic coupling (e.g. in ferromagnetic materials) or lattice interactions (e.g. in SCO systems). Their molecular design was based on an azopyridine photoswitch bound to a Ni(II) porphyrin complex.

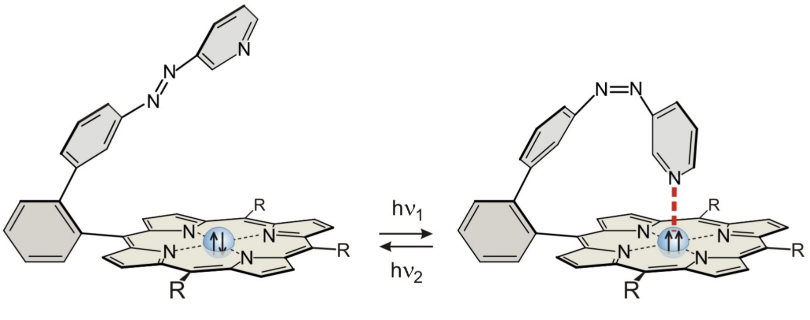

Figure 4. 5. Reversible light-induced magnetic switching of azopyridine functionalized Ni-porphyrin (blue spheres symbolize Ni(II) atom), where the thermal back reaction from paramagnetic *cis* compound to the thermodynamically more stable *trans* isomer at room temperature in the dark is neglectable. ($t_{½}$(**33**-*cis*) = 27 h at 54 °C in acetonitrile).

Several other examples of discrete molecules have been shown, where the spin state is controlled using metal–organic spin-crossover complexes or photochromic complexes.[256–258] While these examples utilize first-row transition metals such as nickel or cobalt, there are fewer reports on all-organic molecules with similar properties.[259–263] Within the reported examples a categorization into roughly two different types can be made comprising either switches that undergo a conformational change upon an external stimulus[259,261] or those where the external stimulus controls the making and breaking of bonds ideally resulting in isomers of different spin-states.[260,264,265]

4.2.1. Photoswitches with Different Spin States Based on Conformational Changes

Toda and Tanaka reported an early example of a paramagnetic diradical that was induced by irradiation. A conformational change stabilized a paramagnetic state, yet no magnetic bistability was achieved (Figure 4. 6a).[263] The thermal back-reaction converted the electron paramagnetic resonance (EPR)-active form reversibly into the diamagnetic form, within a few hours. In contrast, Kubo and co-workers demonstrated magnetic bistability based on a irradiation induced conformational change of an overcrowded aromatic ene (Figure 4. 6b).[259] The molecular design allows to trap the photogenerated paramagnetic form in a least-strained orthogonal conformation with a thermal back-reaction into the diamagnetic form occurring gradually at room temperature. In a subsequent alteration of Kubo's system, Feringa and co-workers introduced additional steric bulk in the *fjord* region and thiaxanthylidene units that stabilize the diradical state. As a result absolute magnetic bistability at room temperature in solution is achieved.[261]

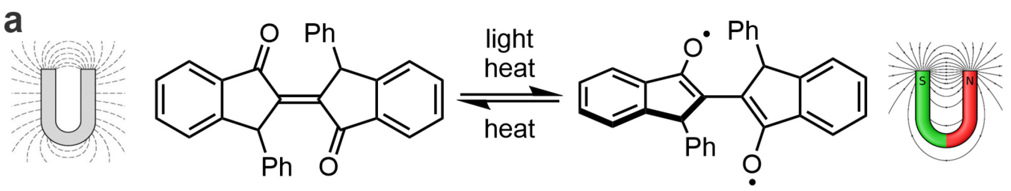

solid-state magnetic switch, $t_{1/2}$ = 1 h at 300 K (Toda & Tanaka 2000)

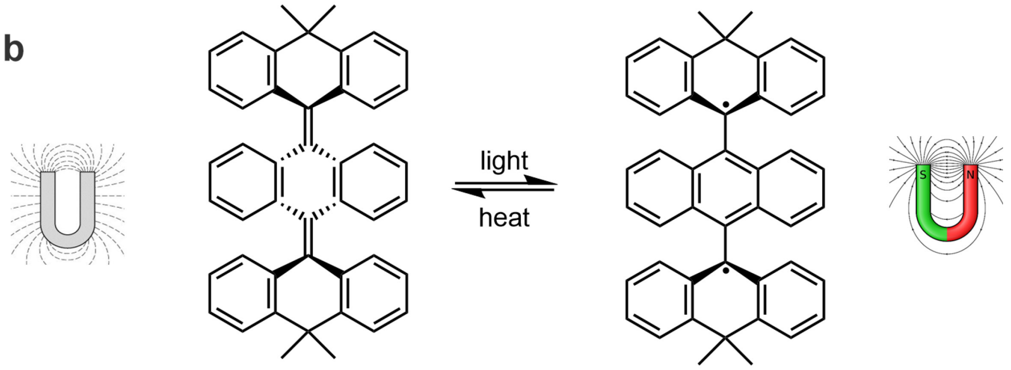

conformational switch $t_{1/2}$ = 2 h at 300 K (Kubo et al. 2020)

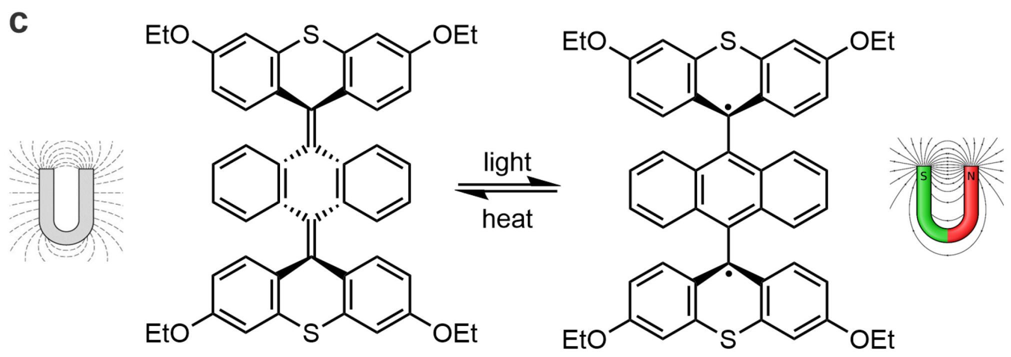

bistable conformational switch (Feringa et al. 2021)

Figure 4. 6. Photomagnetic molecular switches via conformational isomerization.[259,261,263] Gray magnet: EPR-silent form; colored magnet: EPR-active form.

However, the stabilization of spin states exclusively based on conformational changes could limit the future demand of tuned bistability in molecular magnetic switches. Hence, switching mechanisms based on photochemical reactions that involve the making and breaking of chemical bonds are an alternative concept investigated to achieve bistability among the magnetic states.

4.2.2. Photoswitches with Different Spin States Based on Bond Making and Breaking

The group of Oda has demonstrated the photochemical formal 6π retroelectrocyclization of a bis(quinone-extended) thioindigo that partially increases the population of a diradical form with a paramagnetic spin state (Figure 4. 7a).[266] Yet, only a minor change in the ratio of paramagnetic-to-diamagnetic form was achieved due to the permanent thermal population of the triplet state in the dark. Based on a light-induced homolytic cleavage initially reported by Hayashi and Maeda,[267] the group of Abe has developed a single-molecular photochromic switch consisting of hexaarylbisimidazole units, which undergo fast reversible biradical formation with a tunable half-life in the range of 10–100 of milliseconds under ambient conditions (Figure 4. 7b).[264,265] Juríček and co-workers reported a novel photoswitchable dimethylcethrene with the promise of generating a diradical triplet state upon irradiation of the closed diamagnetic form (Figure 4. 7c).[268] In their approach, a photochemical 6π retroelectrocyclization gave rise to the open helical form containing a *para*-quinodimethane (*p*-QDM) motif (Figure 4. 7c, highlighted in red) that exhibits a diradicaloid open-shell singlet structure. However, no population of the triplet state was detected at room temperature, presumably due to a high singlet–triplet energy gap (ΔE_{ST}, calculated to ca. 10 kcal mol^{-1} for the open form). In this regard we would like to highlight, that the term “diradicaloid” is used for singlet ground-state systems with partial radical character and the term “diradical” is used for triplet ground-state systems.

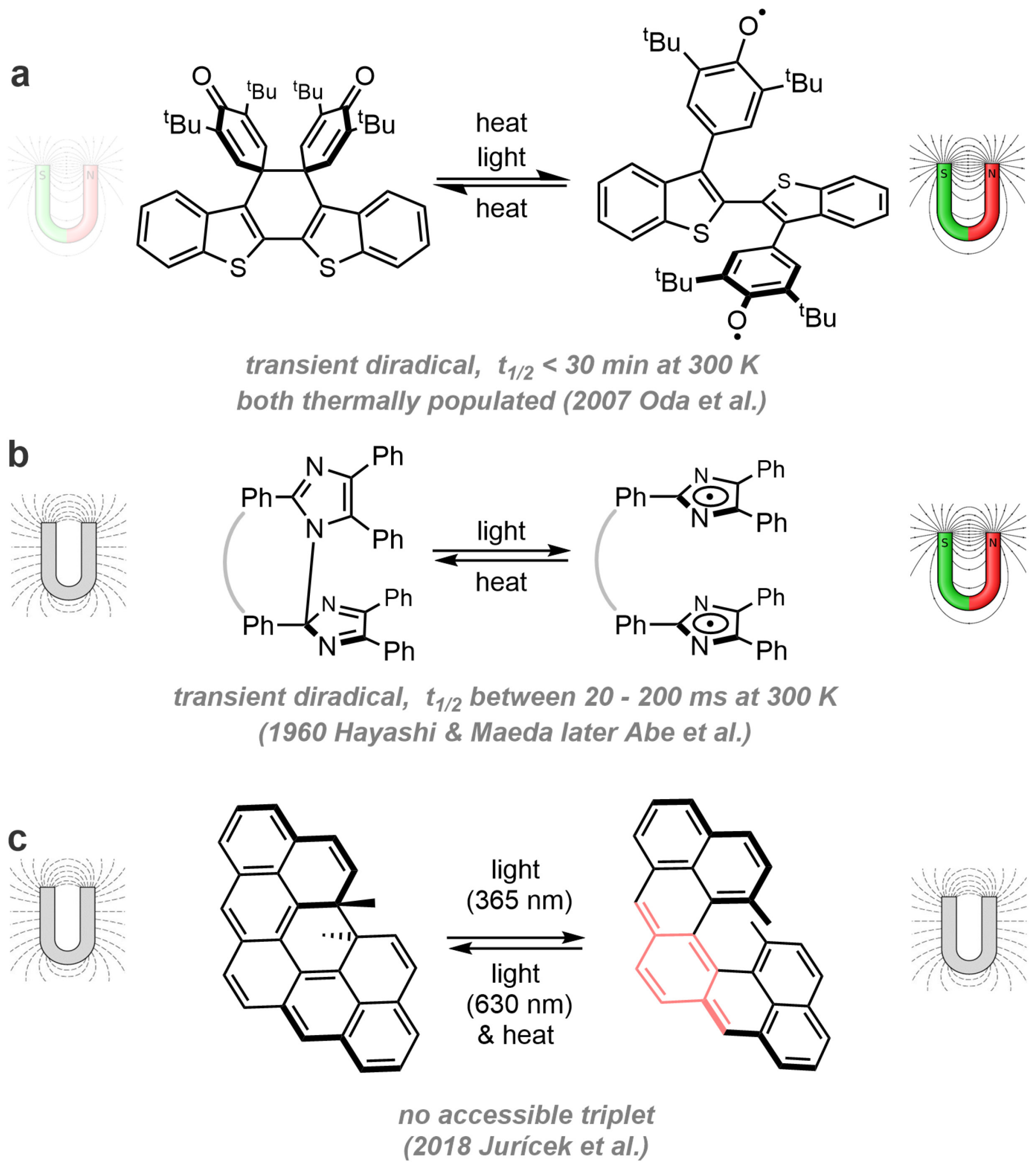

Figure 4. 7. Photomagnetic molecular switches via photochemical bond cleavage. Gray magnet: EPR-silent form; faint-colored magnet: weakly EPR-active form; colored magnet: EPR-active form.[260,265,267,268]

As a result, EPR spectroscopy did not show a paramagnetic resonance signal in one of the isomers. This design motivated Matsuda, and co-workers to synthesize a π-extended dimethylcethrene that underwent the same photoisomerization between a diamagnetic open and closed form.[269]

4.3. Selective Synthesis of [5]Helicene with Radical Stabilizing Functional Groups

Inspired by the aforementioned research we aimed to specifically synthesize the closed diketone (±)-**31-C** and study its photophysical and redox properties. Additionally, the introduction of a well-known radical stabilizing group was investigated to validate our findings. Terminal substitution by cyano groups is an efficient approach to synthesize stable organic radicals. Among them, tetracyano substitution of *p*-QDM derivatives resulted in stable radical anions, such as 7,7,8,8-tetracyanoquinodimethane (TCNQ),[270] 13,13,14,14-tetracyano-4,5,9,l0-tetrahydro-2,7-pyrenoquinodimethane (TCNTP), and 13,13,14,14-tetracyano-2,7-pyrenoquinodimethane (TCNP).[271] More recently, the group of Wu synthesized a series of tetracyano-oligo(*N*-annulated perylene)quinodimethanes, which showed tuneable ground states, varying from a closed-shell quinoidal structure for $n = 1$, to a singlet biradical for $n = 2, 3, 4$, and a triplet biradical for $n = 5, 6$.[272] Based on this knowledge we decided to synthesize a [5]helicene substituted at the 4,11-positions with bis(dicyano)methylidene as radical stabilizing groups.

Configurationally stable [5]helicene (±)-**27** was prepared in three steps from commercially available starting materials according to reported procedures in the literature by Juríček and co-workers.[244] Palladium-catalyzed Miyaura borylation of dibromide (±)-**27** gave bis(boronic acid pinacol ester) (±)-**28** in good yields (74%, Scheme 4. 1).[273] As explained in the introduction of this chapter (Figure 4. 2), we observed the formation of (±)-**31-C** from (±)**-28** upon attempted platinum-macrocyclization. We hypothesized that a bisphenol[5]helicene probably occurred as a transient species during this process.[274] Therefore, we aimed at the selective synthesis of such a bisphenol derivative. Starting from (±)**-28** oxidative hydroxylation is a common chemical transformation for boronic esters in the presence of H_2O_2. This synthetic step allowed the selective formation of (±)-**31-C**. As excess H_2O_2 probably leads to the oxidation of the freshly introduced hydroxyl groups, which immediately results in ring closure, we never observed a bisphenol species.

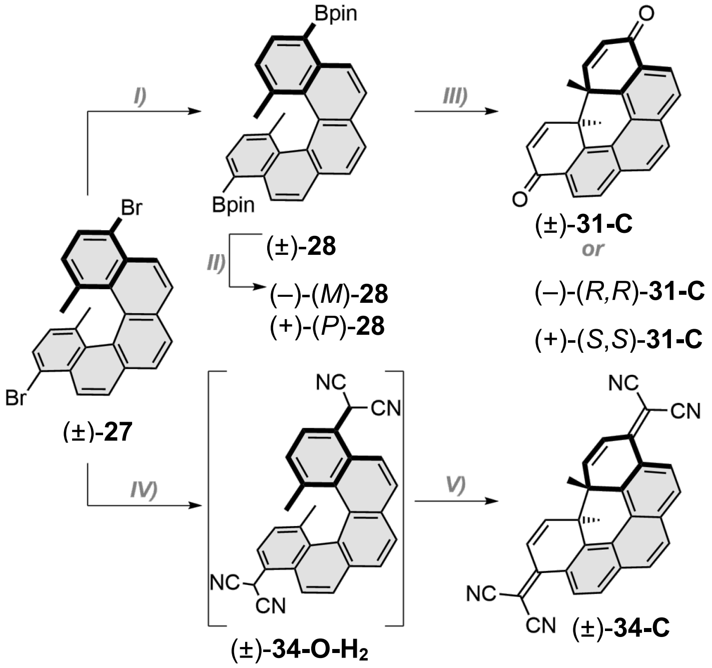

Scheme 4. 1. Synthesis of racemic or enantiopure (±)-**31-C** and racemic (±)-**34-C**. (I) (±)-**27** (1.0 equiv), bis(pinacolato)diboron (2.2 equiv), [Pd(dppf)Cl_2]·CH_2Cl_2 (10 mol %), KOAc (5.0 equiv), 1,4-dioxane, 80 °C, 3.5 h, 74%; (II) enantiomer separation by HPLC on a chiral stationary phase; (III) for (±)-**31-C**: (±)-**28** (1.0 equiv), H_2O_2 (25.0 equiv), THF, 25 °C, 6 h, 78%; (+)-(*S,S*)-**31-C** (70%) from (+)-(*P*)-**28** and (−)-(*R,R*)-**31-C** (63%) from (−)-(*M*)-**28**; (IV) first: malononitrile (6.0 equiv), NaH (10.0 equiv), THF, 0 °C, 0.5 h; second: (±)-**27** (1.0 equiv), [Pd(PPh_3)$_2Cl_2$] (10 mol %), [Pd(PPh_3)$_4$] (10 mol %), THF, 80 °C, 16 h, not isolated; (V) $CHCl_3$, NEt_3, air, 25 °C, 30%; dppf = 1,1′-bis(diphenylphosphino)ferrocene, pin = pinacolato.

Subsequent oxidative deborylation of (±)-**28** with an excess of H_2O_2 leads directly to diketone (±)-**31-C**. Only the closed diketone is observed that is presumably obtained through a diradical mechanism upon oxidation of a transient open bisphenol.[268,274,275] Closed bis(dicyanomethylidene) (±)-**34-C** was synthesized through a Pd-catalyzed Takahashi coupling[276] from dibromide (±)-**27** via dihydro intermediate (±)-**34-O-H₂**, that underwent subsequent oxidation upon deprotonation and formal electrocyclization to give (±)-**34-C**. Furthermore, racemic diboronic ester (±)-**28** can be separated into its (*M*)- and (*P*)-enantiomers via chiral high performance liquid chromatography (HPLC) (Figure 4. 8).

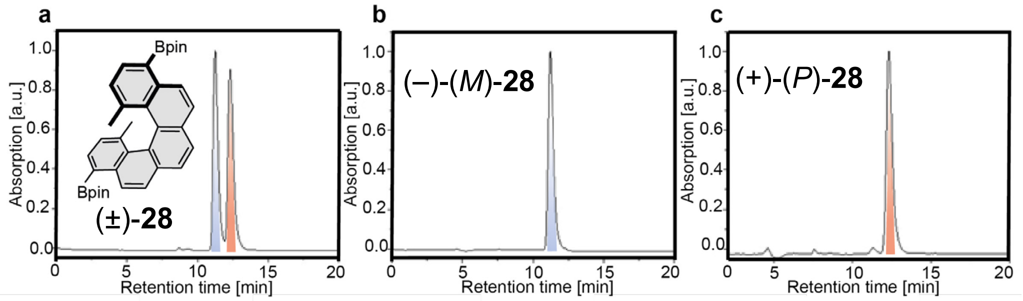

Figure 4. 8. HPLC trace of a) racemic (±)-**28**, b) enantiomerically pure (−)-(*M*)-**28**, and c) enantiomerically pure (+)-(*P*)-**28** (*ee* = 95%).

The absolute configuration was validated using a combination of time-dependent density functional theory (TD-DFT) calculations, optical rotatory dispersion, and electronic circular dichroism spectroscopy (Figure 4. 9).

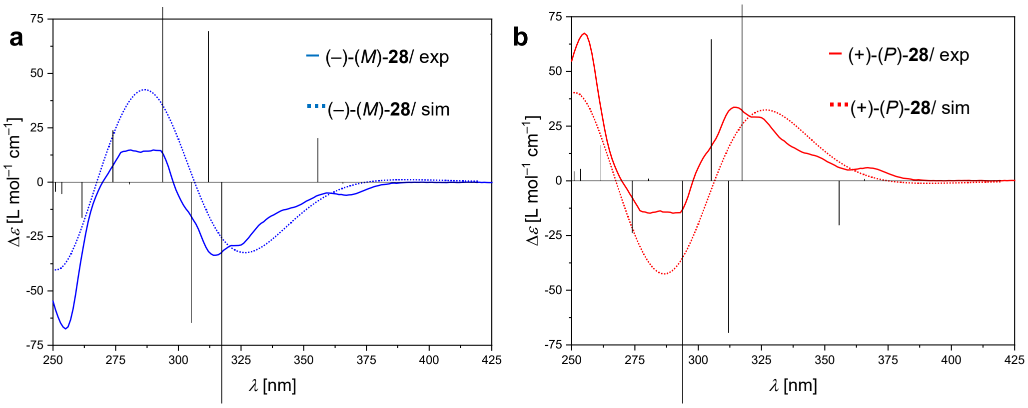

Figure 4. 9. Comparison of the ECD spectra in CH_2Cl_2 at 298 K of a) (−)-(*M*)-**28** (blue solid graphs; $c = 5.7 \cdot 10^{-4}$ M) and the simulated spectra (blue dotted graphs, black vertical graphs for discrete vertical transitions) and b) of (+)-(*P*)-**28** (red solid graphs; $c = 6.1 \cdot 10^{-4}$ M) and the simulated spectra (red dotted graphs, black vertical graphs for discrete vertical transitions) level of theory: TD-DFT/CAM-B3LYP-D3(BJ)/def2-TZVP/CPCM(CH_2Cl_2).

Unambiguous proof of the absolute configuration was obtained by a single-crystal X-ray structure of enantiopure (+)-(*P*)-**28** (Figure 4. 10).

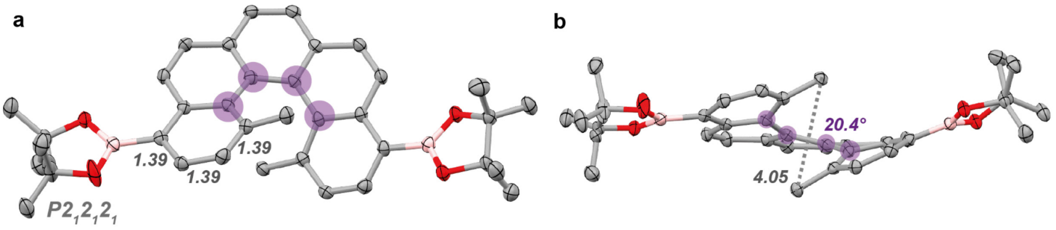

Figure 4. 10. X-ray structure of enantiopure (+)-(*P*)-**28** at 103 K. Ellipsoids are shown at 50% probability, hydrogen atoms and disorder are omitted for clarity. Color code: boron, light pink; carbon, grey; oxygen, red. a) top view displaying the space group and the bond lengths in Å. b) Sideview displaying the heavy atom distance of the methyl groups in Å and the dihedral angle of the purple colored C-atoms, which define the helical pitch angle.

The pure enantiomers of bis(boronic ester) (±)-(*P*/*M*)-**28** could be oxidized separately to give enantiopure stereoisomers (–)-(*R*,*R*)-**31-C** and (+)-(*S*,*S*)-**31-C**. This strategy enables rapid access to enantiopure dimethyl[5]helicene derivatives, as the boronic ester groups allow for a plethora of synthetic transformations. This might prove useful for future applications as chiroptical switches or in chiral materials.[277–280]

The closed helical structures of (±)-**31-C** and (±)-**34-C** were confirmed by ^{1}H and ^{13}C-HMBC NMR spectroscopy showing $^{3}J_{H-C}$ couplings between the protons of the 1,14-dimethyl groups and the bridging carbon atoms (Appendix Figure A. 85 and Figure A. 87). Unambiguous structural proof was obtained by single-crystal X-ray structures for (±)-**31-C** and (±)-**34-C** (Figure 4. 11).

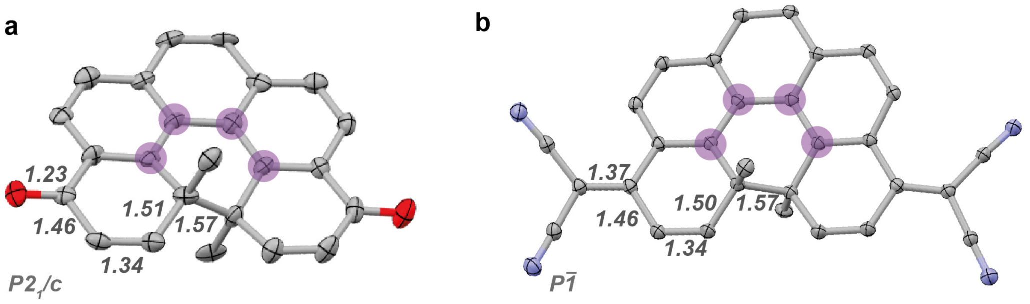

Figure 4. 11. X-ray structures of a) (±)-(P)-**31-C**, b) (±)-**34-C.** Hydrogen atoms are omitted for clarity, and the thermal ellipsoids are shown at a 50% probability level (bond lengths in Å). The carbon atoms defining the helical pitch angle are shaded in purple.

The bridging quaternary carbon atoms exhibit a C–C distance of 1.57 Å for both structures. The helical pitch angle along the inner sp^{2}-hybridized C–C–C–C atoms (shaded in purple) are 6.15° ((±)-**31-C**)) and 14.09° ((±)-**34-C**)). The central methyl groups are axially displaced. Further the X-ray structures reveal that the new compounds (±)-**31-C** and (±)-**34-C** clearly show a quinoidal structure at the terminal benzannulated rings with pronounced alternating bond lengths when compared with the parent aromatic [5]helicene scaffold.

4.4. Variable Temperature UV/vis Spectroscopy of Closed Helicenes

Intrigued by the fact that we only observed the closed form molecules (±)-**31-C** and (±)-**34-C**, we assumed that a photochemical 6π retroelectrocyclization could lead to a diradical open form. Thus, we investigated the photophysical properties of these two compounds and found a hypsochromic shift of (±)-**31-C** to λ_{max} = 342 nm and a bathochromic shift of (±)-**34-C** to λ_{max} = 414 nm compared to open dibromo [5]helicene precursor (±)-**27** (λ_{max} = 362 nm) (Figure 4. 12).

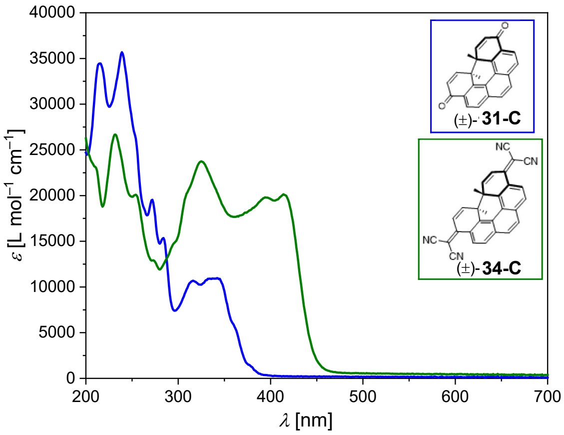

Figure 4. 12. UV/Vis absorption spectra of (±)-**31-C** (blue graph; c = $9.2\cdot10^{-6}$ M) and (±)-**34-C** (green graph; c = $9.5\cdot10^{-6}$ M). The spectra were recorded in acetonitrile at 298 K.

Initial irradiation of (±)-**31-C** or (±)-**34-C** in MeCN with various wavelengths (LED light sources) at 295 K and above resulted in no observable change of the reaction mixture.

Photoswitches are commonly classified as T-type or P-type switches, where a T-type switch undergoes thermal back reaction, with spiropyran as a prominent example.[281,282] P-type switches are thermally stable and can only be converted back upon irradiation, with the most prominent example being the class of diarylethenes extensively studied by Irie and co-workers.[283]

Assuming that (±)-**31-C** and (±)-**34-C** are T-type switches—just as dimethylcethrene but with a faster thermal back-reaction—we turned to irradiation at cryogenic temperatures. Cooling to 77 K and irradiation of (±)-**31-C** and (±)-**34-C** in a glassy matrix of 2-methyltetrahydrofuran (2-MTHF) with a 375 or 405 nm LED, respectively, resulted in significant changes of the UV/vis absorption. After 13 min of irradiation for (±)-**31-C** and 12 min for (±)-**34-C**, a photostationary state (PSS) is reached, which we assigned to a mixture of the open and closed forms (±)-**31-C**/(±)-**31-O** or (±)-**34-C**/(±)-**34-O**. Both derivatives show distinct changes in the UV region of the spectra and several defined isosbestic points supporting a clean photochemical reaction. Several new broad absorption bands arise in the visible region at 400–550 nm due to the presence of (±)-**31-O** and 450–750 nm for (±)-**34-O**, indicative of a diradical character of the open forms (Figure 4. 13).

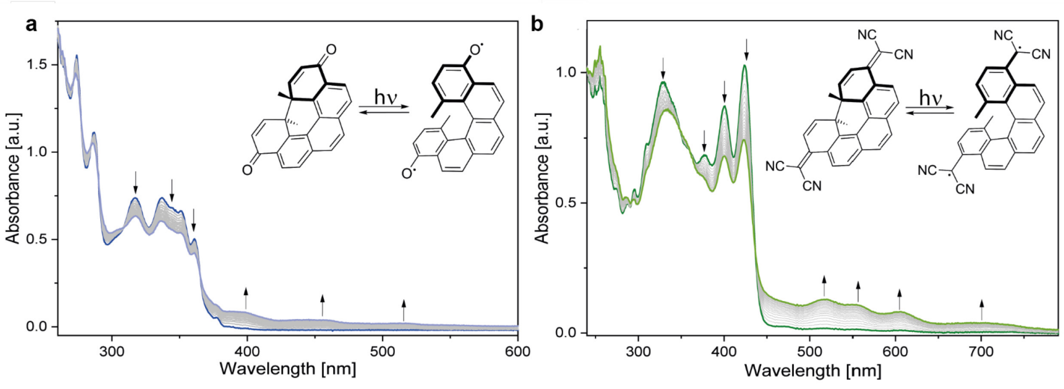

Figure 4. 13. UV/vis absorption spectra of (a) (±)-**31-C** (dark blue trace; $c = 5.6 \cdot 10^{-5}$ M) irradiated with 375 nm light for 13 min (light blue trace) and (b) (±)-**34-C** (dark green trace; $c = 4.1 \cdot 10^{-5}$ M) irradiated with 405 nm light for 12 min (light green trace). All spectra were recorded in 2-MTHF at 77 K; spectra shown as gray traces were recorded every 60 s during irradiation.

In both cases, the photostationary state is retained for at least 1 h at 77 K in the dark with no observable spectral changes. While the photochemical back reaction of (±)-**31-O** and (±)-**34-O** at various tested wavelengths remained unsuccessful (at 77 K), heating above a critical temperature resulted in the complete disappearance of the newly formed absorption bands and the spectra of the closed form was recovered for both derivatives. Detailed variable temperature (VT-)UV/vis absorption spectroscopy of the $\mathrm{PSS}_{405\mathrm{nm}}$ mixture with (±)-**34** revealed a rapid change of absorption bands at 92 K, regenerating the spectrum of the closed form (±)-**34-C**. Hereby it must be mentioned that the temperatures indicated in Figure 4. 14 are rough estimates, since the experimental set-up does not allow to precisely measure the temperature within the cuvette. While heating the $\mathrm{PSS}_{375\mathrm{nm}}$ mixture of (±)-**31-O**, the absorption remained constant until the 2-MTHF matrix started melting at 127 K and no defined critical temperature for the thermal ring closure of (±)-**31-O** to (±)-**31-C** could be determined due to dominating scattering effects of the melting matrix (Figure 4. 14).

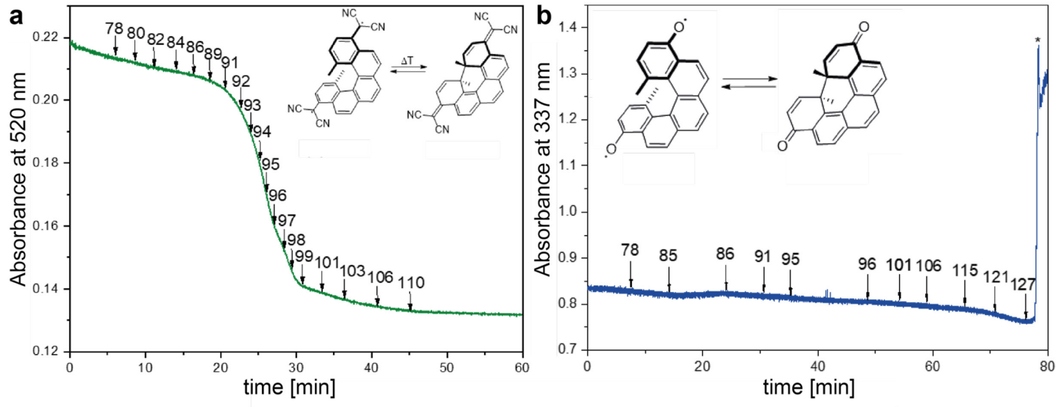

Figure 4. 14. a) UV/Vis absorption at 520 nm of a mixture of (±)-**34-C**/(±)-**34-O** starting at 77 K during the heating process in 2-MTHF. The temperatures are shown as black values in K. b) UV/Vis absorption of (±)-**31-C**/(±)-**31-O** at 337 nm during the heating (blue graph). The temperature is shown as black values as insets in K. The asterisk marks the breakage of the solid matrix.

Trying to retain the liquid aggregation state and cooling a solution of diketon (±)-**31-C** down to 140 K, does not result in spectral changes upon irradiation presumably due to a dominating fast thermal back reaction.

In summary, a defined photochemical reaction can be observed for both derivatives at cryogenic temperatures. This reaction cannot be reversed photochemically, which might originate from insufficient band separation of the two isomers. In contrast, the thermal back reaction is achieved with no observable side-product formation as confirmed by HPLC analysis. The newly formed photoproducts seem to be stable at cryogenic temperatures over a period of at least one hour. Determination of the composition of the PSS is not possible, thus it cannot be clarified how much of (±)-**31-C** or (±)-**34-C** is actually converted. To further elucidate if these newly generated products correspond to an open helical structure with diradical character EPR spectroscopy is required.

4.5. Variable Temperature EPR Spectroscopy on Photoswitchable [5]Helicenes

Successful switching using light as an external stimulus encouraged us to investigate the EPR activity of (±)-**31** and (±)-**34** before and after irradiation in 2-MTHF at 77 K. Before irradiation, the closed forms (±)-**31-C** and (±)-**34-C** are EPR-silent under the experimental conditions. After irradiation for 10 min (±)-**31-C** with 375 nm (LED light source), an intense EPR signal can be observed at $g \approx 2.0$. This process can be reversed upon heating the sample to 293.15 K (Figure 4. 15).

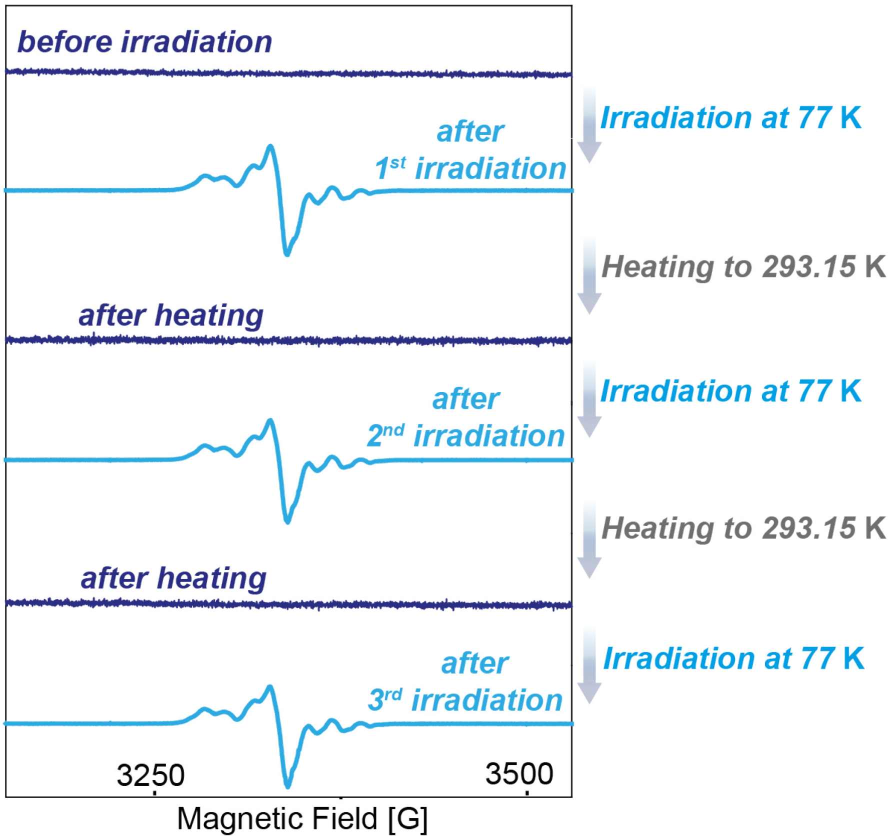

Figure 4. 15. EPR spectra of three switching cycles of (±)-**31** before and after irradiation with 375 nm for 10 min and thermal back reaction through a heating loop to 293.15 K (light blue graphs: X-band EPR, 9.35 GHz, perpendicular mode, 0.5 mW, 1 G modulation amplitude, 77 K; dark blue graphs: same parameters at 13 K).

Heating the $\text{PSS}_{375\text{nm}}$ mixture of diketone (±)-**31-C/O** to room temperature immediately converted it to the pure closed form (±)-**1a-C** as confirmed by its EPR inactivity (77 K, second dark blue graph in Figure 4. 15). Repetition of such a cycle including irradiation at 77 K and subsequent heating was performed up to three times with no observable degradation in the HPLC traces or EPR. The shape of the EPR signal appears unusual for the untrained eye, but the several features can be assigned to the following. First of all, the spectrum does not look symmetrical. Usually solution spectra of organic radicals have a symmetrical set of signals, yet our spectra were measured in a glassy matrix, which makes them the sum of the spectra for all possible orientations of the molecule. The overall shape of the spectra must be interpreted as explained in the following example.[284,285] Considering a paramagnetic species which has a total magnetic moment that is larger in one direction (e.g. in z-direction (μ_z)) an axial symmetry is present. Thus, it matters how it is positioned in an external field. If the z-direction is parallel to the external field B, the energy difference between the two energy levels for the electron will be $2\mu_z B$. As we assumed a large value for the total magnetic moment in z-direction (μ_z), a smaller external magnetic field (B_z) already leads to resonance (Figure 4. 16b). If the radical is placed in the magnetic field with either the x-axis or the y-axis (or any other direction within the xy-plane) parallel to the external field, then the energy difference is $2\mu_{x,y}B$. In Figure 4. 16b $\mu_{x,y}$ is small, resulting in a larger field ($B_{x,y}$) for resonance. The other features of the spectra can be explained with additional hyperfine coupling of the electrons and neighboring ^{1}H nuclei.

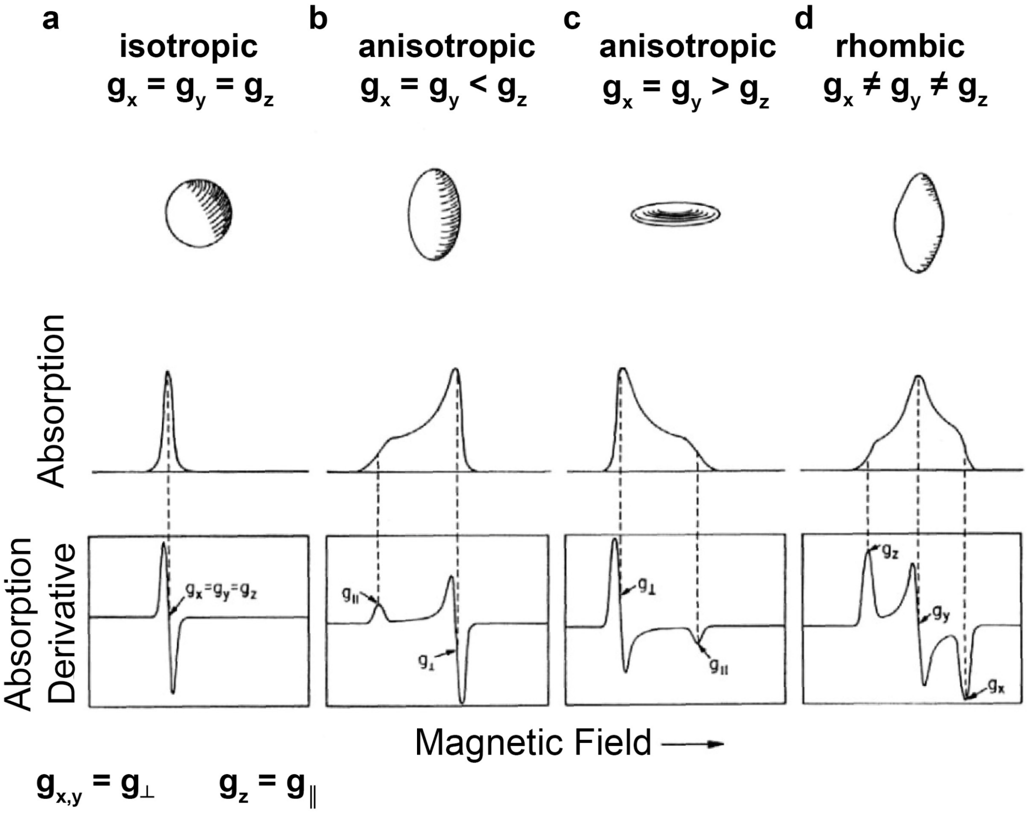

Figure 4. 16. Schematic representation of the *g* tensor and the consequential shape of the EPR spectra. The upper solid bodies show the shapes associated with a) isotropic, b) and c) axial and d) rhombic magnetic moments. Underneath are the corresponding absorption curves and the EPR derivative curves displayed.

The same outcome was observed for such a cycling experiment on (±)-**34-C** (Figure 4. 17). The PSS$_{405nm}$ mixture of bis(dicyano) (±)-**34-C/O** rapidly converted back to the pure closed form (±)-**34-C** upon heating to 93 K with the loss of the EPR signal, in agreement with our VT-UV/vis study (Figure 4. 14a). From our experimental findings, we conclude that diketone (±)-**31-C** and bis-(dicyanomethylidene) (±)-**34-C** can be photochemically switched into a stable EPR-active form and rapidly converted back to an EPR-silent form with a distinct thermal stimulus.

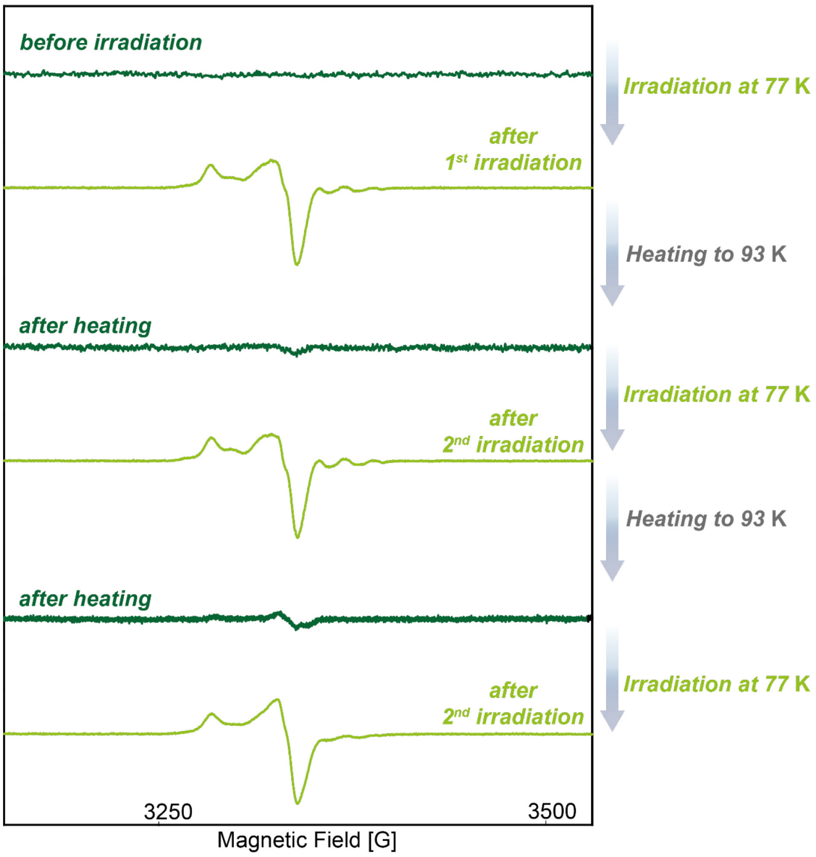

Figure 4. 17. EPR spectra of (±)-**34-C** and (±)-**34-O** in degassed 2-MTHF before and after irradiation with 405 nm for 12 min and thermal back reaction through a heating loop to 93 K (light green graphs: X-band EPR, 9.35 GHz, perpendicular mode, 0.5 mW, 1 G modulation amplitude, 77 K; dark green graphs: same parameters at 93 K).

In general, the singlet and triplet states in diradical(oid)s are thermally distributed with a distinct singlet–triplet energy gap (ΔE_{ST}). The term "diradicaloid" is used for singlet ground-state systems with partial radical character and the term "diradical" is used for triplet ground-state systems, respectively.[286,287] To elucidate what is an appropriate descriptor for out system we performed VT-EPR spectroscopy of the irradiated open forms of (±)-**31-O** and (±)-**34-O** to determine the spin multiplicity of their ground states. The EPR signal intensity of dioxo helicene (±)-**31-O** measured under the same experimental conditions decreases with an increasing temperature from 13 to 77 K, representative of a triplet ground state (Figure 4. 18).

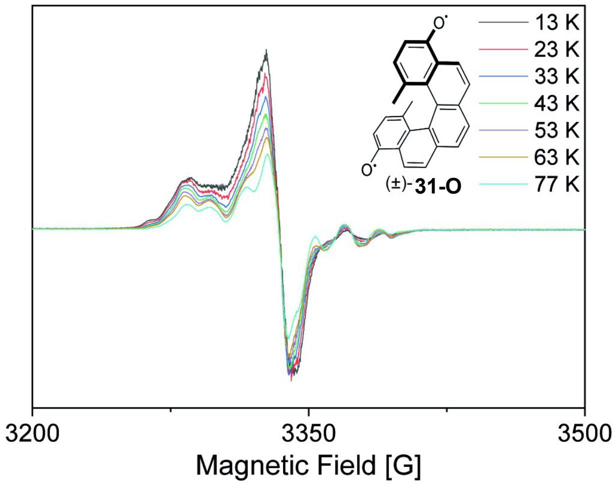

Figure 4. 18. VT-EPR spectra of (±)-**31-O** after irradiation (X-band EPR, 9.35 GHz, perpendicular mode, 0.5 mW, 1G modulation amplitude, 77 K) for 10 min in 2-MTHF.

The triplet–singlet energy gap ($\Delta E_{\mathrm{TS}} = 5.07 \cdot 10^{-2}$ kcal mol^{-1}) of (±)-**31** was determined using non-linear curve-fitting of the data to the Bleaney–Bowers equation (Equation 4.1, graph Figure 4. 19), where C is the Curie constant and $2J$ equals ΔE_{TS}.

$$I = \frac{C}{T}\frac{3e^{\frac{-2J}{k_{\mathrm{B}}T}}}{1 + 3e^{\frac{-2J}{k_{\mathrm{B}}T}}} \tag{4.1}$$

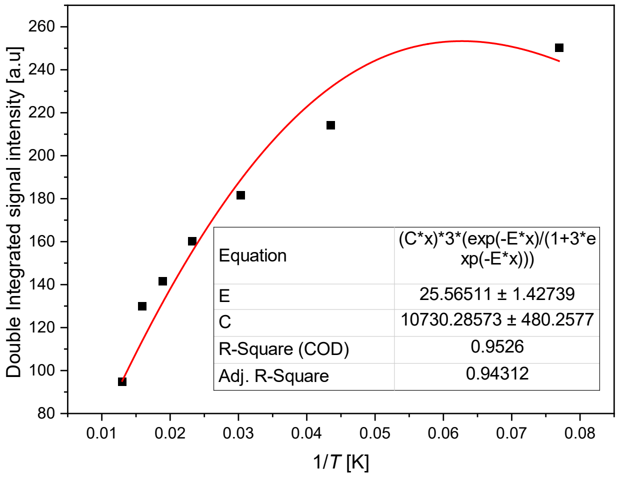

Equation	(C*x)*3*(exp(-E*x)/(1+3*exp(-E*x)))
E	25.56511 ± 1.42739
C	10730.28573 ± 480.2577
R-Square (COD)	0.9526
Adj. R-Square	0.94312

Figure 4. 19. Curie Plot of (±)-**31** with fit to the Bleaney–Bowers equation. The inset shows the transformed Bleaney–Bowers equation used as the fit function. E corresponds to $2J/k_{\mathrm{B}}$ and x equals the Temperature T. C is the Curie constant.

The results are less conclusive for bis-(dicyanomethylidene) (±)-**34**, where the VT-EPR spectra going from 13 K to 77 K does not show a clear signal decay compared to the diketone derivative (Figure 4. 20). Plotting the date and performing a non-linear curve fit using Bleaney–Bowers equation (Equation 4.1) was not possible.

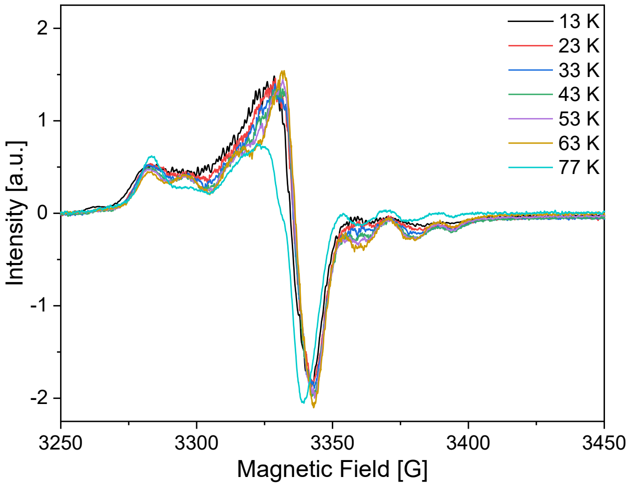

Figure 4. 20. VT-EPR spectra of (±)-**34** in degassed 2-MTHF after 10 min irradiation with 405 nm light at 77 K. Experimental parameters: $T = 13–77$ K, Freq = 9.35 GHz, Modulation Amplitude = 1 G, Microwave power = 0.5 mW.

The presented results strongly indicate a triplet ground state, but future research needs to be focused on more advanced EPR measurements such as pulsed EPR which allows to gain extensive knowledge on structural and dynamical properties of paramagnetic compounds.[288] To gain a deeper understanding we next turned to quantum chemical calculations.

4.6. Theoretical Analysis and Quantum Chemical Calculations on Photoswitchable [5]Helicenes

Bond breaking and making in this [5]helicene switch proceeds through a formal 6π electrocyclization reaction in a conrotatory fashion that is photochemically allowed but thermally forbidden according to Woodward-Hoffman (WH) rules.[250] As we observed a thermal back reaction for this scaffold the influence of a diradical(oid) species becomes feasible, because the WH rules do not apply as strict for open-shell systems. An analysis of the aromaticity based on resonance structures of the closed and open form allows to estimate whether an open- or closed-shell electronic configuration is favored. In the closed forms (±)-**31-C** and (±)-**34-C**, no diradical character is expected due to the presence of two aromatic Clar's sextets and exocyclic double bonds to the quinoidal 4,11-substituents (CCS, Scheme 4. 2).[289–293]

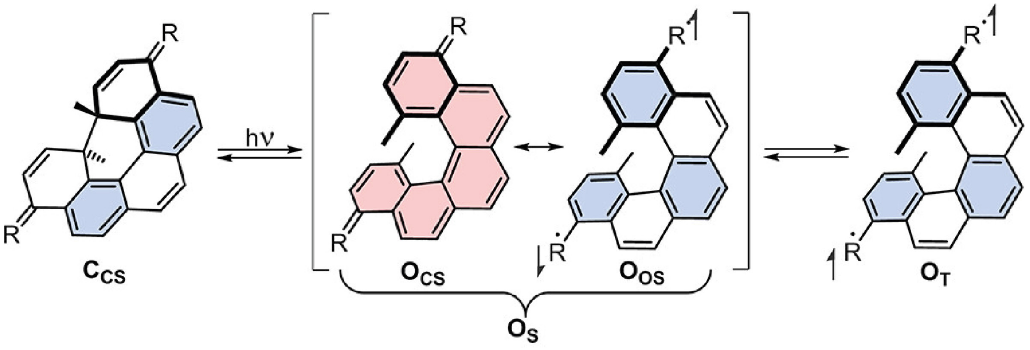

E_{rel} [kcal mol^{-1}], CASSCF	C_S	C_T	O_S	O_T	ΔE O_S–O_T
(±)-**31**	0	50	58	53	–5
(±)-**34**	0	68	54	46	–8

E_{rel} [kcal mol^{-1}], DFT	C_{CS}	C_T	O_{CS}	O_{OS}	O_T	ΔE O_{OS}–O_T
(±)-**31**	0	60	42	33	33	0
(±)-**34**	0	51	29	18	18	0

Scheme 4. 2. Resonance structures and calculated energies of the closed and open Helicenes, where Clar's sextets are highlighted in blue and quinoidal structures in red. The calculated energies for (±)-**31** and (±)-**34** in their closed form as singlet (CS) and triplet (CT, not shown) and open forms as singlet (OS) and triplet (OT). Level of theory: CASSCF(8,8)/6-31G(d,p) and calculated energies for (±)-**31** and (±)-**34** in their closed form as closed-shell singlet (CCS) and triplet (CT, not shown) and open forms as closed-shell singlet (OCS), open-shell singlet (OOS), and triplet (OT). Level of theory: DFT-D3(BJ)-B3LYP/def2-TVZP as unrestricted (for triplets) or restricted broken-symmetry (for open-shell singlets) wave functions.

In contrast, the open form has a major diradical resonance contribution because of the presence of three Clar's sextets (blue) and localization of unpaired electrons at the exocyclic substituents (OOS), which are specifically designed to stabilize the radical better compared to a plain aromatic sp^2-carbon. The closed-shell resonance structure has an unfavorable all-quinoidal structure (red) without localized aromatic Clar's sextets (OCS). Thus, it becomes obvious from this simple analysis that the open form after irradiation has a pronounced open-shell electronic configuration. We further elaborate these considerations with the calculated energies of the open-shell and closed-shell structures for each helicene scaffold (±)-**31** and (±)-**34** (open and closed forms) using CASSCF calculations with an (8,8) active space with the 6- 31G(d,p) basis set (Scheme 4. 2). The energies of the closed triplet (CT) of (±)-**31**-CT and (±)-**34**-CT are significantly higher, by more than 50 kcal mol^{-1}, than their closed-shell singlet states (CCS), thus supporting a pure closed-shell ground state before irradiation. The diradical character index (y) of this ground state was calculated to be 0.003 and 0.004 for (±)-**31-C** and (±)-**34-C**, respectively, confirming a negligible diradical character (calculated by natural occupation orbital numbers analysis).[294] In contrast, the open-form helicenes have a triplet ground state (OT) with a calculated $\Delta E_{TS,calc}$ of 5 and 8 kcal mol^{-1} for (±)-**31-O** and for (±)-**34-O**, respectively. While this CASSCF-calculated value for $\Delta E_{TS,\mathbf{31}}$ is different compared to our experimentally determined value, the trend of the energy levels is retained. In contrast, DFT methods using the approximation of spin-unrestricted (for OT) or spin-restricted broken-symmetry wave functions (for OOS) estimate gaps ΔE_{TS} of 0 kcal mol^{-1} for (±)-**31** and for (±)-**34** in good agreement with the experimentally fitted value for (±)-**31** (0.0507 kcal mol^{-1}, Scheme 4. 2). The diradicaloid character of the thermally accessible singlet state OS is enhanced for the open form which is represented by *y* values of 0.12 and 0.84 for (±)-**31-O** and (±)-**34-O**, respectively. Such ground-state triplet diradicals are rare because the double spin-polarization effect turns the vast majority of diradicals into ground-state singlets with a thermally accessible triplet state.[295–301] However, a triplet ground state, as found in our helical switch system, is desirable for obtaining a maximum response of the EPR-active form.

4.7. Spectroelectrochemistry on Photoswitchable [5]Helicenes

Even though the results obtained upon photoswitching cannot be correlated to the electrochemical properties of the discussed [5]helicene derivatives we aimed to gain a deeper insight into the system exploring the electrochemical switching processes. Electrochemically initiated (retro)electrocyclization reactions have received much less attention compared to their photochemical equivalent.[302–306] The few existing reports on electrochromic diarylethenes motivated us to investigate the redox properties of (±)-**31-C** and (±)-**34-C**. We hypothesized that the corresponding radical anions or dianions undergo ring-opening as the products would gain substantial stabilization due to aromatization compared to their closed forms. In the following only electrochemical reduction will be discussed, as the oxidation does not work reversibly in neither of the two derivatives.

*4.7.1. Spectroelectrochemistry on Diketone (±)-**31-C***

We first turned our attention to diketone (±)-**31-C**, which shows a reversible peak pair at –2.001 V *vs.* Fc/Fc^{+} (E_p^c) at a scan rate of 1 V s^{-1} (dark blue graph, Figure 4. 21). The created radical anion takes up an additional electron at –2.282 V (E_p^{c2}), but this process is irreversible on first sight. Surprisingly, an additional anodic peak is observed at –0.7 V (blue hatched). To elucidate if this anodic peak corresponds to the second reduction potential (E_p^{c2}) a second CV was measured stopping before the second reduction occurs (red dashed graph, Figure 4. 21).

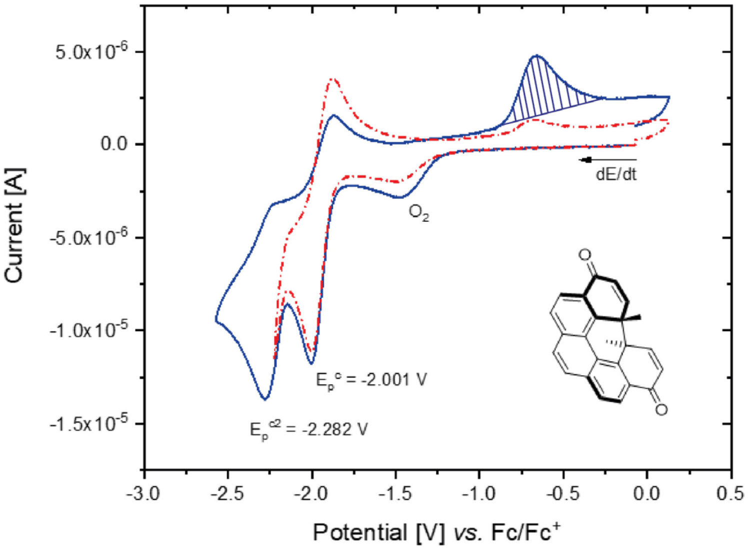

Figure 4. 21. Cyclic voltammogram of (±)-**31-C**. The Experiment was carried out in MeCN with 0.1 M Bu_4NPF_6, $c = 5\cdot10^{-4}$ M, platinum disk, $d = 1.6$ mm, scan rate $\mathrm{d}E/\mathrm{d}t = 1$ V s^{-1}, T = 295 K. Blue graph going to a more negative potential, red dashed graph stopping at a less negative potential.

The red dashed graph clearly shows the two anodic peaks as well. To exclude irreversible electrochemical processes a UV/vis spectra was taken before the electrochemical reduction and after the re-oxidation (Figure 4. 22). Here much lower scan rates were applied and interestingly the first reduction at −2.001 V becomes only quasireversible, as indicated by the disappearance of the re-oxidation (blue arrow Figure 4. 22).

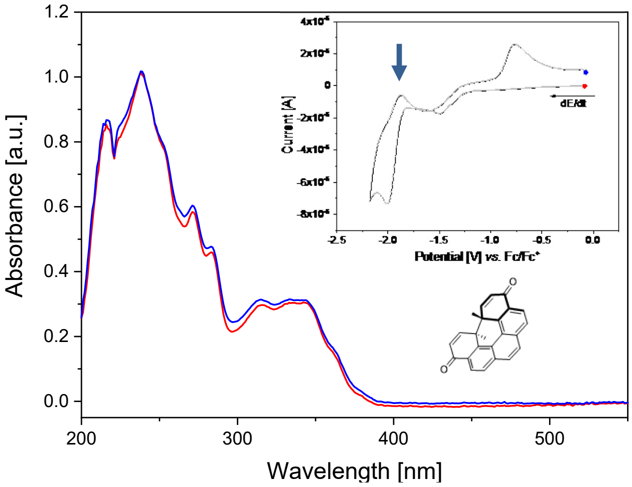

Figure 4. 22. Spectroelectrochemistry of (±)-**31-C** before and after cycling as indicated in inset showing the corresponding cyclic voltammogram. The dots show at which point in the electrochemical experiment the UV/vis spectra were measured. The experiment was carried out in a thin layer quartz glass spectroelectrochemical cell (*d* = 0.5 mm) in MeCN with 0.1 M Bu_4NPF_6, T = 295 K.

Such a complex behavior can be explained for example with an ECE or a DISP mechanism (*vide infra*).[307,308] For our study the exact mechanism is not relevant and thus was not further investigated, as it is experimentally challenging.

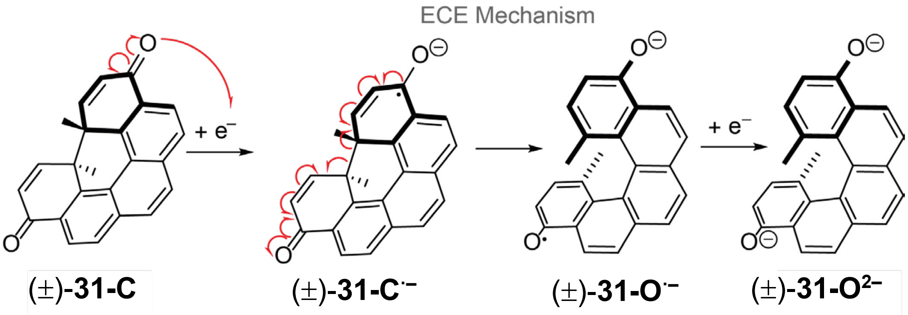

Figure 4. 23. Proposed mechanism for the formation of ring-open diphenolate (±)-**31-O**$^{2-}$ via ECE mechanism during the two-electron reduction of (±)-**31-C**.

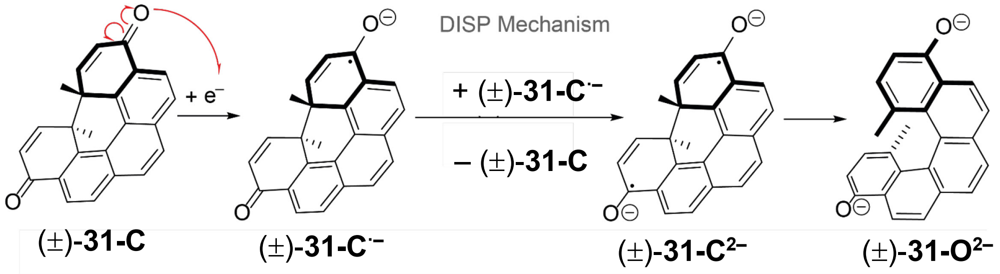

Figure 4. 24. Proposed mechanism for the formation of ring-open diphenolate (±)-**31-O**$^{2-}$ via DISP (= disproportion) mechanism during the two-electron reduction of (±)-**31-C**.

Nevertheless, these findings are clear indicators that our proposed reduction induced ring-opening is very likely to happen for the helical closed diketone (±)-**31-C**. A full spectroelectrochemical analysis shows a clean reaction with several defined isosbestic points and a new absorption band arises between 700 and 900 nm for reduction and re-oxidation (Figure 4. 25). This new broad red-shifted band can be assigned to the radical anion (±)-**31**-C$^{\cdot-}$, which is continuously produced and exists prior to the subsequent second reduction to give the open form dianion (±)-**31-O**$^{2-}$ with a new absorption maximum at 460 nm. Trapping of the bisphenol upon protonation was not possible, but quantum chemical calculation of the UV/vis absorption spectrum of (±)-**31-O**$^{2-}$ are well in accordance to the experimentally extracted graph (Appendix Figure A. 31 and Figure A. 32).

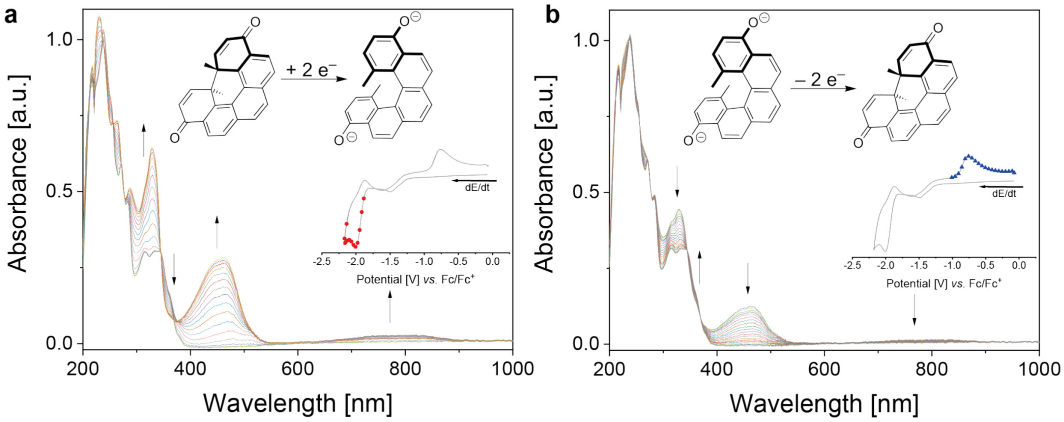

Figure 4. 25. Spectroelectrochemistry of (±)-**31-C** a) a stable intermediate is formed upon two-electron reduction of (±)-**31-C** b) reoxidation of the intermediate giving back (±)-**31-C**. Insets showing the corresponding cyclic voltammograms with red dots or blue triangles marking when UV/ vis spectra were measured. The experiment was carried out in MeCN with 0.1 M Bu_4NPF_6, c = 6 · 10^{-4} M ((±)-**31-C**), d*E*/d*t* = 10 mV s^{-1}.

Upon inverting the potential in CV, the dianion (±)-**31-O**$^{2-}$ is stable up to an onset potential of −1.0 V vs Fc/Fc$^+$ where an anodic current is observed and the intermediate is re-oxidized to regain the closed neutral form (±)-**31-C**.

*4.7.2. Spectroelectrochemistry on Bis(dicyanomethylidene) (±)-**34-C***

Bis(dicyanomethylidene) (±)-**34-C** shows an equivalent electrochemically induced switching. At the same scan rates (scan rate: 1 V·s^{-1}), as for the diketone, only one irreversible reduction wave is observed at E_p^c = −1.32 V vs Fc/Fc$^+$, which we assign to a two electron transfer and the direct formation of the open dianion (±)-**34-O**$^{2-}$ (Figure 4. 26).

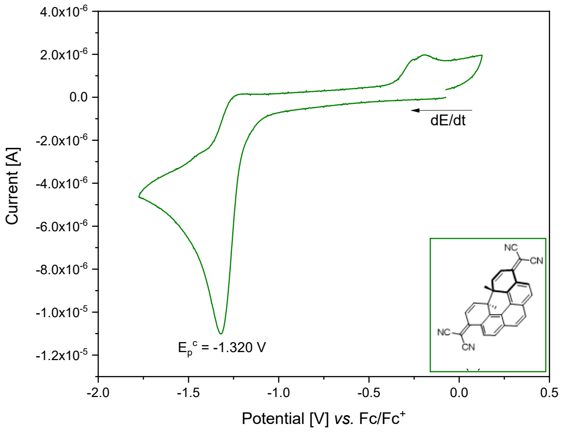

Figure 4. 26. Cyclic voltammogram of (±)-**34-C.** The Experiment was carried out in MeCN with 0.1 M Bu_4NPF_6, *c* = 5·10^{-4} M, platinum disk, *d* = 1.6 mm, scan rate d*E*/d*t* = 1 V s^{-1}, T = 295 K.

The open dianion is stable up to an anodic onset potential of −0.4 V, where back-oxidation leads to electrocyclization reforming the neutral closed (±)-**34-C**. The intensity of the re-oxidation wave is small, which is a results of the scan rate. Reducing the scan rate as usually done in spectroelectrochemical experiments a much more intense re-oxidation wave is observed (Figure 4. 27 inset).

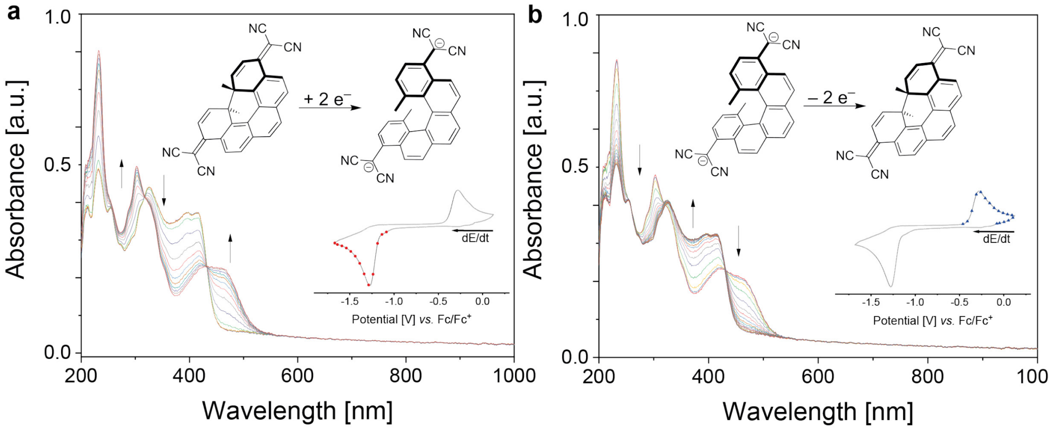

Figure 4. 27. Spectroelectrochemistry of (±)-**34-C**. a) A stable intermediate formed upon two-electron reduction and b) re-oxidation of the intermediate giving back (±)-**34-C**. Insets showing the corresponding cyclic voltammograms with red dots or blue triangles marking when UV/ vis spectra were measured. The experiment was carried out in MeCN with 0.1 M Bu_4NPF_6, $c = 4 \cdot 10^{-4}$ M ((±)-**34-C**), $dE/dt = 10$ mV s^{-1}.

The spectra of the assumed dianion (±)-**34-O**$^{2-}$ are –again as for the diketone– well in accordance to the calculated (TD-DFT) spectra (see Appendix Figure A. 33 and Figure A. 34). Since only one irreversible reduction wave is observed at −1.32 V (vs Fc/Fc^{+}), an ECE mechanism in analogy to that of the diketone (Figure 4. 23) is proposed. Here, the radical anion (±)-**34-C**$^{\cdot-}$ spontaneously opens to (±)-**34-O**$^{\cdot-}$ and the second reduction, confirmed by quantitative electrolysis, occurs instantly under these conditions.[309] Terminology and notations are provided for multistep electrochemical reaction mechanisms. Therefore, in contrast to the diketone, no absorption of a transient radical anion species arises above 550 nm upon reduction. Equivalent to the diketone, the absorption spectrum of the closed form (±)-**34-C** is fully recovered after anodic oxidation (Figure 4. 27).

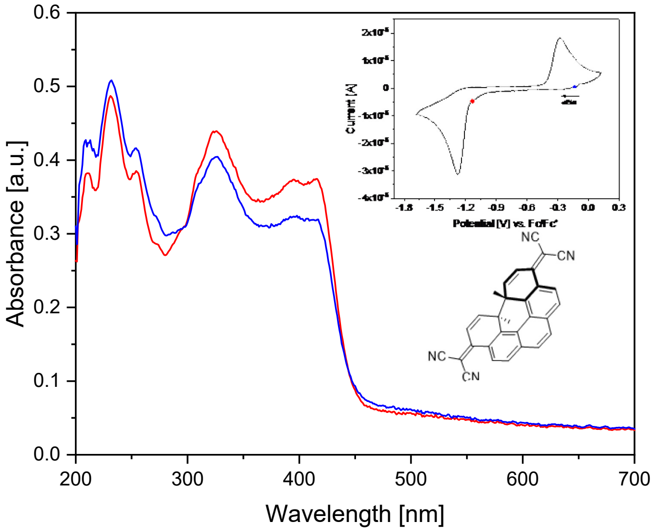

Figure 4. 28. Spectroelectrochemistry of (±)-**34-C.** Absorption changes during CV, insets showing the corresponding cyclic voltammograms with dots marking when UV/vis spectra were measured. The differences between the two spectra derives from residues of the reduced species (±)-**34-O**$^{2-}$. The Experiment was carried out in a thin layer quartz glass spectroelectrochemical cell (d = 0.5 mm) in MeCN with 0.1 M Bu_4NPF_6, T = 295 K.

Finally, we aimed for an unambiguous structural proof for the electrochemical retroelectrocyclization product under quantitative electrolysis. As we have proposed at the beginning of the chapter and found clear evidence the following approach allowed us to unambiguously prove the electrochemical ring opening. Coulometric reduction leads to the reduced helical dianion of either the diketone or the bis(dicyanomethylidene) (±)-**34-O**$^{2-}$. Contrary, to the diketone, the dianion (±)-**34-O**$^{2-}$ can be protonated and subsequent HPLC analysis confirmed the formation of the open protonated open form (±)-**34-O-H**$_2$ (Figure 4. 29). We are sure about this, as the synthesis of (±)-**34-C** offered an authentic isolated sample of (±)-**34-O-H**$_2$ for comparison (Scheme 4. 1).

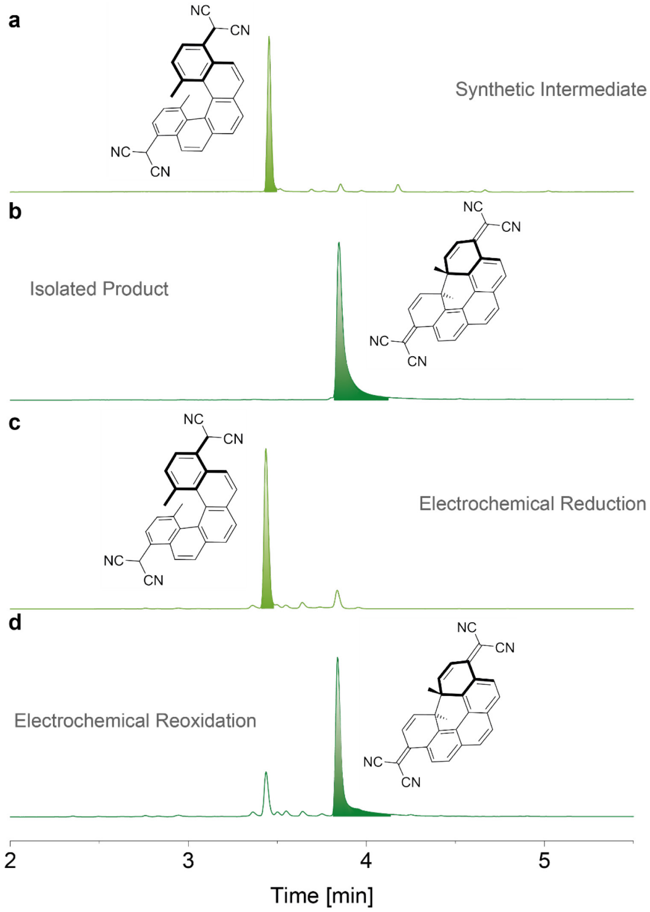

Figure 4. 29. HPLC chromatograms of a) authentic sample of (±)-**34-O-H**$_2$ obtained as synthetic intermediate (**Scheme 4. 1**), b) authentic sample of (±)-**34-C** isolated during preparation, c) (±)-**34-O-H**$_2$ obtained from (almost) quantitative electrolysis of (±)-**34-C** and protic quenching, and d) (±)-**34-C** after coulometric reduction and reoxidation starting from (±)-**34-C**.

The gross charge of the reductive coulometric process was determined for both [5]helicene derivatives as a two-electron process. Diketone (±)-**31-C** and bis(dicyanomethylidene) (±)-**34-C**, with a quantified 78 and 72% reoxidation, respectively. In both coulometric experiments with (±)-**31-C** and (±)-**34-C**, no significant side products were observed.

4.8. Summary and Conclusion

In this chapter we originally describe the planed and failed synthesis of a [5]helicene CPP-type macrocycle. The observation of an unprecedented side-product led to the investigation of two derivatives of dimethyl[5]helicenes. For both substitution patterns we established the photoswitching under cryogenic temperatures between a diamagnetic EPR-silent and a paramagnetic EPR-active form. Installing radical-stabilizing substituents in the 4,11-positions is straightforward starting from the dibromo precursor and will enable several other molecular designs.

Photochemical retroelectrocyclization of the singlet closed form (±)-**31-C** or (±)-**34-C** at cryogenic temperatures gave rise to an open-shell diradical form (±)-**31-O** or (±)-**34-O**, where our data strongly suggests a triplet ground state for (±)-**31-O**. The favored diradical character in (±)-**31-O** and (±)-**34-O** is established through aromatization of the helicene core and stabilization of the radical spin density at the 4,11-oxo substituents or the 4,11-dicyanomethylidene substituents to avoid an energetically unfavored quinoidal closed-shell configuration. While the EPR active triplet state of the open form is stable at cryogenic temperatures, we found that this process is fully reversible through a thermal back reaction upon heating the systems to distinct temperatures. The process can be monitored by UV/vis spectroscopy and EPR spectroscopy. To gain deeper knowledge on our newly developed platform we investigated the electrochemical properties of the two derivatives as well and showed that the ring opening can be induced upon reduction as well.

This system establishes the concept of photoswitching between different bistable spin states through making and breaking of bonds. We envision that the presented 4,11-substitution pattern of radical-stabilizing groups in conjunction with the 1,14-dimethyl groups[268] at the [5]helicene core has the potential for tuning various parameters of this spin-state switch system through a wide range of future derivatizations. In the future it would be especially desirable to operate these switches under ambient conditions in solution to enable fast and robust optimizations work-flows in regard of the molecular design. The presented concept of induced spin-state switching through bond breaking and making could serve the future demand on single-molecule magnets for applications in spintronics, data storage devices, and quantum information processing.[310–314]

Conclusion and Outlook

Conclusion and Outlook

This thesis started with the aim to establish a solution-based synthesis of a carbonaceous material with tubular topology. Therefore, the principles of dynamic covalent chemistry were intended to synthesize covalent organic nanotubes (CONTs). The motivation for this approach developed from the typical desire of a synthetic chemist to build everything from scratch. Humbled by the quest to make ends meet and efficiently synthesize the desired macrocyclic precursors, novel supramolecular hosts were obtained in *Chapter 2* and *3.* As a take-home message we can summarize that the macrocyclization step remains a formidable challenge, but synthetic advances might circumvent the herein experienced difficulties. A special emphasis must be put on the newly developed method using dinuclear gold(I)complexes, since recent studies have shown that this chemistry between gold(I) and the aromatic sp^2-carbon is actually covalent and dynamic.[81] While this could not be elucidated in detail in this thesis we believe the current evidence is well in line with our observed moderate yield for the one-pot cyclooligomerization the discussed metallacycle **26[4]**. While no dynamic covalent chemistry is known up-to date for C_{Ar}–C_{Ar} this chemistry might prove powerful in the future to build complex phenyl-based molecules and materials.

As similar dynamic behavior has been reported for Pt–C_{Ar} bonds future endeavors using this chemistry might need to take a step back and first deepen our understanding on this synthetic approach. The efficient synthesis of the herein presented macrocycles will allow a plethora of supramolecular follow-up studies. Nevertheless, to put the bottom-up synthesis of CONTs within reach, new molecular designs have to be devised. A clear focus therefore must lie on an efficient synthesis of the macrocyclic pre-cursors, as their preparation has been the limiting step throughout *Chapter 2* and *3*.

Further, another area of research might actually be well suited to host such shape-persistent curved macrocycles — namely artificial membrane channels. Membranes are ubiquitous due to the plentiful advantages of compartmentalization spanning from biological to purely chemical systems.[315,316] The implementation of shape persistent macrocycles with a defined inner void volume into membranes might be an ideal opportunity to enable the selective transport of various goods across artificial and natural membranes. As a first step the incorporation into such membranes needs to be tested and studied in detail.

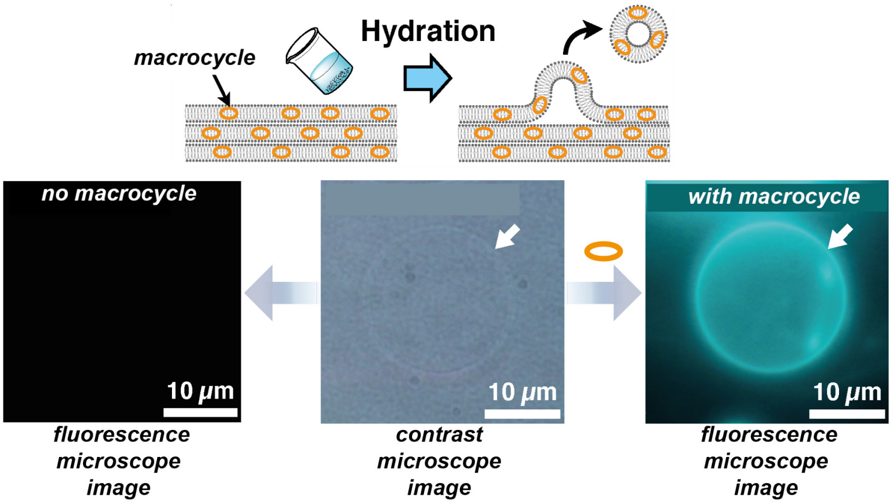

Figure 5. 1. Scheme on the implementation of shape persistent fluorescent macrocycles into artificial membranes. (Based on preliminary data obtained by Dr. Kohei Sato, Tokyo Institute of Technology).

To analyze the incorporation of molecules into membranes fluorescent microscopy is a versatile method.[317] Here the size dependent fluorescence of CPP-type macrocycles is of great benefit.

In *Chapter 3* the aim was to focus on the inherently unique properties of strained aromatic macrocycles on a molecular scale by implementation of chiral subunits. This starting point remains an intriguing target, since it is seeking a functional molecule with superb chiroptical properties. Even though, this could not be achieved a completely new photoswitchable system was found. Reversible photochromic systems are well-known in literature but reports on all-organic molecules that can be reversibly switched between a diamagnetic and a paramagnetic state are rare. Especially the parental dibromo[5]helicene precursors offers facile transformation into various follow-up molecular designs. A first goal is to push the operational temperature to higher temperature to study the ongoing processes in solution, which will allow more efficient feedback-loops to improve the overall performance of these Photoswitches. Therefore the [5]helicene scaffold offers a variety of functionalizations that can be studied, with a primary focus on the R-groups at positions 4 and 11 (Figure 5. 2, top).

In general, stable organic diradicals feature unique electronic properties and therefore show potential for applications in molecular electronics such as organic field-effect transistors (OFETs).[318,319] Our presented example now adds to the field of organic diradicals, as it allows to switch this property on and off. Furthermore, the [5]helicene is chiral and with the emerging field of chirality-induced-spin-selectivity (CISS)[320] we believe that it would be very interesting to study the electronic properties on the molecular level. A similar set-up as shown in figure (Figure 5. 2, bottom) is routinely used to study closed-shell and open-shell aromatic molecules.[321]

This would inevitably lead to a refined understanding of this exciting molecular scaffold.

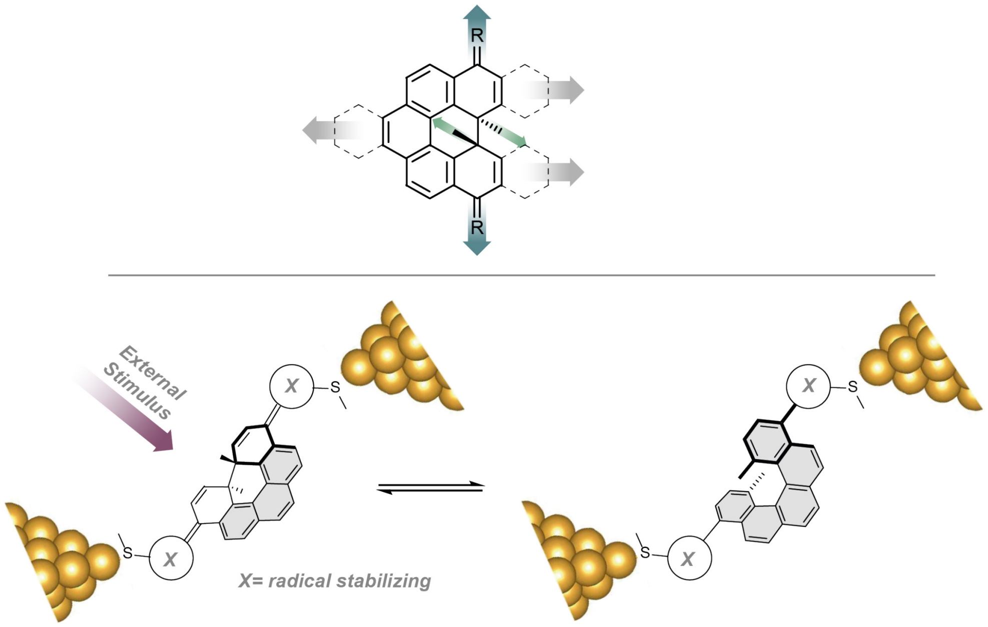

Figure 5. 2. Positions of the [5]helicene scaffold that allow functionalization (top) and the use of 4,11-disubstituted-[5]helicene between two Au electrodes in the open and the closed form.

Appendix A

Experimental Details and Synthetic Procedures

A. Appendix Experimental Details and Synthetic Procedures

Appendix contains the materials and experimental methods, synthetic procedures, and additional experimental data.

A.1. Materials and Experimental Methods

Reagents (Acros, AlfaAesar, Sigma-Aldrich, ABCR, Fluorochem, and TCI) were purchased as reagent grade and used without further purification, unless otherwise specified.

Solvents for synthesis were dried using a Pure Solv Micro Solvent Purification System from Innovative Technology and stored over molecular sieves 3–4 Å.

Glassware. All non-aqueous reactions were performed in oven-dried glassware and under a N_2 atmosphere.

Automated Medium Pressure Column Chromatography (MPLC) was performed on a Teledyne ISCO CombiFlashRf 300 system with 200 mL/min max flow, 200 psi, equipped with integrated ELSD and 200-800 nm UV/Vis variable wavelength detector.

High-Performance Liquid Chromatography (HPLC) was run on a Waters 600 HPLC System equipped with a Waters 600 solvent pump, a Waters 600 controller, and a Waters 996 photodiode array detector.

Ultra-Performance Liquid Chromatography coupled with Mass Spectrometry (HPLC/MS) was performed with a Waters ACQUITY HPLC H-Class, equipped with a quaternary solvent manager (QSM), a sample manager-flow through needle (SM-FTN), a column heater, a column manager, a ACQUITY HPLC BEH Phenyl 1.7 µm, 2.1 × 100 mm column, a ACQUITY HPLC BEH C18 1.7 µm, 2.1 × 100 mm column and a photodiode array detector (PDA eλ), and a ACQUITY QDa detector. The mobile phase is a gradient of MeCN/H_2O individually optimized for each separation.

Recycling gel permeation chromatography (GPC) was performed with a JAI LC-9210NEXT using trichloromethane with 4% ethanol as a stabilizer as the eluent. The GPC was equipped with the following set of columns: PSS SDV 50 Å, 20 × 600 mm; PSS SDV 1000 Å, 20 × 600 mm; Jaigel-2H 5 Å, 20x600 mm. The flow rate was kept at 4.5 mL min^{-1}.

Thin layer chromatography (TLC) was conducted on aluminum sheets coated with SiO_2-60 F_{254} obtained from Merck; visualization with a UV lamp (254 or 366 nm).

Evaporation *in vacuo* was performed at 40–60 °C and 700–10 mbar. All products were dried under vacuum (ca. 10^{-2} mbar) before analytical characterization.

Reported yields refer to spectroscopically and chromatographically pure compounds that were dried under high vacuum (ca. 10^{-2} mbar) before analytical characterization, unless otherwise specified.

Nuclear magnetic resonance (NMR) spectra were recorded using a Bruker Avance II 300 (300 MHz for ^{1}H and 75 MHz for ^{13}C) and a Bruker Avance II 500 (500 MHz for ^{1}H and 126 MHz for ^{13}C) at room temperature and are reported as follows: chemical shift (*d*) in ppm (multiplicity, coupling constant *J* in Hz, number of protons; assignment). The residual deuterated solvent was used as the internal reference ($CDCl_3$: δ_H = 7.26 ppm, CD_2Cl_2: δ_H = 5.32 ppm, CD_3OD: δ_H = 3.31 ppm, $(CD_3)_2SO$: δ_H = 2.50 ppm; ($CDCl_3$: δ_C = 77.16 ppm, CD_2Cl_2: δ_C = 54.00 ppm, CD_3OD: δ_C = 49.00 ppm, $(CD_3)_2SO$: δ_C = 39.52 ppm; The resonance multiplicity is described as s (singlet), d (doublet), t (triplet), q (quartet), quint (quintet), sept. (septet), m (multiplet), and br. (broad).

Melting Points (m.p.) were measured using an MPM-H2 by Schorpp Gerätetechnik in open capillaries and are uncorrected.

Infrared (IR) spectra were recorded on a Vertex 70v spectrometer by Bruker equipped with a diamond ATR attachment and are basegraph-corrected. The spectra were measured between 4000 and 400 cm^{-1}. Absorption bands are reported in wavenumbers (cm^{-1}) and their relative intensities described as s (strong), m (medium), or w (weak).

High-resolution mass spectrometry (HRMS) data were recorded on a Q-Exactive by Thermo Fisher via direct injection at flow rates between 20 and 100 µL min^{-1} in positive and negative mode, a resolution of 35000, an AGC Target Value of 10^6, a max inject time of 50 ms, and Mass Ranges between 200 and 1000 m/z.

Single crystal X-ray data were measured with a BRUKER D8 VENTURE area detector with Mo-Kα radiation (λ = 0.71073 Å). Multi-scan absorption corrections implemented in SADABS[322] 1 were applied to the data. The structures were solved by intrinsic phasing method (SHELXT-2013)[323] and refined by full matrix least square procedures based on F2 with all measured reflections (SHELXL-2014)[324] in the graphical user interface (OLEX2)[325] with anisotropic temperature factors for all non-hydrogen atoms. All hydrogen atoms were added geometrically and refined by using a riding model. The calculation of the voids resulting from heavily disordered solvent molecules in the structure was achieved using the tool implemented in OLEX2[326] or by using the PLATON/SQUEEZE protocol.[327,328]

Ultraviolet–Visible (UV/Vis) absorbance spectroscopy was performed on Agilent Cary 50 and Cary 60 instruments connected to a cryostat from Unisoku Scientific Instruments (temperature accuracy ±0.1 K) in 10 × 10 mm quartz cuvettes with 3 mL volume. Weighing of small quantities was performed on a Sartorius ME5 analytical microbalance.

Variable Temperature Ultraviolet–Visible (VT-UV/Vis) absorbance spectroscopy was performed on Agilent Cary 60 instruments equipped with a OptistatDN from Oxford Instruments connected with a MercuryiTC temperature controller from Oxford Instruments in a 221.001-QS quartz cuvette from neoLab with 3 mL volume.

Ultraviolet–Visible fluorescence spectroscopy was performed on a Varian Cary Eclipse Fluorescence spectrometer using 10.0×10.0 mm quartz cuvettes. All solutions were degassed prior to use. Weighing of small quantities was performed on a Sartorius ME5 analytical microbalance.

Electron paramagnetic resonance (EPR) spectroscopy was performed on a Bruker EMXplus Instrument at a frequency of 9.35 GHz (X-Band). All samples were measured in an interval of temperature from 13 to 93 K as glassy frozen solutions (powder spectra) with a liquid helium recirculating cooling system provided by ColdEdge.

Electronic circular dichroism (ECD) spectra were recorded in a 1.00 mm path length cuvette using a Cary 50 Bio Spectrophotometer by Varian.

Optical rotatory dispersion (ORD) was recorded on a DIP-370 digital polarimeter by Jasco using a 10.0 cm cuvette; concentrations c are given in g/100 mL.

Cyclic voltammetry (CV) was performed using a PG310 USB (HEKA Elektronik) potentiostat interfaced to a PC with PotMaster v2x43 (HEKA Elektronik) software for data evaluation. A three-electrode configuration contained in a nondivided cell consisting of a platinum disc (d = 1.6 mm) as the working electrode, a platinum plate as the counter electrode, and a saturated calomel electrode (SCE) with an agar–agar plug in a Luggin capillary with a diaphragm as the reference electrode was used. Measurements were carried out in acetonitrile (HPLC-grade, dried over calcium hydride and distilled) containing 0.1 M Bu_4NPF_6 using a scan rate of $\mathrm{d}E/\mathrm{d}t$ = 1 V s^{-1}. The data is given in reference to the ferrocene redox couple (Fc/Fc^+), which was used as an external standard.

Spectroelectrochemistry was performed in a SEC-C Thin Layer Quartz Glass Spectroelectrochemical cell with a 0.5 mm optical path length, with platinum mesh electrode as a working electrode, counter electrode: platinum wire, reference electrode: non aqueous reference electrode Ag/Ag^+ (0.01 M $AgNO_3$ in 0.1 M Bu_4NPF_6 acetonitrile), ALS Co., Ltd (Tokyo, Japan) spectrometer: AvaSpec-2048x14 with AvaLight-DH-S-BAL, and AvaSoft 7.7.2, Avantes S3 (Apeldoorn, Netherlands) Potentiostat: PGSTAT 128N, Deutsche Metrohm GmbH & Co. KG (Filderstadt, Germany) and software: NOVA 1.10. Scan rate for all measurements dE/dt = 10 mV s^{-1}.

A.2. Synthetic Procedures

A.2.1 Synthetic Procedures for Compounds Prepared within Chapter 1

Pyrene-4,5,9,10-tetrone (2)[178]

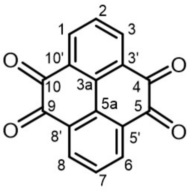

The following procedure was adapted from the literature and modified.[178] A solution of pyrene (20 g, 98.9 mmol) in CH_2Cl_2 (300 mL) was treated with MeCN (300 mL), H_2O (375 mL), and $RuCl_3{\cdot}H_2O$ (2.5 g, 11.1 mmol) and degassed by bubbling N_2 through the solution for 15 min. The suspension was cooled to 3 °C using an ice–water bath, $NaIO_4$ (85 g, 398 mmol) was added and the suspension was stirred with an overhead mechanical stirrer for 15 min. While stirring, the ice bath was removed allowing the suspension to warm up to 25 °C. The suspension was cooled again with an ice bath under nitrogen atmosphere, and treated with an additional portion of $NaIO_4$ (85 g, 398 mmol). The ice bath was removed and the suspension was stirred for 2 h at 25 °C. The organic solvents were removed at 40 °C under reduced pressure and the remaining aqueous phase was vacuum filtered through a Büchner funnel. The obtained solid was purified by liquid extraction using a Soxhlet apparatus (CH_2Cl_2, 7 d). The crude solid suspension (in CH_2Cl_2) was diluted with the same volume of EtOAc and the volatile phase (mostly CH_2Cl_2) was carefully evaporated under reduced pressure. The resulting orange–brown precipitate in the remaining solvent (mostly ethyl acetate) was filtered, washed with EtOAc, and MeOH. Drying under vacuum afforded **2** (7.10 g, 27%) as a brown solid. The characterization data is in agreement with the literature.[178]

R_f = 0.3 (SiO_2; cyclohexane/EtOAc 2:1); ^{1}H NMR (500 MHz, $(CD_3)_2SO$, 25 °C): δ = 8.33 (d, J = 7.80 Hz, 4H, 4 H–C(1,3,6,8)), 7.44 ppm (t, J = 7.80 Hz, 2H, 2 H–C(2,7)); ^{13}C NMR (126 MHz $(CD_3)_2SO$, 25 °C, assignments based on ^{1}H,^{13}C HSQC NMR spectra): δ = 177.14 (C(4,5,9,10)), 134.2 (C(3a,5a)), 131.5 (C(1,3,6,8)), 130.2 ppm (C(2,7)); IR (ATR): $\tilde{\nu}_{max}$ = 3068 (w), 1672 (s), 1558 (s), 1451 (m), 1421 (s), 1336 (m), 1272 (s), 908 (s), 708 cm^{-1} (s); HR-ESI-MS: m/z: 263.0333 ($[M + H]^+$ calcd. for $C_{16}H_7O_4^+$: 263.0339).

2,7-Dibromo-pyrene-4,5,9,10-tetrone (10)[186]

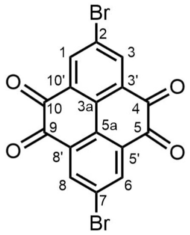

The following procedure was adapted from the literature and modified.[186] A solution of pyrene-4,5,9,10-tetrone (**2**) (5.6 g, 21.3 mmol) was dissolved in concentrated H_2SO_4 (95–97%, 270 mL). The reaction mixture was degassed with a constant flow of

N_2. NBS (11.4 g, 63.8 mmol) was added gradually over 4 h at 25°C. The reaction mixture was stirred over night, poured over ice, filtered and suspended in MeOH. The MeOH suspension was filtered, and the resulting yellow solid washed several times with MeOH. Drying under high vacuum afforded **10** (7.8 g, 87%) as a yellow solid. The characterization data is in agreement with the literature.[186]

R_f = 0.15 (SiO_2; cyclohexane/EtOAc 1:2); ^1H NMR (500 MHz, $CHCl_3$, 25 °C): δ = 8.60 ppm (s 4H, 4 H–C(1,3,6,8)); ^{13}C NMR did not resolve in sufficient signal to noise ratios in common NMR solvents; HR-ESI-MS: *m*/*z*: 419.8450 ([*M* + H]$^+$ calcd. for $C_{16}H_7O_4^+$: 419.8456).

2,7-Dibromo-pyrene-4,5,9,10-tetra(ethyleneglycol)ketal (9)[186]

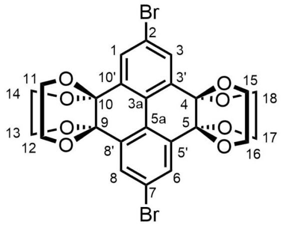

Based on a modified procedure in the literature,[182] a suspension of dibromide **10** (4.1 g, 9.8 mmol), ethylene glycol (11.0 mL, 0.20 mol), (+)-camphorsulfonic acid (0.34 g, 1.5 mmol), in dry THF (28 mL) was degassed with a constant flow of N_2 in an oven-dried 100 mL-pressure tube, sealed, and heated to 120 °C for 24 h. The mixture was cooled to 23 °C, filtered and subsequently was washed with MeOH (3 x 60 mL) and diethyl ether (3 x 50 mL), and dried under high-vacuum to obtain **9** (3.9 g, 68%) as a beige solid. The characterization data is in agreement with the literature.[182]

R_f = 0.1 (SiO_2; cyclohexane/EtOAc 1:2); ^1H NMR (500 MHz, CD_2Cl_2, 25 °C): δ = 7.88 (s, 4H, 4 H–C(1,3,6,8)), 4.18 (br., 8H, 8 H–C(11–18)), 3.64 ppm (br., 8H, 8 H–C(11–18)); ^{13}C NMR (126 MHz, CD_2Cl_2, 25 °C, assignments based on ^1H,^{13}C-HSQC NMR spectra): δ = 135.68 (C(2,7)), 131.03 (C(1,3,6,8)), 127.67 (C(3a,5a)), 124.29 (C(3',5',8',10')), 92.44 (C(4,5,9,10)), the signal for the carbon atoms of the ethylene glycol groups are not observed, due to the dynamics of six-membered rings; HR-ESI-MS: *m*/*z*: 596.9577 ([*M* + H]$^+$calcd. for $C_{24}H_{21}Br_2O_8{}^+$: 596.9583).

Pyrene-4,5,9,10-tetra(ethylenglycol)ketal (7)[182]

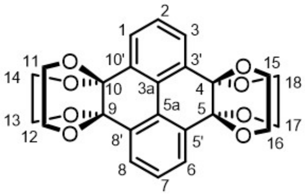

Based on a modified procedure in the literature,[182,211] a suspension of tetraketone **2** (1.00 g, 3.81 mmol), ethylene glycol (4.00 mL, 71.5 mmol), (+)-camphorsulfonic acid (133 mg, 0.572 mmol), in MeOH (8 mL) was degassed with a constant flow of N_2 in an oven-dried 25 mL-pressure tube, sealed, and heated to 120 °C for 24 h. The mixture was cooled to 23 °C, filtered, the solid was washed with MeOH (3 x 50 mL) and diethyl ether (3 x 50 mL), and dried for 24 h under high-vacuum to obtain **7** (1.22 g, 73%) as a beige solid. The characterization data is in agreement with the literature.[182]

R_f = 0.4 (SiO_2; cyclohexane/EtOAc 2:1); ^{1}H NMR (400 MHz, $CDCl_3$, 25 °C): δ = 7.77 (d, J = 7.77 Hz, 4H, 4 H–C(1,3,6,8)), 7.50 (t, J = 7.72 Hz, 2H, 2 H–C(2,7)), 4.19 (br., 8H, 8 H–C(11–18)), 3.66 ppm (br., 8H, 8 H–C(11–18)); ^{13}C NMR (75 MHz, $CDCl_3$, 25 °C, assignments based on ^{1}H,^{13}C NMR spectra): δ = 133.1 (C(4,5,9,10)), 129.6 (C(2,7)), 129.3 (C(3a,5a)), 127.1 (C(1,3,6,8), 92.7 (C(4,5,9,10)), 61.5 ppm (br., C(11–18)); (FT)ATR-IR: $\tilde{\nu}_\mathrm{max}$ = 3068 (w), 2988 (w), 2874 (m), 1437 (m), 1267 (m), 1181 (m), 1081 (s), 1012 (s), 957 (s), 816 (m), 744 cm^{-1} (m); HR-ESI-MS: m/z: 439.1386 ([M + H]$^+$calcd. for $C_{24}H_{23}O_8^+$: 439.1387).

2,7-Bis(4,4,5,5-tetramethyl-1,3,2-dioxaborolan-2-yl)-4,5,9,10-tetra(ethyleneglycol)ketal-pyrene (6)[182]

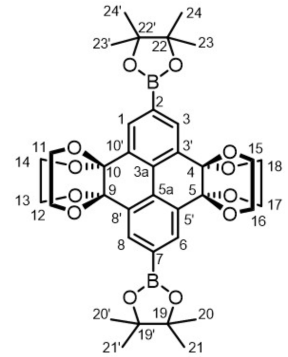

Adapted with changes from the literature,[182,329] a solution of **7** (1.00 g, 2.28 mmol) in degassed dry 1,4-dioxane (23 mL, 22 ppm H_2O by Karl–Fischer titration) was treated with 4,4'-di-*tert*-butyl-2,2'-bipyridine (dtbpy, 61 mg, 228 µmol, 5 mol%), bis(pinacolato)diboron (2.32 g, 9.12 mmol), and $[Ir(OMe)COD]_2$ (76 mg, 114 µmol), degassed for 10 min. until the color changed from dark brown–red to a brighter reddish color, sealed, and heated to 120 °C for 48 h while stirring. The mixture was cooled to 6 °C (fridge) for 30 min to complete precipitation of a colorless solid. The suspension was filtered, the solid was washed with MeOH and cyclohexane, and dried under high-vacuum for 18 h to afforded **6** (1.36 g, 84%) as a colorless solid. The characterization data is in agreement with the literature.[182]

R_f = 0.5 (SiO_2; cyclohexane/EtOAc 2:1); ^{1}H NMR (400 MHz, $CDCl_3$, 25 °C): δ = 8.21 (s, 4H, 4 H–C(1,3,6,8)), 4.20 (br., 8H, 8 H–C(11–18)), 3.66 (br., 8H, 8 H–C(11–18), 1.32 ppm (s, 24H, 8 H_3C); ^{13}C NMR (101 MHz, $CDCl_3$, 25 °C, assignments based on ^{1}H,^{13}C-HSQC NMR spectra): δ = 133.5 (C(1,3,6,8)), 132.6 (C(3’,5’,8’,10’)), 131.7 (C(3a,5a)), 92.8 (C(4,5,9,10)), 84.1 (C(19,19’,22,22’), 63.0–61.0 (br., C(11–18)), 25.0 ppm (C(20,20’,21,21’,23,23’,24,24’)) the signal of C(2,7) is hidden by the noise due to quadrupolar relaxation induced by the boron nuclei); (FT)ATR-IR: $\tilde{\nu}_\mathrm{max}$ = 2975 (s), 1616 (m), 1470 (m), 1373 (s), 1331 (m), 1288 (m), 1261 (s), 1094 (s), 958 (s), 852 (m), 690 cm^{-1} (m); HR-ESI-MS: m/z: 691.3091 ([M + H]$^+$ calcd. for $C_{30}H_{40}B_2O_8^+$: 691.3092).

2,7-Bis(trimethylstannyl)-4,5,9,10-tetra(ethyleneglycol)ketal-pyrene (6)

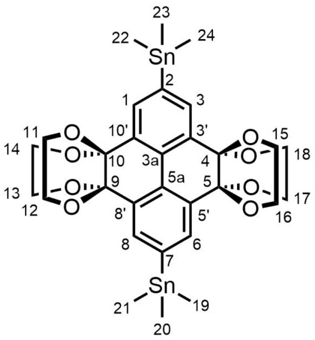

Dibromide **9** (1.5 g, 2.5 mmol), 2,4,6-tri-tert-butylphenol (0.7 mg, 0.25 mmol), lithium chloride (0.5 g, 12.6 mmol) were suspended in dry 1,4-dioxane (90 mL) and degassed with a constant flow of N_2 in an oven-dried 350 mL-pressure tube. 1,1,1,2,2,2-hexamethyldistannane (2.06 g, 6.3 mmol), tetrakis(triphenylphosphine)-palladium(0) (0.29 g, 0.25 mmol), were added afterwards and the reaction mixture was sealed and heated to 110 °C for 2 h. The reaction mixture was allowed to cool down to 25 °C and filtered over a pad of silica. The solvent was evaporated under reduced pressure (careful: must be performed in a fume hood; all instruments should be cleaned thoroughly afterwards due to remaining organostannanes). Purification by preparative MPLC (SiO_2, gradient cyclohexane/CH_2Cl_2 3:1→0:1) and drying under vacuum gave **6** (1.48 g, 77%) as a colorless solid.

R_f = 0.4 (SiO_2; CH_2Cl_2); ^{1}H NMR (500 MHz, CD_2Cl_2, 25 °C): δ = 7.86 (s, 4H, H–C(1,3,6,8)), 4.19 (br. 8H, H–C(11–18)), 3.64 (br. 8H, H–C(11–18), 0.36 ppm (s, 18H, H–C(19–24)); ^{13}C NMR (126 MHz, CD_2Cl_2, 25 °C, assignments based on ^{1}H,^{13}C-HSQC NMR spectra): δ = 145.38 (C(2,7)), 134.76 (C(1,3,6,8)), 132.12 (C(3',5',8',10')), 129.40 (C(3a,5a)), 93.33 (C(4,5,9,10)), 61.82 (br., C(11–18), 9.07 ppm (C(19–24)); HR-ESI-MS: *m/z* (%): 765.0677 (**6**, [*M* + H]$^+$, calcd. for $C_{30}H_{38}O_8Sn_2$ H+: 765.0457).

[4]-Cyclo-2,7-(platinum(cyclooctadiene)pyren-4,5,9,10-tetraketal (5)

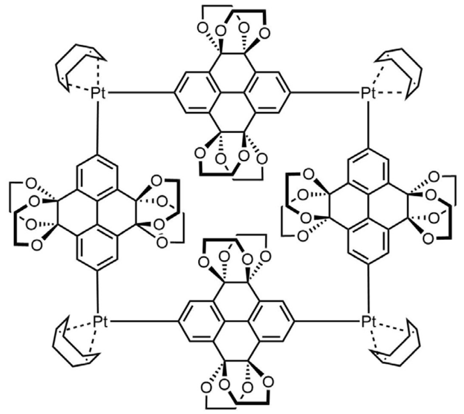

Adapted from the literature,[68] a suspension of dichloro(cycloocta-1,5-diene)platinum(II) (189.7 mg, 507 µmol), CsF (924 mg, 6.1 mmol), and **6** (350.0 mg, 507 µmol) in dry CH_2Cl_2 (140 mL, 5.2 ppm H_2O by Karl-Fischer titration) in an oven-dried 350 mL-pressure tube was degassed using a stream of N_2 for 10 min, sealed, and stirred at 45 °C for 24 h. The mixture was cooled to 23 °C, diluted with cyclohexane (140 mL), and the major volatile CH_2Cl_2 was evaporated to induce precipitation. The resulting suspension was filtered and the pale brown solid was washed with cyclohexane and MeOH. Drying under vacuum afforded **5** (277.5 mg, 74%) as an off-white solid.

R_f = 0.2 (SiO_2; $CHCl_3$/MeOH 99:1); ^{1}H NMR (400 MHz, CD_2Cl_2, 25 °C): δ = 7.41 (br. s, 16H, 16 H–C(1,3,6,8)), 5.21 (br. s, 16H, 16 H_2–C(cod)), 4.35–2.90 (m, 64H, 16 H–C(11–18)), 2.56 ppm (br. s, 32H, 16 H_2–C(cod); ^{13}C NMR measurements gave no sufficient signal-to-noise ratio due to low solubility; (FT)ATR-IR: $\tilde{\nu}_{max}$ = 3051 (m), 2949 (m), 2873 (m), 2190 (w), 2045 (w), 1438 (m), 1264 (m), 1176 (m), 1091 (s), 1011 (s), 958 (s), 897 (m), 730 (m), 583 cm^{-1} (w); MALDI-TOF-MS: m/z (%): 2995.39 ([M + K]$^+$, calcd. for $C_{120}H_{100}O_{40}K^+$: 2995.66).

[*n*]Cyclo-2,7-(4,5,9,10-tetra(ethyleneglycol)ketal)-pyrenylene (4[*n*] *n* = 4–8)

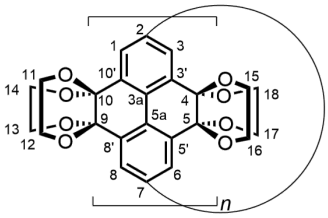

A solution of **5** (50.9 mg, 16.9 µmol) and triphenylphosphine (180.6 mg, 688.5 µmol) in dry 1,2-dichlorobenzene (5 mL) was degassed for 30 min with a constant flow of N_2 under sonication. The reaction vial was sealed and the mixture was heated in a microwave reactor to 180 °C and kept at that temperature for 1 min (typical heating time: 5 min). After cooling to 100 °C, the brown–orange mixture was vacuum-filtered through a PTFE filter (pore size 0.2 µm) to remove insoluble linear oligomers. The filtrate was loaded onto a short pad of silica and was eluted with $CHCl_3$ (ca. 150 mL — major side products and remaining triphenylphosphine are first eluted) followed by $CHCl_3$/MeOH 96:4 (ca. 100 mL), which elutes the cyclic product fraction. Evaporation gave a yellow solid (containing macrocyclic products *n* = 4–8 with minor amounts of linear oligomers) that was further purified via GPC (five cycles in sum). Each macrocyclic product fraction (*n* = 4–8) was again purified individually via GPC to get analytically pure compound.

4[*n*] *n* = 4: Yellow solid (2.79 mg, 7.3% with regard to the total amount of pyrene fragments added to the reaction). R_f = 0.4 (SiO_2; $CHCl_3$/MeOH 96:4); ^{1}H NMR (500 MHz, $CDCl_3$, 25 °C): δ = 7.90 (s, 16H, 16 H–C(1,3,6,8)), 4.23 (br. m, 16H), 4.11 (br. m, 16H), 3.66 (br. m, 16H, 16 H–C), 3.58 ppm (br. m, 16H); ^{13}C NMR (126 MHz, $CDCl_3$, 25 °C, assignments based on ^{1}H,^{13}C-HSQC and HMBC NMR spectra): δ = 139.5 (C(3a,5a)), 134.0 (C(2,7 or 3',5',8'10')), 128.23 (C(1,3,6,8)), 125.7 (C(2,7 or 3',5',8'10')), 93.2 (C(4,5,9,10)) 61.8 (C(11–18)), 61.4 ppm (C(11–18)); MALDI-TOF-MS: m/z: 1744.42 ([M], calcd. for $C_{96}H_{80}O_{32}$: 1744.46).

4[*n*] *n* = 5: Yellow solid (8.2 mg, 12.3% with regard to the total amount of pyrene fragments added to the reaction). R_f = 0.3 (SiO_2; $CHCl_3$/MeOH 96:4); ^{1}H NMR (500

MHz, $CDCl_3$, 25 °C, assignments based on $^1H,^{13}C$-HSQC and HMBC NMR spectra): δ = 7.89 (s, 16H, 16 H–C(1,3,6,8)), 4.19 (broad s, 20H, 16 H–C(out of C11–C18)), 4.13 (broad s, 20H, 16 H–C(out of C11–C18)), 3.69 (broad s, 20H, 16 H–C(out of C11–C18)), 3.65 ppm (broad s, 20H, 16 H–C(out of C11–C18)); ^{13}C NMR (126 MHz, $CDCl_3$, 25 °C, assignments based on $^1H,^{13}C$-HSQC and HMBC NMR spectra): δ = 140.2 (C(3a,5a)), 134.0 (C(2,7 or 3',5',8'10')), 129.1 (C(1,3,6,8)), 125.6 (C(2,7 or 3',5',8'10')), 93.0 (C(4,5,9,10)), 61.7 (C(11–18)), 61.4 ppm (C(11–18)); MALDI-TOF-MS: *m/z*: 2180.57 ([*M*], calcd. for $C_{120}H_{100}O_{40}$: 2180.59).

4[*n*] *n* = 6: Yellow solid (5.8 mg, 8.7% with regard to the total amount of pyrene fragments added to the reaction). R_f = 0.3 (SiO_2; $CHCl_3$/MeOH 96:4); ^1H NMR (500 MHz, $CDCl_3$, 25 °C, assignments based on $^1H,^{13}C$ HMBC NMR spectra): δ = 7.89 (s, 24H, 16 H–C(1,3,6,8)), 4.17 (broad s, 48H, 16 H–C(out of C11–C18)), 3.70 (broad s, 24H, 16 H–C(out of C11–C18)), 3.60 ppm (broad s, 24H, 16 H–C(out of C11–C18)); ^{13}C NMR measurements gave no sufficient signal-to-noise ratio due to low solubility; $^1H,^{13}C$-HMBC NMR spectra, extracted ^{13}C signals (600 MHz, $CDCl_3$, 25 °C) δ = 141.2, 128.8, 125.4, 92.7 ppm; MALDI-TOF-MS: *m/z* (%): 2616.76 (**1**$_{[6]}$, [*M*], calcd. for $C_{144}H_{120}O_{48}$: 2616.70).

4[*n*] *n* = 7: Yellow solid (5.9 mg, 8.8% with regard to the total amount of pyrene fragments added to the reaction). R_f = 0.3 (SiO_2; $CHCl_3$/MeOH 96:4); ^1H NMR (500 MHz, $CDCl_3$, 25 °C, assignments based on $^1H,^{13}C$-HSQC NMR spectra): δ = 7.98 (s, 28H, 16 H–C(1,3,6,8)), 4.20 (broad s, 56H, 16 H–C(out of C11–C18)), 3.71 ppm (broad s, 56H, 16 H–C(out of C11–C18)); ^{13}C NMR (126 MHz, $CDCl_3$, 25 °C, assignments based on $^1H,^{13}C$-HSQC, $^1H,^{13}C$-HMBC and HMBC NMR spectra): δ = 140.8 (C(3a,5a)), 133.9 (C(2,7 or 3',5',8'10')), 128.8 (C(1,3,6,8)), 125.7 (C(2,7 or 3',5',8'10')), 92.9 (C(4,5,9,10)), 61.7 ppm (C(11–18)); MALDI-TOF-MS: *m/z*: 3052.95 ([*M*], calcd. for $C_{168}H_{140}O_{56}$: 3052.81).

4[*n*] *n* = 8: Beige solid (2.1 mg, 3.1% with regard to the total amount of pyrene fragments added to the reaction). R_f = 0.2 (SiO_2; $CHCl_3$/MeOH 96:4); ^1H NMR (500 MHz, $CDCl_3$, 25 °C): δ = 8.04 (s, 16H, 16 H–C(1,3,6,8)), 4.23 (broad s, 16H, 16 H–C(out of C11–C18)), 3.68 ppm (broad s, 16H, 16 H–C(out of C11–C18)); ^{13}C NMR measurements gave no sufficient signal-to-noise ratio due to low solubility. MALDI-TOF-MS: *m/z*: 3489.10 ([*M*], calcd. for $C_{192}H_{160}O_{64}$: 3488.93).

The low yields and the laborious purification process led to variations in yields for the individual ring sizes. Therefore, an average yield from three reaction runs was calculated (Table A 1).

Table A 1. Scale and yields for 4**[*4–8*]** of three independent performed reactions.

Scale	**Yield 4[4]**	**Yield 4[5]**	**Yield 4[6]**	**Yield 4[7]**	**Yield 4[8]**
100 mg	3.8%	4.1%	2.6%	1.6%	0.7%
150 mg	6.2%	8.7%	7.3%	10.3%	4.3%
100 mg	7.3%	12.3%	8.7%	8.8%	3.1%
Average	5.8%	8.4%	6.2%	6.9%	2.7%

A.2.2 Synthetic Procedures for Compounds Prepared within Chapter 2

If applicable the nomenclature follows the suggestions proposed by the IUPAC and the IUPAC phane nomenclature for the macrocyclic scaffolds.[330,331] Numbering of atoms in the structures follows the numbering of the IUPAC name.

3,6-Dibromophenanthrene-9,10-quinone (21)[211]

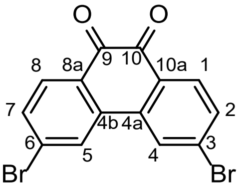

The synthesis of **21** was carried out according to the procedure reported by Isobe and co-workers*.* 3,6-dibromophenanthrene-9,10-quinone (50.00 g, 240.38 mmol), dibenzoyl peroxide (1.45 g, 6.01 mmol) and an initial amount of bromine (5 g, 31.25 mmol) in nitrobenzene (100 mL) was heated to 120 °C. When the formation of HBr started, bromine (87.31 g, 545.66 mmol) was added dropwise and stirring was continued for 1 h. After cooling to 25 °C, ethanol (500 ml) was added, the precipitate was filtered off and washed with ethanol until the washing solution was colorless. Drying under vacuum afforded **21** (10.10 g, 93%, Lit:[221] 80%) as a golden solid. The characterization data is in agreement with the literature.[221]

R_f = 0.54 (SiO_2; CH_2Cl_2); m.p. = 279–281° C; ^{1}H NMR (500 MHz, $CDCl_3$, 25 °C): δ = 8.12 (d, J = 1.7 Hz, 2H, H–C(4,5)), 8.08 (d, 2H, H–C(1,8)), 7.67 (dd, J = 8.3, 1.7 Hz, 2H H–C(2,7)); ^{13}C NMR (126 MHz, $CDCl_3$, 25 °C): δ = 179.0 (C(9,10)), 136.1 (C(4a,4b)), 133.6 (C(2,7)), 132.1 (C(3,6)), 132.0 (C(1,8)), 130.0 (C(8a,10a)), 127.5 ppm (C(4,5)); IR (ATR): $\tilde{\nu}_{max}$ = 3341 (w), 3100 (m), 3070 (m), 3034 (m), 2362 (m), 1671 (s), 1578 (s), 1468 (s), 1391 (m), 1326 (m), 1269 (s), 1222 (m), 1129 (w), 1077 (m), 918 (m), 823 cm^{-1} (m); HR-ESI-MS: m/z (%): 364.8806 (80, $[M + H]^+$, calcd. for $C_{14}H_7Br_2O_2^+$: 364.8807).

3,6-Dibromophenanthrene-9,10-di(ethyleneglycol)ketal (16)[211]

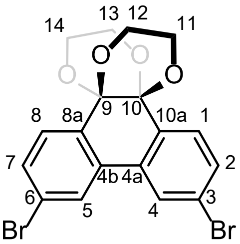

The synthesis of **16** was performed under the conditions reported by Isobe and co-workers.[221] Dibromide **21** (10.00 g, 27.32 mmol), camphorsulfonic acid (0.93 g, 4.09 mmol) and ethylene glycol (30 mL, 564 mmol) were dispersed in a 350 mL-pressure tube in anhydrous methanol (140 mL). The orange suspension was degassed for 10 min under vigorous stirring with a constant flow of nitrogen. The reaction vessel was capped and the suspension was stirred at 120 °C for 16 h until an orange solid formed. The reaction mixture was allowed to cool down to 25 °C, filtered, and the solid was washed with methanol (500 mL) and diethyl ether (300 mL). Drying under vacuum afforded **16** (10.10 g, 93%, Lit:[221] 80%) as a pale pinkish solid. The characterization data is in agreement with the literature.[221]

R_f = 0.65 (SiO_2; CH_2Cl_2); m.p. > 280 °C; ^{1}H NMR (500 MHz, $CDCl_3$, 25 °C): δ = 7.96 (d, J = 1.7 Hz, 2H, H–C(4,5)) 7.62 (dd, J = 8.3 Hz, 2H, H–C(1,8)), 7.57 (dd, J = 8.3, 1.8 Hz, 2H, H–C(2,7)), 4.24 (br., 4H, H–C(11,12,13,14)), 3.69 ppm (br., 4H, H–C(11,12,13,14)); ^{13}C NMR (126 MHz, $CDCl_3$, 25 °C): δ = 134.0 (C(4a,4b)), 132.4 (C(2,7)), 132.3 (C(3,6)), 128.4 (C(1,8)), 127.2 (C(4,5)), 124.6 (C(8a,10a)), 92.3 (C(9,10)), 61.5 ppm (C(11,12,13,14)); IR (ATR): $\tilde{\nu}_{max}$ = 3080 (w), 2980 (m), 2963 (m), 2926 (m), 2873 (m), 2631 (m), 1760 (m), 1539 (m),1558 (m), 1478 (m), 1387 (m), 1282 (m), 1244 (m), 1186 (m), 1047 (s), 1019 (m), 997 (m), 947 (m), 889 (m), 868 (m) 813 cm^{-1} (m); HR-ESI-MS: m/z (%): 452.9343 (15, [M + H]$^+$, calcd. for $C_{18}H_{15}Br_2O_4^+$: 452.9332).

3,6-Bis(4,4,5,5-tetramethyl-1,3,2-dioxaborolan-2-yl)-2,3-dihydro-4a,12b-(epoxyethanooxy)phenanthro[9,10–b][1,4]dioxine (18)[224]

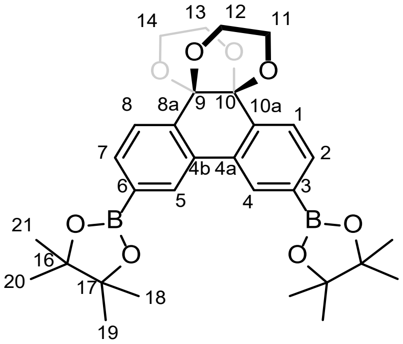

The synthesis of **18** was carried out according to an improved procedure reported by Isobe and co-workers.[221] Dibromophenanthrene **16** (10.50 g, 23.05 mmol), Pd(dppf)Cl_2 (0.51 g, 0.69 mmol), *bis*(pinacolato)diboron (12.88 g, 50.72 mmol) and potassium acetate (11.31 g, 115.27 mmol) were dispersed in 1,4-dioxane (300 mL) and degassed for 10 min under vigorous stirring *via* a constant nitrogen flow. The suspension was stirred for 16 h at 80 °C. After cooling the reaction mixture to 25 °C, water (300 mL) was added. The aqueous layer was extracted with $CHCl_3$ (3 x 200 mL) and the combined organic phases were washed with brine (300 mL) and dried over $MgSO_4$. The product mixture was filtered over a short pad of silica, concentrated, and washed with methanol (200 mL). Drying under vacuum afforded **18** (10.25 g, 81%, Lit:[221] 89%) as an off-white solid. The characterization data is in agreement with the literature.[221]

R_f = 0.57 (SiO_2; $CHCl_3$); m.p. > 280 °C; ^{1}H NMR (400 MHz, $CDCl_3$, 25 °C): δ = 8.41 (s, 2H, H–C(4,5)), 7.87 (d, J = 7.6 Hz, 2H, H–C(2,7)), 7.74 (d, J = 7.7 Hz, 2H, H–C(1,8)), 4.19 (br., 4H, H_2–C(11,12,13,14)), 3.64 (br., 4H, H_2–C(11,12,13,14)), 1.39 ppm (s, 24H, H_3–C(18,19,20,21)); ^{13}C NMR (126 MHz, $CDCl_3$, 25 °C): δ = 135.6 (C(2,7)), 135.4 (C(8a,10a)), 132.67 (C(4a,4b)), 130.5 (C(4,5)), 125.5 (C(1,8)), 92.8 (C(9,10)), 84.2 (C(16,17)), 61.7 (C(11,12,13,14)), 25.2 ppm (C(18,19,29,21)), (C(3,6) are not observed due to the quadrupolar relaxation induced by the boron nuclei); IR (ATR):

$\tilde{\nu}_{\text{max}}$ = 2986 (m), 2361 (m), 1766 (m), 1611 (m), 1451 (m), 1421 (m), 1388 (m), 1358 (s), 1325 (m), 1269 (m), 1189 (m), 1143 (m), 1092 (s), 1052 (m), 1032 (m), 1005 (m), 979 (m), 955 (m), 848 cm^{-1} (m); HR-ESI-MS: *m/z* (%): 547.2904 (100, [*M* + H]$^+$, calcd. for $C_{30}H_{39}B_2O_8^+$: 547.2898).

3,6-Bis(3'-bromophenyl)phenanthrene-9,10-di(ethyleneglycol)ketal (19)

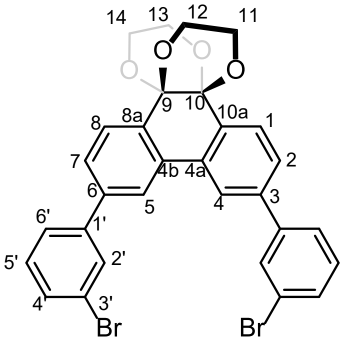

Borylated phenanthrene **19** (2.00 g, 3.65 mmol), 1,3-dibromobenzene (2.58 g, 10.95 mmol), Pd(dppf)Cl_2 (0.13 g, 0.18 mmol), and potassium carbonate (2.52 g, 18.2 mmol) were suspended in DMSO (40 mL) and the reaction mixture was degassed for 10 min under vigorous stirring *via* a constant nitrogen flow. The reaction mixture was stirred at 80 °C for 4 h and subsequently cooled down to 25 °C. The crude mixture was diluted with CH_2Cl_2 (40 mL) and washed successively with water (3 x 40 mL) and brine (40 mL). The organic layer was dried over $MgSO_4$ and filtered over a short pad of silica. Purification by preparative MPLC (SiO_2, gradient cyclohexane/CH_2Cl_2 3:1→0:100) and drying under vacuum gave **19** (1.26 g, 57%) as a colorless solid.

R_f = 0.43 (SiO_2; CH_2Cl_2); m.p. > 250 °C decomposition; ^{1}H NMR (400 MHz, $CDCl_3$, 25 °C): δ = 8.09 (d, *J* = 1.8 Hz, 2H, H–C(4,5)), 7.86 (d, *J* = 8.0 Hz, 2H, H–C(1,8)), 7.78 (t, *J* = 1.9 Hz, 2H, 2 H–C(2')), 7.61 (dd, *J* = 8.0, 1.7 Hz, 2H, H–C(2,7)), 7.59–7.55 (m, 2H, 2 H–C(6')), 7.55–7.51 (m, 2H, 2 H–C(4')), 7.36 (t, *J* = 7.9 Hz, 2H, 2 H–C(5')), 4.26 (br. 4H, H–C(11,12,13,14)), 3.72 ppm (br. 4H, H–C(11,12,13,14)); ^{13}C NMR (126 MHz, $CDCl_3$, 25 °C): δ = 143.1 (C(3')), 141.8 (C(9,10)), 133.4 (C(3,6)), 132.8 (C(10a,8a)), 130.9 (C(6')), 130.6 (C(2')), 130.5 (C(5')), 128.1 (C(2,7)), 127.2 (C(1,8)), 126.2 (C(4')), 123.1 (C(1')), 123.0 (C(4,5)), 61.5 ppm (C(11,12,13,14)), signals for C(4a,4b) are hidden by the noise; IR (ATR): $\tilde{\nu}_{\text{max}}$ = 2940 (m), 2877 (m), 1592 (m), 1556 (m), 1472 (m), 1386 (m), 1279 (m), 1210 (m), 1183 (m), 1091 (s), 980 (m), 953 (m), 887 (m), 832 (m), 783 (m), 728 (m), 698 cm^{-1} (m); HR-ESI-MS: *m/z* (%): 604.9976 (15, [*M* + H]$^+$, calcd. for $C_{30}H_{23}Br_2O_4^+$: 604.9958).

1,3(3,6)-Bis(phenanthrene-9,10-di(ethyleneglycol)ketal)-2,4(1,3)-dibenzenacyclotetraphane (11)

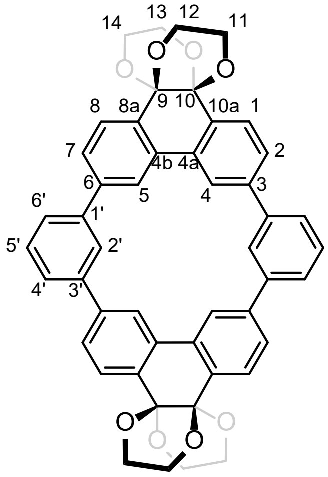

A solution of boronic ester **18** (0.90 g, 1.64 mmol) and dibromide **19** (1.00 g, 1.64 mmol) in 1,4-dioxane (1.1 L) was degassed for 5 min by bubbling a constant stream of N_2 through the reaction mixture. The mixture was treated with $Pd(OAc)_2$ (0.02 g, 0.08 mmol) and SPhos (0.07 g, 0.16 mmol), degassed for 5 min, diluted with aqueous 3 M K_3PO_4 (5.5 mL), degassed again for 5 min, and heated to 60 °C for 4 h. After cooling to 25 °C, the mixture was concentrated and dissolved in $CHCl_3$ (200 mL) and water (200 mL) was added subsequently. The phases were separated, and the aqueous phase was extracted with $CHCl_3$ (3 x 100 mL). The combined organic phases were washed with brine (100 mL), dried over $MgSO_4$, and filtered over a short pad of silica. The filtrate was concentrated under reduced pressure, dried under high vacuum, and the resulting brown mixture was purified by MPLC (cyclohexane/EtOAc, 2:1→0:100) to yield **11** (0.16 g, 13%) as a colorless solid.

Alternative one-pot procedure: In a three-neck 1 L-flask equipped with a mechanical overhead stirrer, a solution of 1,3-dibromobenzene (775 mg, 3.29 mmol) in dioxane (500 mL) was degassed using a stream of N_2 and the reaction mixture was kept under inert conditions with a constant stream of N_2 throughout the reaction time. Aqueous K_3PO_4 (2 M, 50 mL), $Pd(OAc)_2$ (28.5 mg, 136.8 μmol), and SPhos (112.3 mg, 273.6 μmol) were added to the reaction mixture and it was stirred for 5 min. Under vigorous stirring, boronic ester **18** (300 mg, 547 μmol) was added. The mixture was heated to 60 °C for 30 min and subsequently another portion of **18** (300 mg, 547 μmol) was added. The addition of **18** was repeated until no 1,3-dibromobenzene was detected in the reaction mixture (monitoring of aliquots via ^{1}H NMR spectroscopy). In total 1.5 g of **18** (2.74 mmol) were added. After a total reaction time of 4 h, the mixture was allowed to cool to 21 °C. The phases were separated, the aqueous phase was diluted with water (100 mL), and extracted with $CHCl_3$ (4 x 50 mL). The organic phases were combined, dried over $MgSO_4$, filtered, and evaporated to dryness. The obtained solid was purified by MPLC (cyclohexane/EtOAc, 2:1→0:100) and via *r*GPC to obtain analytically pure **11** (73 mg, 7%) as a colorless solid.

R_f = 0.65 (SiO_2; EtOAc/cyclohexane 2:1); m.p. > 360 °C; ^{1}H NMR (400 MHz, $CDCl_3$, 25 °C): δ = 8.69 (d, J = 1.8 Hz, 4H, H–C(4,5)), 8.34 (t, J = 1.9 Hz, 2H, H–C(2')), 7.89 (d, J =

7.9 Hz, 4H, H–C(1,8)), 7.84 (dd, J = 8.0, 1.6 Hz, 4H, H–C(2,7)), 7.76 (dd, J = 7.7, 1.8 Hz, 4H, H–C(4',6')), 7.59 (t, 2H, H–C(5')), 4.29 (br., 8H, H–C(11,12,13,14)), 3.78 ppm (br., 8H, H–C(11,12,13,14)); ^{13}C NMR (126 MHz, $CDCl_3$, 25 °C): δ = 142.0 (C(3)), 140.8 (C(1',3')), 133.3 (C(4a,4b)), 132.8 (C(8a,10a)), 129.8 C(5'), 127.2 C(1,8), 126.8 C(2,7), 126.3 C(2'), 125.9 C(4',6'), 123.2 C(4,5), 93.0 (C(9,10)), 61.7 ppm (C(11,12,13,14)); IR (ATR): $\tilde{\nu}_{\max}$ = 3822 (m), 3765 (m), 3733 (m), 3690 (m), 2935 (m), 2876 (m), 2381 (m), 2349 (m), 2325 (m), 2240 (m), 2200 (m), 2053 (m), 2031 (m), 1988 (m), 1724 (m), 1597 (m), 1560 (m), 1449 (m), 1374 (m), 1277 (m), 1246 (m), 1180 (m), 1087 (s), 1023 (m), 1001 (m), 978 (m), 953 (s), 886 (m), 834 cm^{-1} (m); HR-ESI-MS: m/z (%): 741.2472 (100, $[M + H]^+$, calcd. for $C_{48}H_{37}O_8^+$: 741.2483); a single-crystal X-ray structure was obtained for this compound (see below).

2^5,4^5-Bis(4,4,5,5-tetramethyl-1,3,2-dioxaborolan-2-yl)-1,3(3,6)-*bis*(phenanthrena-9,10-di(ethyleneglycol)ketal)-2,4(1,3)-dibenzenacyclotetraphane (20)

Using Ir-catalyzed C–H borylation of 11 (Routes A & B):

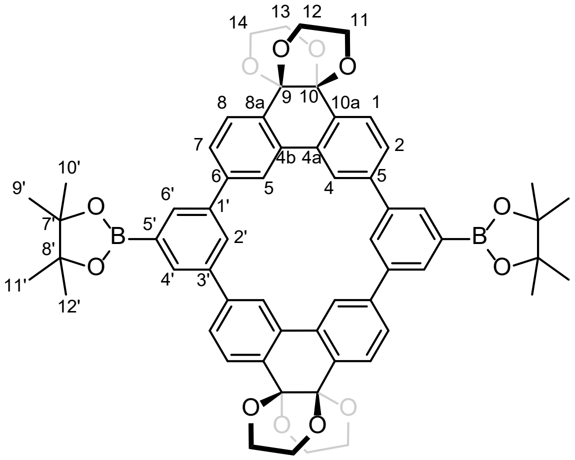

A suspension of **11** (102 mg, 55 µmol), 4,4'-di-*tert*-butyl-2,2'-bipyridine (15 mg, 55 µmol), $[Ir(OMe)COD]_2$ (18 mg, 28 µmol), and B_2pin_2 (280 mg, 1101 µmol) in dry 1,4-dioxane (2 mL) in an oven-dried 10 mL-pressure tube was degassed with three freeze–pump–thaw cycles upon which the mixture turned red. After heating the reaction mixture to 120 °C for 36 h in the sealed pressure tube, the solvent was evaporated azeotropically using toluene as co-solvent. The dark brown solid was suspended in MeOH (30 mL) and the insoluble beige solid was filtered off and washed several times with MeOH. Drying under high vacuum afforded **20** (100 mg, 73%) as a beige solid.

R_f = 0.64 (SiO_2; CH_2Cl_2/MeOH 96:4); m.p. > 314 °C decomposition; ^1H NMR (500 MHz, $CDCl_3$, 25 °C): δ = 8.67 (d, J = 1.8 Hz, 4H, H–C(4,5)), 8.47 (dd, J = 1.9 Hz, 2H, H–C(2')), 8.22 (d, J = 1.8 Hz, 4H, H–C(4',6')), 7.96 (dd, J = 8.0, 1.6 Hz, 4H, H–C(2,7)), 7.88 (dd, J = 7.7, 4H, H–C(1,8')), 4.29 (br., 8H, H–C(11,12,13,14)), 3.78 (br., 8H, H–C(11,12,13,14)), 1.41 ppm (s, 24H; H–C(9',10',11',12')); ^{13}C NMR (126 MHz, $CDCl_3$, 25 °C): δ = 141.8 (C(3,6)), 140.0 (C(1',3')), 133.3 (C(8a,10a)), 132.6 (C(4a,4b)), 132.2 (C(4',6')), 128.8 (C(2')), 127.1 (C(2,7)), 127.0 (C(1,8)), 123.1 (C(4,5)), 93.1 (C(9,10)), 84.3 (C(7',8')), 25.1 ppm (C(9’,10’,11’,12’)), signals for C(11,12,13,14) are hidden by the noise; IR (ATR): $\tilde{\nu}_{\mathrm{max}}$ = 2958 (m), 2931 (m), 2869 (m), 1596 (m), 1555 (m), 1509 (m), 1449 (s), 1374 (m), 1275 (m), 1186 (m), 1086 (s), 1025 (m), 977 (m), 955 (m), 891 (m), 823 (m), 764 cm^{-1} (m); HR-ESI-MS: *m/z* (%): 991.4268 (75, [*M* + H]$^+$, calcd. for $C_{60}H_{59}B_2O_{12}^+$: 991.4260); a single-crystal X-ray structure was obtained for this compound (see below).

1,3-Dibromo-5-trimethylsilylbenzene (35)[332]

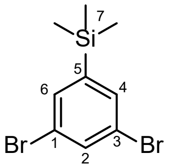

The synthesis of **35** followed the procedure reported by Tamborski and co-workers.[332] A suspension of 1,3,5-tribromobenzene (21.54 g, 68.42 mmol) in diethyl ether (500 mL) was treated dropwise with *n*-butyllithium (2.5 M in hexane, 30.1 mL, 75.27 mmol) over 30 min at −78 °C and the resulting mixture was stirred for 1 h at that temperature. The reaction mixture was treated with trimethylsilyl chloride (9.6 mL, 75.27 mmol) at −78 °C and stirred without further cooling overnight. The product mixture was diluted with CH_2Cl_2 (200 mL) and filtered over a pad of silica. The filtrate was concentrated to afford a brown oil (21.30 g, 96%, Lit.:[332] 84%), which was used without further purification. Analytically pure samples were obtained by Kugelrohr distillation (2 mbar, 112 °C) and preparative MPLC (SiO_2, neat cyclohexane). This compound has been reported previously and the characterization data agreed accordingly.[333]

R_f = 0.99 (SiO_2; cyclohexane); m.p. = 39–40 °C (Lit.:[333] 40–41 °C); ^{1}H NMR (500 MHz, $CDCl_3$, 25 °C): δ = 7.64 (t, *J* = 1.8 Hz, 1H, H–C(2)), 7.51 (d, *J* = 1.8 Hz, 2H, H–C(4,6)), 0.27 ppm (d, *J* = 1.8 Hz, 9H, H–C(7)); ^{13}C NMR (126 MHz, $CDCl_3$, 25 °C): δ = 146.2 (C(1,3)), 134.6 (C(2)), 134.3 (C(4,6)), 123.3 (C(5)), −1.2 ppm (C(7)); IR (ATR): $\tilde{\nu}_{\mathrm{max}}$ = 3059 (w), 2956(s), 2869 (m), 1596 (s), 1555 (w), 1508 (w), 1450 (w), 1375 (m), 1275 (m), 1246 (m), 1184 (w), 1086 (s), 1024 (m), 977 (m), 954 (m), 889 (w), 824 (s), 761 (w), 728 (w), 669 (w), 583 (w), 527 cm^{-1} (w).

3,6-Bis(3’-bromo-5’-trimethylsilylphenyl)phenanthrene-9,10-di(ethyleneglycol)ketal (23)

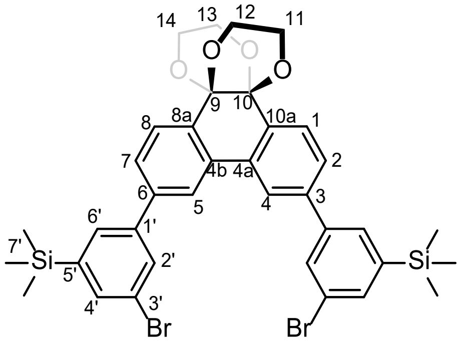

A suspension of borylated phenanthrene **18** (6.00 g, 10.90 mmol), 3,5-dibromo-1-trimethylsilylbenzene **35** (10.01 g, 32.8 mmol), Pd(dppf)Cl_2 (0.44 g, 0.55 mmol), and potassium carbonate (7.56 g, 54.70 mmol) in DMSO (300 mL) was degassed for 10 min under vigorous stirring *via* a constant nitrogen flow. The reaction mixture was stirred at 80 °C for 4 h and subsequently cooled down to 25 °C. The crude mixture was diluted with CH_2Cl_2 (300 mL) and washed successively with water (3 x 300 mL) and brine (300 mL). The organic layer was dried over $MgSO_4$ and filtered over a short plug of silica. Purification by preparative MPLC (SiO_2, gradient cyclohexane/CH_2Cl_2 3:1→0:100) and drying under vacuum gave **23** (4.51 g, 55%) as a yellowish solid.

R_f = 0.52 (SiO_2; CH_2Cl_2); m.p. = 248–250 °C; ^{1}H NMR (400 MHz, $CDCl_3$, 25 °C): δ = 8.08 (d, *J* = 1.8 Hz, 2H, H–C(4,5)), 7.86 (d, *J* = 8.0 Hz, 2H, H–C(1,8)), 7.74 (dd, *J* = 1.9 Hz, 2H, 2 H–C(2’)), 7.64 (m, *J* = 8.0, 1.7 Hz, 2H, H–C(4’,6’)), 7.60 (dd, 2H, H–C(2,7)), 4.26 (br, 4H, H–C(11,12,13,14)), 3.72 ppm (br, 4H, H–C(11,12,13,14)), *s*0.32 (s, 18H, H–C(7’); ^{13}C NMR (126 MHz, $CDCl_3$, 25 °C): δ = 144.5 (C(3’)), 142.6 (C1’)), 142.2 (C(3,6)), 135.4 (C(6’)), 133.4 (C(4a,4b)), 132.7 (C(8a,10a)), 130.8 (C(2’,4’), 128.2 C(2,7), 127.1 (C(1,8)), 123.5 (C(5’)), 123.1 (C(4,5)), 92.8 (C(9,10)), −1.2 ppm (C(7’)), signals for C(4a,4b) are hidden by the noise; IR (ATR): $\tilde{\nu}_{\max}$ = 2958 (m), 2870 (m), 2319 (m), 1596 (m), 1554 (m), 1508 (m), 1450 (m), 1374 (m), 1276 (m), 1246 (m), 1185 (m), 1087 (s), 1025 (m), 977 (m), 955 (m), 890 (m), 824 (s), 762 cm^{-1} (m); HR-ESI-MS: *m/z* (%): 749.0761 (100, [*M* + H]$^+$, calcd. for $C_{36}H_{39}Br_2O_4Si_2^+$: 749.0748).

2^5,4^5-*Bis*(trimethylsilyl)-1,3(3,6)-bis(phenanthrena-9,10-di(ethyleneglycol)ketal)-2,4(1,3)-dibenzenacyclotetraphane (24)

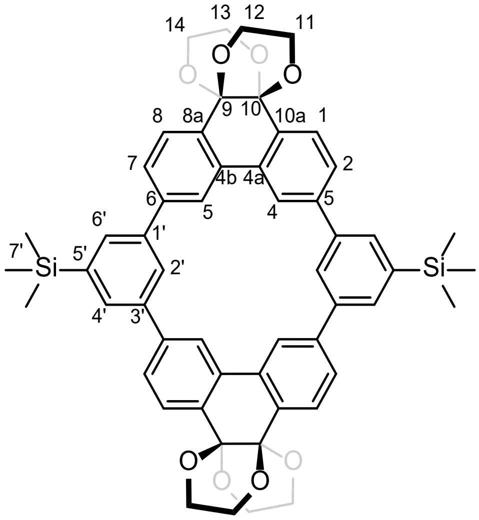

A solution of boronic ester **18** (2.81 g, 5.13 mmol) and dibromide **23** (3.50 g, 4.63 mmol) in 1,4-dioxane (2.2 L) was degassed for 45 min *via* a constant stream of N_2. The mixture was treated with Pd$(OAc)_2$ (0.21 g, 0.93 mmol) and SPhos (0.77 g, 1.86 mmol), degassed for 10 min, diluted with aqueous 2 M K_3PO_4 (220 mL), degassed again for 5 min, and heated to 60 °C for 2 h. After cooling down to 25 °C, the mixture was concentrated and dissolved in $CHCl_3$ (200 mL) and water (200 mL) was added subsequently. The phases were separated, and the aqueous phase was extracted with $CHCl_3$ (3 x 200 mL). The combined organic phases were washed with brine (200 mL), dried over $MgSO_4$, and filtered over a short pad of silica. The filtrate was concentrated under reduced pressure, dried under high vacuum, and the resulting brown mixture was purified by MPLC (SiO_2, cyclohexane/CH_2Cl_2, 2:1→0:100) to yield **24** (0.68 g, 23%) as a colorless solid.

R$_f$ = 0.28 (SiO_2; CH_2Cl_2); m.p. > 360 °C; ^{1}H NMR (400 MHz, $CDCl_3$, 25 °C): δ = 8.65 (d, *J* = 1.8 Hz, 4H, H–C(4,5)), 8.31 (t, *J* = 1.9 Hz, 2H, H–C(2’)), 7.91–7.85 (m, 12H, H–C(1,2,7,8,4’,6’)), 4.29 (br., 8H, H–C(11,12,13,14)), 3.78 (br., 8H, H–C(11,12,13,14)), 0.40 ppm (s, 18H, H–C(7’)); ^{13}C NMR (126 MHz, $CDCl_3$, 25 °C): δ = 142.5 (C(5’)), 142.3 (C(3)), 140.1 (C(1’,3’)), 133.3 (C(4a,4b)), 132.7 (C(8a,10a)), 130.8 (C(4’,6’)), 127.1 (C(1,8)), 127.0 C(2’), 126.7 (C(2,7)), 123.5 (C(4,5)), 93.04 (C(9,10)); 53.6 (C(11,12,13,14)), –0.8 ppm (C(7’)); IR (ATR): $\tilde{\nu}_{max}$ = 2959 (m), 2869 (m), 2322 (m), 1596 (m), 1556 (m), 1509 (m), 1450 (m), 1374 (m), 1275 (m), 1185 (m), 1086 (s), 1025 (m), 977 (m), 955 (m), 890 (m), 824 cm^{-1} (m); HR-ESI-MS: *m/z* (%): 885.3268 (40, [*M* + H]$^+$, calcd. for $C_{54}H_{53}O_8Si_2^+$: 885.3273); a single-crystal X-ray structure was obtained for this compound (see below).

2^5,4^5-Diiodo-1,3(3,6)-bis(phenanthrena-9,10-di(ethyleneglycol)ketal)-2,4(1,3)-dibenzenacyclotetraphane (25)

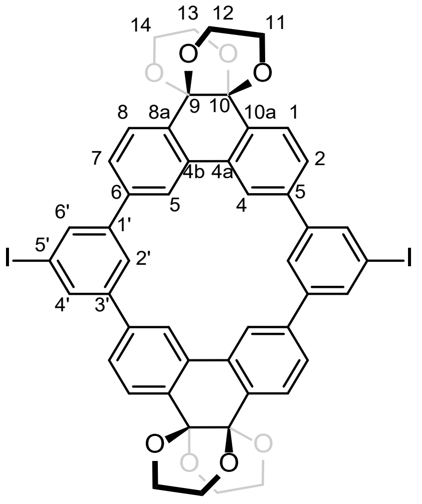

A solution of silylated macrocycle **24** (0.32 g, 0.36 mmol) in dichloromethane (15 mL) was treated with iodine monochloride (1.08 mL, 1.08 mmol, 1 M in dichloromethane) at 25 °C in the dark. The reaction mixture was stirred for 30 min and subsequently diluted with saturated aq. $Na_2S_2O_3$ (15 mL). The organic phase was separated and washed with water (3 x 15 mL), brine (15 mL), and dried over $MgSO_4$. The filtrate was concentrated under reduced pressure and dried under high vacuum to yield **25** (0.34 g, 95%) as a pale yellowish powder.

R$_f$ = 0.82 (SiO_2; CH_2Cl_2/MeOH 96:4); m.p. > 360 °C; ^{1}H NMR (400 MHz, DMF–*d*$_7$, 25 °C): δ = 9.33 (d, *J* = 1.8 Hz, 4H, H–C(4,5)), 9.19 (dd, *J* = 1.9 Hz, 2H, H–C(2’)), 8.34 (d, *J* = 7.9 Hz, 4H, H–C(4’,6’)), 8.09 (dd, *J* = 8.0, 1.6 Hz, 4H, H–C(2,7)), 7.84 (dd, *J* = 7.7 Hz, 4H, H–C(1,8)), 4.27 (br., 8H, H–C(11,12,13,14)), 3.72 ppm (br., 8H, H–C(11,12,13,14)); ^{13}C NMR (126 MHz, $CDCl_3$, 25 °C): δ = 143.2 (C(1’,3’), 140.6 (C(4a,4b)), 135.1 (C(3,6)), 134.7 (C(4’,6’)), 134.6 (C(8a,10a)), 128.0 (C(1,8)), 127.7 (C(2’)), 127.2 (C(2,7)), 125.6

(C(4,5)), 93.8 ppm (C(9,10)), signals for C(5',11,12,13,14) are hidden by the noise; IR (ATR): $\tilde{\nu}_{\max}$ = 2958 (m), 2931 (m), 2869 (m), 1596 (m), 1555 (m), 1509 (m), 1449 (m), 1374 (m), 1275 (m), 1186 (m), 1086 (s),1025 (m), 977 (m), 955 (m), 891 (m), 823 (m), 764 cm^{-1} (m); HR-ESI-MS: *m/z* (%): 993.0417 (15, [*M* + H]$^+$, calcd. for $C_{48}H_{45}I_2O_8^+$: 993.0411); a single-crystal X-ray structure was obtained for this compound (see below).

2^5,4^5-Bis(4,4,5,5-tetramethyl-1,3,2-dioxaborolan-2-yl)-1,3(3,6)-*bis*(phenanthrena-9,10-di(ethyleneglycol)ketal)-2,4(1,3)-dibenzenacyclotetraphane (20)

Using Pd-catalyzed Miyaura borylation from diiodide 25 (Route C):

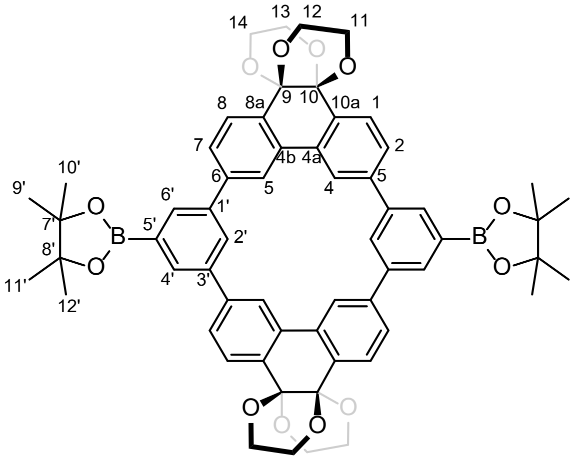

Oven-dried potassium acetate (0.12 g, 0.12 mmol) was added to a flame-dried round bottom flask. Both, the flask and potassium acetate, were flame-dried again. Iodinated macrocycle **25** (0.24 g, 0.24 mmol), Pd(dppf)Cl_2 (0.04 g, 0.05 mmol), and bis(pinacolato)diboron (0.24 g, 0.96 mmol) were added. The solids were dispersed in *N*,*N*-dimethylformamide (20 mL) and degassed for 15 min under vigorous stirring *via* a constant nitrogen flow. The solution was stirred for 1 h at 100 °C. After cooling the reaction mixture to 25 °C, water (30 mL) and CH_2Cl_2 (30 mL) were added. The organic layer was washed with water (3 x 20 mL) and brine (20 mL), and dried over $MgSO_4$. The solution was filtered over a short pad of silica and concentrated. Remaining traces of *N*,*N*-dimethylformamide were removed *via* azeotropic distillation with toluene as co-solvent. The product was sonicated for 10 min in methanol (20 mL), filtered, and dried under vacuum to afford **20** (0.22 g, 92%) as a brown solid.

The characterization data is equivalent to that obtained from the iridium catalyzed C–H borylation protocol of **20** (see above).

Fourfold Gold(I)–Aryl Macrocycle (26[4])

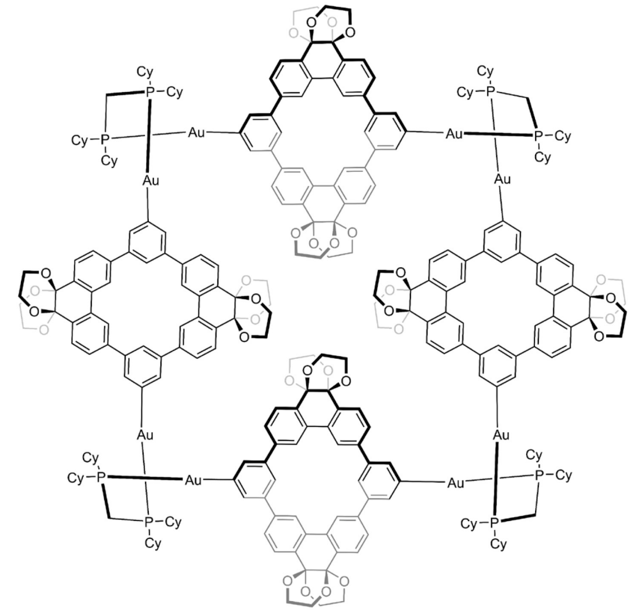

A 350 mL-pressure tube was filled with $Au_2(dcpm)Cl_2$ (367 mg, 420 µmol),[54] bis(boronic ester) **20** (417 mg, 420 µmol), Cs_2CO_3 (821 mg, 2521 µmol), and a mixture of toluene/EtOH/H_2O 4:1:1 (24 mL). The mixture was degassed using a stream of nitrogen and stirred at 50 °C for 20 h. After cooling to 21 °C, the reaction mixture was filtered, and the obtained solid of the filter cake was washed with toluene, EtOH, H_2O, and again EtOH. The solid was dissolved in $CHCl_3$ (200 mL) and washed with water (3x80 mL). The organic phase was dried over $MgSO_4$, and the solvent was evaporated. The crude solid was purified via recycling GPC to obtain **26[4]** (215 mg, 33%) as a beige solid.

^1H NMR (500 MHz, $C_2D_2Cl_4$, 25 °C): δ = 8.65–8.40 (br. 4H), 8.06–7.62 (br. m, 12H), 4.27–3.47 (br. m, 16H), 2.30 (br, 4H), 2.13 (br, 8H), 1.93 (br, 6H), 1.73 (br, 6H), 1.34 ppm (br. 12H); ^{31}P NMR (202 MHz, $C_2D_2Cl_4$, 25 °C): δ = 46.88 ppm. ^{13}C NMR (151 MHz, $C_2D_2Cl_4$, 25 °C): No sufficient signal to noise ratio was obtained due to limited solubility. All our efforts to obtain a significantly resolved mass signal using MALDI mass spectrometry failed. A single-crystal X-ray structure was obtained for this compound (see below).

[*n*]Cyclo-2^5,4^5-(platinum(cyclooctadiene)-1,3(3,6)-bis(phenanthrena-9,10-di(ethyleneglycol)ketal)-2,4(1,3)-dibenzenacyclotetraphanylene) (26-Pt[*n*])

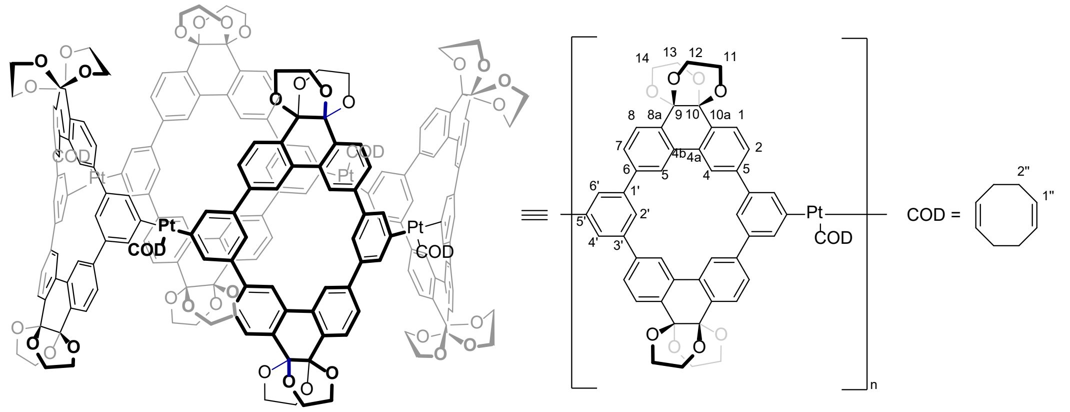

Bis(borylated) macrocycle **20** (0.10 mg, 0.10 mmol), Pt(COD)Cl_2 (0.38 mg, 0.10 mmol), and cesium fluoride (0.92 mg, 0.60 mmol) were suspended in THF (50 mL) and degassed for 15 min *via* a constant stream of N_2. After heating the reaction mixture in a sealed pressure tube to 66 °C for 24 h, the mixture was cooled down to 25 °C. The solvent was removed under reduced pressure to yield **13** (0.17 g) as an off-white powder. The platinated macrocycle **26-Pt[*n*]** was used without further purification, as is commonly reported. All our attempts to isolate or purify this intermediate **26-Pt[*n*]** led to significantly less satisfactory yields (or purity) in the following reductive elimination step.

R_f = 0.35 (SiO_2; CH_2Cl_2/MeOH 96:4); m.p. > 360 °C; ^{1}H NMR (500 MHz, $CDCl_3$, 25 °C): δ = 8.63 (m, 16H, H–C(4,5)), 7.81–7.50 (m, 8H, H–C(1,2,7,8,4',6')), 5.83 (m, 4H, H–C(1'')), 4.18 (br., 24H, H–C(11,12,13,14)), 3.70 (br., 24H, H–C(11,12,13,14)), 2.55 ppm (m, 8H, H–(C(2'')); IR (ATR): $\tilde{\nu}_{\max}$ = 2958 (m), 2870 (m), 2320 (m), 1596 (m), 1554 (m), 1508 (m), 1450 (m), 1374 (m), 1276 (m), 1246 (m), 1185 (m), 1087 (s), 1025 (m), 977 (m), 955 (m), 890 (m), 823 (m), 762 cm^{-1} (m).

[4]Cyclo-2^5,4^5-1,3(3,6)-bis(phenanthrena-9,10-di(ethyleneglycol)ketal)-2,4(1,3)-dibenzenacyclotetraphanylene (12[4])

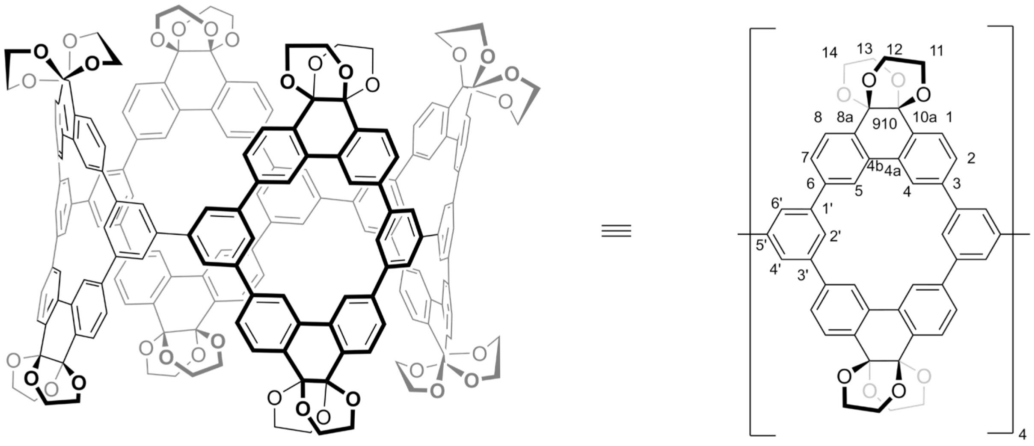

From four-fold Gold(I)–Aryl Macrocycle 26[4]: A solution of macrocycle **26[4]** (30 mg, 4.87 µmol) in dry CH_2Cl_2 (12 mL) was degassed using a stream of nitrogen and cooled to −45 °C using a bath of MeCN and dry ice. A degassed solution of iodobenzene dichloride (3.2 mL, 6.3 mmolar) in dry CH_2Cl_2 is added dropwise upon which the reaction mixture becomes bright yellow. After the addition, the reaction mixture is allowed to warm to 21 °C. The mixture turned colorless again and was heated to 40 °C in an oil bath for 30 min. Afterwards, the solvent is evaporated under reduced pressure and the remaining beige solid is purified by MPLC (SiO_2, first CH_2Cl_2/EtOAc 100:0→90:10 then CH_2Cl_2/MeOH 100:0→92:8). The obtained solid is purified using *r*GPC to yield **12[4]** (2.8 mg, 20%) as an off-white solid. The Au-complex can be isolated and recycled via column chromatography (CH_2Cl_2/EtOAc 9:1) as reported in the literature.[54]

R_f = 0.42 (SiO_2; CH_2Cl_2/MeOH 96:4); ^{1}H NMR (600 MHz, $CDCl_3$, 25 °C): δ = 8.34 (s 16H, H–C(4,5)), 7.95 (s, 8H, H–C(2')), 7.78 (d, J = 7.8 Hz, 16H, H–C(1,8)), 7.79 (d, J = 7.8 Hz, 16H, H–C(2,7)), 7.78 (s, 16H, H–C(4',6')), 4.25 (br., 24H, H–C(11,12,13,14)), 3.77 ppm (br., 24H, H–C(11,12,13,14)); ^{13}C NMR (151 MHz, $CDCl_3$, 25 °C): δ = 143.25 (either C(1', 3') or C(3, 6)), 143.21 (either C(C1', C3') or C(C3, C6)) 141.58 (C(5')), 132.76 (C(4a, 4b, 8a, 10a)), 127.02 (C(2')), 126.91 (C(1, 2, 7, 8)), 125.47 (C(4', 6')), 125.41 (C(4', 6'), 93.12 (C(9, 10)), 61.63 ppm (C(11, 12, 13, 14)). HR-MADLI-MS: *m/z*: 2975.36 ([M + Na]$^+$, calcd. for $C_{192}H_{136}O_{32}Na^+$: 2975.89), 2991.28 ([M + K]$^+$, calcd. for $C_{192}H_{136}O_{32}K^+$: 2991.87); a single-crystal X-ray structure was obtained for this compound (see below).

[*m*]Cyclo-2^5,4^5-1,3(3,6)-*bis*(phenanthrena-9,10-di(ethyleneglycol)ketal)-2,4(1,3)-dibenzenacyclotetraphanylene (with *m* = 4: 12[4] and *m* = 5: 12[5])

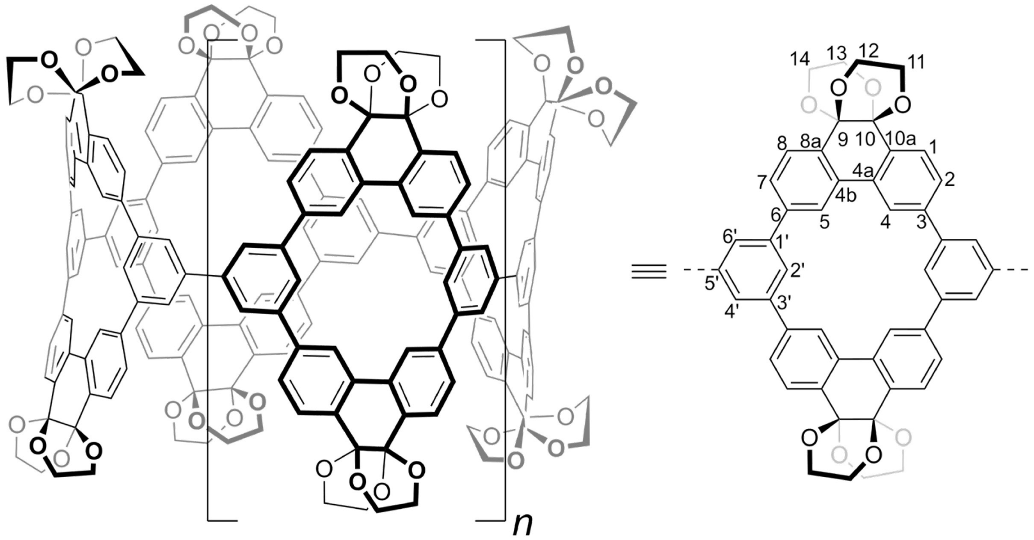

From 26[*n*]: Freshly prepared Pt-macrocycle **26-Pt[*n*]** (0.17 g) and triphenylphosphine (0.42 g, 1.6 mmol) were suspended in toluene (25 mL) and degassed for 15 min by bubbling a constant stream of N_2 through the reaction mixture. The suspension was heated to 100 °C for 22 h. The reaction mixture was cooled to 25 °C and the solvent was removed under reduced pressure. The residue was suspended in MeOH (50 mL) and filtered. Subsequently, the solid of the filter cake was dissolved in $CHCl_3$ and filtered. The filtrate was concentrated and subjected to recycling GPC ($CHCl_3$/EtOH, 96:4) to afford **12[4]** (0.8 mg, < 1% with regard to **20** over two steps) and **12[5]** (0.2 mg, < 1% with regard to **20** over two steps) as a colorless solid, each.

12[4]: The characterization data is equivalent to that obtained for **12[4]** from the macrocycle **26[4]**.

12[5]: R_f = 0.42 (SiO_2; CH_2Cl_2/MeOH 96:4); ^1H NMR (500 MHz, $CDCl_3$, 25 °C): δ = 8.47 (d, *J* = 1.8 Hz, 20H, H–C(4,5)), 8.06 (t, *J* = 1.9 Hz, 10H, H–C(2')), 7.89 (dd, *J* = 1.6 Hz, 20H, H–C(2',4')), 7.84 (dd, *J* = 8.0, 20H, H–C(1,8)), 7.81 (dd, *J* = 7.7, 1.8 Hz, 20H, H–C(2,7)), 4.21 (br., 24H, H–C(11,12,13,14)), 3.70 ppm (br., 24H, H–C(11,12,13,14)); HR-MADLI-MS: *m/z*: 3713.46 ([*M* + Na]$^+$, calcd. for $C_{240}H_{170}O_{40}Na^+$: 3714.12), 3729.39 ([*M* + K]$^+$, calcd. for $C_{240}H_{170}O_{40}K^+$: 3730.09).

A.2.3 Synthetic Procedures for Compounds Prepared within Chapter 3

1,4-Bis(triphenylmethylenephosphonium)benzene dibromide (36)[334]

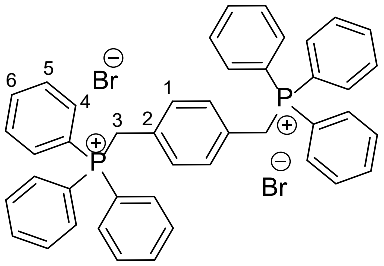

Based on a procedure reported in the literature,[334] 1,4-bis(bromomethyl)benzene (50 g, 189.4 mmol) and triphenylphosphine (105 g, 397.8 mmol) were dissolved in dry DMF (500 mL). The solution was degassed for 15 min using a stream of nitrogen and the reaction mixture was heated to 175 °C for 4 h. The mixture was cooled down to 23 °C, the precipitate was filtered over a Büchner funnel, washed thoroughly with an excess of diethyl ether, and dried under reduced pressure to afford **36** as a colorless powdery solid (141 g, 95%, Lit:[334] 97%).

m.p. > 360 °C (decomposition); ^{1}H NMR (500 MHz, $CDCl_3$, 25 °C, assignments based on ^{1}H,^{1}H-COSY and ^{1}H,^{13}C-HSQC NMR spectra): δ = 7.76–7.59 (m, 30H, H–C(4,5,6)), 6.90 (s, 4H, H–C(1)), 5.35 ppm (d, J = 13.2 Hz, 4H, $H_2C(3)$); ^{13}C NMR (126 MHz, $CDCl_3$, 25 °C) δ = 135.2, 134.5, 132.1, 130.4, 117.9, 117.2, 30.3 ppm; FTIR (ATR): $\tilde{\nu}_{max}$ = 3052 (w), 2879 (m), 2781 (m), 1662 (m), 1621 (m), 1588 (m), 1513 (m), 1484 (s), 1335 (m), 1110 (s), 762 (s), 741 (s), 718 (s), 685 (s), 525 cm^{-1} (s); HR-ESI-MS: m/z (%): 787.0896 (6), 789.0851 (100, $[M + H]^+$ calcd. for $C_{44}H_{39}{}^{79}Br_2P_2^+$, 787.0888), 791.0817 (44).

1,4-Bis(2-bromo-5-methylstyryl)benzene (37)[244]

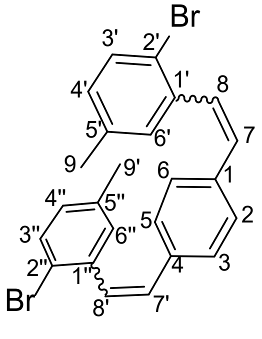

Based on a procedure reported in the literature,[244] 2-bromo-5-methylaldehyde (10 g, 50.2 mmol), **36** (20 g, 25.1 mmol), and 18-crown-6 (1.38 g, 5.02 mmol) were dissolved in dry CH_2Cl_2 (325 mL) and the solution cooled down to −78 °C. Freshly ground potassium hydroxide (7.6 g, 115.5 mmol) was added and the mixture degassed using a stream of nitrogen for 20 min. The reaction mixture was stirred for 1.5 h at −78 °C, allowed to warm up to 23 °C, and stirred for 16 h. The mixture was filtered over a glass-sintered Büchner funnel and the obtained yellow filtrate was washed with sat. aq. NH_4Cl (250 mL), water (250 mL), and brine (250 mL). The organic phase was dried over anhydrous $MgSO_4$, filtered, and the solvent removed under reduced pressure. The pale yellow oil was loaded onto silica and purified twice (serial) by preparative MPLC (120 g spherical SiO_2, prepacked from Teledyne ISCO; gradient cyclohexane:EtOAc 100:0→99:1) to afford **37** as a yellow oil (ca. 15:9:1 (*cis*,*cis*)/(*cis*,*trans*)/(*trans*,*trans*) isomers by ^{1}H NMR integral analysis, 10.8 g, 92%, Lit:[244] 90%). The (*cis*,*cis*)/(*cis*,*trans*)/(*trans*,*trans*) isomer ratio has no influence on the yields in the following synthetic step.

R_f = 0.39 (SiO_2; cyclohexane); ^{1}H NMR (500 MHz, CD_2Cl_2, 25 °C): δ = 7.59–7.38 (m) 7.18–6.92 (m), 6.68–6.54 (m), 2.36 (s, (*trans*,*trans*) isomer), 2.34 (s, (*cis*,*trans*) isomer), 2.17 (s, (*cis*,*trans*) isomer), 2.14 ppm (s, (*cis*,*cis*) isomer) (the sum of the integrals in the range of 7.59–6.54 ppm correspond to the number of aromatic (10) and olefinic (4) protons, as does the sum of the integrals in the range of 2.36–2.14 ppm corresponds to the number of protons of the methyl groups (6); ^{13}C NMR (126 MHz, CD_2Cl_2, 25 °C) δ = 138.4, 138.2 (d), 137.9, 137.7, 137.1, 136.8, 136.7, 136.1, 133.3, 133.0, 132.9, 131.8 (d), 131.3 (d), 131.2, 130.5, 130.3 (d), 130.1, 129.9, 129.3, 127.8 (d), 127.8, 127.1, 121.4, 121.3, 120.8, 120.7, 21.3 (d), 21.1 ppm (d), (the amount of signals results from the different isomers); FTIR (ATR): $\tilde{\nu}_{max}$ = 3076 (w), 3010 (w), 2361 (w), 1568 (m), 1508 (s), 1463 (s), 1136 (m), 1026 (s), 958 (m), 888 (s), 833 (s), 764 (s), 711 (s), 678 (s), 603 (s), 577 (s), 504 (s), 488 (s), 469 (s), 457 (s), 433 cm^{-1} (s).

(±)-7,14-Dibromo-10,11-dimethyldibenzo[*c*,*g*]phenanthrene ((±)-27)[244]

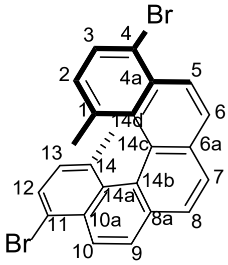

Adapted with changes from a published procedure,[244] the reaction was performed in a three-neck 6 L immersion well photoreactor with a quartz cooling tube, equipped with a 700 W mercury pressure lamp from Heraeus. For safety reasons, the setup was put in a metal bucket, wrapped with Al foil and the temperature was monitored inside the reaction mixture. A solution of **37** (ca. 15:9:1 (*cis*,*cis*)/(*cis*,*trans*)/(*trans*,*trans*) isomers, 1.01 g, 2.01 mmol), iodine (1.05 g, 4.13 mmol), and THF (24 mL, 289 mmol) in toluene (4.2 L) was purged with Argon for 45 min and irradiated for 12 h maintaining the temperature at 40 °C. The reaction mixture was concentrated to a final volume of 800 mL by evaporation and the remaining mixture was washed with aqueous $Na_2S_2O_3$ (10% w/w, 3 × 150 mL), water (2 × 200 mL), and brine (200 mL). The organic phase was dried over $MgSO_4$, filtered, concentrated, and the residue was purified using column chromatography (120 g spherical SiO_2, prepacked from Teledyne ISCO, cyclohexane) to yield a yellow solid. Crystallization from

CH_2Cl_2/toluene 20:1 (42 mL, 25 °C) by slow evaporation over 3 d gave (±)-**27** as yellow crystals (368 mg, 38%, Lit:[244] 73%).

R_f = 0.55 (SiO_2; cyclohexane); m.p. = 180–181 °C (Lit:[244] 177–179 °C); ^1H NMR (500 MHz, $CDCl_3$, 25 °C, assignments based on $^1H,^1H$-COSY, $^1H,^{13}C$-HSQC, and $^1H,^{13}C$-HMBC NMR spectra): δ = 8.40 (d, J = 8.7 Hz, 2H, H–C(5,10)), 8.08 (s, 2H, H–C(7,8)), 8.00 (d, J = 8.7 Hz, 2H, H–C(6,9)), 7.78 (d, J = 7.8 Hz, 2H, H–C(3,12)), 6.95 (d, J = 7.8 Hz, 2H, H–C(2,13)), 0.89 ppm (s, 6H, H_3C–C(1,14)); ^{13}C NMR (126 MHz, $CDCl_3$, 25 °C, assignments based on $^1H,^1H$-COSY, $^1H,^{13}C$-HSQC, and $^1H,^{13}C$-HMBC NMR spectra): δ = 134.7 (C(1,14)), 133.9 (C(14a,14d), 131.5 (C(6a,8a)), 131.4 (C(4a,10a)), 130.2 (C(3,12)), 129.3 (C(2,13)), 127.1 (C(6,9)), 127.0 (C(7,8)), 126.6 (C(5,10)), 126.2 (C(14b,14c)), 119.9 (C(4,11)), 22.4 ppm (CH_3); note: despite multiple attempts, we were unable to obtain a meaningful ATR-FTIR spectrum of recrystallized (±)-**27** in the solid state.

(±)-2,2'-(10,11-Dimethyldibenzo[*c*,*g*]phenanthrene-7,14-diyl)bis(4,4,5,5-tetramethyl-1,3,2-dioxaborolane) ((±)-28) and Enantiopure (+)-(*P*)-28 and (–)-(*M*)-28

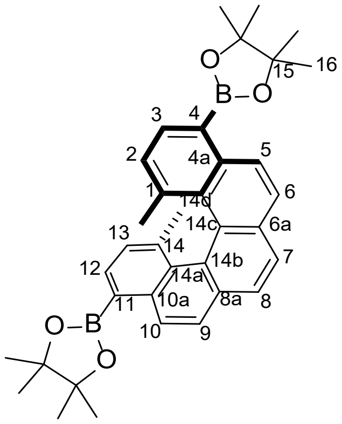

A solution of (±)-**27** (0.54 g, 1.15 mmol), bis(pinacolato)diboron (0.65 g, 2.56 mmol), and potassium acetate (0.56 g, 5.75 mmol) in dry 1,4-dioxane (40 mL) was degassed for 10 min under vigorous stirring via a constant flow of nitrogen. The solution was treated with $Pd(dppf)Cl_2 \cdot CH_2Cl_2$ (70.4 mg, 86.2 µmol) whereupon a yellow coloration was observed. The reaction mixture was stirred for 3.5 h at 80 °C, during which a change of color to dark brown was observed. After the reaction mixture has cooled down to 23 °C, CH_2Cl_2 (40 mL) was added and the solution was washed with water (60 mL). The aqueous phase was extracted with CH_2Cl_2 (2 x 50 mL). The combined organic layers were dried over anhydrous $MgSO_4$, filtered, and the solvents were removed under reduced pressure. The obtained brown solid was dissolved in a small amount of CH_2Cl_2 and filtered over a short pad of silica. Purification of the crude product (0.69 g) via preparative MPLC (40 g SiO_2, prepacked from Macherey-Nagel; CH_2Cl_2:cyclohexane 85:15→100:0) and drying under vacuum gave (±)-**2** (0.47 g, 74%) as a pale yellow solid. Preparative HPLC using a Regis Whelk-O1 (*S*,*S*) solid phase and *n*-hexane/$CHCl_3$ as a mobile phase (see Section S4) gave enantiopure (+)-(*P*)-**28** (retention time t_R = 11 min) and (–)-(*M*)-**28** (t_R = 12.5 min) as glassy yellow solids (70% recovery).

(±)-**28**: R_f = 0.34 (SiO_2; cyclohexane/CH_2Cl_2 1:1); m.p. > 290 °C decomposition; ^1H NMR (500 MHz, $CDCl_3$, 25 °C, assignments based on $^1H,^1H$-COSY, $^1H,^{13}C$-HSQC, and $^1H,^{13}C$-HMBC NMR spectra): δ = 8.87 (d, *J* = 8.7 Hz, 2H, H–C(5,10)), 8.05 (d, *J* = 7.1 Hz, 2H, H–C(3,12)), 8.02 (s, 2H, H–C(7,8)), 7.93 (d, *J* = 8.7 Hz, 2H, H–C(6,9)), 7.05 (d, *J* = 7.2 Hz, 2H, H–C(2,13)), 1.49 (s, 24H, $H_3C(16)$), 0.90 ppm (s, 6H, H_3C–C(1,14)); ^{13}C NMR (126 MHz, $CDCl_3$, 25 °C, assignments based on $^1H,^1H$-COSY, $^1H,^{13}C$-HSQC, and $^1H,^{13}C$-HMBC NMR spectra) δ = 138.6 (C(1,14)), 137.1 (C(14b,14c)), 135.0 (C(3,12)), 132.1 (C(14a,14d)), 130.6 (C(6a,8a)), 127.7 (C(2,13)), 127.5 (C(5,10)), 126.5 (C(4a,10a)), 126.0 (C(7,8)), 125.8 (C(6,9)), 115.1 (hidden by the noise, but visible as 2D-cross signal in $^1H,^{13}C$-HSQC NMR spectrum, C(4,11)), 83.8 (C(15)), 25.1 (C(16), two out of four), 24.9 (C(16), two out of four), 22.9 ppm (CH_3); FTIR (ATR): $\tilde{\nu}_{max}$ = 2978 (m), 1566 (m), 1476 (m), 1457 (m), 1354 (s), 1300 (s), 1272 (s), 1196 (s), 1125 (s), 1093 (s), 993 (m), 808 (s), 799 (s), 773 (s), 736 cm^{-1} (s); HR-ESI-MS: *m*/*z*: 559.3120 ($[M + H]^+$ calcd. for $C_{36}H_{41}B_2O_2^+$: 559.3185).

(*P*)-**28**: $[\alpha]_D^{25}$ = +450 ± 10 (*c* = 0.110 in CH_2Cl_2); Unambiguous structural proof is provided by single-crystal X-ray diffraction of (*P*)-**28** after chiral HPLC separation.

(*M*)-**28**: $[\alpha]_D^{25}$ = –450 ± 10 (*c* = 0.113 in CH_2Cl_2).

(±)-7a,7b-Dimethyl-7a,7b-dihydrobenzo[*ghi*]perylene-5,10-dione ((±)-31-C) and Enantiopure ((+)-(*S,S*)--C) and ((–)-(*R,R*)-1a-C)

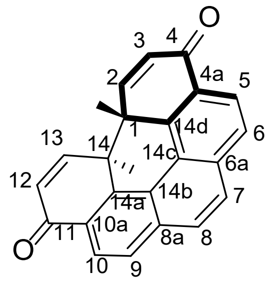

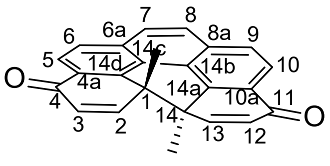

A solution of (±)-**28** (100 mg, 179.1 µmol) in THF (100 mL) was treated with aq. H_2O_2 (30% in H_2O, 0.45 mL, 4.47 mmol) and stirred for 6 h at room 23 °C. The reaction mixture was washed with aq. sat. $Na_2S_2O_3$ (75 mL), water (75 mL), and brine (75 mL). The organic phase was dried over anhydrous $MgSO_4$, filtered, and the solvents were removed under reduced pressure. The yellow crude product was purified via preparative MPLC (40 g SiO_2, prepacked from Macherey-Nagel; cyclohexane/ethyl acetate 100:0→0:100) to obtain (±)-**31-C** (47 mg, 78%) as pale-yellow powder.

(*R,R*)-configurated enantiomer ((–)-(*R,R*)-**31-C**) (7 mg, 63%) and (*S,S*)-configurated enantiomer ((+)-(*S,S*)-**31-C**) (8 mg, 70%) were obtained from (–)-(*M*)-**28** (20 mg, 35.8 µmol) and (+)-(*P*)-**28** (20 mg, 35.8 µmol) under identical conditions.

R_f = 0.26 (SiO_2; cyclohexane/ethyl acetate 1:1); m.p. 272–273 °C; ^1H NMR (500 MHz, $CDCl_3$, 25 °C, assignments based on $^1H,^1H$-COSY, $^1H,^{13}C$-HSQC, and $^1H,^{13}C$-HMBC NMR spectra): δ = 8.45 (d, J = 8.4 Hz, 2H, H–C(5,10)), 8.02 (s, 2H, H–C(7,8)), 8.01 (d, J = 8.5 Hz, 2H, H–C(6,9)), 7.72 (d, J = 10.3 Hz, 2H, H–C(2,13)), 6.81 (d, J = 10.3 Hz, 2H, H–C(3,12)), 1.20 ppm (s, 6H, H_3C–C(1,14)); ^{13}C NMR (126 MHz, $CDCl_3$, 25 °C, assignments based on $^1H,^1H$-COSY, $^1H,^{13}C$-HSQC, and $^1H,^{13}C$-HMBC NMR spectra) δ = 183.8 (C(4,11)), 149.6 (C(2,13)), 144.2 (C(14a,14d)), 133.6 (C(6a,8a)), 130.6 (C(3,12)), 129.8 (C(4a,10a)), 129.6 (C(7,8)), 127.4 (C(6,9)), 125.0 (C(5,10)), 124.7 (C(14b,14c)), 45.1 (C(1,14)), 26.8 ppm (CH_3); FTIR (ATR): $\tilde{\nu}_{max}$ = 2961 (w), 2917 (w), 2850 (w), 1654 (s), 1600 (s), 1498 (w), 1403 (w), 1325 (s), 1124 (m), 865 (m), 834 (s), 791 (s), 758 (m), 587 (w), 421 cm^{-1} (m); HR-ESI-MS: m/z: 337.1220 ($[M + H]^+$ calcd. for $C_{24}H_{17}O_2^+$: 337.1223). Unambiguous structural prove is provided by single-crystal X-ray diffraction.

(S,S)-**31-C**: $[\alpha]_D^{25}$ = +298 ± 10 (c = 0.097 in CH_2Cl_2);

(R,R)-**31-C**: $[\alpha]_D^{25}$ = –298 ± 10 (c = 0.101 in CH_2Cl_2).

(±)-2,2'-(7a,7b-dimethyl-7a,7b-dihydrobenzo[*ghi*]perylene-5,10-diylidene) dimalononitrile ((±)-34-C)

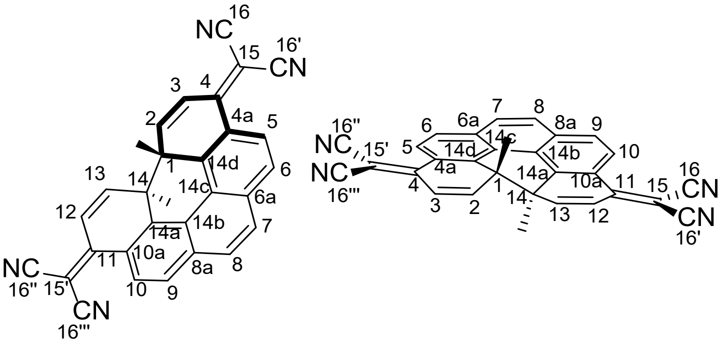

A solution of malononitrile (85 mg, 1.3 mmol) in dry THF (25 mL) slowly treated in portions with NaH (60% dispersion in mineral oil, 90 mg, 2.3 mmol) at 0 °C and stirred for 0.5 h. The reaction mixture was warmed to 23 °C and (±)-**27** (100 mg, 215.4 µmol), tetrakis(triphenylphosphine)-palladium(0) (25 mg, 21.5 µmol), and bis(triphenylphosphine)palladium(II)-dichloride (15 mg, 21.5 µmol) were added. The yellow suspension was degassed for 10 min with a constant flow of N_2 and stirred for 16 hours at 80 °C. The reaction mixture was quenched by slow addition of aqueous HCl (2 M), diluted with CH_2Cl_2 (50 mL), and washed with water (50 mL) and brine (50 mL). The organic phase was dried over anhydrous $MgSO_4$, filtered, and the solvents were removed under reduced pressure. The residue was dissolved in CH_2Cl_2 (100 mL), filtered over a short pad of silica, and evaporated. The yellow intermediate ((±)-**34-O-H$_2$**; see Main Text; Scheme 1) was dissolved in $CHCl_3$ (20 mL) and oxidized by addition of NEt_3 (0.1 mL) on air and evaporation of the volatiles. The obtained yellow-orange crude solid was purified via preparative MPLC (40 g SiO_2, prepacked from Macherey-Nagel; CH_2Cl_2/ethyl acetate 100:0→80:20) and r-GPC to afford (±)-**34-C** (28 mg, 30%) as yellow solid.

R_f = 0.52 (SiO_2; cyclohexane/ethyl acetate 3:2); m.p. > 320 °C decomposition; ^1H NMR (500 MHz, CD_2Cl_2, 25 °C, assignments based on ^1H,^1H-COSY, ^1H,^{13}C-HSQC, and ^1H,^{13}C-HMBC NMR spectra): δ = 8.94 (d, J = 8.7 Hz, 2H, H–C(5,10)), 8.10 (d, J = 8.7 Hz, 2H, H–C(6,9)), 8.08 (s, 2H, H–C(7,8)), 7.48 (s, 4H, H–C(2,3,9,10), 1.09 ppm (s, 6H, H_3C–C(1,14)), note: two doublets are expected for the signal at 7.48 ppm, similar to (±)-**27**, (±)-**28**, and (±)-**31-C**. In CD_2Cl_2, however, only one singlet occurs; ^{13}C NMR (126 MHz, CD_2Cl_2, 25 °C, assignments based on ^1H,^1H-COSY, ^1H,^{13}C-HSQC, and ^1H,^{13}C-HMBC NMR spectra) δ = 156.2 (C(4,10)), 146.1 (C(2,13)), 142.5 (C(14a,14d)), 134.3 (C(6a,8a)), 130.6 (C(7,8)), 128.3 (C(6,9)), 126.8 (C(3,12)), 126.2 (C(4a,10a)), 125.8 (C(5,10)), 125.3 (C(14b,14c)), 115.7 (CN), 78.1 C(15,15’), 47.1 C(1,14), 27.2 ppm (CH_3); FTIR (ATR): $\tilde{\nu}_{max}$ = 2917 (m), 2848 (m), 2208 (s), 1635 (s), 1508 (s), 1491 (s), 1450 (s), 1434 (s), 1343 (s), 1202 (s), 1070 (m), 850 (s), 774 (s), 460 cm^{-1} (m); HR-ESI-MS: m/z: 433.1459 ($[M + H]^-$ calcd. for $C_{30}H_{17}N_4^-$ 433.1458). Unambiguous structural proof is provided by single crystal X-ray diffraction.

A.3. Methods for Supramolecular Complexation Experiments

A.3.1 Isothermal UV/vis Titration Experiments

Titrations were performed to determine the association constant (K_a) of the complexation between **4[5–6]** (referred to as the host) and different crown ethers with respective ions (referred to as the guest). Titrations were performed at 298 K. Stock solutions containing crown ether and corresponding salts were always prepared according to the following procedure. Crown ether was dissolved in $CHCl_3$. The corresponding salts were added in a slight excess and the solution was sonicated. Afterwards the solution was filtered. This procedure allows the assumption that only insignificant amounts of free crown ether should be present. Whenever crown ether and salts were added as pure substances, ionic salts were always added in a slight excess.

Preparation of Solutions. A solution of host (**4[5]**) (~ 4 mM) in an appropriate solvent (typically $CHCl_3$) was prepared first. This solution was then used as parent solution to prepare a second solution as a mixture of host and guest ([G] at least 10-fold of the host concentration). The constant component during the titration is referred to as "host" and the varied component as "guest" throughout.

Association Constant Determination. A solution of a known concentrations of guest $[G]_0$ (excess) with $[H]_0$ was added successively to the parent solution of $[H]_0$ until saturation of the change in UV/vis absorption ΔA at a selected wavelength was observed. The association constants were determined by non-linear curve fitting (using Igor Pro v. 8.04 software or Origin 2019b) of the titration curves according to the Benesi–Hildebrand method.[209] The fitting curves were obtained by plotting the absorbance changes at a selected wavelength (ΔA) for UV/vis titrations.[209] The data was fitted to the equation (Eq. 2.1, *Chapter 2*).[210]

$$\Delta A = \frac{\varepsilon_{host\cdot guest}}{2} \cdot \left[\left([\mathrm{host}]_{Tot} \cdot [\mathrm{guest}] + \frac{1}{K_\mathrm{a}} \right) - \sqrt{\left([\mathrm{host}]_{Tot} + [\mathrm{guest}] + \frac{1}{K_\mathrm{a}} \right)^2 - (4 \cdot [\mathrm{host}]_{Tot} \cdot [\mathrm{guest}])} \right] \qquad \text{(Eq 2.1)}$$

, where the unknown parameters are: $\varepsilon_{\mathrm{host\cdot guest}}$ as the extinction coefficient of the complex and K_a as the association constant. An error of 20% was estimated for these values.

A.3.2 . Supplementary Binding Studies Based on UV/vis

4[4]: In the following graphs of this section, **4[4]** is referred to as host.

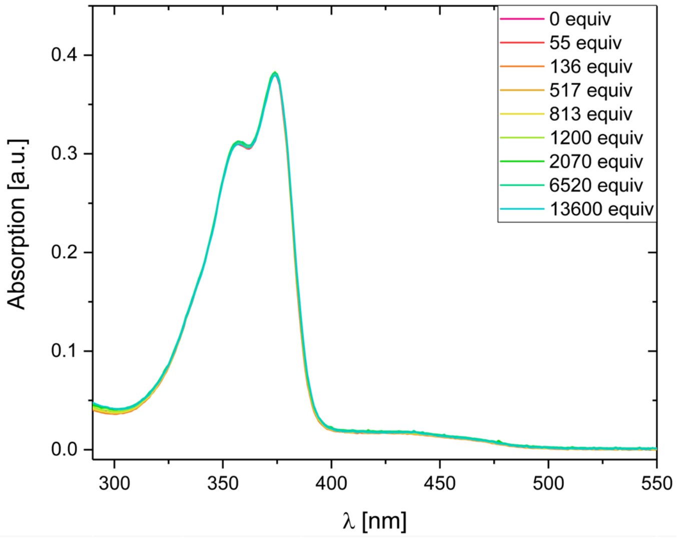

Figure A. 1. Isothermal UV/vis absorption binding titration. Spectra of **4[4]** at 25 °C, in $CHCl_3$, (c(**4[4]**) = $4.3 \cdot 10^{-6}$ mol L^{-1}) upon subsequent addition of a 12-crown-4 and LiCl stock-solution in $CHCl_3$.

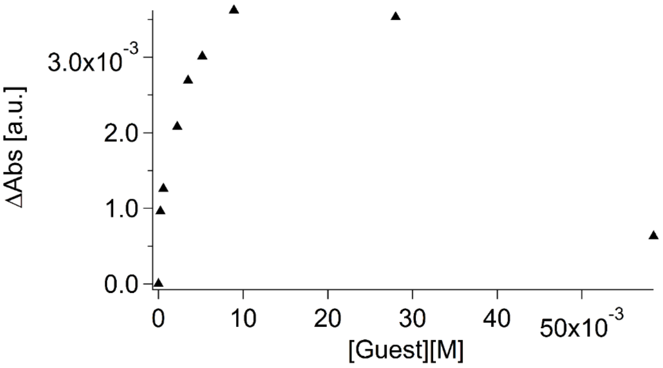

Figure A. 2. The difference in absorption at 375 nm plotted against the concentration of added 12-crown-4·LiCl. Non-linear least-square curve fitting is not possible with this data obtained from UV/vis spectroscopic isothermal binding titration (c(**4[4]**) = $4.3 \cdot 10^{-6}$ mol L^{-1}, in $CHCl_3$ at 298 K).

4[6]: In the following graphs of this section, **4[6]** is referred to as host.

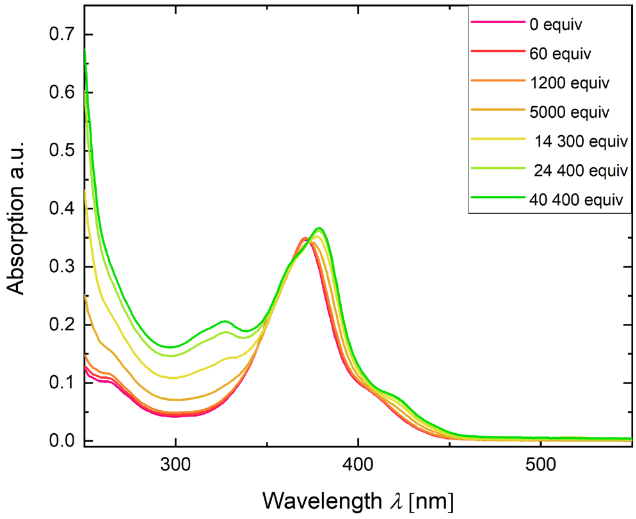

Figure A. 3. Isothermal UV/vis absorption binding titration. Spectra of **4[6]** at 25 °C, in $CHCl_3$, (c(**4[6]**) = $3.7 \cdot 10^{-6}$ mol L^{-1}) upon subsequent addition of a 15-crown-5·$NaBF_4$ stock solution in $CHCl_3$.

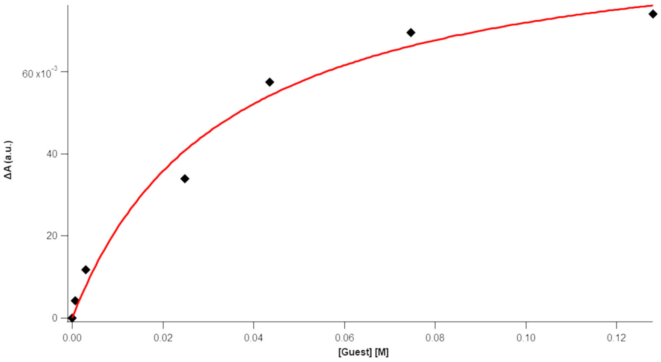

Figure A. 4. Non-linear least-square curve fitting analysis obtained from UV/vis spectroscopic isothermal binding titration (c(**4[6]**) = $3.7 \cdot 10^{-6}$ mol L^{-1}, in $CHCl_3$ at 298 K) upon addition of a 15-crown-5·$NaBF_4$ stock solution in $CHCl_3$. ΔA taken at 380 nm. The association constant K_a was determined to be: K_a = 28 M^{-1}.

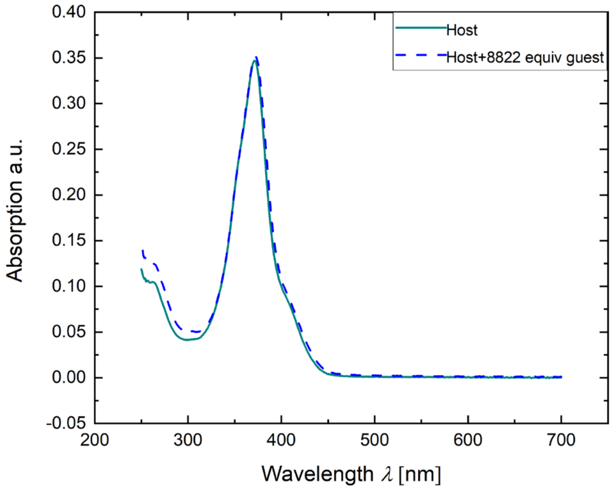

Figure A. 5. UV/vis absorption spectra of **4[6]** at 25 °C, in $CHCl_3$, (c(4[6]) = $3.7\cdot10^{-6}$ M) upon addition of 8822 equiv 18-crown-6·KBF_4 via stock solution in $CHCl_3$.

A.3.3 Isothermal NMR Titration Experiments

Titrations were performed at 298 K to determine the association constant (K_a) of the complexation between different host and guest molecules.

Preparation of Solutions. A solution of host (e.g. **12[4]**) (~ 0.2–0.5 mM) in an appropriate solvent (e. g. $CDCl_3$, *o*–dichlorobenzene-d_4) was prepared first. This solution was then used as parent solution to prepare a second solution as a mixture of host and guest. The constant component during the titration is referred to as "host" and the varied component as "guest" throughout.

Association Constant Determination. A solution of a known concentrations of guest $[G]_0$ (excess) with $[H]_0$ was added successively to the parent solution of $[H]_0$. To achieve higher addition of guest. Solid guest was added for the last additions if stated. The association constants were determined by non-linear curve fitting (using Origin 2019b) of the titration curves according to the Benesi–Hildebrand method.[209] The fitting curves were obtained by plotting the change of chemical shift of the host signals against the concentration of the guest.[209] The data was fitted to the following equation:[210]

$$\Delta\delta = \delta_{\Delta(\mathrm{HG})} \frac{\frac{1}{2}\cdot\left[\left([\mathrm{host}]_{Tot}\cdot[\mathrm{guest}]+\frac{1}{K_\mathrm{a}}\right)-\sqrt{\left([\mathrm{host}]_{Tot}+[\mathrm{guest}]+\frac{1}{K_\mathrm{a}}\right)^2-(4\cdot[\mathrm{host}]_{Tot}\cdot[\mathrm{guest}])}\right]}{[\mathrm{host}]_{Tot}} \qquad \text{Eq. 2.1}$$

, where the unknown parameters are: $\delta_{\Delta(\mathrm{HG})}$ as the chemical shift of the host–guest complex and K_a as the association constant. An error of 20% is estimated for these values.

A.3.4 Supplementary Binding Studies Based on NMR

^{1}H NMR of 4[5] and C_{60}

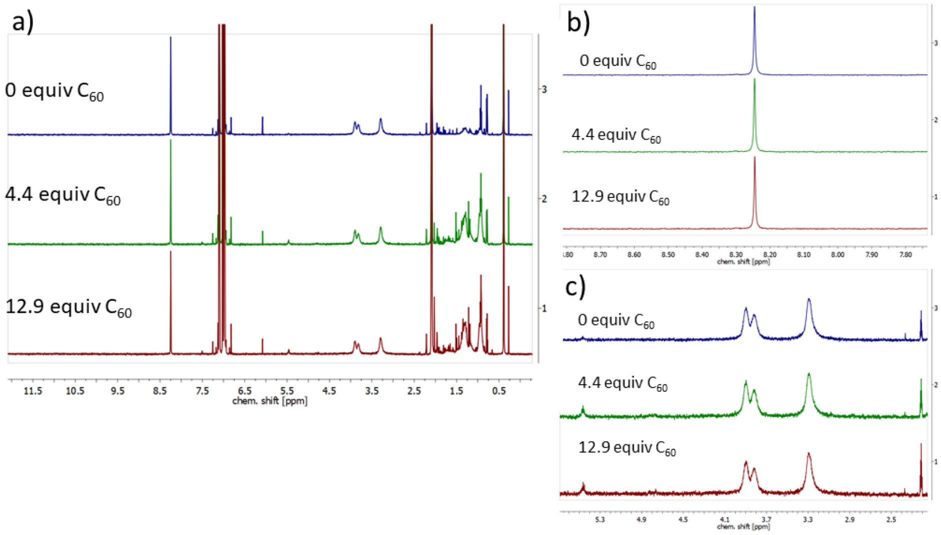

Figure A. 6. ^{1}H NMR spectra of **4[5]** (500 MHz, 25 °C) in toluene-d_8 a) full spectrum, b) aromatic region, and c) showing the region of the ethylene glycol groups; upon addition of 0 equiv C_{60} c(**4[5]**) = 4.77·10^{-4} M (blue spectrum); 4.4 equiv C_{60} c(**4[5]**) = 2.78·10^{-4} M (green spectrum); 12.9 equiv C_{60} c(**4[5]**) = 2.78·10^{-4} M (red spectrum).

^{1}H NMR of 4[6] and C_{60}

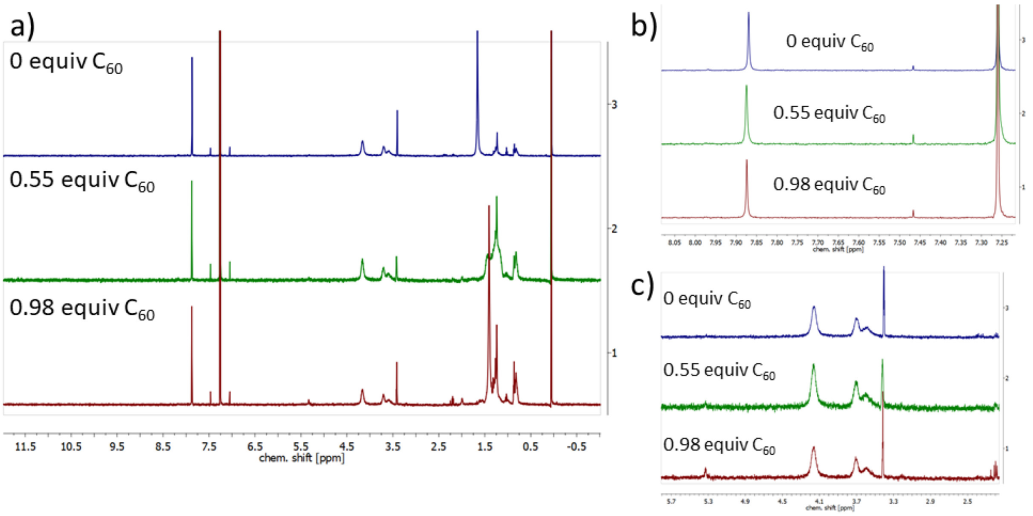

Figure A. 7. ^{1}H NMR spectra of **4[6]** (500 MHz, 25 °C, in $CDCl_3$) a) full spectrum, b) aromatic region, and c) showing the region of the ethylene glycol groups; upon addition of 0 equiv C_{60}, c(**4[6]**) = 2.11·10^{-4} M (blue spectra); 0.55 equiv C_{60}, c(**4[6]**) = 1.58·10^{-4} M (green spectra); 0.98 equiv C_{60}, c(**4[6]**) = 1.76·10^{-4} M (red spectra).

^{1}H NMR of **12[4]** Rigid Planar Aromatic Guests

In the following the titration data and the curve fitting for **12[4]** and rigid planar aromatic guests such as pyrene, perylene, and coronene is shown as an addition to the shown data in *Chapter 3*.

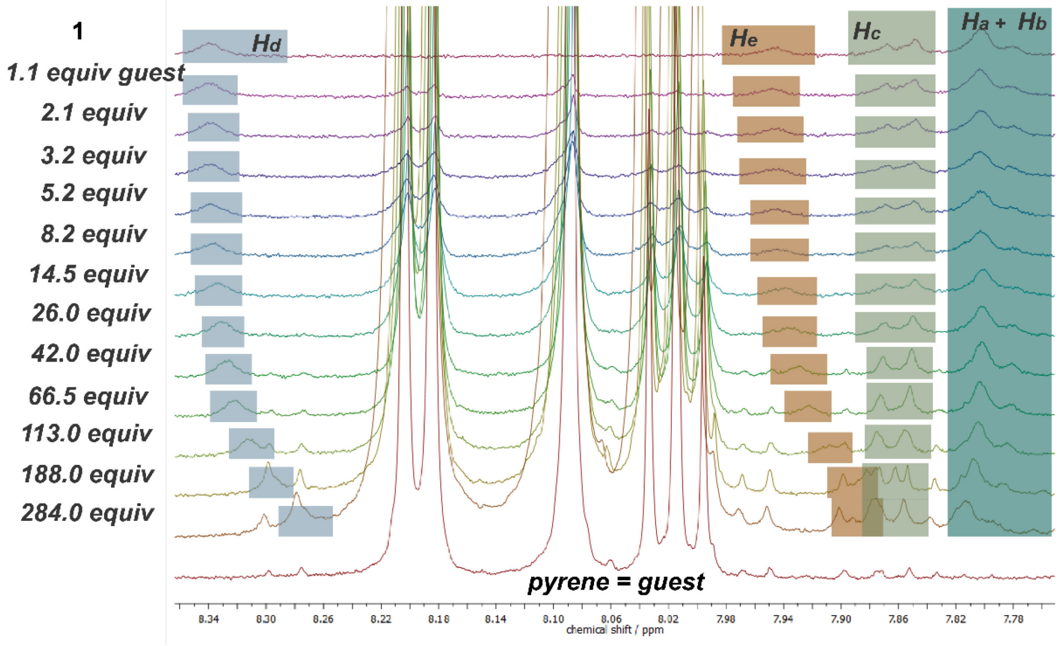

Figure A. 8. Isothermal NMR binding titration, zoom into the chemical shift region where the host protons change. ^{1}H NMR spectra of **12[4]** at 25 °C, in $CDCl_3$, (c(**12[4]**) = $2.71 \cdot 10^{-4}$ mol L^{-1}) upon subsequent addition of a pyrene as a stock-solution and as solid (last addition).

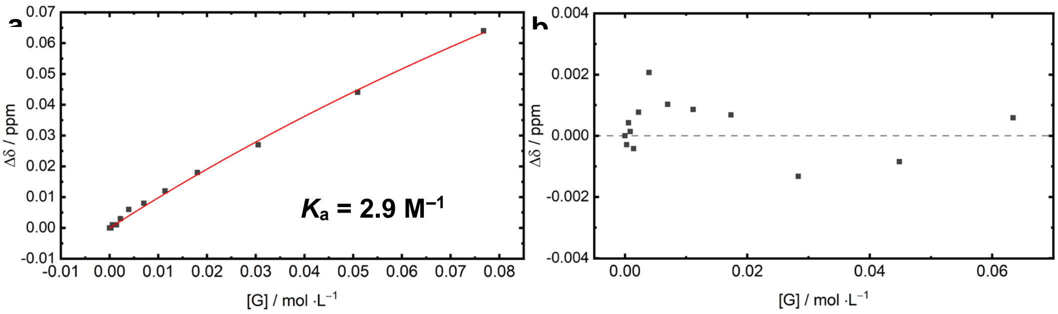

Figure A. 9. a) Non-linear least-square curve fitting analysis obtained from the isothermal binding titration (c(**12[4]**) = $2.71 \cdot 10^{-4}$ mol L^{-1}, in $CDCl_3$ at 298 K) upon addition of pyrene. $\Delta\delta$ taken for proton H_d. The association constant K_a was determined to be: $K_a = 2.9$ M^{-1} with an R^2 of 0.9972. b) Residual difference plot of the predicted values of the fit vs experimental values. Data acquired by isothermal binding titration with 1:1 stoichiometry.

As the cavity of macrocycle **12[4]** is large enough to bind at least two pyrene molecules we tried to fit the data against a 1:2 binding model using the program bindfit[233] for which we obtained no conclusive association constants. Regarding the size of the cavity larger perylene can potentially bind with more CH-π interactions and was therefore studied as well using isothermal NMR binding titration (Figure A. 10).

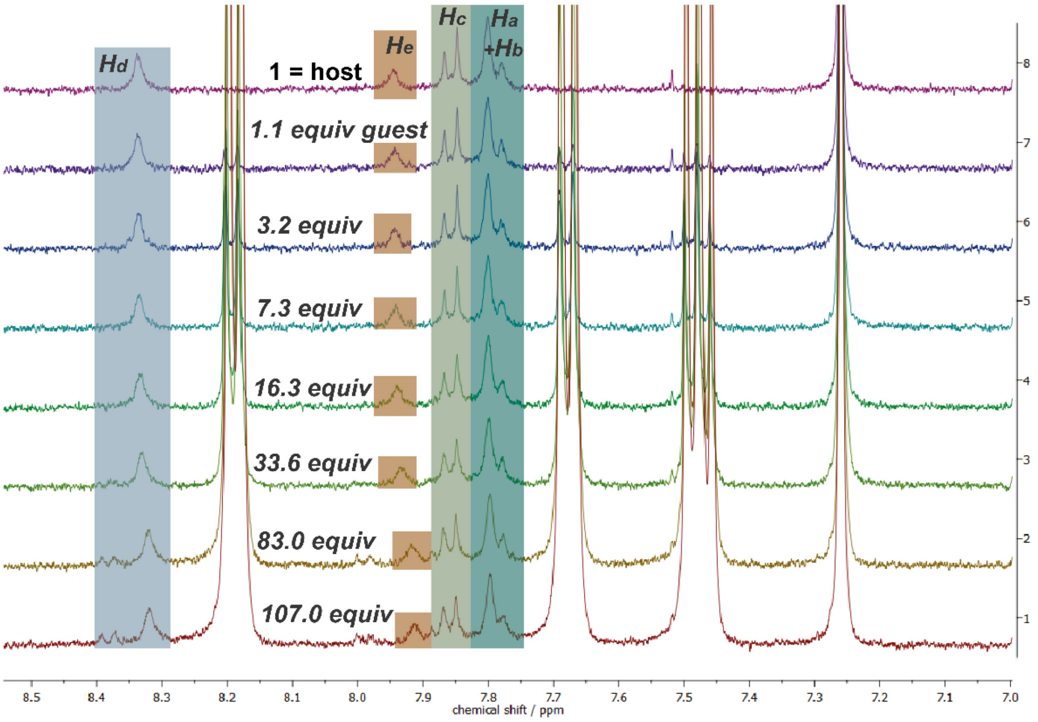

Figure A. 10. Isothermal NMR binding titration zoom into the chemical shift region where the host protons change. ^{1}H NMR spectra of 1 at 25 °C, in CDCl$_3$, (c(**12[4]**) = 2.71·10^{-4} mol L^{-1}) upon subsequent addition of a perylene as a stock-solution and as solid (last two additions).

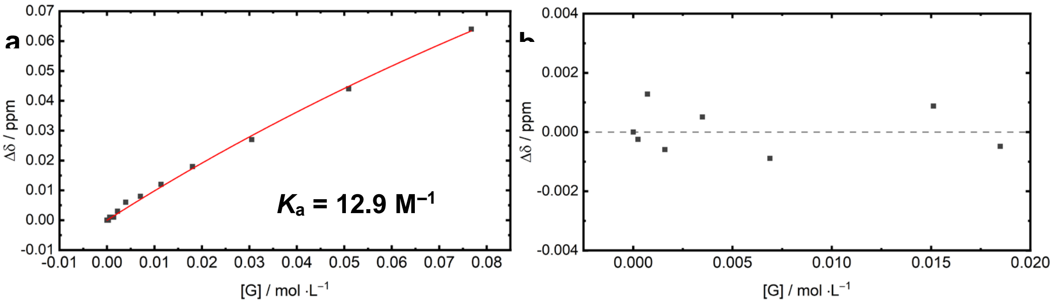

Figure A. 11. Non-linear least-square curve fitting analysis obtained from the isothermal binding titration (c(**12[4]**) = 2.71·10^{-4} mol L^{-1}, in CDCl$_3$ at 298 K) upon addition of perylene. $\Delta\delta$ taken for proton H$_d$. The association constant K_a was determined to be: K_a = 12.9 M^{-1} with an R^2 of 0.9867. b) Residual difference plot of the predicted values of the fit vs experimental values. Data acquired by isothermal binding titration with 1:1 stoichiometry.

Depending on the arrangement of perylene inside the cavity of macrocycle **12[4]** more than one molecule could bind inside the void volume, yet fitting of the data against a 1:2 binding model using the program bindfit[233] did not result in a conclusive association constant.

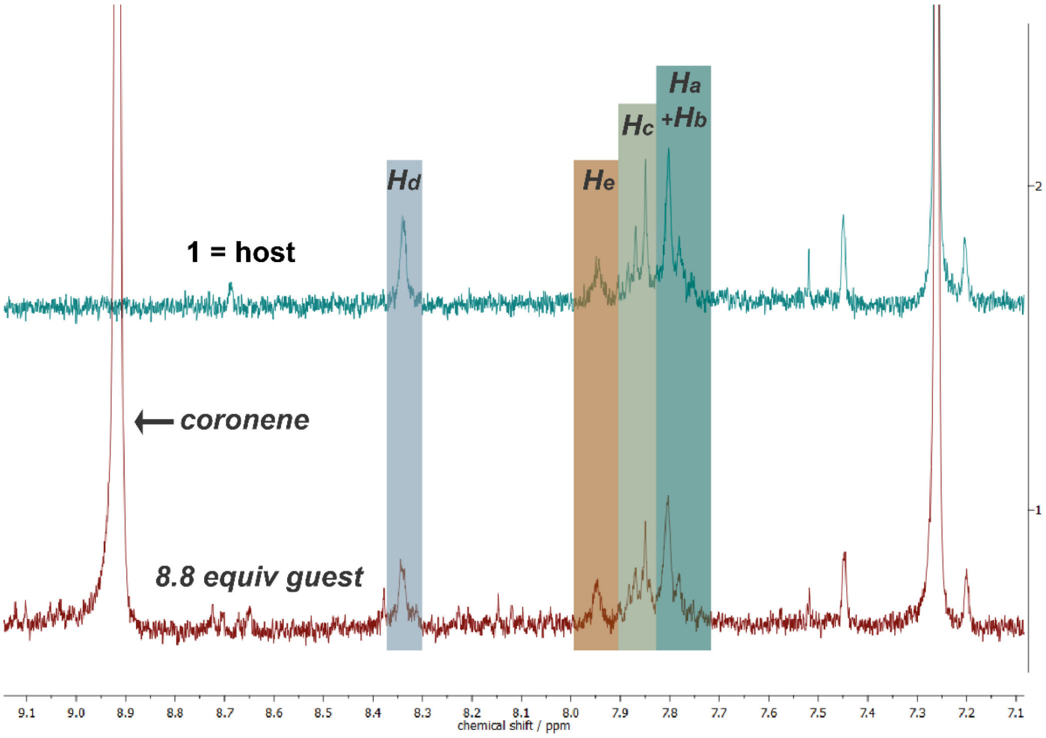

Figure A. 12. Isothermal NMR binding titration zoom into the chemical shift region where the host protons were assumed to change. ^{1}H NMR spectra of 1 at 25 °C, in $CDCl_3$, (c(1) = $1.91 \cdot 10^{-4}$ mol L^{-1}) upon subsequent addition of coronene as solid (at 8.8 equiv. the solution was saturated with coronene).

As no change was observed and the solution was saturated no data plotting was performed.

^{1}H NMR of 12[4] and Fullerenes, [6–7]CPP

In the following the titration data and the curve fitting for proton H_e of **12[4]** is shown as an addition to the shown data in *Chapter 3* of proton H_d.

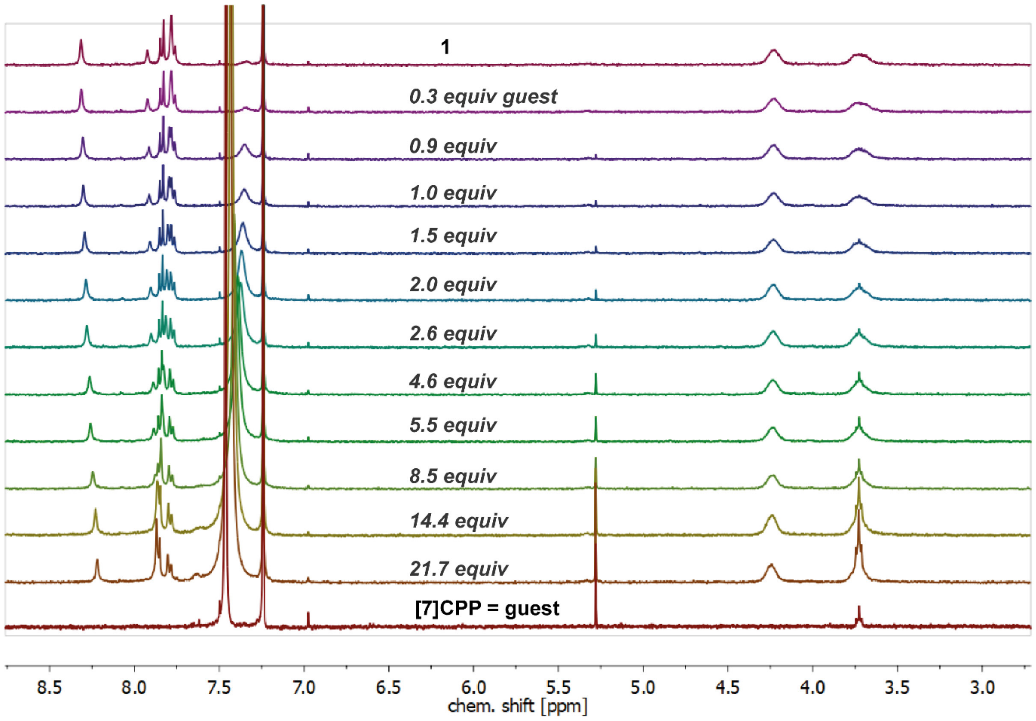

Figure A. 13. Isothermal ^{1}H NMR binding titration. Spectra of **12[4]** at 25 °C, in $CDCl_3$, (c(**1**) = 4.93•10^{-4} mol L^{-1}) upon subsequent addition of a [7]CPP as stock-solution in $CDCl_3$ or solid (last two additions).

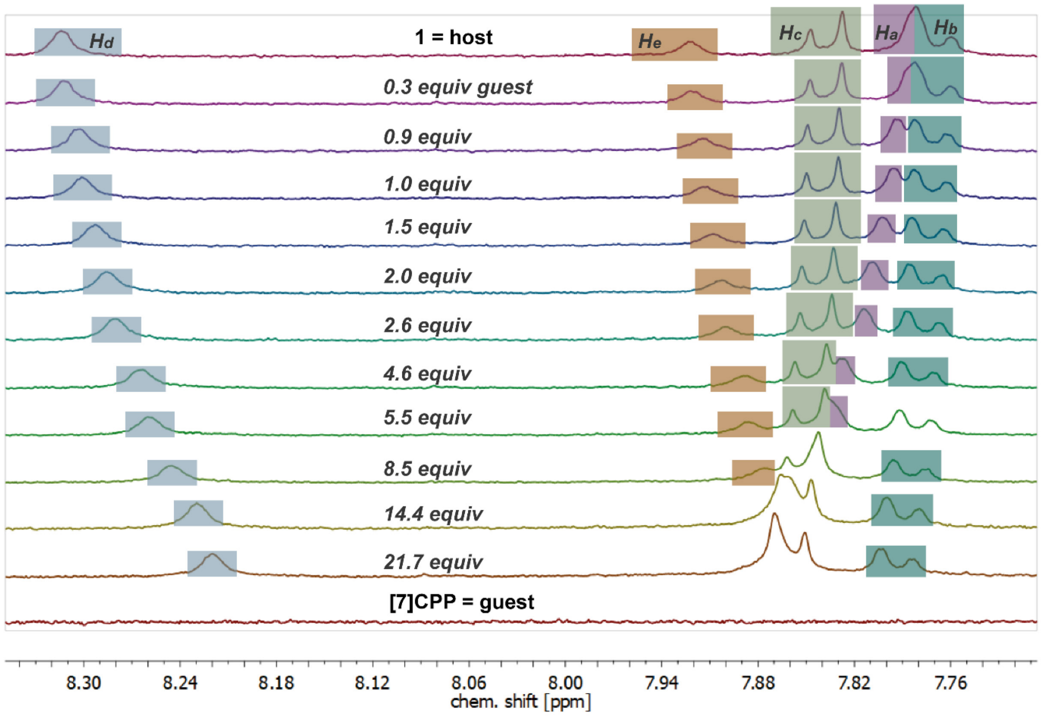

Figure A. 14. Isothermal NMR binding titration, zoom into the chemical shift region where the host protons change. Spectra of **12[4]** at 25 °C, in $CDCl_3$, (c(**12[4]**) = 4.93•10^{-4} mol L^{-1}) upon subsequent addition of [7]CPP as stock-solution in $CDCl_3$ or as a solid (last two additions).

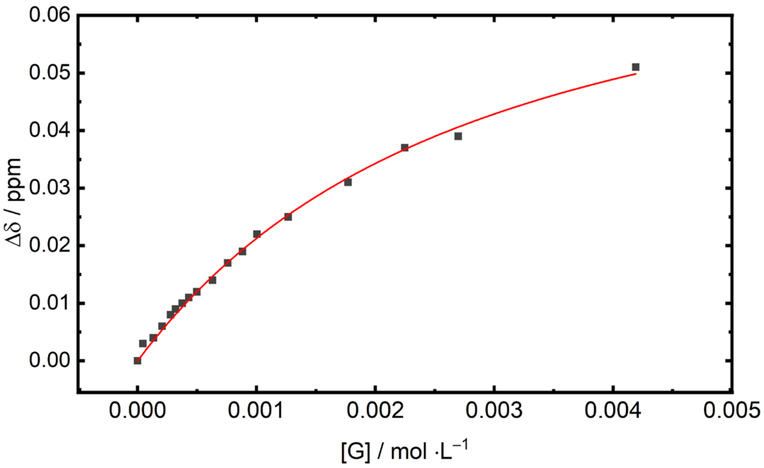

Figure A. 15. Non-linear least-square curve fitting analysis obtained from the isothermal binding titration (c(**12[4]**) = $4.93 \cdot 10^{-4}$ mol L^{-1}, in CDCl$_3$ at 298 K) upon addition of [7]CPP. $\Delta\delta$ taken for proton H$_e$. The association constant K_a was determined to be: $K_a = 4.0 \cdot 10^2$ M^{-1} with an R^2 of 0.9964. The last two additions could not be considered due to an overlap of the signals; hence the K_a of this fit is rather erroneous, and thus neglected.

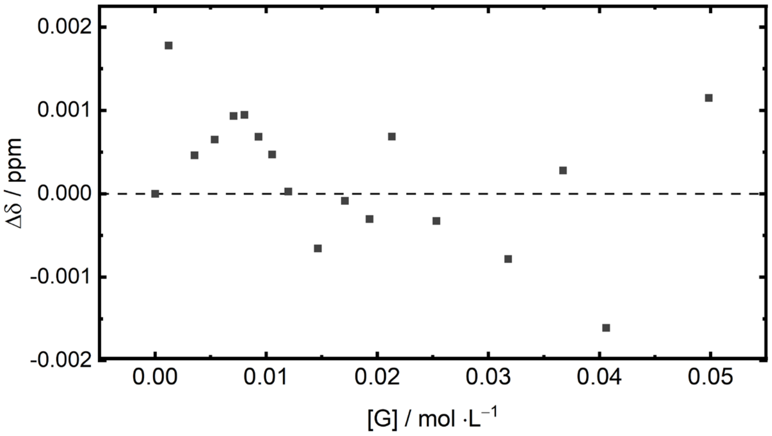

Figure A. 16. Residual difference plot of the predicted values of the fit vs experimental values. Data acquired by isothermal binding titration with 1:1 stoichiometry (c(**12[4]**) = $4.93 \cdot 10^{-4}$ mol L^{-1}, in CDCl$_3$ at 298 K) upon addition of [7]CPP. $\Delta\delta$ taken for proton H$_e$.

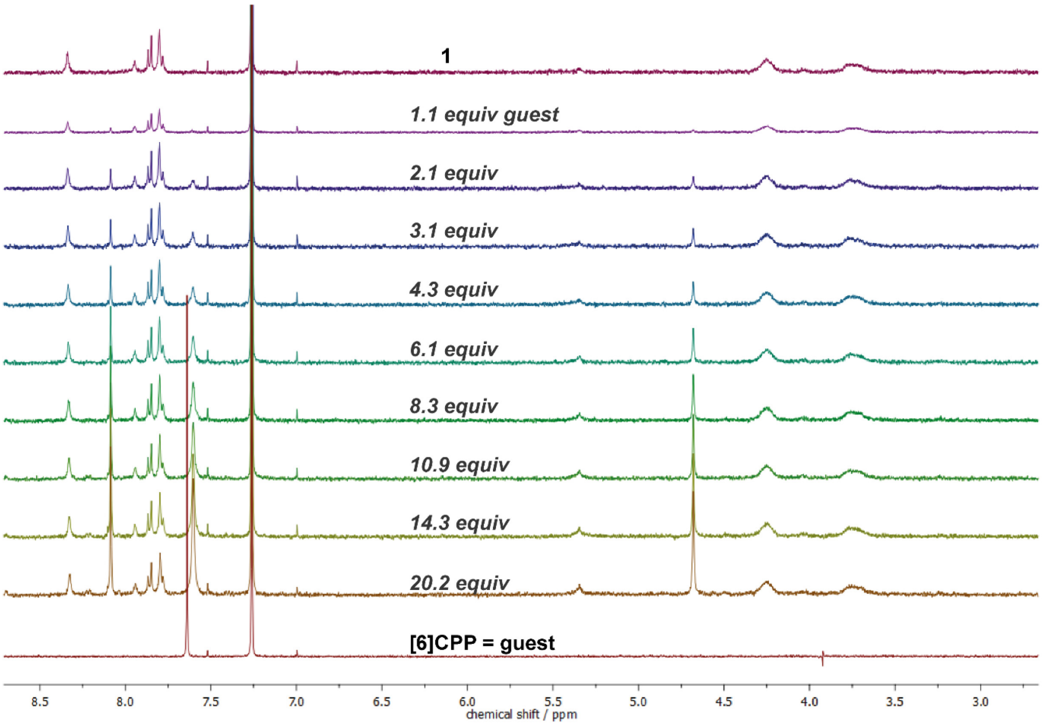

Figure A. 17. Isothermal NMR binding titration. Spectra of **12[4]** at 25 °C, in CDCl$_3$, (c(**12[4]**) = 1.9•10^{-4} mol L^{-1}) upon subsequent addition of a [6]CPP stock-solution in CDCl$_3$.

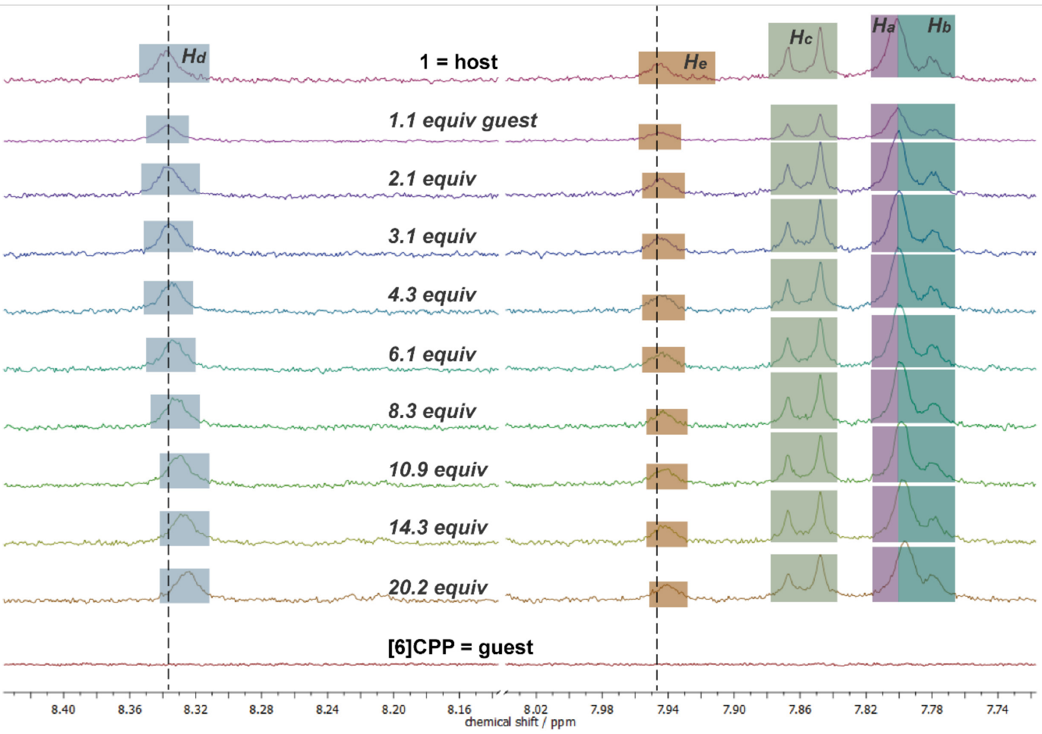

Figure A. 18. Isothermal NMR binding titration, zoom into the chemical shift region where the host protons change. Dashed lines as a guidance for the small $\Delta\delta$. Spectra of **12[4]** at 25 °C, in CDCl$_3$, (c(**12[4]**) = 1.9•10^{-4} mol L^{-1}) upon subsequent addition of [6]CPP as stock-solution in CDCl$_3$.

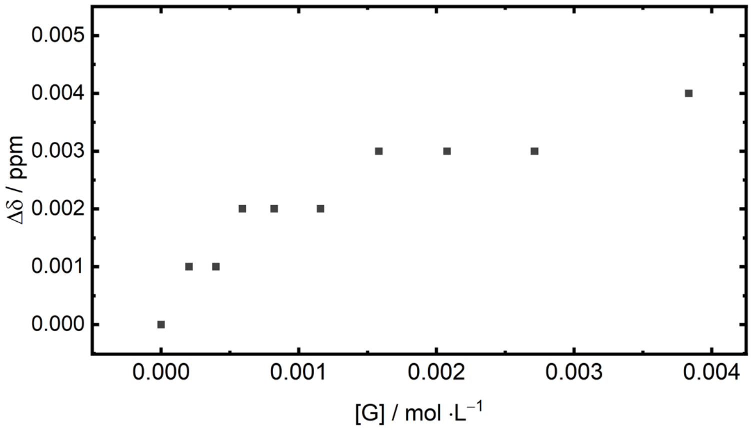

Figure A. 19. Non-linear least-square curve fitting analysis to the obtained data from the isothermal binding titration (c(**12[4]**) = 4.93·10^{-4} mol L^{-1}, in $CDCl_3$ at 298 K) upon addition of [6]CPP was not possible.

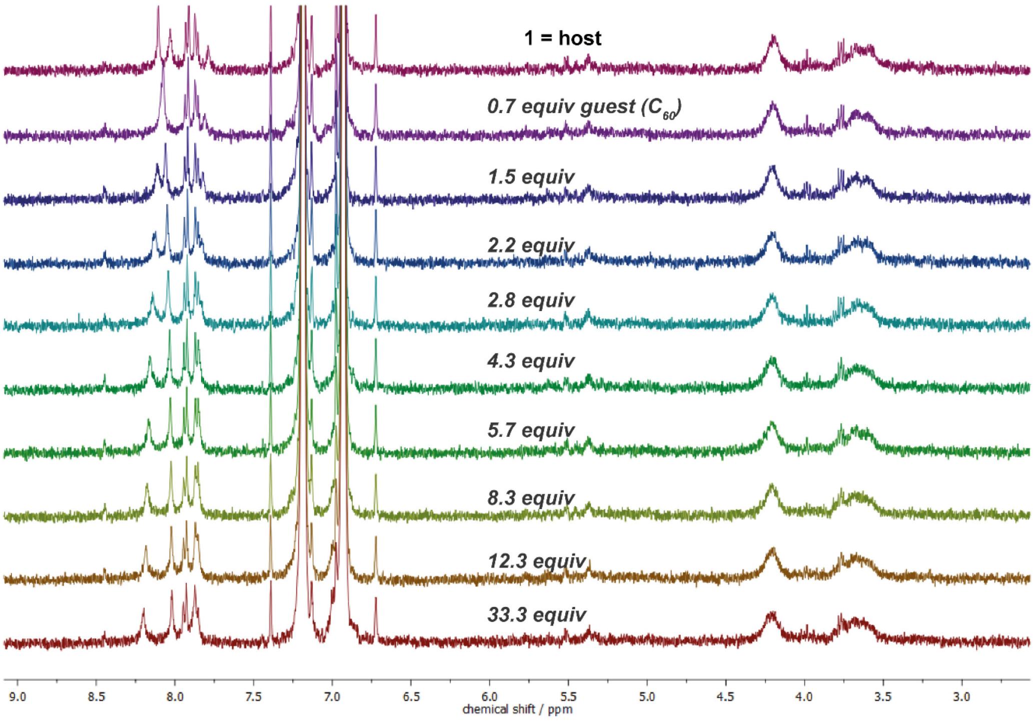

Figure A. 20. Isothermal NMR binding titration. ^1H NMR spectra of **12[4]** at 25 °C, in *o*-DCB(d_4), (c(**12[4]**) = 2.79·10^{-4} mol L^{-1}) upon subsequent addition of C_{60} as a stock-solution in *o*-DCB(d_4) and as solid (last two additions).

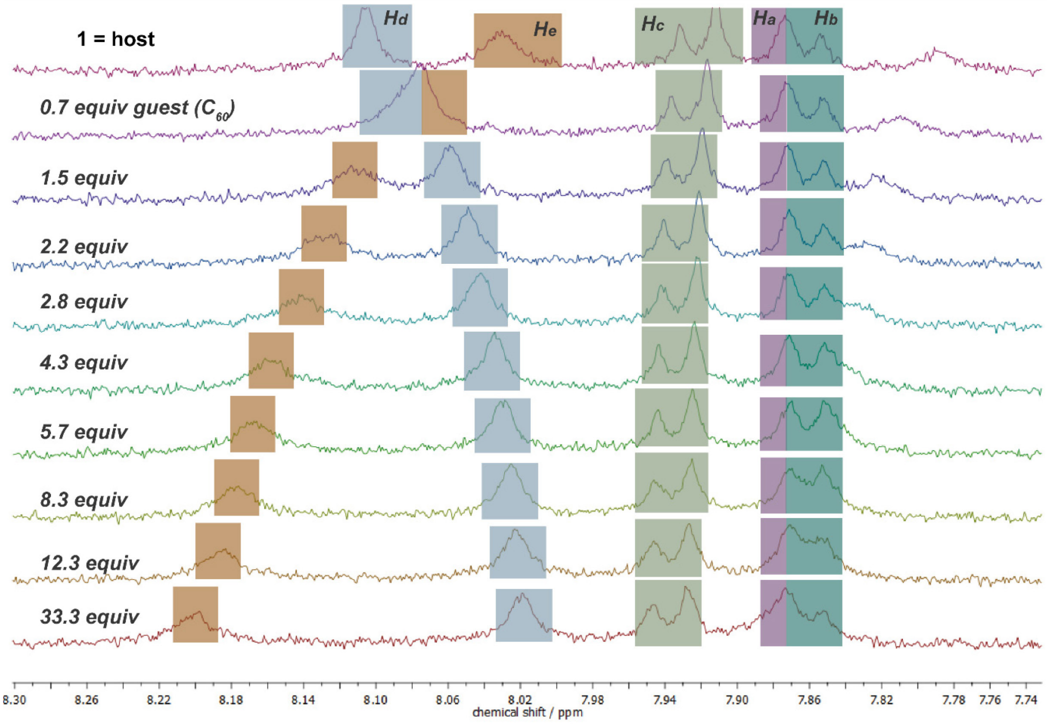

Figure A. 21. Isothermal NMR binding titration, zoom into the chemical shift region where the host protons change. ^{1}H NMR spectra of **12[4]** at 25 °C, in *o*-DCB(d_4), (c(**12[4]**) = $2.79 \cdot 10^{-4}$ mol L^{-1}) upon subsequent addition of C_{60} as a stock-solution in *o*-DCB(d_4) and as solid (last two additions).

.

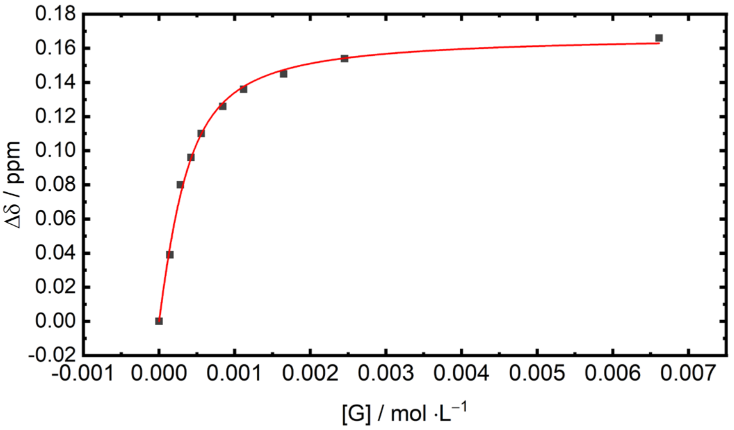

Figure A. 22. Non-linear least-square curve fitting analysis obtained from the isothermal binding titration (c(**12[4]**) = $2.79 \cdot 10^{-4}$ mol L^{-1}, in *o*-DCB(d_4) at 298 K) upon addition of C_{60}. $\Delta\delta$ taken for proton H_e. The association constant K_a was determined to be: $K_a = 5.16 \cdot 10^3$ M^{-1} with an R^2 of 0.9971.

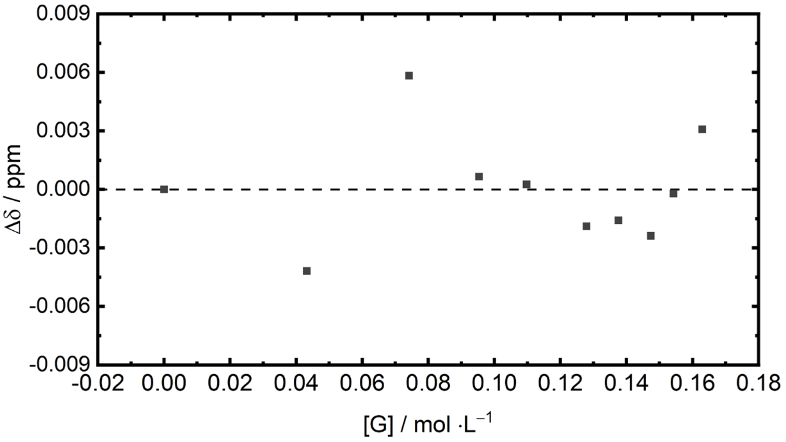

Figure A. 23. Residual difference plot of the predicted values of the fit vs experimental values. Data acquired by isothermal binding titration with 1:1 stoichiometry (c(**12[4]**) = 2.79•10^{-4} mol L^{-1}, in *o*-DCB(d_4) at 298 K) upon addition of C_{60}. Δ*δ* taken for proton H_e.

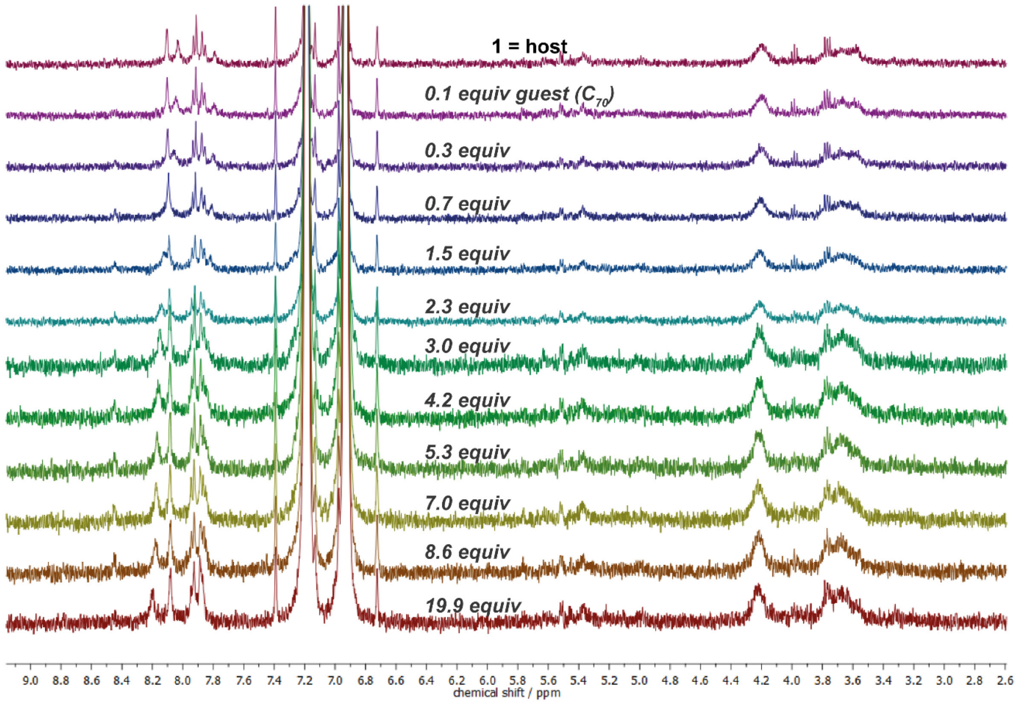

Figure A. 24. Isothermal NMR binding titration. ^{1}H NMR spectra of **12[4]** at 25 °C, in *o*-DCB(d_4), (c(**12[4]**) = 2.92•10^{-4} mol L^{-1}) upon subsequent addition of a C_{70} as a stock-solution in *o*-DCB(d_4) and as solid (last addition).

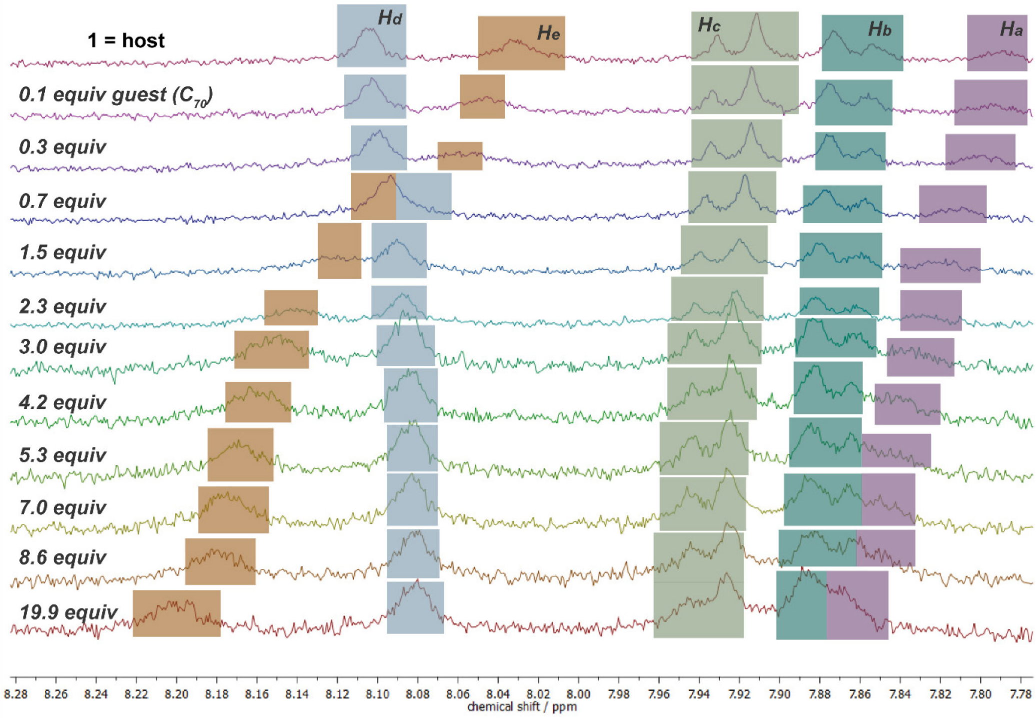

Figure A. 25. Isothermal NMR binding titration, zoom into the chemical shift region where the host protons change. Spectra of **12[4]** at 25 °C, in *o*-DCB(d_4), (c(**12[4]**) = $2.92 \cdot 10^{-4}$ mol L^{-1}) upon subsequent addition of C_{70} as a stock-solution in *o*-DCB(d_4) and as solid (last addition).

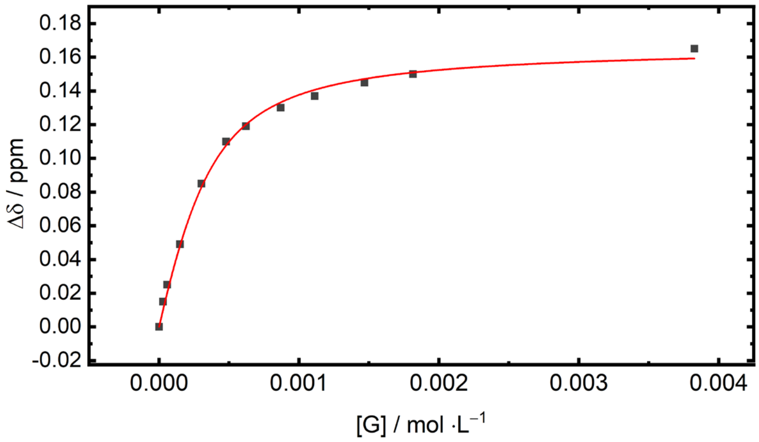

Figure A. 26. Non-linear least-square curve fitting analysis obtained from the isothermal binding titration (c(**12[4]**) = $2.92 \cdot 10^{-4}$ mol L^{-1}, in *o*-DCB(d_4) at 298 K) upon addition of C_{70}. $\Delta\delta$ taken for proton H_e. The association constant K_a was determined to be: $K_a = 6.33 \cdot 10^3$ M^{-1} with an R^2 of 0.9967.

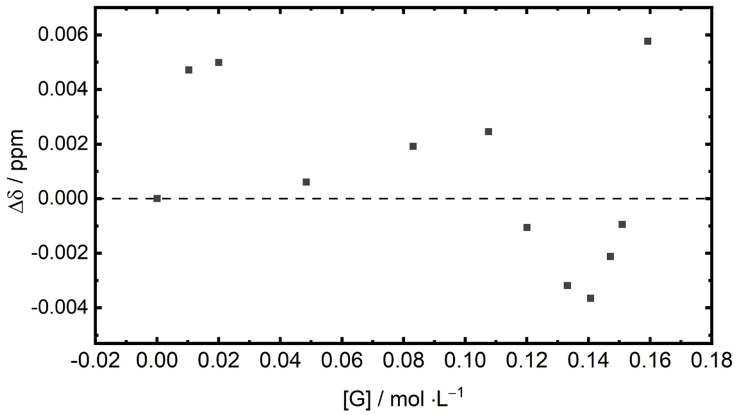

Figure A. 27. Residual difference plot of the predicted values of the fit vs experimental values. Data acquired by isothermal binding titration with 1:1 stoichiometry (c(**12[4]**) = 2.92·10^{-4} mol L^{-1}, in o-DCB(d_4) at 298 K) upon addition of C_{70}. $\Delta\delta$ taken for proton H_e.

A.4. ECD Spectroscopy

The following shows the ECD spectra of the separated enantiomers of (±)-**28**. Subsequent oxidation allowed the synthesis of enantiomerically pure (–)-(*R,R)*-**31-C** as well as *(+)-(S,S)*-**31-C**, of which the ECD spectra are shown as well.

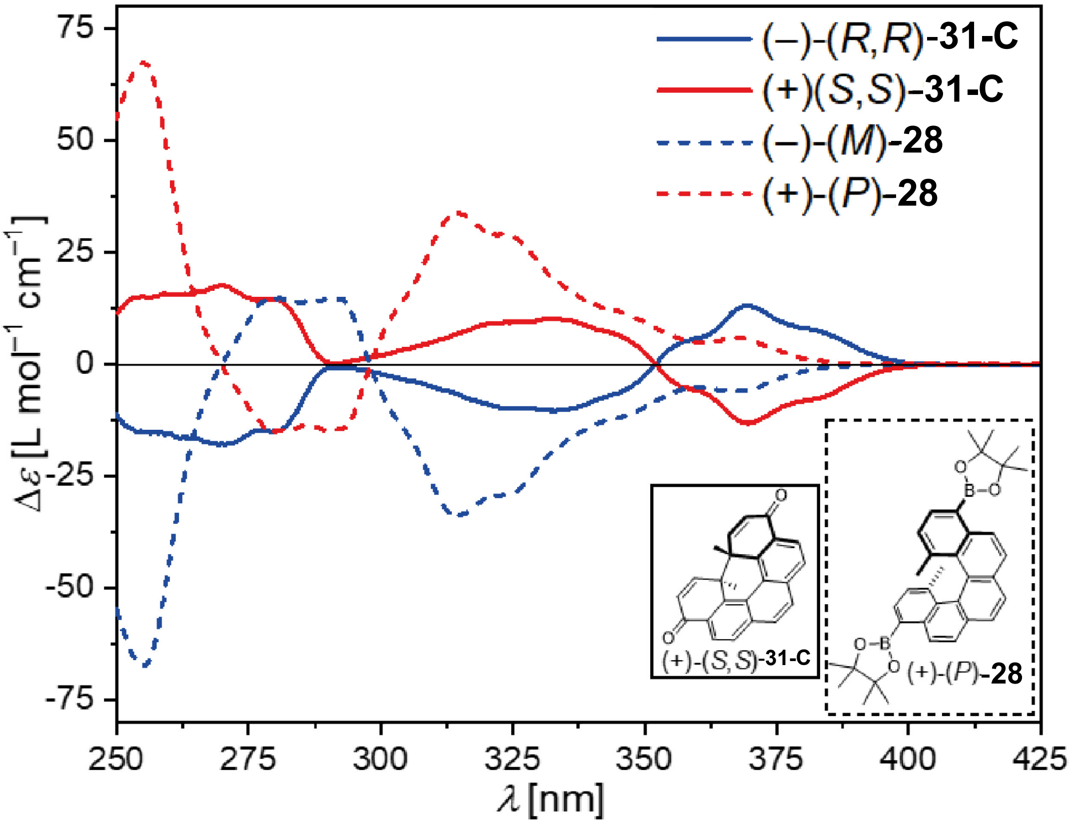

Figure A. 28. ECD spectra of the enantiomers of **28** (dotted graphs; *c* = 6•10^{-4} M) and of the enantiomers of **31-C** (solid graphs; *c* = 2•10^{-4} M)). The spectra were recorded in CH_2Cl_2 at 298 K.

The comparison of the ECD spectra of ring-open helicene (±)-**28** and ring-closed helicene (±)-**31-C** show a decrease of the molar ellipticity in the second Cotton effect and an inversion in the first Cotton effect. The TD-DFT-simulated spectra (see below) reveal that these differences are based on discrete transitions.

The SpecDis software, developed by Bringmann and co-workers, was used to compare the experimental and calculated spectra.[335] All calculated spectra are shown with standard deviation (graph width fitting parameter *σ*) of *σ* = 0.3 eV.

Table A 2. Parameters for the comparison of experimentally determined and calculated spectra.

	UV Correction [nm]	Scaling Factor	Similarity Factor [%]
(–)-(*R*,*R*)-**31-C**	+21	1.789	80.6
(+)-(*S*,*S*)-**31-C**	+21	1.819	80.1
(–)-(*M*)-**28**	+16	1.051	92.3
(+)-(*P*)-**28**	+16	1.002	92.5

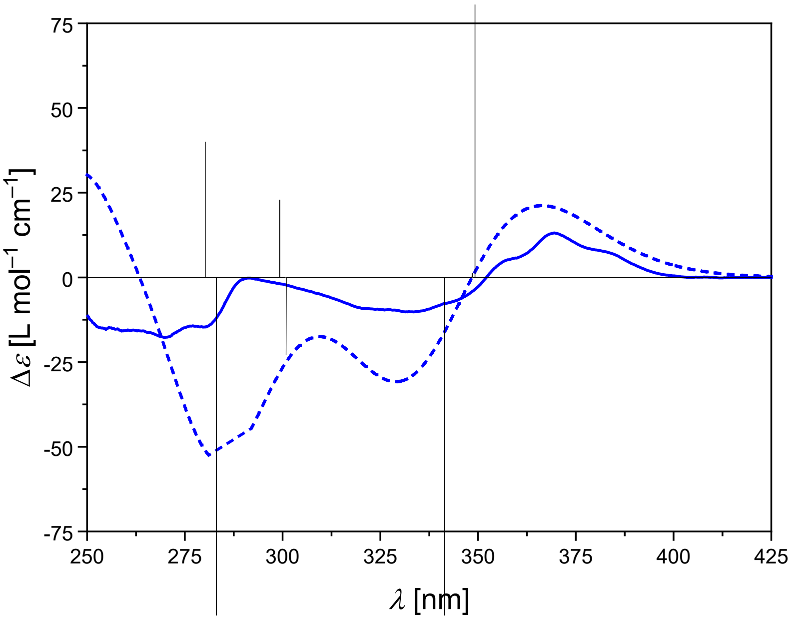

Figure A. 29. Comparison of the ECD spectra of (–)-(*R*,*R*)-**31-C** (blue solid graphs; *c* = $2.2\cdot10^{-4}$ M) and the simulated spectra (blue dotted graphs and black vertical graphs for discrete vertical transitions, level of theory: TD-DFT-D3(BJ)/CAM-B3LYP/def2-TZVP/CPCM(CH_2Cl_2). The spectrum was recorded in CH_2Cl_2 at 298 K.

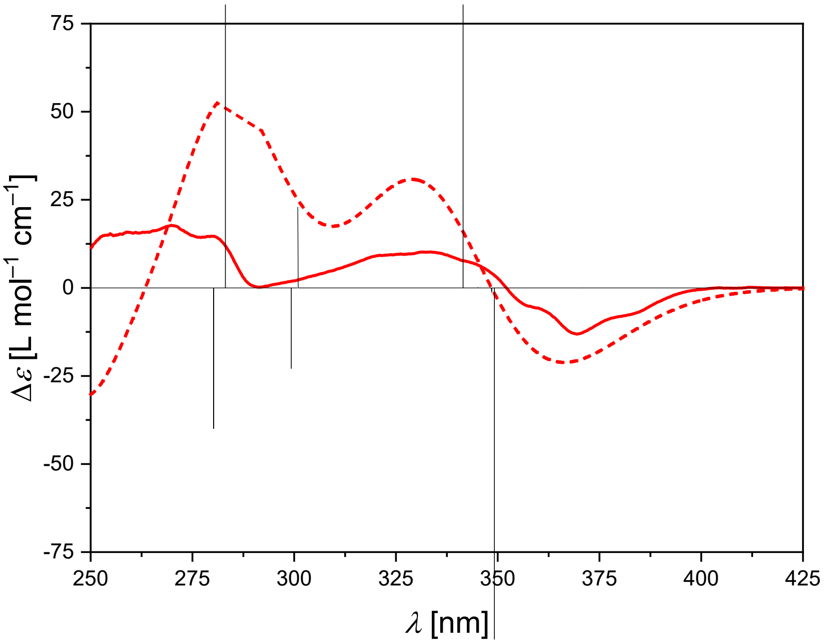

Figure A. 30. Comparison of the ECD spectra of (+)-(*S*,*S*)-**31-C** (red solid graphs; *c* = 1.9·10^{-4} M) and the simulated spectra (red dotted graphs and black vertical graphs for discrete vertical transitions, level of theory: TD-DFT-D3(BJ)/CAM-B3LYP/def2-TZVP/CPCM(CH_2Cl_2). The spectrum was recorded in CH_2Cl_2 at 298 K.

A.5. Computational Methods

All calculations were conducted with Gaussian 16 Revision A.03 on the chccs-cluster of the Department of Chemistry at Humboldt University of Berlin. The structures are confirmed ground-state minima according to the analysis of their analytical frequencies computed at the same level, which show no imaginary frequencies.

Unless otherwise stated exclusively the (*M*)-enantiomer for the open helicene or the (*R*,*R*)-enantiomer for the closed quinoidal molecule were calculated. All geometry optimizations of the molecules (±)-**31-C** and (±)-**34-C** as closed-shell singlets (CS) or as triplets (T) were performed at the DFT-D3[336]/UB3LYP[337,338]/6-31G(d,p)[339] level of theory. In order to describe the molecules (±)-**31-C** and (±)-**34-C** as open-shell singlet's (OS) the *guess=mix* keyword was used to create as initial wave function a 1:1 mixture of singlet and triplet states with a squared spin expectation value $<S^2> = 1$. The final energies were calculated at the DFT-D3(BJ)[340]/UB3LYP/def2-TZVP[341] level of theory.

*A.5.1 Calculation of the UV/vis Spectra of Electrochemically Obtained Dianions of (±)-**31-C** and (±)-**34-C***

The time-dependent density-functional theory (TD-DFT) calculations were performed on the geometry-optimized structures at the TD-DFT-D3(BJ)/UCAM-B3LYP/def2-TZVP level of theory incorporating 120 states. The UV/Vis spectra of the dianions (±)-**31-O**$^{2-}$ and (±)-**34-C-O**$^{2-}$ were additionally calculated at the TD-DFT-

D3(BJ)/UCAM-B3LYP/aug-cc-pVTZ[342] level of theory. The conductor-like polarizable continuum model (CPCM)[343] was used as solvent model with dichloromethane (ECD), acetonitrile (spectroelectrochemistry).

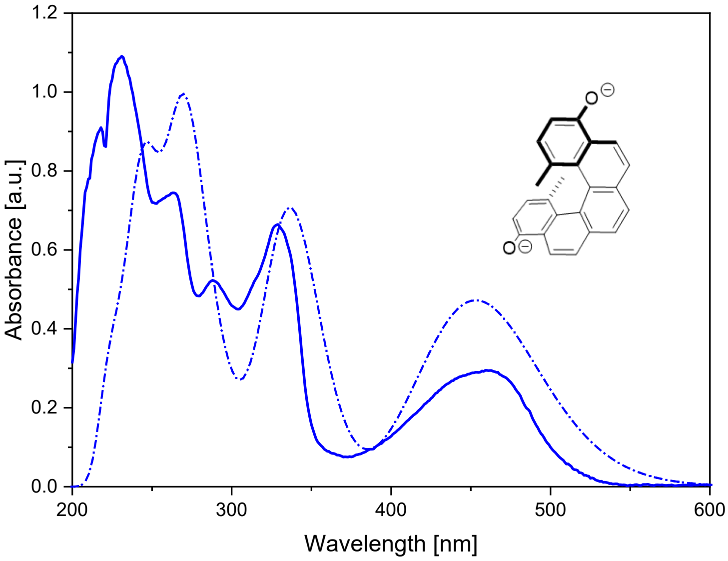

Figure A. 31. Comparison of the UV/Vis spectra of (±)-**31-O**$^{2-}$ (blue solid graph, $c = 6{\cdot}10^{-4}$ M) and the TD-DFT-calculated spectra (blue dotted graph, level of theory: TD-DFT-D3(BJ)/UCAM-B3LYP/def2-TZVP/CPCM(acetonitrile). The experimental spectrum was recorded in acetonitrile at 295 K. The calculated spectrum is shown with a UV correction of 26 nm, a scaling factor of $2.02{\cdot}10^{-5}$, and a standard deviation (graph width fitting parameter σ) of σ = 0.29 eV. The comparison was performed using the SpecDis software, which computed a similarity factor of 93%.[335]

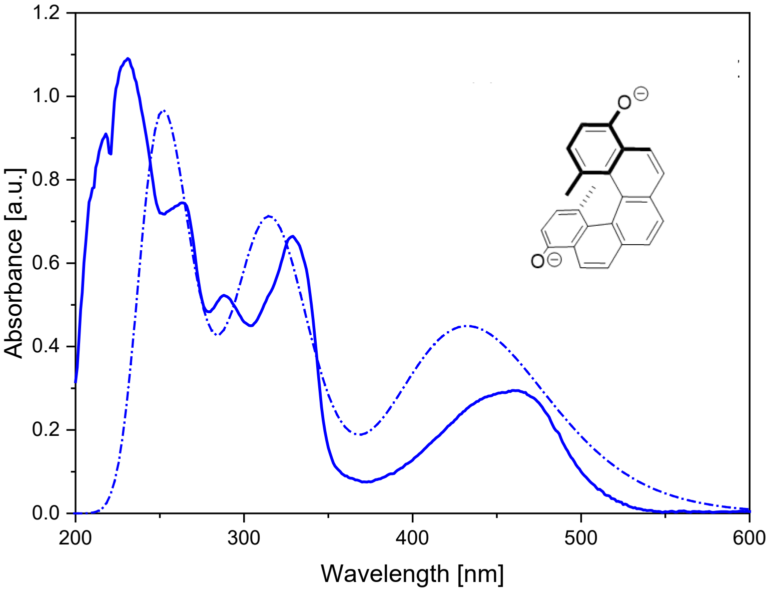

Figure A. 32. Comparison of the UV/Vis spectra of (±)-**31-O**$^{2-}$ (blue solid graph, $c = 6{\cdot}10^{-4}$ M) and the TD-DFT-calculated spectra (blue dotted graph, level of theory: TD-DFT-D3(BJ)/UCAM-B3LYP/aug-cc-pVTZ/CPCM(acetonitrile). The experimental spectrum was recorded in acetonitrile at 295 K. The calculated spectrum is shown with a UV correction of 20 nm, a scaling factor of $2.14{\cdot}10^{-5}$, and a standard deviation (graph width fitting parameter σ) of σ =

0.35 eV. The comparison was performed using the SpecDis software, which computed a similarity factor of 78%.[335]

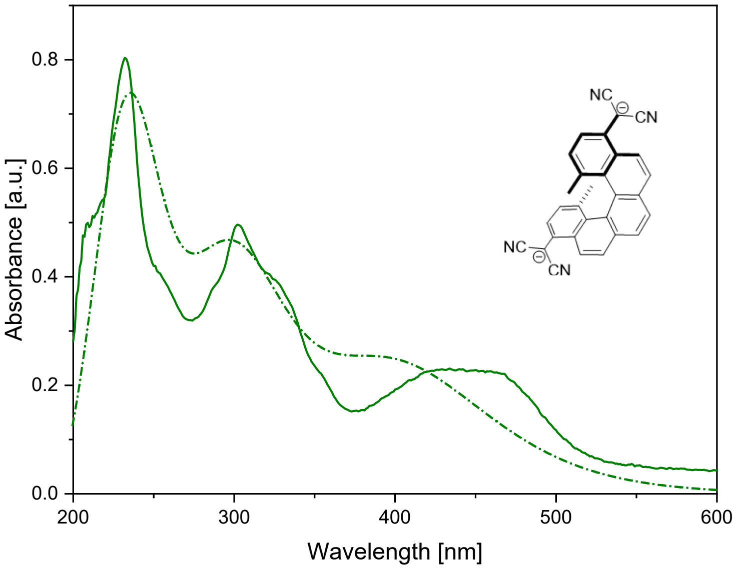

Figure A. 33. Comparison of the UV/Vis spectra of (±)-**34-O**$^{2-}$ (green solid graph, $c = 4\cdot10^{-4}$ M) and the simulated spectra (green dotted graph, level of theory: TD-DFT-D3(BJ)/UCAM-B3LYP/def2-TZVP/CPCM(acetonitrile). The experimental spectrum was recorded in acetonitrile at 298 K. The calculated spectrum is shown with a UV Correction of 24 nm, a scaling factor of $1.24\cdot10^{-5}$, and a standard deviation (graph width fitting parameter σ) of σ = 0.49 eV. The comparison was performed using the SpecDis software, which computed a similarity factor of 82%.[335]

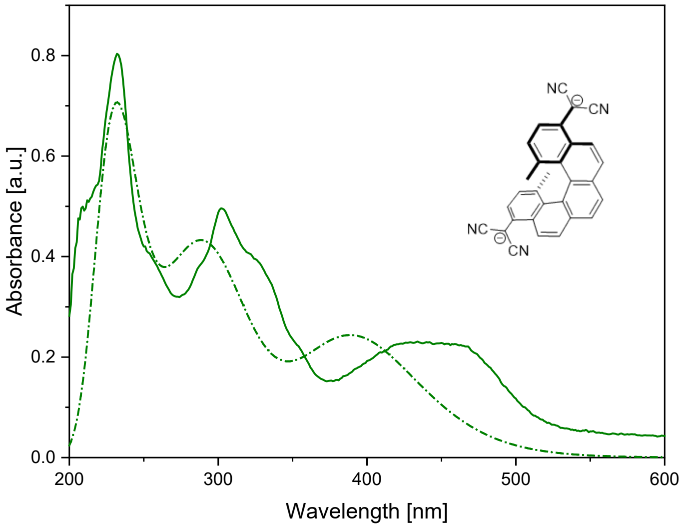

Figure A. 34. Comparison of the UV/Vis spectra of (±)-**34-O**$^{2-}$ (green solid graph, $c = 4\cdot10^{-4}$ M) and the simulated spectra (green dotted graph, level of theory: TD-DFT-D3(BJ)/UCAM-B3LYP/aug-cc-pVTZ/CPCM(acetonitrile). The experimental spectrum was recorded in acetonitrile at 298 K. The calculated spectrum is shown with a UV Correction of 11 nm, a scaling factor of $1.03\cdot10^{-5}$, and a standard deviation (graph width fitting parameter σ) of σ = 0.39 eV. The comparison was performed using the SpecDis software, which computed a similarity factor of 76%.[335]

The comparison of the ECD spectra of ring-open helicene (±)-**2** and ring-closed helicene (±)-**1a-C** show a decrease of the molar ellipticity in the second Cotton effect and an inversion in the first Cotton effect. The TD-DFT-simulated spectra (see below) reveal that these differences are based on discrete transitions.

The SpecDis software, developed by Bringmann and co-workers, was used to compare the experimental and calculated spectra.[335] All calculated spectra are shown with standard deviation (graph width fitting parameter σ) of σ = 0.3 eV.

Table A 3. Parameters for the comparison of experimentally determined and calculated spectra.

	UV Correction [nm]	Scaling Factor	Similarity Factor [%]
(−)-(*R*,*R*)-**1a-C**	+21	1.789	80.6
(+)-(*S*,*S*)-**1a-C**	+21	1.819	80.1
(−)-(*M*)-**2**	+16	1.051	92.3
(+)-(*P*)-**2**	+16	1.002	92.5

A.6. Spectroelectrochemical Data on [5]Helicene Derivatives (±)-31-C and (±)-34-C

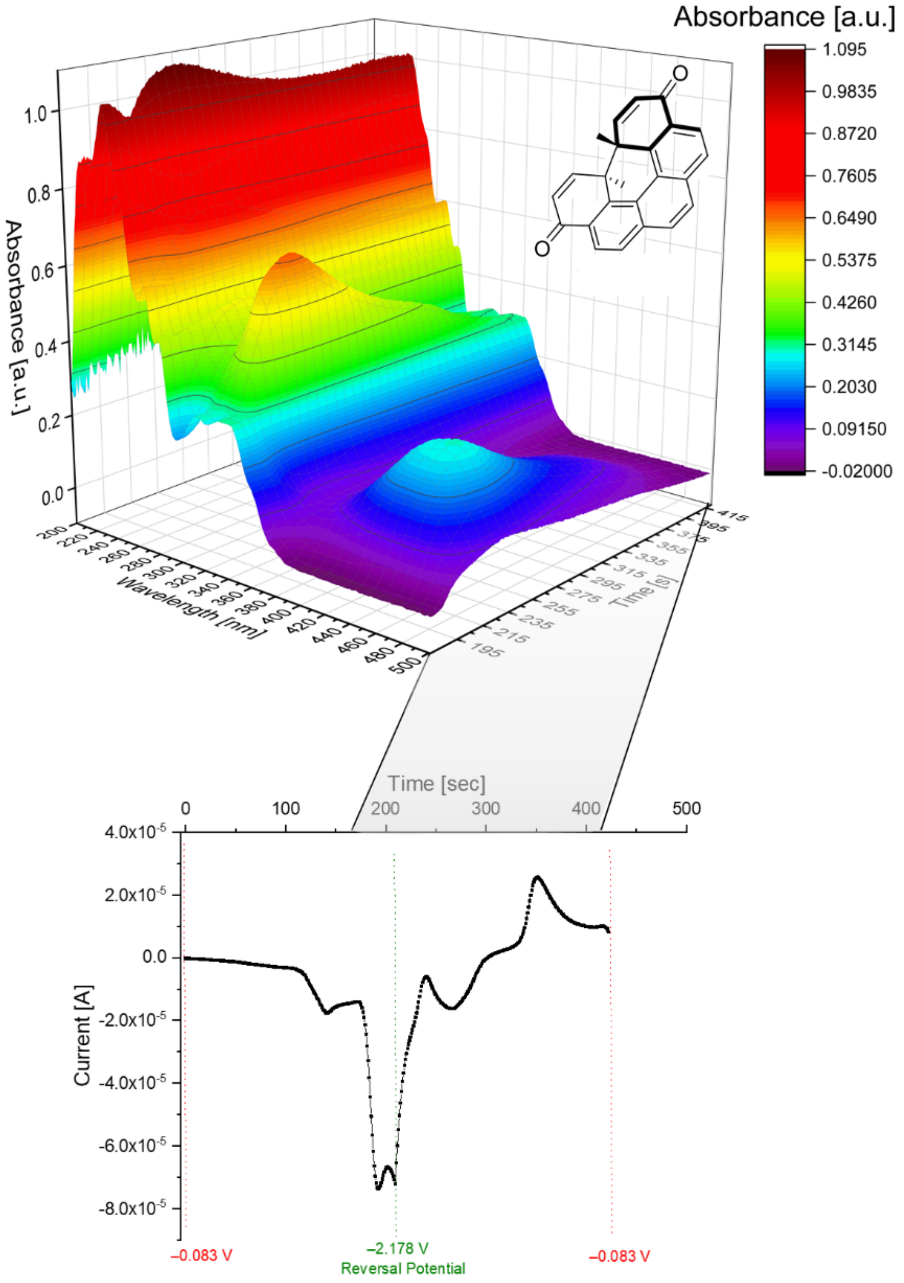

Figure A. 35. (Top) Spectroelectrochemistry of (±)-**31-C**. Plotted is the absorbance (in a.u.), the wavelength (between 200–500 nm) and the experiment time (in seconds). The latter corresponds to a certain voltage. The Experiment was carried out in a thin layer quartz glass spectroelectrochemical cell (d = 0.5 mm) in MeCN with 0.1 M Bu_4NPF_6, platinum mesh electrode, $c = 6\cdot10^{-4}$ M, $dE/dt = 10$ mV s^{-1}, T = 295 K. (Bottom) The corresponding current flow in the above shown time span of the spectroelectrochemistry, including start- and end-potential (red), as well as the reversal potential (green).

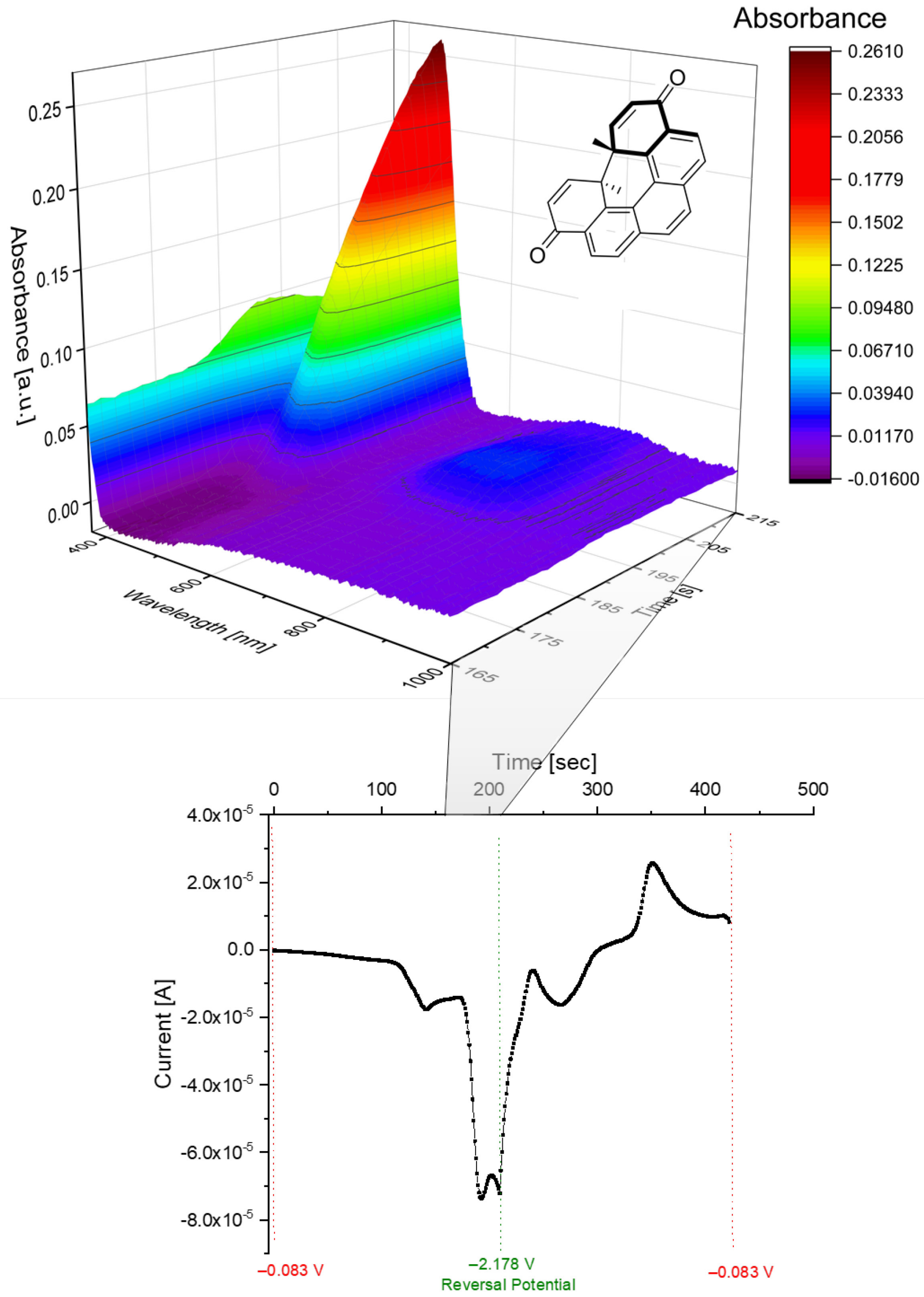

Figure A. 36. (Top) Spectroelectrochemistry of (±)-**31-C**. Plotted is the absorbance (in a.u.), the wavelength (between 370–1000 nm) and the experiment time (in seconds) to visualize the absorption between 600 and 800 nm of the transient radical anion that subsequently opens via formal retroelectrocyclization. The Experiment was carried out in a thin layer quartz glass spectroelectrochemical cell ($d = 0.5$ mm) in MeCN with 0.1 M Bu$_4$NPF$_6$, platinum mesh electrode, $c = 6{\cdot}10^{-4}$ M, $dE/dt = 10$ mV s^{-1}, T = 295 K. (Bottom) The corresponding current flow in the above shown time span of the spectroelectrochemistry, including start- and end-potential (red), as well as the reversal potential (green).

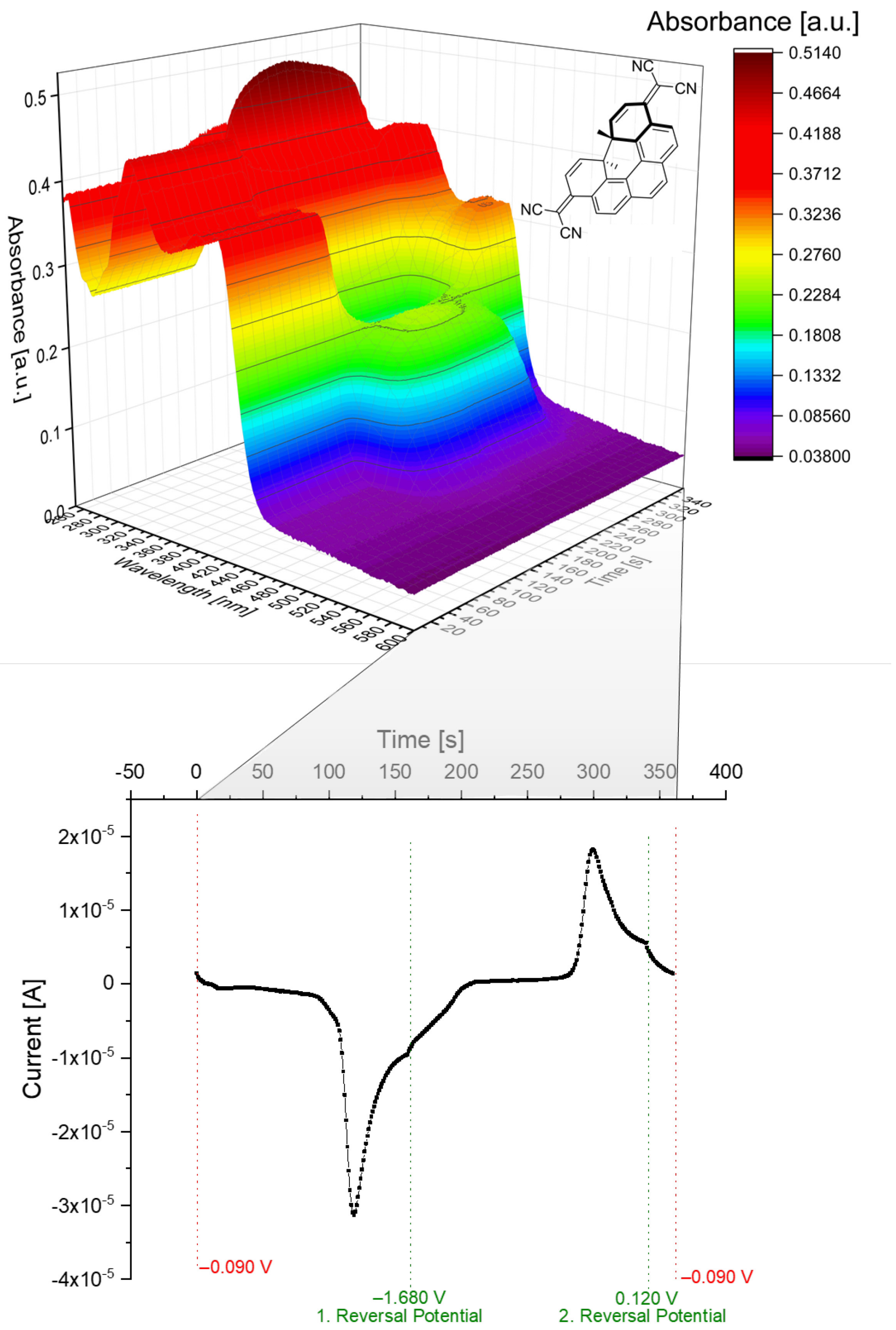

Figure A. 37. (Top) Spectroelectrochemistry of (±)-**34-C**. Plotted is the absorbance (in a.u.), the wavelength (between 250–600 nm) and the experiment time (in seconds). The Experiment was carried out in a thin layer quartz glass spectroelectrochemical cell (d = 0.5 mm) in MeCN with 0.1 M Bu_4NPF_6, platinum mesh electrode, $c = 6 \cdot 10^{-4}$ M, dE/dt = 10 mV s^{-1}, T = 295 K. (Bottom) The corresponding current flow in the above shown time span of the spectroelectrochemistry, including start- and end-potential (red), as well as the first and second reversal potential (green).

A.7. Coulometry of (±)-31-C and (±)-34-C

Coulometry experiments (nearly quantitative electrolysis), performed under potentiostatic conditions, were conducted in a double-H cell. The electrolyte solution for the work, counter, and reference electrodes is separated by a ceramic membrane. The counterelectrode is a platinum wire and a standard calomel electrode was employed as the reference electrode. The main cell contains a platinum net electrode which performs the electrolysis and has a volume of approximately 45 mL electrolyte solution, which is stirred by a magnetic stir bar while the solution is degassed with a stream of argon gas. The potential is set through a double potentiostat (HEKA, Reutlingen, Germany) equipped with an integrator unit (current ▪ time, I ▪ t) allowing for well-defined and controlled electron transfer.

Table A 4. Parameters for the coulometry of (±)-**31-C** and (±)-**34-C**.

	(±)-**31-C**	(±)-**34-C**
c [mmol L^{-1}]	0.57	0.27
(I ▪ t)$_{\text{theor.}}$ [mCb e^{-1}]	1792	1026
$E_{\text{A, Red.}}$ [V] vs. SCE	–1.700	–1.200
$(I \cdot t)_{\text{final, Red.}}$ [mCb e^{-1}]	2671	1365
$E_{\text{A, Re-Ox.}}$ [V] vs. SCE	0.500	0.700
$(I \cdot t)_{\text{final, Re-Ox.}}$ [mCb e^{-1}]	2083	980
Electron transfer [e mol^{-1}]	1.5	1.4
Reoxidation [%]	78	72

A.8. Crystallographic Data

X-ray Crystallography. CCDC-1940871 (**2**), CCDC-2049516 (**7**), CCDC-2049515 (**6**), CCDC-2050148 (**4[4]**), CCDC-1876252 (**4[6]**), CCDC-2049763 (**4[5]**···18-crown-6·K^{+} (BF$_4^{-}$)), CCDC 2209128 (**11**), CCDC 2033332 (**24**), CCDC 2207451 (**25**), CCDC 2055826 (**20**), CCDC 2208548 (**26[4]**), CCDC 2208573 (**12[4]**), CCDC 2022746 (+)-(*P*)-**28**, CCDC 2129548 (±)-**31-C**, and CCDC 2104623 (±)-**34-C**, contain the supplementary crystallographic data for this paper, including structure factors and refinement instructions. These data can be obtained free of charge from the joint Cambridge Crystallographic Data Centre and Fachinformationszentrum Karlsruhe Access Structures service (Cambridge Crystallographic Data Centre, 12 Union Road, Cambridge CB2 1EZ, UK (fax: +44(1223)-336-033; e-mail: deposit@ccdc.cam.ac.uk), or online via www.ccdc.cam.ac.uk/structures.

Remark on X-ray Crystal Structure Determination of Macrocycles

Generally, single crystals of macrocycles are difficult to grow due to limited solubility, and they must be handled, picked, and mounted carefully to prevent solvent loss. The resulting statistical indicators cannot be compared to results typically obtained for small molecule structures due to several problems (e.g. disordered solvent, low resolution). Even though some solvent molecules could be refined, the solvent mask tool implemented in OLEX2 was used for the following three structures.[326]

Single-crystal X-ray Data and Structure Refinement for Pyrene-4,5,9,10-tetrone (2)

Clear red plates were grown by recrystallization from hot $(CH_3)_2SO$ upon slow cooling.

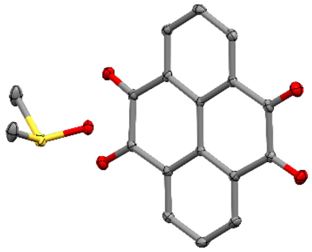

Figure A. 38. X-ray structure of **2** at 103 K. Ellipsoids are shown at 50% probability, hydrogen atoms are omitted for clarity. Color code: carbon, grey; oxygen, red; sulfur, yellow.

Table A 5. Crystal data and structure refinement for **2.**

CCDC Deposition number	1940871
Empirical formula	$C_{16}H_6O_4 \cdot (CH_3)_2SO$
Formula weight	340.34
Temperature/K	100.0
Crystal system	triclinic
Space group	*P*-1
a/Å	8.1346(6)
b/Å	9.4800(7)
c/Å	10.2701(7)
α/°	72.789(2)
β/°	83.483(2)
γ/°	72.502(2)
Volume/Å^3	721.26(9)
Z	2
ρ_{calc}g/cm^3	1.567
μ/mm^{-1}	0.252
F(000)	352.0
Crystal size/mm^3	1.036 × 0.24 × 0.234
Radiation	MoKα (λ = 0.71073)
2Θ range for data collection/°	4.688 to 56.712
Index ranges	$-10 \le h \le 10$, $-12 \le k \le 12$, $-13 \le l \le 13$
Reflections collected	24164
Independent reflections	3594 [R_{int} = 0.0773, R_{sigma} = 0.0496]
Data/restraints/parameters	3594/0/219

Goodness-of-fit on F^2	1.061
Final R indexes [$I \geq 2\sigma(I)$]	$R_1 = 0.0504$, $wR_2 = 0.1114$
Final R indexes [all data]	$R_1 = 0.0732$, $wR_2 = 0.1219$
Largest diff. peak/hole /e Å^{-3}	0.46/−0.44

Single-crystal X-ray Data and Structure Refinement for Pyrene-4,5,9,10-tetra(ethyleneglycol)ketal (7)

Clear colorless cubes were grown by slow evaporation from $CHCl_3$.

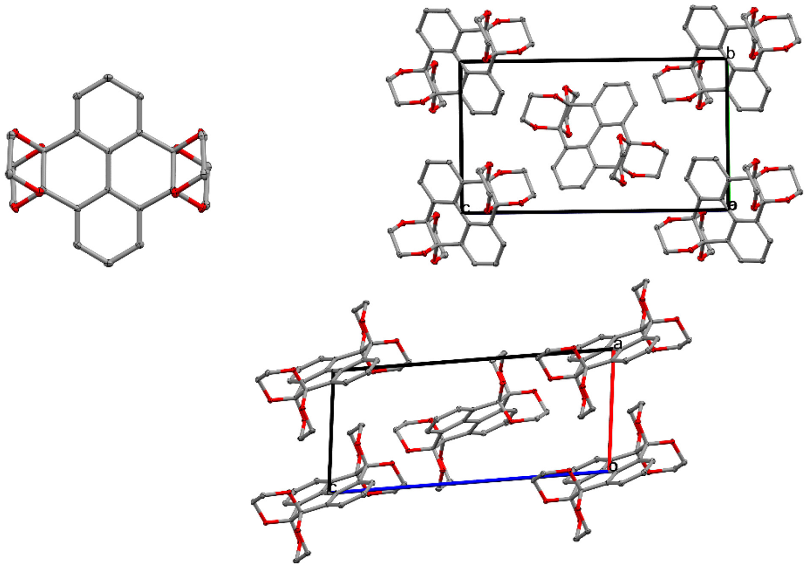

Figure A. 39. X-ray structure of **7** at 100 K. Ellipsoids are shown at 50% probability, hydrogen atoms are omitted for clarity. Color code: carbon, grey, oxygen, red.

Table A 6. Crystal data and structure refinement for **7**.

CCDC Deposition number	2049516
Empirical formula	$C_{24}H_{22}O_8$
Formula weight	438.41
Temperature/K	100.01
Crystal system	monoclinic
Space group	$P2_1/n$
a/Å	6.866(3)
b/Å	8.750(3)
c/Å	15.594(6)
α/°	90
β/°	96.617(16)
γ/°	90
Volume/Å^3	930.6(6)

Z	2
ρ_{calc}g/cm^3	1.565
μ/mm^{-1}	0.118
F(000)	460.0
Crystal size/mm^3	0.13 × 0.1 × 0.08
Radiation	MoKα (λ = 0.71073)
2Θ range for data collection/°	5.26 to 61.186
Index ranges	$-9 \leq h \leq 9$, $-12 \leq k \leq 12$, $-22 \leq l \leq 22$
Reflections collected	34316
Independent reflections	2855 [R_{int} = 0.0719, R_{sigma} = 0.0306]
Data/restraints/parameters	2855/0/145
Goodness-of-fit on F^2	1.041
Final R indexes [$I \geq 2\sigma(I)$]	R_1 = 0.0411, wR_2 = 0.1059
Final R indexes [all data]	R_1 = 0.0496, wR_2 = 0.1110
Largest diff. peak/hole /e Å^{-3}	0.56/−0.28

Single-crystal X-ray Data and Structure Refinement for 2,7-Bis-pinacolatoboron-pyren-4,5,9,10-tetra(ethyleneglycol)ketal (6)

Clear colorless blocks were grown via slow evaporation from a $CDCl_3$ solution.

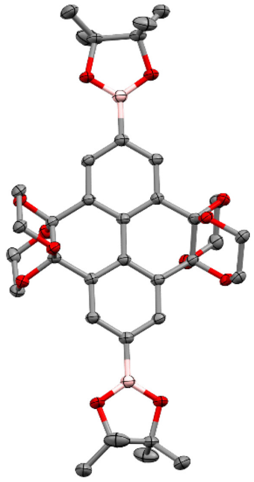

Figure A. 40. X-ray structure of **6** at 100 K. Ellipsoids are shown at 50% probability, hydrogen atoms are omitted for clarity. Color code: carbon, grey; oxygen, red; boron, rosé.

Table A 7. Crystal data and structure refinement for **6.**

CCDC Deposition number	2049515
Empirical formula	$C_{36}H_{44}B_2O_{12}$
Formula weight	690.33
Temperature/K	100.15

Crystal system	trigonal
Space group	$P3_121$
a/Å	10.1130(8)
b/Å	10.1130(8)
c/Å	28.979(2)
α/°	90
β/°	90
γ/°	120
Volume/Å^3	2566.7(4)
Z	3
ρ_{calc}g/cm^3	1.340
μ/mm^{-1}	0.818
F(000)	1098.0
Crystal size/mm^3	0.1 × 0.1 × 0.1
Radiation	CuKα (λ = 1.54178)
2Θ range for data collection/°	10.1 to 144.992
Index ranges	$-12 \le h \le 12$, $-12 \le k \le 12$, $-35 \le l \le 35$
Reflections collected	52326
Independent reflections	3399 [R_{int} = 0.1063, R_{sigma} = 0.0333]
Data/restraints/parameters	3399/0/231
Goodness-of-fit on F^2	1.019
Final R indexes [$I \ge 2\sigma$ (I)]	R_1 = 0.0439, wR_2 = 0.1123
Final R indexes [all data]	R_1 = 0.0515, wR_2 = 0.1174
Largest diff. peak/hole /e Å^{-3}	0.86/−0.20

Single-crystal X-ray Data, Structure Refinement and Structure analysis for 5[4]

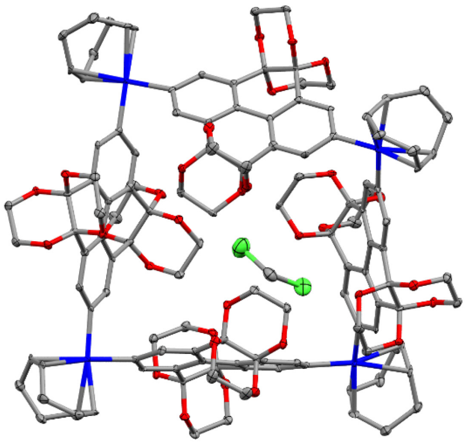

Figure A. 41. X-ray structure of **5[4]** at 100 K. Ellipsoids are shown at 50% probability, hydrogen atoms are omitted for clarity. Color code: carbon, grey; oxygen, red; chlorine, green; platinum, blue.

Table A 8. Crystal data and structure refinement for **5[4]**.

CCDC Deposition number	2049559
Empirical formula	$C_{128}H_{128}O_{32}Pt_4 \cdot 4(CH_2Cl_2)$
Formula weight	3298.36
Temperature/K	100.0
Crystal system	tetragonal
Space group	$I4_1/acd$
a/Å	31.4833(8)
b/Å	31.4833(8)
c/Å	35.7073(11)
α/°	90
β/°	90
γ/°	90
Volume/Å^3	35393(2)
Z	8
ρ_{calc}g/cm^3	1.238
μ/mm^{-1}	3.329
$F(000)$	13056.0
Crystal size/mm^3	0.461 × 0.291 × 0.11
Radiation	MoKα (λ = 0.71073)
2Θ range for data collection/°	4.482 to 52.166
Index ranges	$-38 \le h \le 38$, $-38 \le k \le 38$, $-44 \le l \le 44$
Reflections collected	549070
Independent reflections	8768 [R_{int} = 0.0973, R_{sigma} = 0.0163]
Data/restraints/parameters	8768/0/397
Goodness-of-fit on F^2	1.048
Final R indexes [I>=2σ (I)]	R_1 = 0.0277, wR_2 = 0.0700
Final R indexes [all data]	R_1 = 0.0376, wR_2 = 0.0762
Largest diff. peak/hole / e Å^{-3}	0.63/-0.73

Single-crystal X-ray Data, Structure Refinement and Structure analysis for 4[4]

Yellow cuboids were grown via layer diffusion of MeOH into a $CDCl_3$ solution of the compound.

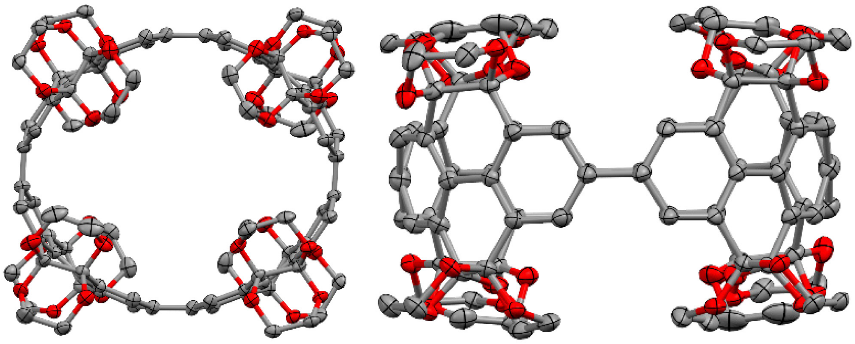

Figure A. 42. X-ray structure of **4[4]** at 100 K. Ellipsoids are shown at 50% probability, hydrogen atoms and solvent molecules are omitted for clarity. Color code: carbon, grey; oxygen; red.

Table A 9. Crystal data and structure refinement for **4[4]**.

CCDC Deposition number	2050148
Empirical formula	$C_{96}H_{78}O_{32}$
Formula weight	1743.58
Temperature/K	100.0
Crystal system	triclinic
Space group	*P*-1
a/Å	14.1927(11)
b/Å	14.2123(13)
c/Å	15.9989(14)
α/°	103.089(3)
β/°	112.535(3)
γ/°	100.195(3)
Volume/Å^3	2775.7(4)
Z	1
ρ_{calc}g/cm^3	1.043
μ/mm^{-1}	0.079
F(000)	910.0
Crystal size/mm^3	0.17 × 0.126 × 0.124
Radiation	MoKα (λ = 0.71073)
2Θ range for data collection/°	3.764 to 50.92
Index ranges	$-17 \le h \le 17$, $-17 \le k \le 17$, $-19 \le l \le 19$
Reflections collected	108475
Independent reflections	10206 [R_{int} = 0.0562, R_{sigma} = 0.0253]
Data/restraints/parameters	10206/0/577

Goodness-of-fit on F^2	1.114
Final R indexes [$I \geq 2\sigma(I)$]	$R_1 = 0.0655$, $wR_2 = 0.1743$
Final R indexes [all data]	$R_1 = 0.0822$, $wR_2 = 0.1852$
Largest diff. peak/hole /e Å^{-3}	0.57/−0.44

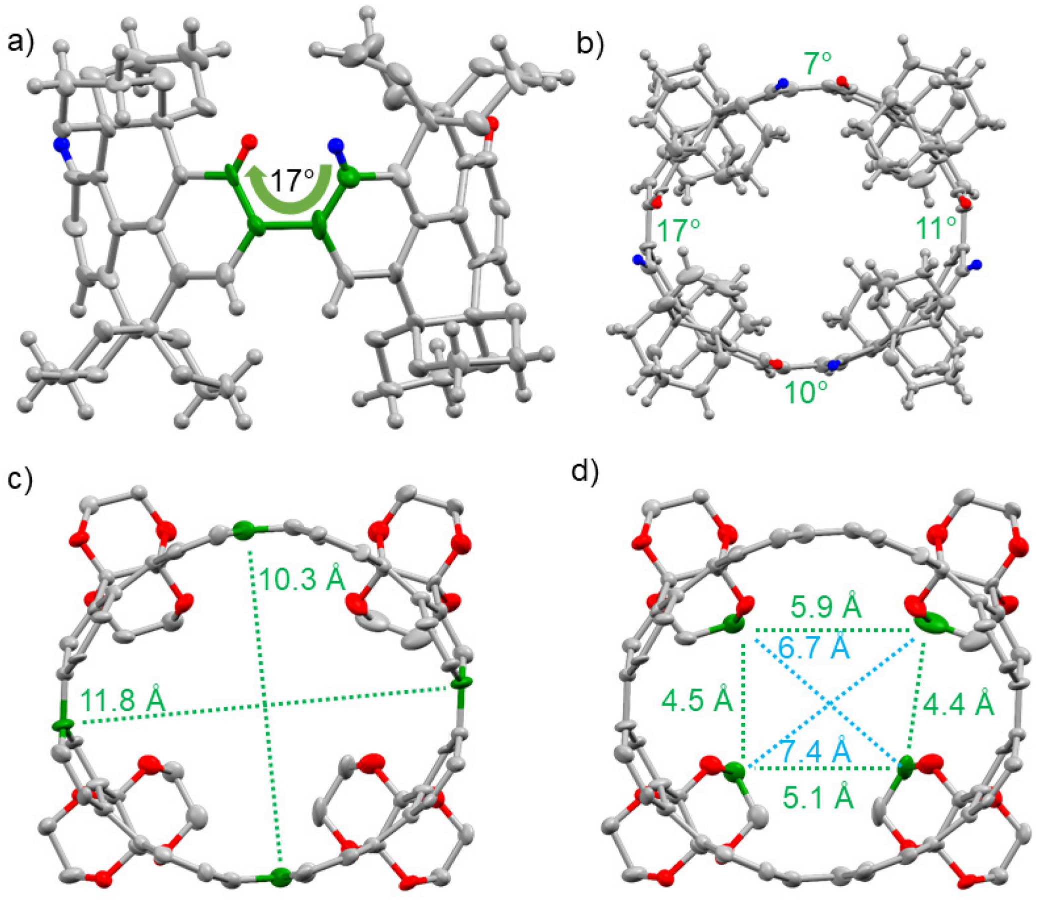

Figure A. 43. a) Exemplary representation of dihedral angle measurement (green); b) dihedral angles (green) between the different pyrene units, according H atoms pointing into the ring center are marked red and out of the ring center are marked blue; c) short and long diameter in the central plane of the molecule between the respective carbon atoms (green); d) heavy atom distances between the carbons atoms (green) of the protecting groups marking the opening of the internal molecular cavity.

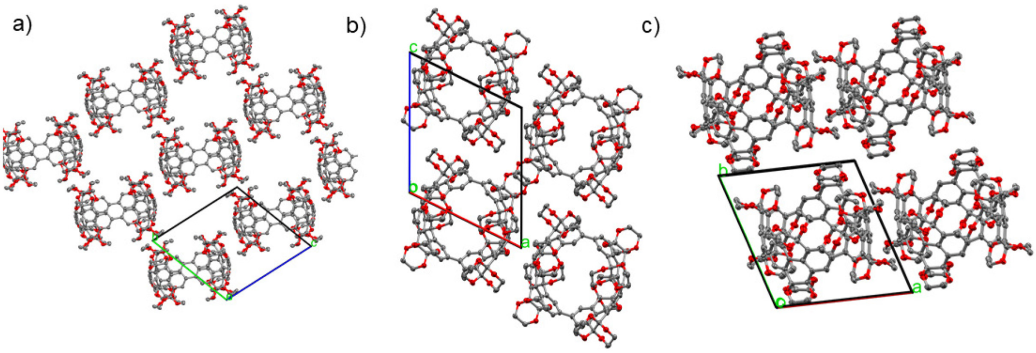

Figure A. 44. Single crystal X-ray packing of **4[4]** a) along the *a*-axis, b) along the *b*-axis, c) along the *c*-axis.

Single-crystal X-ray Data, Structure Refinement and Structure analysis for 4[6]

Clear plates were grown via slow evaporation from a $CHCl_3$ solution.

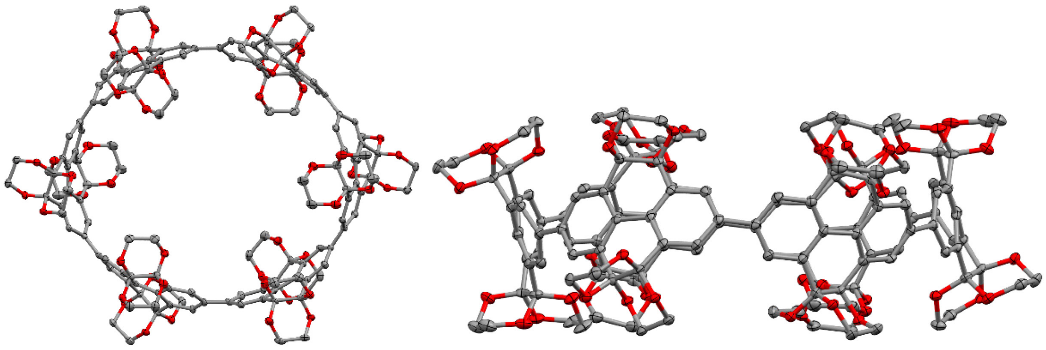

Figure A. 45. X-ray structure of **4[6]** at 100 K. Ellipsoids are shown at 50% probability, hydrogen atoms and solvent molecules are omitted for clarity. Color code: carbon, grey; oxygen, red.

Table A 10. Crystal data and structure refinement for **4[6].**

CCDC Deposition number	1876252
Empirical formula	$C_{144}H_{120}O_{48} \cdot 18\ CHCl_3$
Formula weight	4767.02
Temperature/K	100.15
Crystal system	triclinic
Space group	*P*-1
a/Å	14.5936(12)
b/Å	18.1558(15)
c/Å	20.4131(18)
α/°	93.925(3)
β/°	99.896(3)
γ/°	103.790(3)
Volume/Å^3	5140.6(8)

Z	1
ρ_{calc}g/cm^3	1.540
μ/mm^{-1}	0.780
$F(000)$	2412.0
Crystal size/mm^3	0.1 × 0.1 × 0.1
Radiation	MoKα (λ = 0.71073)
2Θ range for data collection/°	3.88 to 51.54
Index ranges	$-17 \le h \le 17$, $-22 \le k \le 22$, $-24 \le l \le 24$
Reflections collected	207617
Independent reflections	19611 [R_{int} = 0.1092, R_{sigma} = 0.0494]
Data/restraints/parameters	19611/0/1189
Goodness-of-fit on F^2	1.032
Final R indexes [$I \ge 2\sigma(I)$]	R_1 = 0.0858, wR_2 = 0.2253
Final R indexes [all data]	R_1 = 0.1231, wR_2 = 0.2546
Largest diff. peak/hole /e Å^{-3}	2.12/−1.45

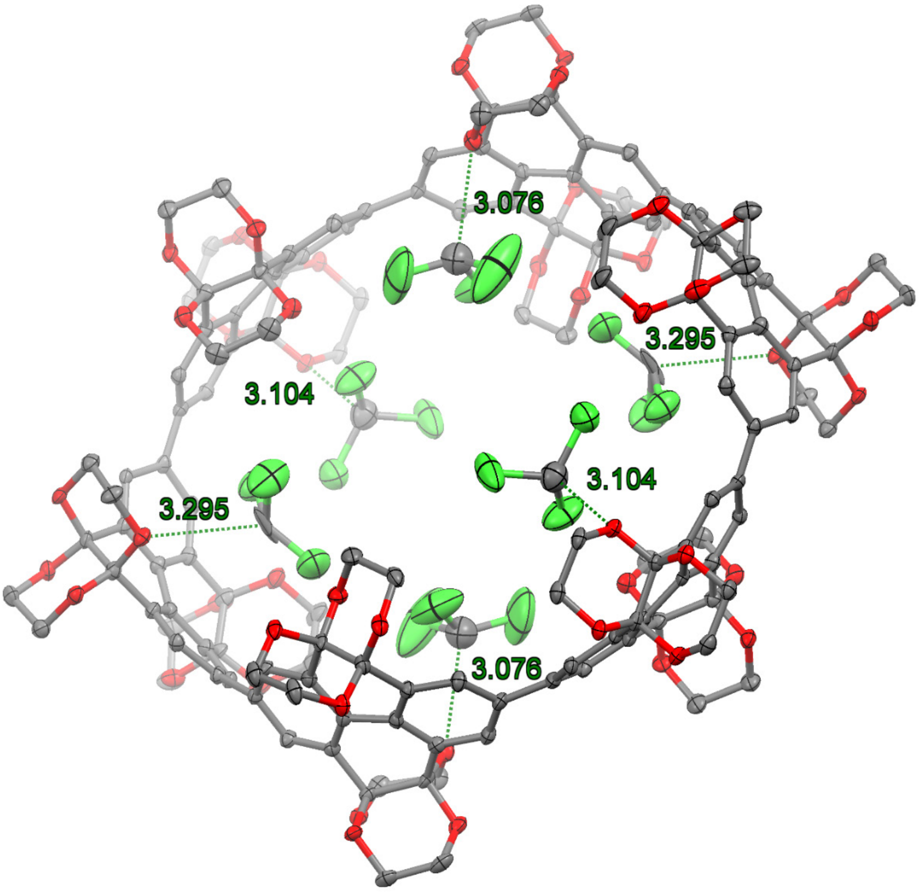

Figure A. 46. Singe-crystal X-ray structures of **4[6]** and six chloroform molecules within the cavity. The green dashed lines show the heavy atom distance between the chloroform carbon and the ethylene glycol oxygen demonstrating C–H···O hydrogen bonding. Distances in Å.

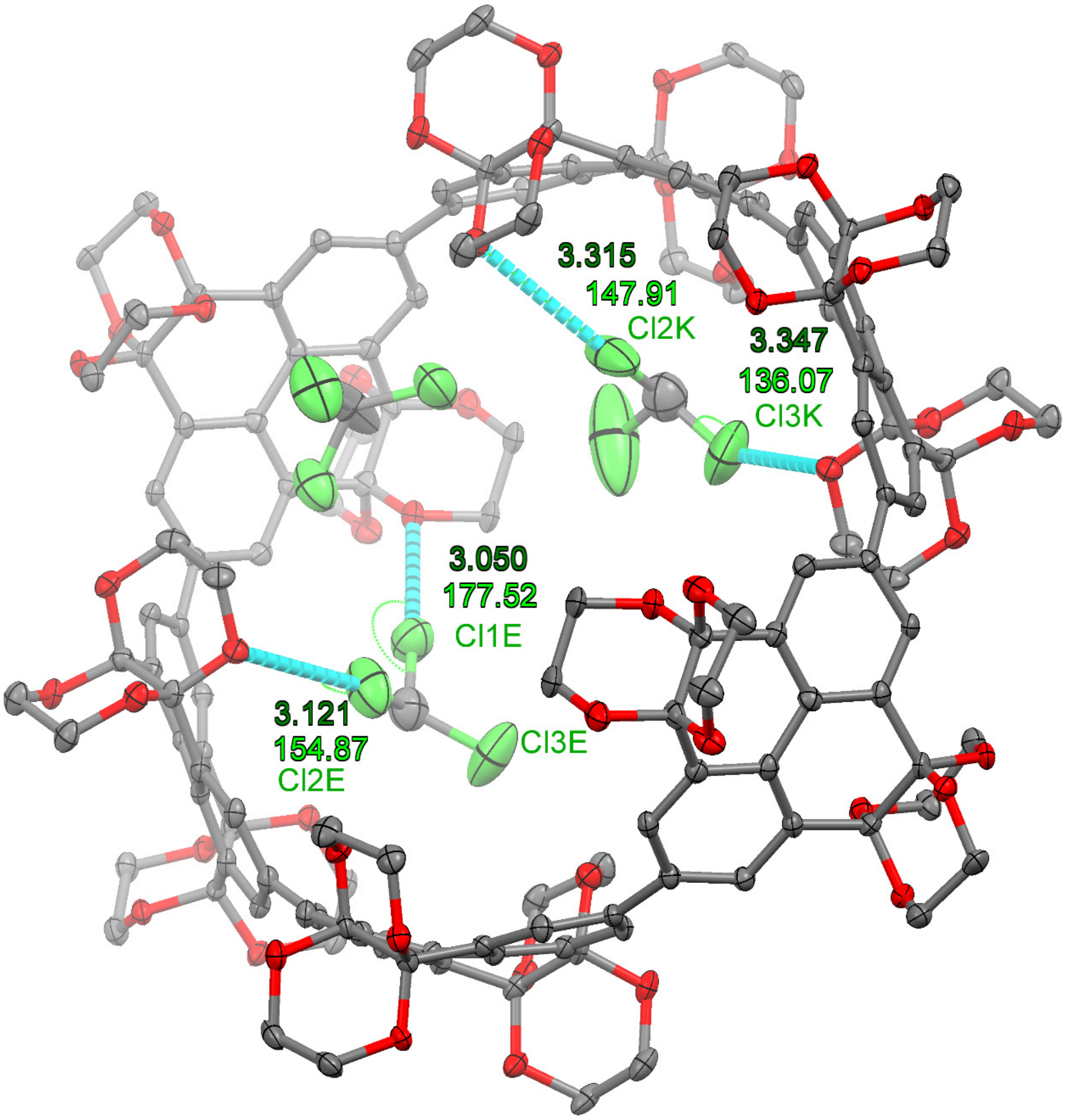

Figure A. 47. Singe-crystal X-ray structures of **4[6]** and three chloroform molecules inside the cavity. The light blue dashed lines show the heavy atom distance between the chloroform chlorine and the ethylene glycol oxygen demonstrating C–Cl··· O halogen bonding. Distances (dark green) in Å, angles (light green) in degree (top).

XB inside the cavity:

1. Angle(O···Cl—C) = 178°, *d*(O···Cl) = 3.05 Å, 7% below the sum of the vdW radii (at chlorine 1E).

additional weak XB:

2. angle(O···Cl—C) = 154°, *d*(O···Cl) = 3.12 Å, 5% below the sum of the vdW radii (at chlorine 2E).

3. angle(O···Cl—C) = 148°, *d*(O···Cl) = 3.32 Å, 4% below the sum of the vdW radii (at chlorine 2K).

4. angle(O···Cl—C) = 136°, *d*(O···Cl) = 3.35 Å, 3% below the sum of the vdW radii (at chlorine 3K).

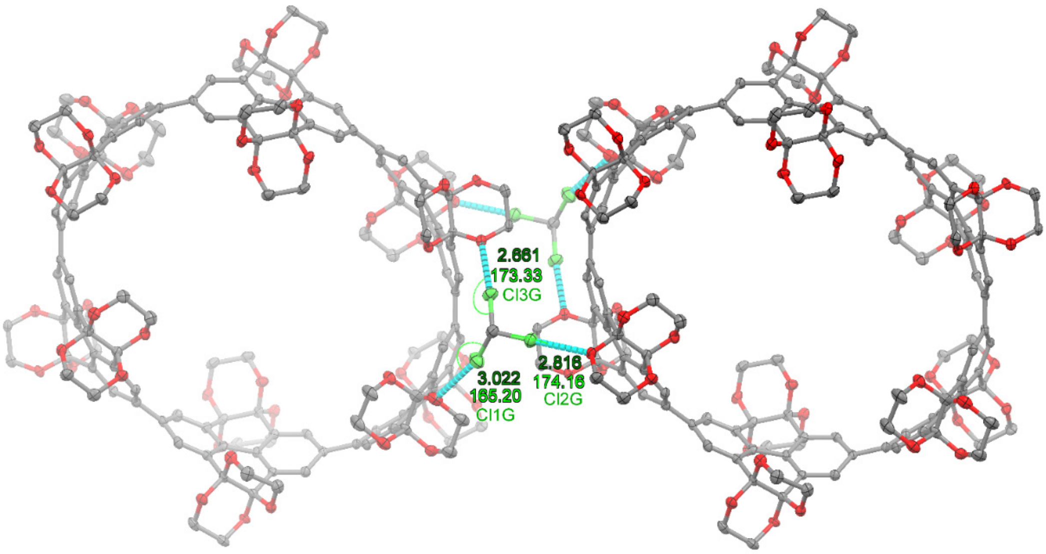

Figure A. 48. Singe-crystal X-ray structures of two molecules of **4[6]** interconnected by two chloroform molecules. Each chlorine is part of a C–Cl···O halogen bond shown with the light blue dashed lines (angles C–Cl···O in ° (light green), $d_{Cl\cdots O}$ in Å (dark green)).

Ring-to-ring side-on packing along one dimension of **4[6]** is dominated by an impressive network of six halogen bonds, where two chloroform solvates contribute with all six chlorine atoms to very short Cl···O distances with down to –19% of the sum of the vdW radii (*r*(Cl) + *r*(O)= 327 pm) and nearly linear angles O···Cl–C of 165°–174°. Additional halogen bonds are found inside the cavity, where chloroform solvates gain structural resolution through a combination of O···Cl (178°, –7% vdWr) interactions and O···H–CCl_3 hydrogen bonds.

Ring-to-ring $CHCl_3$-mediated XB:

5. angle(O···Cl—C) = 173°, *d*(O···Cl) = 2.66 Å, 19% below the sum of the vdW radii (at chlorine 3G).

6. angle(O···Cl—C) = 174°, *d*(O···Cl) = 2.82 Å, 14% below the sum of the vdW radii (at chlorine 2G).

7. angle(O···Cl—C) = 165°, *d*(O···Cl) = 3.02 Å, 8% below the sum of the vdW radii (at chlorine 1G)

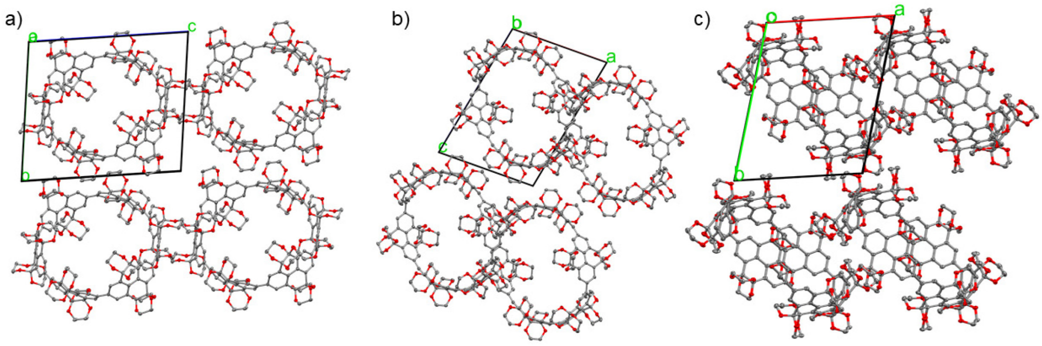

Figure A. 49. Single crystal X-ray packing of **4[6]** a) along the *a*-axis, b) along the *b*-axis, c) along the *c*-axis.

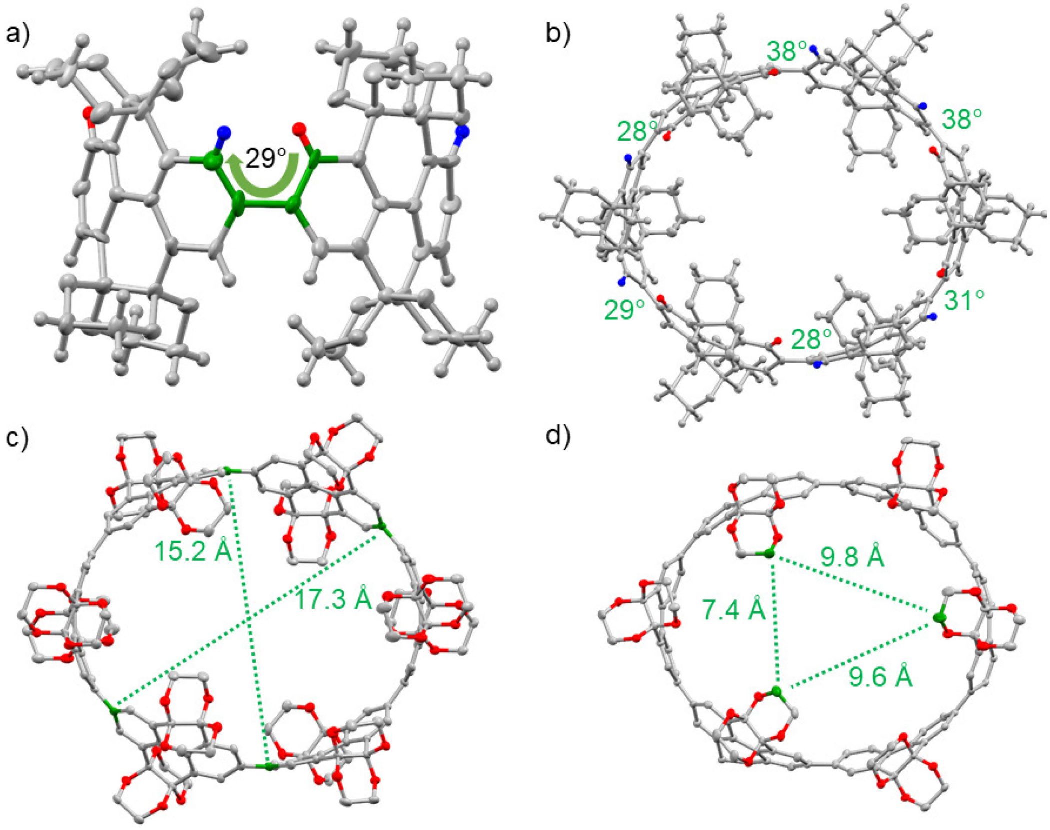

Figure A. 50. a) Exemplary representation of dihedral angle is measurements (green); b) dihedral angles (green) between the different pyrene units, according H atoms pointing into the ring center are marked red and out of the ring center are marked blue; c) short and long diameter in the central plane of the molecule between the respective carbon atoms (green); d) heavy atom distances between the carbons atoms (green) of the ethylene glycol protecting groups marking the opening of the internal molecular cavity.

Single-crystal X-ray Data, Structure Refinement and Structure analysis for 4[5] ···18-crown-6·K(BF4)

Golden rods were grown via layer diffusion of MeOH into a $CHCl_3$ solution of **4[5]** and an excess of 18-crown-6 as well as KBF_4 at 23 °C. The data was collected at the MX 14.2 Beamline of the BESSYII synchrotron at the Helmholtz-Zentrum Berlin. The low completeness is due to lack of full angular freedom of the sample holder (missing four-circle kappa goniometer) at this beamline. A full data collection on this triclinic (*P*-1) crystal was therefore not obtained. Reflections of multiple crystals were collected, each in different orientation, and gave the same result after refinement each. The large displacement parameters are due to the disorder of the $CHCl_3$ solvent molecules and the BF_4^- anion that could not be improved further. Despite several attempts in other solvents (DMSO, 1,2-dichlorobenzene) and different techniques (vapor diffusion, slow evaporation) higher quality crystals could not be grown.

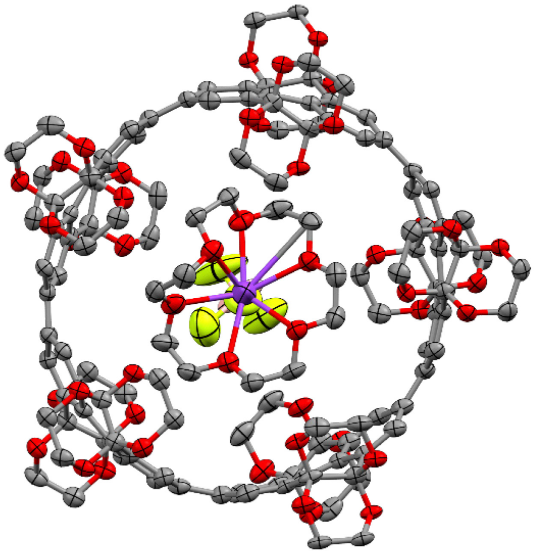

Figure A. 51. **X**-ray structure of **4[5]**···18-crown-6·K(BF_4) at 100 K. Ellipsoids are shown at 50% probability, hydrogen atoms, solvent molecules, and disorder are omitted for clarity. Color code: carbon, grey; oxygen, red; potassium, purple; fluorine, yellow; boron, rosé.

Table A 11. Crystal data and structure refinement for **4[5]**···18-crown-6·K(BF_4).

CCDC Deposition number	2049763
Empirical formula	$C_{132}H_{124}BF_4KO_{46} \cdot 4\ CHCl_3$
Formula weight	3049.69
Temperature/K	100
Crystal system	triclinic
Space group	*P*-1
a/Å	11.020(2)
b/Å	19.153(4)
c/Å	31.999(6)
α/°	87.92(3)
β/°	81.74(3)
γ/°	82.00(3)

Volume/Å^3	6618(2)
Z	2
ρ_{calc}g/cm^3	1.530
μ/mm^{-1}	0.379
F(000)	3152.0
Crystal size/mm^3	0.1 × 0.1 × 0.1
Radiation	Synchrotron (λ = 0.82656)
2Θ range for data collection/°	1.286 to 48.814
Index ranges	$-12 \leq h \leq 12$, $-20 \leq k \leq 20$, $-37 \leq l \leq 37$
Reflections collected	70246
Independent reflections	19999 [R_{int} = 0.0662, R_{sigma} = 0.0591]
Data/restraints/parameters	19999/224/1847
Goodness-of-fit on F^2	1.560
Final R indexes [$I \geq 2\sigma(I)$]	R_1 = 0.1283, wR_2 = 0.3787
Final R indexes [all data]	R_1 = 0.1687, wR_2 = 0.4098
Largest diff. peak/hole /e Å^{-3}	1.59/–1.17

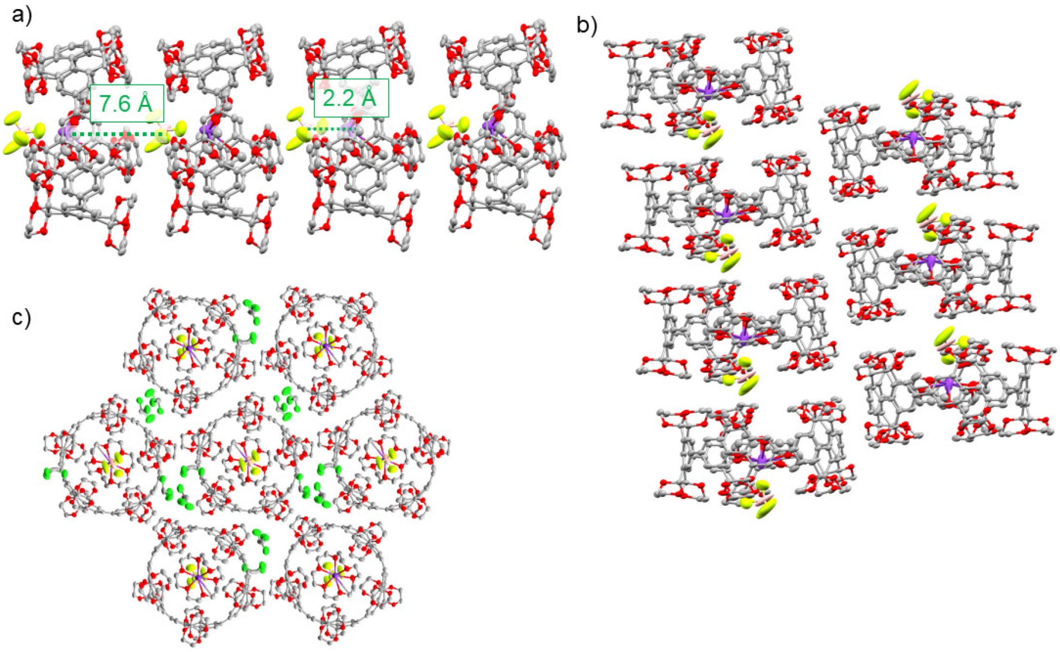

Figure A. 52. a) Columnar packing of **4[5]**···18-crown-6·K(BF$_4$) without solvent, showing the distances between the K$^+$ cation and the BF$_4^-$ anion; b) anti-parallel packing of two neighboring columns; c) cross-section through columnar packed **4[5]**···18-crown-6·K(BF$_4$) with solvent molecules.

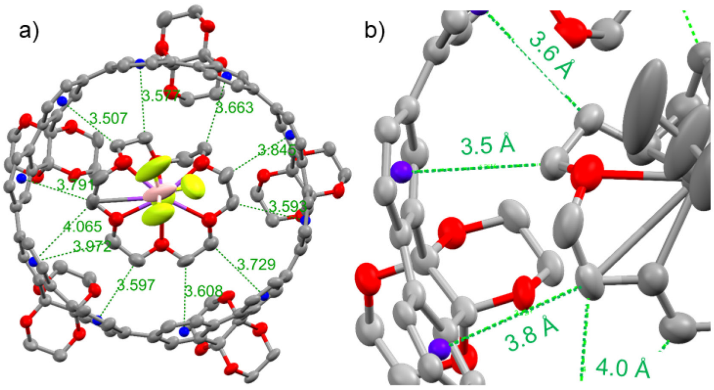

c)

CH-π	Distance [Å]	∅ [Å]
1	3.5	3.7
2	3.6	
3	3.7	
4	3.8	
5	3.6	
6	3.7	
7	3.6	
8	3.6	
9	4.0	
10	3.8	

Figure A. 53. a) Heavy atom distances (in Å) between the blue centroids places in the middle of the individual phenyl rings and the closest carbon atoms of the 18-crown-6 ether moiety; b) enlarged representation of the interaction; c) table showing all heavy atom distances between the constructed centroids of the regarding phenyl rings and the carbon atoms of the 18-crown-6 ether.

For the following representation of hydrogen bonds in the crystal structure between host and guest, the guest is colored and divided into three different sections.

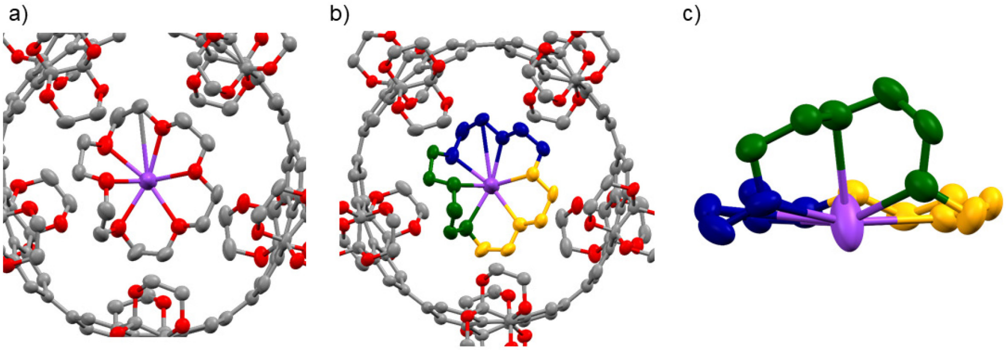

Figure A. 54. a) Enlarged view on the 18-crown-6·K$^+$ inside the cavity, b) coloring of the guest resulting in three parts, c) enlarged view on the colored guest.

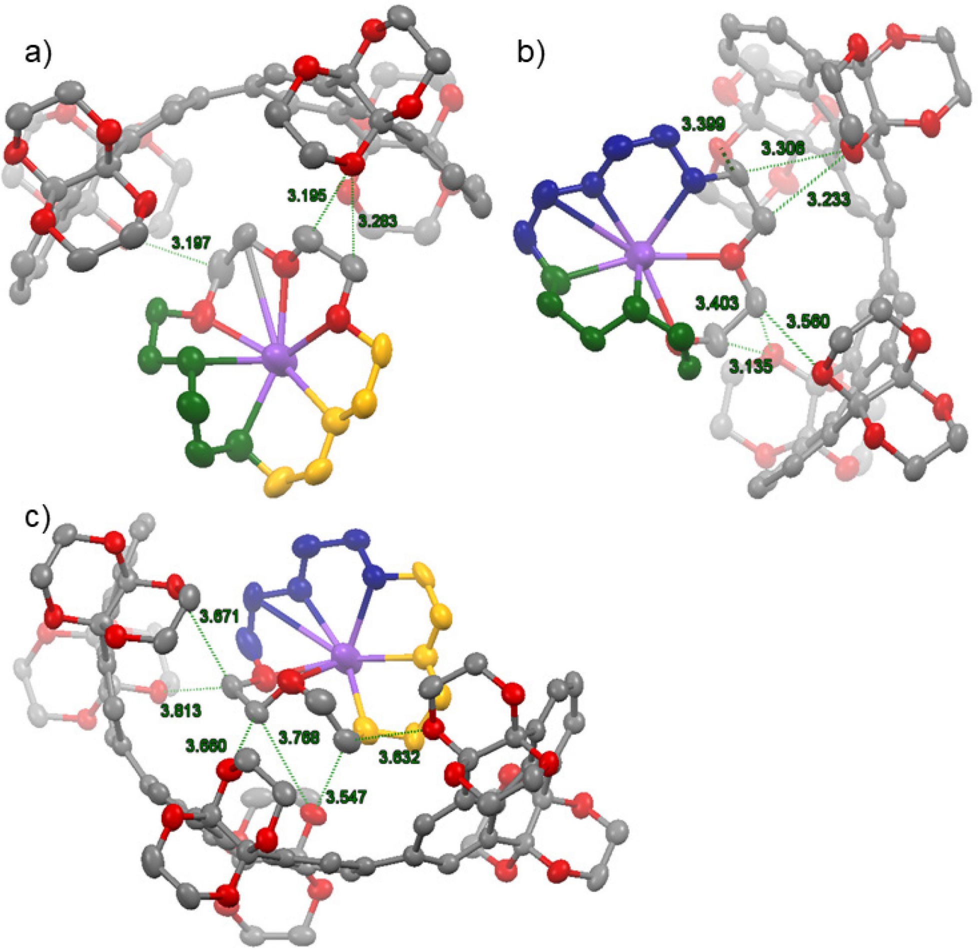

Figure A. 55. a) Close contacts (in Å) between the blue part of the guest and the host; b) close contacts (in Å) between the blue part of the guest and the host; c) close contacts (in Å) between the blue part of the guest and the host.

Geometrical Considerations and Volume Analysis of the Hosts [n]Cyclo-pyrenylenes **4[4–8]**

The following section shows single crystal X-ray and geometry optimized structures (B3LYP-D3/def2SVP) of **4[4–8]** and the heavy atom distances, which define the diameter (d_{cavity}) of the opening and the diameter of the cavity (d_{gate}) in the corresponding macrocycle. Eventually, the average is used to calculate the ratio q between the two parameters.

$$q = \frac{d_{\text{gate}}}{d_{\text{cavity}}} \qquad \text{(Equation A1)}$$

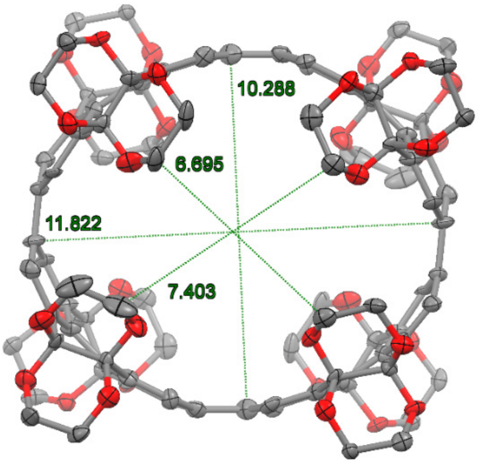

Figure A. 56. Single crystal X-ray structure of **4[4]**, the dashed green lines mark the heavy atom distance between the C atoms of d_{cavity} (11.822 Å, 10.288 Å), and the heavy atom distance between the C atoms of d_{gate} (6.695 Å, 7.403 Å).

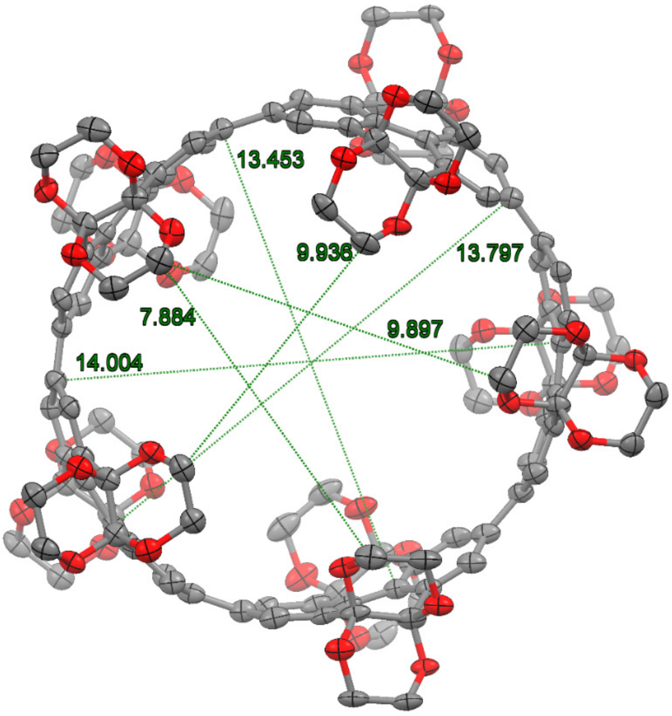

Figure A. 57. Single crystal X-ray structure of **4[5]** (without guest and solvent molecules), the dashed green lines mark the heavy atom distance between the C atoms of d_{cavity} (14.004 Å, 13.453 Å, 13.797 Å), and the heavy atom distance between the C atoms of d_{gate} (7.884 Å, 9.897 Å, 9.936 Å).

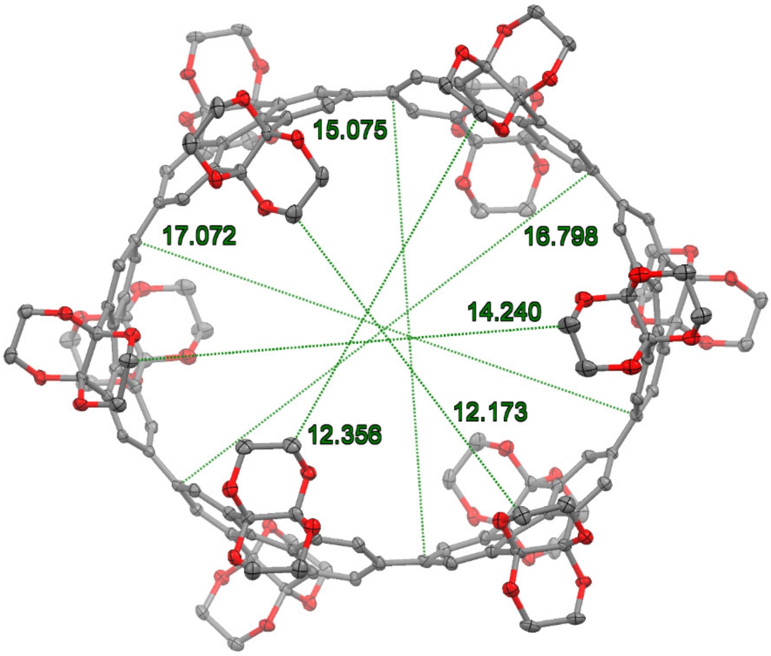

Figure A. 58. Single crystal X-ray structure of **4[6]**, the dashed green lines mark the heavy atom distance between the C atoms of d_{cavity} (17.072 Å, 15.075 Å, 16.798 Å), and the heavy atom distance between the C atoms of d_{gate} (12.356 Å, 12.173 Å, 14.240 Å).

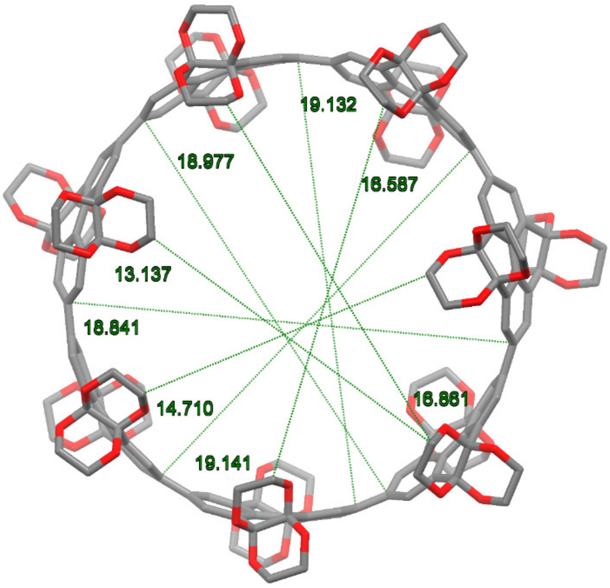

Figure A. 59. Geometry optimized structure of **4[7]**, the dashed green lines mark the heavy atom distance between the C atoms of d_{cavity} (18.977 Å, 19.132 Å, 18.841 Å, 19.141 Å), and the heavy atom distance between the C atoms of d_{gate} (14.710 Å, 13.137 Å, 16.587 Å, 16.861 Å).

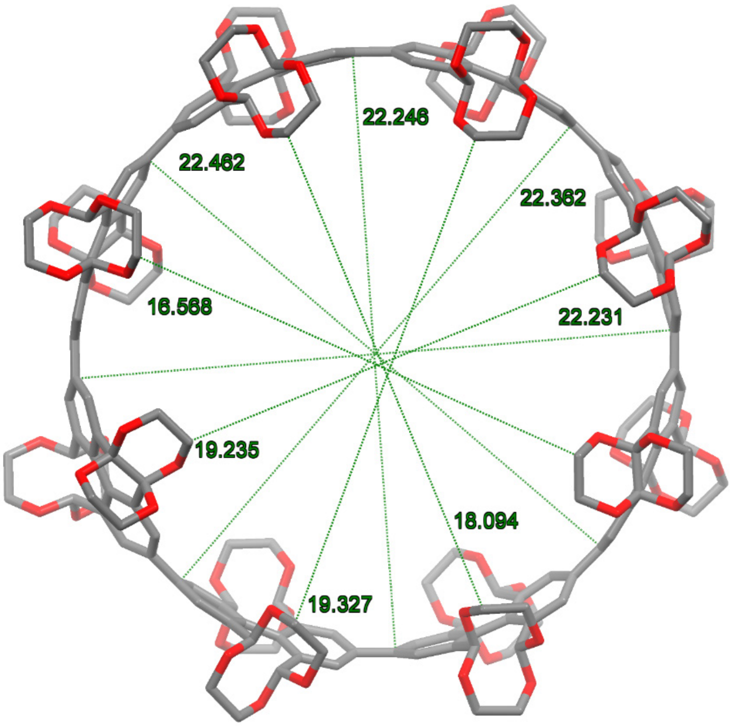

Figure A. 60. Geometry optimized structure of **4[8]**, the dashed green lines mark the heavy atom distance between the C atoms of d_{cavity} (22.462 Å, 22.246 Å, 22.362 Å, 22.231 Å), and the heavy atom distance between the C atoms of d_{gate} (16.568 Å, 19.235 Å, 19.327 Å, 18.094 Å).

Table A 12. The average of d_{cavity}, d_{gate}, and the corresponding ratio to determine the degree of confinement of the space within the presented macrocycles.

	4[4]	**4[5]**	**4[6]**	**4[7]**	**4[8]**
Average d_{cavity} [Å]	11.055	13.751	16.315	19.023	22.325
Average d_{gate} [Å]	7.049	9.239	12.923	15.324	18.306
	64%	67%	79%	81%	82%

X-ray single-crystal data and structure refinement for 1,3(3,6)-bis(phenanthrena-9,10-di(ethyleneglycol)ketal)-2,4(1,3)-dibenzenacyclotetraphane (11)

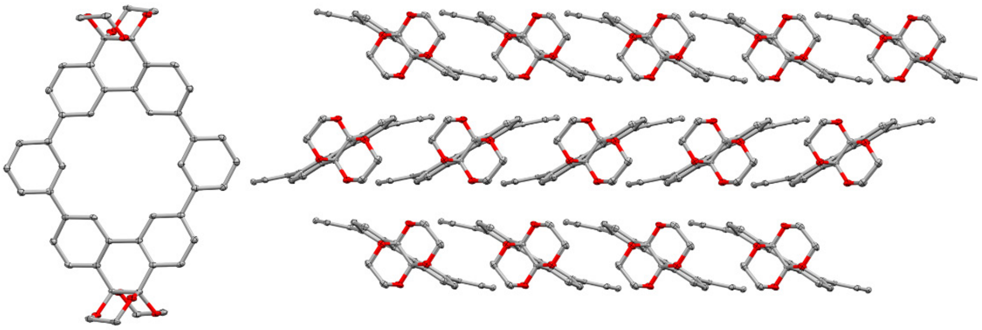

Figure A. 61 Singe-crystal X-ray structure of macrocycle **11** at 100 K. Solvent molecules and hydrogen atoms are omitted for clarity. The ellipsoids are displayed at 50% probability level. R_1 = 4.01%. The crystals were grown by layer diffusion of hexane into a saturated solution of 4 in $CHCl_3$ over 3 days at 25 °C. Color code: C, gray; O, red.

Table A 13. X-ray single crystal data and structure refinement for of macrocycle **11**.

CCDC No.	2209128
Empirical formula	$C_{48}H_{36}O_8\cdot CDCl_3$
Formula weight	740.77
Temperature/K	100.04
Crystal system	orthorhombic
Space group	*Cmce*
a/Å	36.174(2)
b/Å	7.4547(5)
c/Å	12.4206(8)
α/°	90
β/°	90
γ/°	90
Volume/Å^3	3349.4(4)
Z	4
ρ_{calc}/g cm^{-3}	1.469
μ/mm^{-1}	0.100
F(000)	1552.0
Crystal size/mm^3	0.251 × 0.187 × 0.11
Radiation	MoKα (λ = 0.71073 nm)
2Θ range for data collection/°	4.504 to 51.422
Index ranges	$-44 \le h \le 40$, $-9 \le k \le 9$, $-15 \le l \le 15$
Reflections collected	23285
Independent reflections	1624 [R_{int} = 0.0584, R_{sigma} = 0.0235]
Data/restraints/parameters	1624/0/130
Goodness–of–fit on F^2	1.048
Final *R* indexes [$I \ge 2\sigma(I)$]	R_1 = 0.0401, wR_2 = 0.1013
Final *R* indexes [all data]	R_1 = 0.0500, wR_2 = 0.1067
Largest diff. peak/hole / e Å^{-3}	0.22/–0.27

X-ray single-crystal data and structure refinement for 2^5,4^5-bis(trimethylsilyl)-1,3(3,6)-bis(phenanthrena-9,10-di(ethyleneglycol)ketal)-2,4(1,3)-dibenzenacyclotetraphane (24)

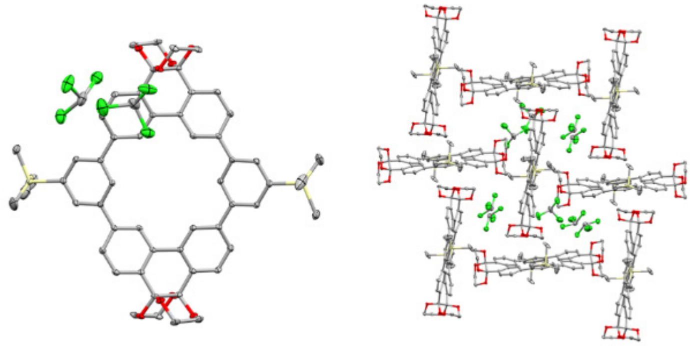

Figure A. 62. The crystal structure as well as the packing of compound **24** is displayed top view and side view. The data were obtained by X-ray diffraction measurements at 100 K. Hydrogen atoms and disorder are omitted for clarity. The ellipsoids are displayed at 50% probability level. R_1 = 6.65%. The crystals were obtained by layer diffusion of cyclohexane into a saturated solution of **24** in $CHCl_3$. Color code: C, gray; O, red; Cl, green; Si, beige.

Table A 14. X-ray single crystal data and structure refinement of silylated macrocycle **24.**

CCDC No.	2033332
Empirical formula	$C_{54}H_{52}O_8Si_2 \cdot 4\ CDCl_3$
Formula weight	1362.60
Temperature/K	100.15
Crystal system	monoclinic
Space group	$C2/c$
a/Å	32.757(3)
b/Å	16.3824(12)
c/Å	13.4938(12)
α/°	90
β/°	101.779(3)
γ/°	90
Volume/Å^3	7088.8(10)
Z	4
ρ_{calc}/g cm^{-3}	1.277
μ/mm^{-1}	0.548
F(000)	2800.0
Crystal size/mm^3	0.586 × 0.334 × 0.22
Radiation	MoKα (λ = 0.71073 nm)
2Θ range for data collection/°	3.962 to 55.034
Index ranges	$-42 \le h \le 42$, $-21 \le k \le 21$, $-17 \le l \le 17$
Reflections collected	175378
Independent reflections	8147 [R_{int} = 0.0394, R_{sigma} = 0.0123]
Data/restraints/parameters	8147/0/394

Goodness–of–fit on F^2	1.138
Final R indexes [$I \geq 2\sigma(I)$]	$R_1 = 0.0665$, $wR_2 = 0.1396$
Final R indexes [all data]	$R_1 = 0.0708$, $wR_2 = 0.1419$
Largest diff. peak/hole / e Å^{-3}	0.83/–0.75

X-ray Single-crystal Data and Structure refinement for 2^5,4^5-diiodo-1,3(3,6)-bis(phenanthrena-9,10-di(ethyleneglycol)ketal)-2,4(1,3)-dibenzenacyclotetraphane (25)

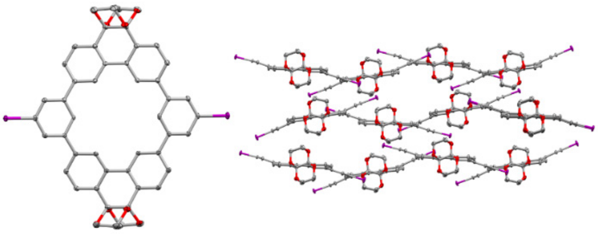

Figure A. 63. The crystal structure as well as the packing of compound **25** is displayed top view and side view. The data were obtained by X-ray diffraction measurements at 100 K. Solvent molecules and hydrogen atoms are omitted for clarity. The electron density attributed to solvent molecules was not modelled due to the severe disorders, and the structures were refined by using the PLATON/SQUEEZE protocol.[327,328] The ellipsoids are displayed at 50% probability level. R_1 = 3.89%. The crystals were obtained by layer diffusion of methanol into a saturated solution of **25** in DMF. Color code: C, gray; O, red; I, purple.

Table A 15. X-ray single crystal data and structure refinement for of iodinated macrocycle **25**.

CCDC No.	2207451
Empirical formula	$C_{48}H_{34}I_2O_8 \cdot CH_3OH$
Formula weight	1024.59
Temperature/K	100.0
Crystal system	orthorhombic
Space group	*Pnnm*
a/Å	11.6919(7)
b/Å	17.5607(12)
c/Å	22.7660(15)
α/°	90
β/°	90
γ/°	90
Volume/Å^3	4674.3(5)
Z	4
ρ_{calc}/g cm^{-3}	1.456
μ/mm^{-1}	1.398
F(000)	2040.0
Crystal size/mm^3	0.281 × 0.177 × 0.058
Radiation	MoKα (λ = 0.71073 nm)
2Θ range for data collection/°	3.916 to 58.312
Index ranges	$-16 \leq h \leq 16$, $-24 \leq k \leq 24$, $-31 \leq l \leq 31$
Reflections collected	133413
Independent reflections	6440 [$R_{int} = 0.0677$, $R_{sigma} = 0.0219$]

Data/restraints/parameters	6440/0/271
Goodness–of–fit on F^2	1.104
Final R indexes [$I \geq 2\sigma(I)$]	R_1 = 0.0389, wR_2 = 0.0790
Final R indexes [all data]	R_1 = 0.0450, wR_2 = 0.0813
Largest diff. peak/hole / e Å^{-3}	1.53/–1.25

X-ray single crystal data und structure refinement for 2^5,4^5-Bis(4,4,5,5-tetramethyl-1,3,2-dioxaborolan-2-yl)-1,3(3,6)-bis(phenanthrena-9,10-di(ethyleneglycol)ketal)-2,4(1,3)-dibenzenacyclotetraphane (20)

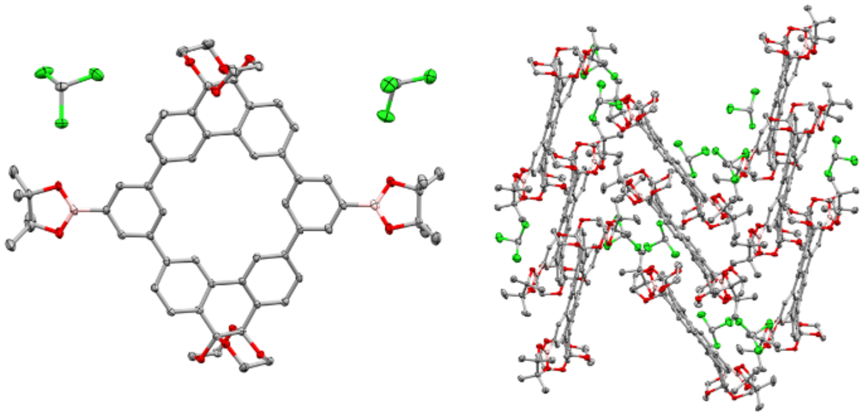

Figure A. 64. The crystal structure as well as the packing of compound **20** is displayed in top view and side view, respectively. The data were obtained by X-ray diffraction measurements at 100 K. Solvent molecules and hydrogen atoms are omitted for clarity. The ellipsoids are displayed at 50% probability level. R_1 = 7.11%. The crystals were obtained by layer diffusion of methanol into a saturated solution of **20** in $CHCl_3$. Color code: C, gray; O, red; Cl, green; B, pink.

Table A 16. X-ray single crystal data and structure refinement for of borylated macrocycle **20.**

CCDC No.	2055826
Empirical formula	$C_{62}H_{58}B_2O_{12} \cdot 2\ CHCl_3$
Formula weight	1231.42
Temperature/K	100.0
Crystal system	monoclinic
Space group	$P2_1/n$
a/Å	19.4455(16)
b/Å	17.2951(14)
c/Å	19.4455(16)
α/°	90
β/°	108.36
γ/°	90
Volume/Å^3	6206.9(9)
Z	4
ρ_{calc}/g cm^{-3}	1.318
μ/mm^{-1}	0.337

$F(000)$	2560.0
Crystal size/mm^3	0.245 × 0.124 × 0.124
Radiation	MoKα (λ = 0.71073 nm)
2Θ range for data collection/°	4.284 to 50.91
Index ranges	$-23 \leq h \leq 23$, $-20 \leq k \leq 20$, $-23 \leq l \leq 23$
Reflections collected	119824
Independent reflections	11395 [R_{int} = 0.0592, R_{sigma} = 0.0247]
Data/restraints/parameters	11395/0/747
Goodness-of-fit on F^2	1.119
Final R indexes [I>=2σ (I)]	R_1 = 0.0711, wR_2 = 0.1658
Final R indexes [all data]	R_1 = 0.0803, wR_2 = 0.1709
Largest diff. peak/hole / e Å^{-3}	1.20/−0.91

X-ray single crystal data und structure refinement for Au-macrocycle (26[4])

Remaining electron density originating from solvent molecules that could not be refined was masked using the solvent mask tool implemented in OLEX2.[326]

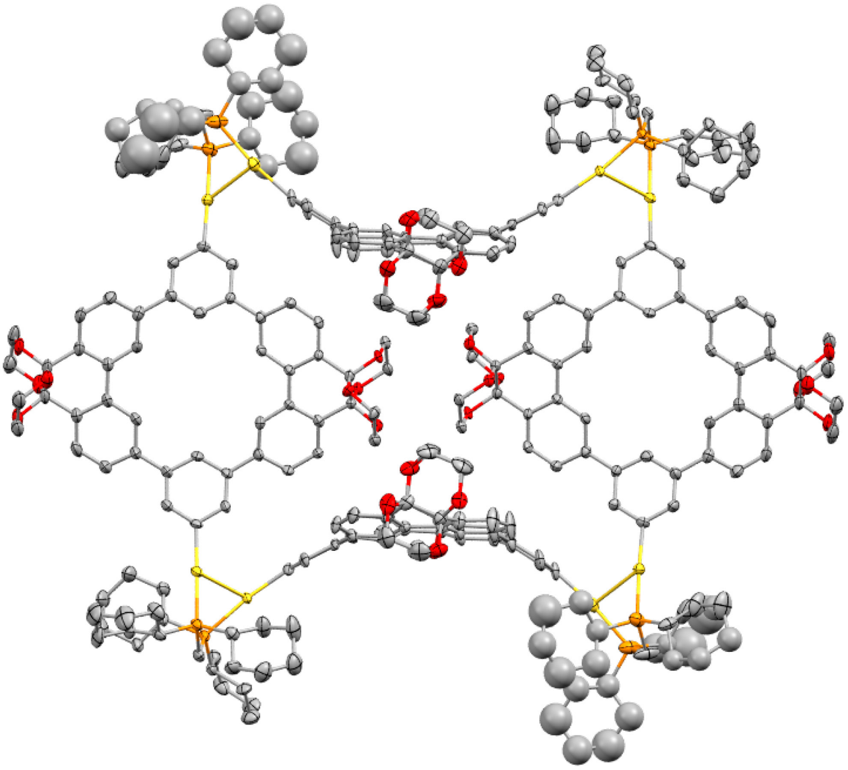

Figure A. 65. The crystal structure of compound **26[4]** is displayed top view. The data were obtained by X-ray diffraction measurements at 100 K. Solvent molecules and hydrogen atoms are omitted for clarity. Non-ellipsoid carbo atoms of the phosphine ligand had to be refined isotropically to obtain a converged model. The ellipsoids are displayed at 50% probability level. R_1 = 5.67%. The crystals were obtained by slow evaporation from a $CDCl_3$ solution. Color code: C, gray; O, red; Cl, green; B, pink.

Table A 17. X-ray single crystal data and structure refinement for of Au-macrocycle **26[4]**.

CCDC No.	2208548
Empirical formula	$C_{292}H_{318}Au_8O_{32}P_8 \cdot 10\ CHCl_3$
Formula weight	7356.62
Temperature/K	100.0
Crystal system	triclinic
Space group	P–1
a/Å	20.9830(8)
b/Å	24.3888(7)
c/Å	24.4181(8)
α/°	83.3270(10)
β/°	72.4010(10)
γ/°	71.8960(10)
Volume/Å^3	11318.0(7)
Z	1
ρ_{calc}/g cm^{-3}	1.079
μ/mm^{-1}	2.830
F(000)	3658.0
Crystal size/mm^3	0.401 × 0.339 × 0.263
Radiation	MoKα (λ = 0.71073 nm)
2Θ range for data collection/°	3.632 to 60.41
Index ranges	$-29 \leq h \leq 29$, $-34 \leq k \leq 34$, $-34 \leq l \leq 34$
Reflections collected	585588
Independent reflections	66909 [R_{int} = 0.1024, R_{sigma} = 0.0626]
Data/restraints/parameters	66909/151/1611
Goodness-of-fit on F^2	1.013
Final R indexes [$I \geq 2\sigma(I)$]	R_1 = 0.0567, wR_2 = 0.1197
Final R indexes [all data]	R_1 = 0.1026, wR_2 = 0.1453
Largest diff. peak/hole / e Å^{-3}	3.02/–2.77

There are several non-covalent interactions that stabilize the conformation of individual molecules within the crystal packing. A key interaction is here the aurophilicity between the Au(I) centers resulting in an Au···Au distance of 3.125 Å and 3.124 Å, creating an angle of 53.06 ° and 48.07°.

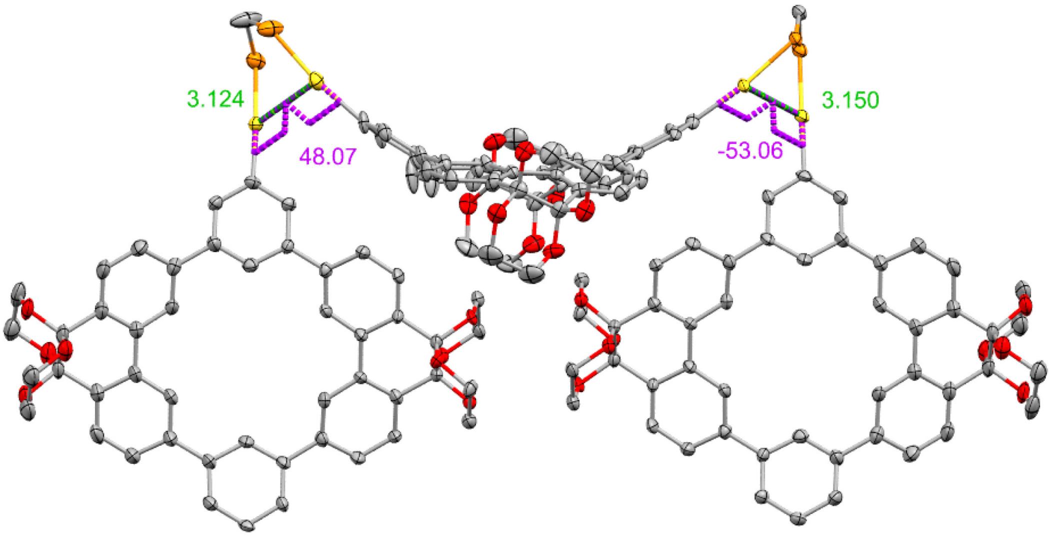

Figure A. 66. Excerpt of the X-ray structure of **26[4]** showing the Au···Au distances in Å (green) and the torsion angles along the C–Au···Au–C bonds in ° (purple).

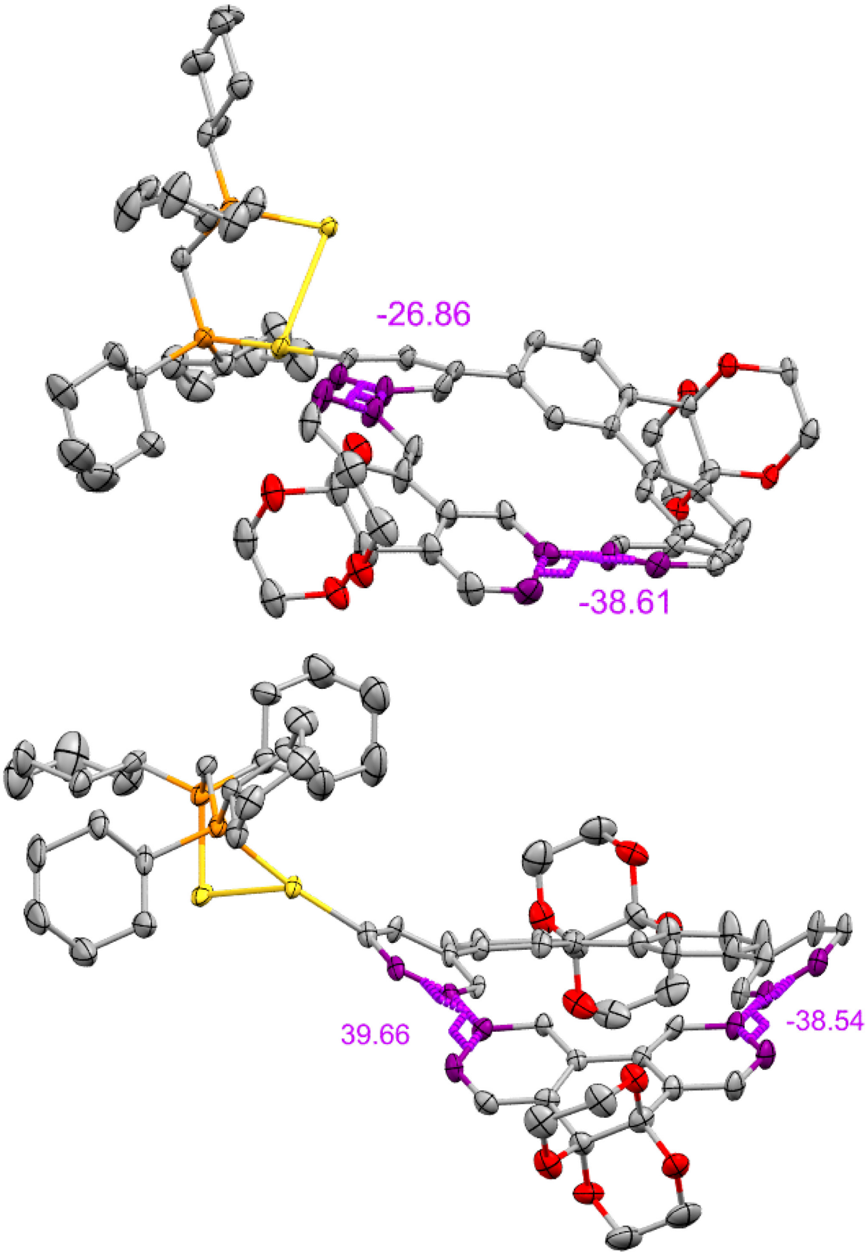

Figure A. 67. Excerpt of the X-ray structure of **26[4]** showing dihedral angle between the phenyl subunit and the phenanthrene subunit (highlighted in purple, angles in °) that lead to a “chair” (top) and a “boat” (bottom) conformation of the individual macrocyclic repeating units.

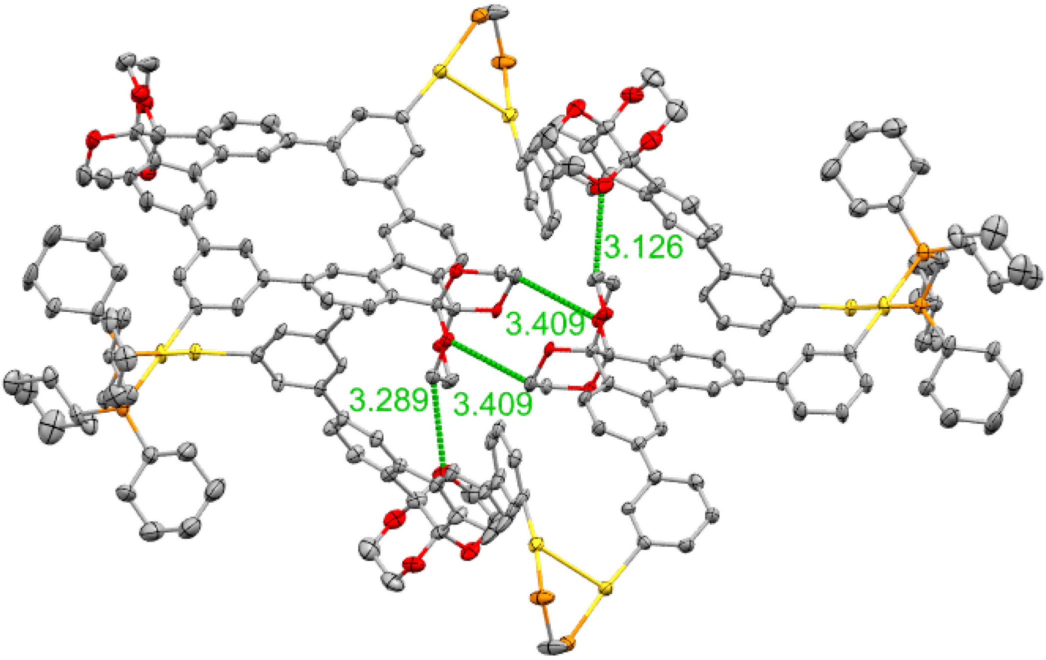

Figure A. 68. Excerpt of the X-ray structure of **26[4]** showing hydrogen bonding network. The heavy atom distances (in Å) of carbon and oxygen atoms engaging in hydrogen bonding between the polarized C–H bonds and the oxygen atoms of the ethylene glycol units in the center of the Au-macrocycle **26[4]** are depicted.

X-ray single crystal data und structure refinement for [4]Cyclo-2^5,4^5-1,3(3,6)-*bis*(phenanthrena-9,10-di(ethyleneglycol)ketal)-2,4(1,3)-dibenzenacyclotetraphanylene (12[4])

Colorless blocks were grown via layer diffusion of benzene into a $CDCl_3$ solution of **12[4]**. The data was collected at the MX 14.2 Beamline of the BESSYII synchrotron at the Helmholtz-Zentrum Berlin. Remaining electron density originating from solvent molecules that could not be refined was masked using the solvent mask tool implemented in OLEX2.[326]

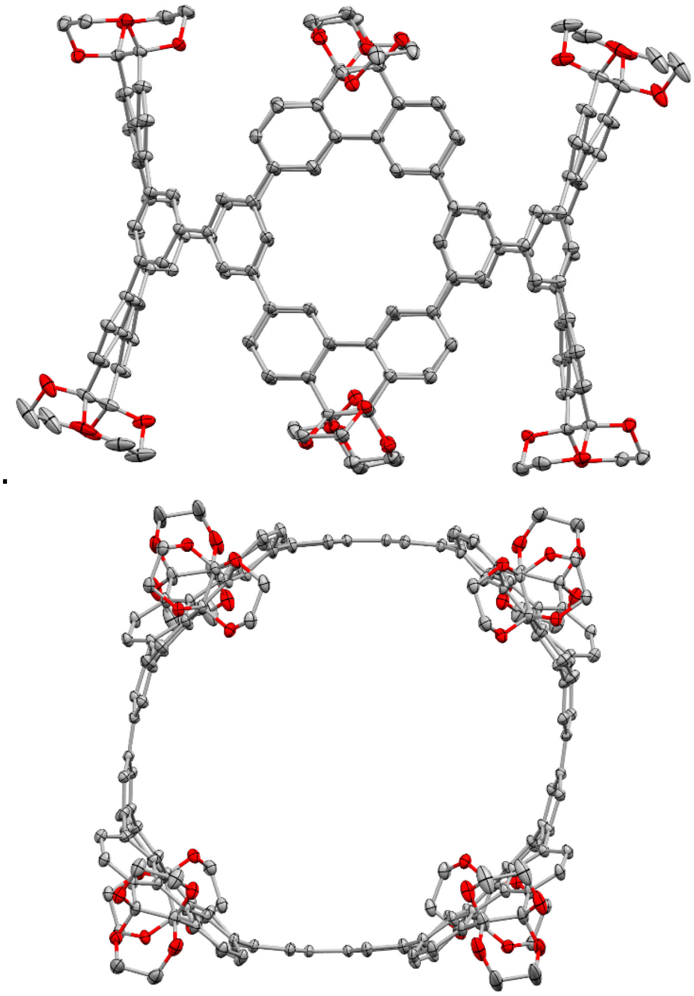

Figure A. 69. The crystal structure of compound **12[4]** is displayed side view (left) and top view (right). The data were obtained by X-ray diffraction measurements at 100 K. Solvent molecules and hydrogen atoms are omitted for clarity (they are discussed below). The ellipsoids are displayed at 50% probability level. R_1 = 8.57%. The crystals were obtained from a $CDCl_3$ solution layered with C_6H_6. Color code: C, gray; O, red; Cl, green; B, pink.

Table A 18. X–ray single crystal data and structure refinement for macrocycle **12[4]**.

CCDC No.	2208573
Empirical formula	$C_{192}H_{132}O_{32}\cdot 8\ CDCl_3\cdot 4\ C_6H_6$
Formula weight	4218.34
Temperature/K	100.0
Crystal system	monoclinic
Space group	$P2_1/n$
a/Å	25.640(5)
b/Å	19.370(4)
c/Å	26.890(5)
α/°	90
β/°	102.69(3)
γ/°	90

Volume/Å^3	13029(5)
Z	2
ρ_{calc}/g cm^{-3}	1.075
μ/mm^{-1}	0.428
F(000)	4344.0
Crystal size/mm^3	0.212 × 0.203 × 0.075
Radiation	Synchrotron (λ = 0.7999)
2Θ range for data collection/°	2.236 to 73.334
Index ranges	$38 \leq h \leq 37$, $-27 \leq k \leq 27$, $-39 \leq l \leq 40$
Reflections collected	220686
Independent reflections	41252 [R_{int} = 0.0365, R_{sigma} = 0.0245]
Data/restraints/parameters	41252/0/1261
Goodness-of-fit on F^2	1.050
Final R indexes [$I \geq 2\sigma(I)$]	R_1 = 0.0857, wR_2 = 0.2753
Final R indexes [all data]	R_1 = 0.0937, wR_2 = 0.2832
Largest diff. peak/hole / e Å^{-3}	1.93/–1.63

X-ray single crystal data und structure refinement for (+)-(*P*)-2,2'-(10,11-dimethyldibenzo[*c*,*g*]phenanthrene-7,14-diyl)bis(4,4,5,5-tetramethyl-1,3,2-dioxaborolane) ((+)-(*P*)-28)

Clear rods of (+)-(*P*)-28 were grown by slow evaporation from CH_2Cl_2 at 25 °C.

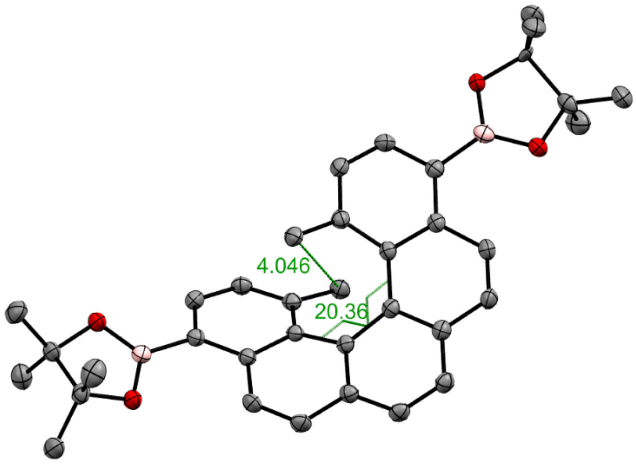

Figure A. 70. X-ray structure of (+)-(*P*)-**28** at 103 K. Ellipsoids are shown at 50% probability, hydrogen atoms and disorder are omitted for clarity. Color code: boron, pink; carbon, grey; oxygen, red.

Table A 19. X-ray single-crystal data and structure refinement for (+)-(*P*)-**28**

CCDC number	2022746
Empirical formula	$C_{36}H_{40}B_2O_4$
Formula weight	558.30
Temperature/K	103.0

Crystal system	orthorhombic
Space group	$P2_12_12_1$
a/Å	10.808(2)
b/Å	12.044(3)
c/Å	23.286(5)
α/°	90
β/°	90
γ/°	90
Volume/Å^3	3031.3(12)
Z	4
ρ_{calc} / g/cm^3	1.223
μ/mm^{-1}	0.602
F(000)	1192.0
Crystal size/mm^3	0.919 × 0.285 × 0.22
Radiation	CuKα (λ = 1.54178)
2Θ range for data collection/°	7.592 to 142.302
Index ranges	$-13 \leq h \leq 13$, $-14 \leq k \leq 13$, $-28 \leq l \leq 28$
Reflections collected	49529
Independent reflections	5718 [R_{int} = 0.0601, R_{sigma} = 0.0257]
Data/restraints/parameters	5718/0/455
Goodness-of-fit on F^2	1.074
Final R indexes [$I \geq 2\sigma$ (I)]	R_1 = 0.0299, wR_2 = 0.0765
Final R indexes [all data]	R_1 = 0.0305, wR_2 = 0.0776
Largest diff. peak/hole / e Å^{-3}	0.18/–0.15
Flack parameter	–0.05(5)

X-ray single crystal data und structure refinement for (±)-7a,7b-dimethyl-7a,7b-dihydrobenzo[*ghi*]perylene-5,10-dione

Clear cubes of (±)-**31-C** were grown by slow evaporation from 2-methyltetrahydrofuran at 25 °C.

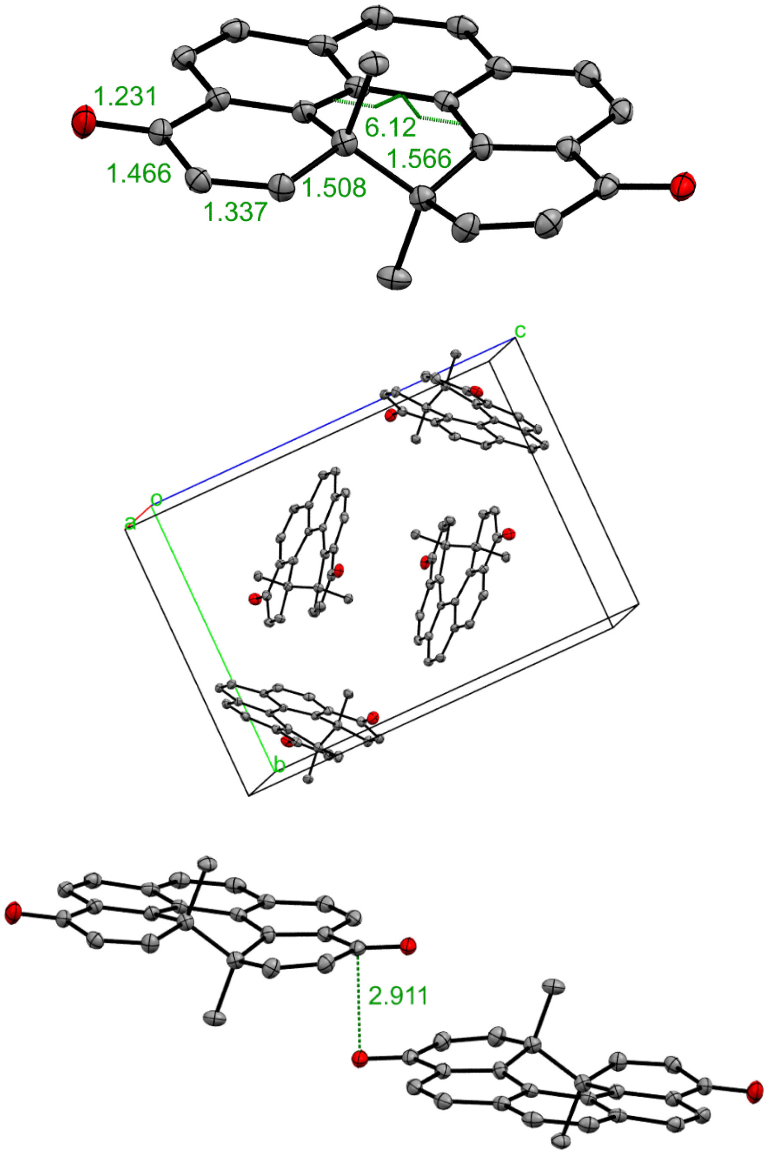

Figure A. 71. X-ray structure of (±)-**31-C** at 100 K. Ellipsoids are shown at 50% probability, hydrogen atoms and disorder are omitted for clarity. Color code: carbon, grey; oxygen, red.

Table A 20. X-ray single-crystal data and structure refinement for (±)-**31-C**.

CCDC number	2129548
Empirical formula	$C_{24}H_{16}O_2$
Formula weight	336.37
Temperature/K	100.0
Crystal system	monoclinic
Space group	$P2_1/c$
a/Å	7.9720(6)
b/Å	12.2915(9)
c/Å	16.8593(13)
α/°	90
β/°	97.686(3)
γ/°	90
Volume/Å^3	1637.2(2)
Z	4
ρ_{calc} / g/cm^3	1.365
μ/mm^{-1}	0.086
F(000)	704.0
Crystal size/mm^3	0.345 × 0.255 × 0.163
Radiation	MoKα (λ = 0.71073)
2Θ range for data collection/°	4.876 to 55.82
Index ranges	$-10 \leq h \leq 10$, $-16 \leq k \leq 16$, $-22 \leq l \leq 22$
Reflections collected	58487
Independent reflections	3909 [R_{int} = 0.0958, R_{sigma} = 0.0396]
Data/restraints/parameters	3909/0/237
Goodness-of-fit on F^2	1.013
Final R indexes [$I \geq 2\sigma$ (I)]	R_1 = 0.0507, wR_2 = 0.1176
Final R indexes [all data]	R_1 = 0.0857, wR_2 = 0.1435
Largest diff. peak/hole / e Å^{-3}	0.46/–0.16

X-ray single crystal data und structure refinement for (±)2,2'-(7a,7b-dimethyl-7a,7b-dihydrobenzo[*ghi*]perylene-5,10-diylidene)dimalononitrile ((±)-34-C)

Yellow-orange rods of (±)-**34-C** were grown by slow evaporation from $CHCl_3$ at 25 °C.

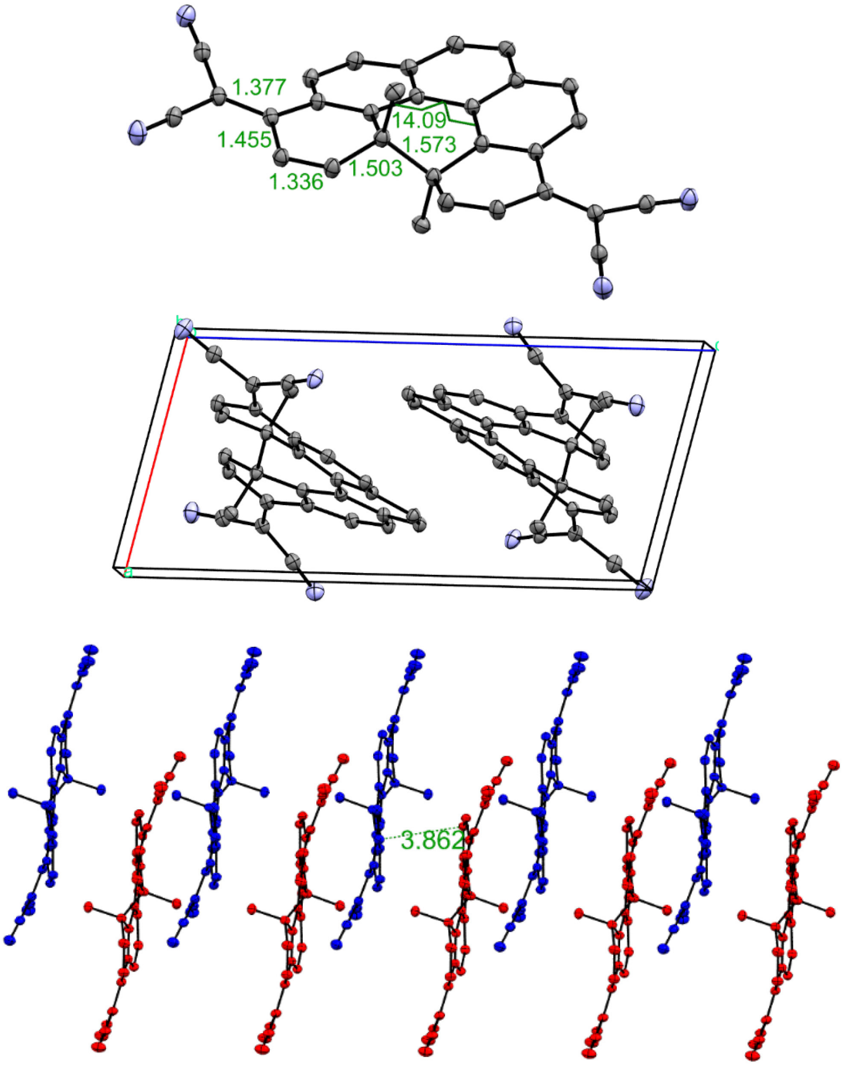

Figure A. 72. X-ray structure of (±)-**34-C** at 100 K. Ellipsoids are shown at 50% probability, hydrogen atoms and disorder are omitted for clarity. Color code: carbon, grey; nitrogen, cyan.

Table A 21. X-ray single-crystal data and structure refinement for (±)-**34-C**.

CCDC number	2104623
Empirical formula	$C_{30}H_{16}N_4$
Formula weight	432.47
Temperature/K	100.0
Crystal system	triclinic
Space group	P-1
a/Å	7.3280(4)
b/Å	10.0893(5)
c/Å	15.4098(9)
α/°	103.198(2)
β/°	99.808(2)
γ/°	105.416(2)
Volume/Å^3	1036.41(10)
Z	2
ρ_{calc} / g/cm^3	1.386
μ/mm^{-1}	0.084
F(000)	448.0
Crystal size/mm^3	0.266 × 0.197 × 0.104
Radiation	MoKα (λ = 0.71073)
2Θ range for data collection/°	4.374 to 61.184
Index ranges	$-10 \le h \le 10$, $-14 \le k \le 14$, $-22 \le l \le 22$
Reflections collected	62900
Independent reflections	6360 [R_{int} = 0.0670, R_{sigma} = 0.0357]
Data/restraints/parameters	6360/0/309
Goodness-of-fit on F^2	1.063
Final R indexes [$I \ge 2\sigma$ (I)]	R_1 = 0.0473, wR_2 = 0.1233
Final R indexes [all data]	R_1 = 0.0726, wR_2 = 0.1431
Largest diff. peak/hole / e Å^{-3}	0.52/–0.33

A.9. Selected NMR Spectra

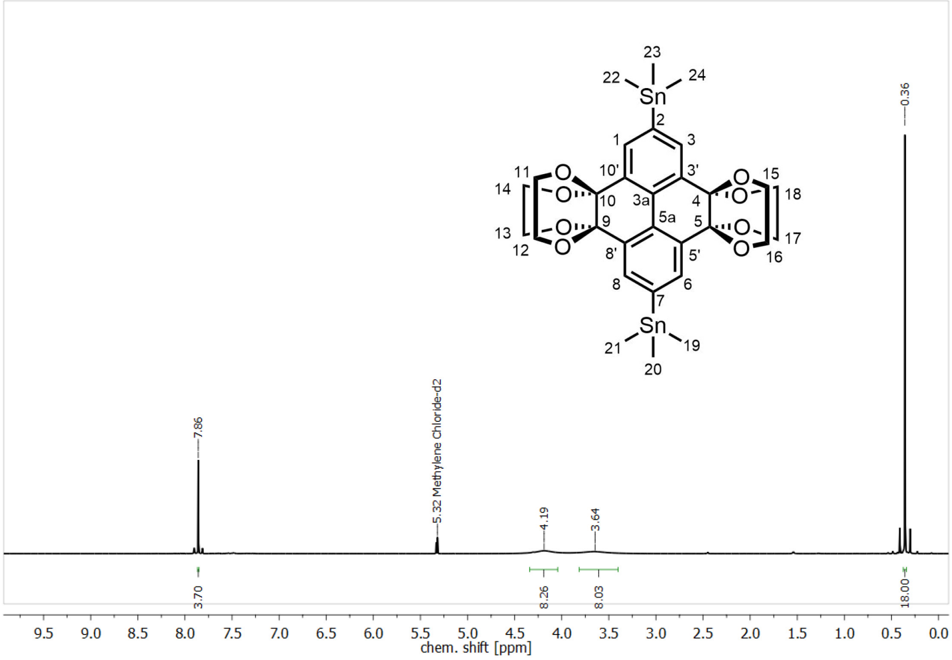

Figure A. 73. ^{1}H NMR spectrum (500 MHz, 298 K) of 2,7-Bis(trimethylstannyl)-4,5,9,10-tetra(ethyleneglycol)ketal-pyrene (**6**) in CD_2Cl_2.

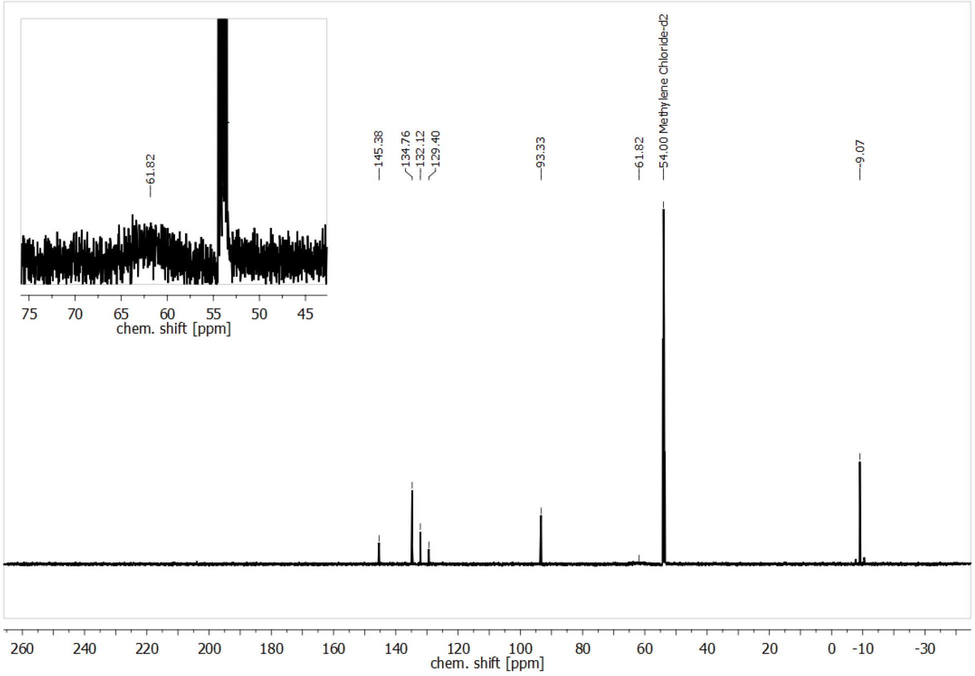

Figure A. 74. ^{13}C NMR spectrum (126 MHz, 298 K) of 2,7-Bis(trimethylstannyl)-4,5,9,10-tetra(ethyleneglycol)ketal-pyrene (**6**) in CD_2Cl_2.

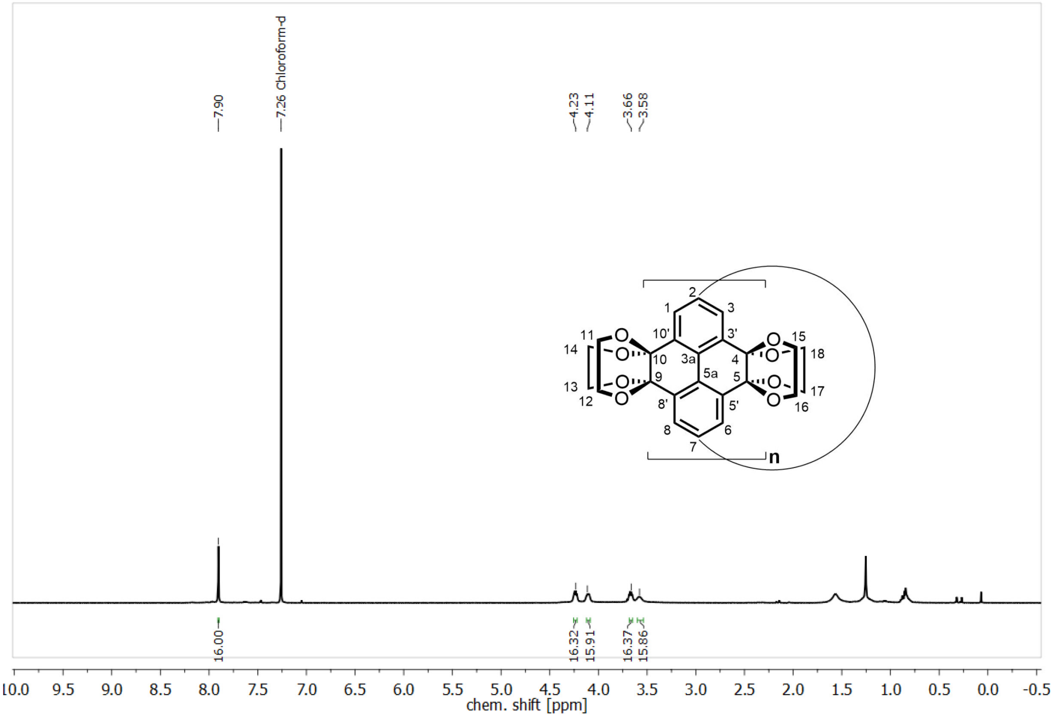

Figure A. 75. ^{1}H NMR spectrum (500 MHz, 298 K) of [4]cyclo-2,7-pyren-(4,5,9,10-tetra(ethyleneglycol)ketal)ylene (**4[4]**) in CDCl$_3$.

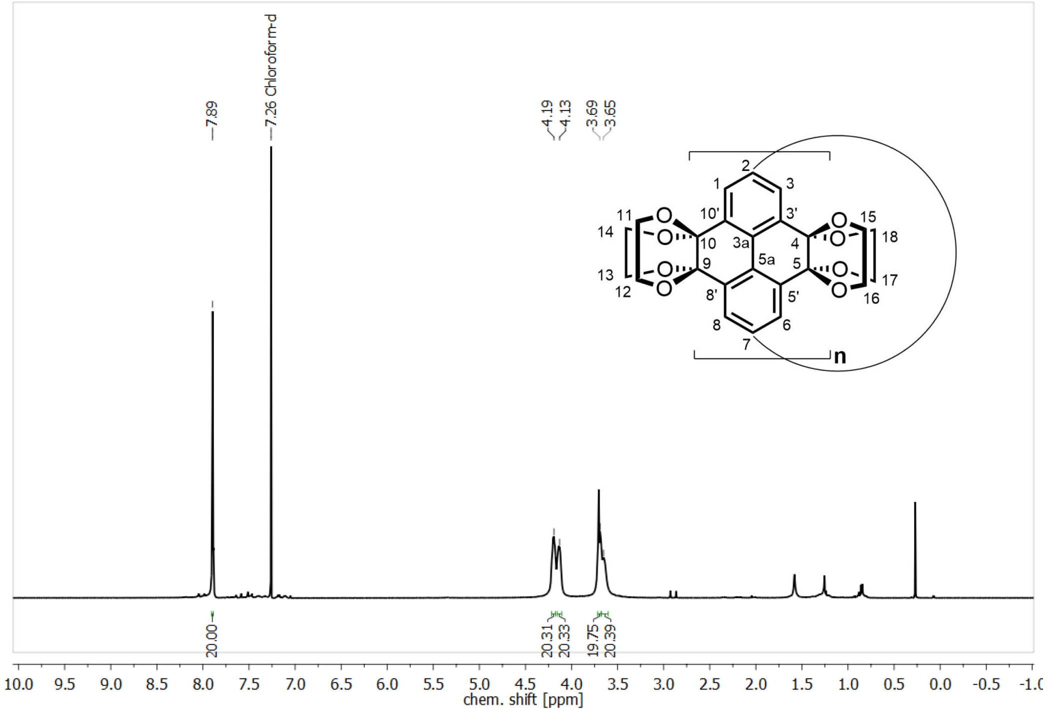

Figure A. 76. ^{1}H NMR spectrum (500 MHz, 298 K) of [5]cyclo-2,7-pyren-(4,5,9,10-tetra(ethyleneglycol)ketal)ylene (**4[5]**) in CDCl$_3$.

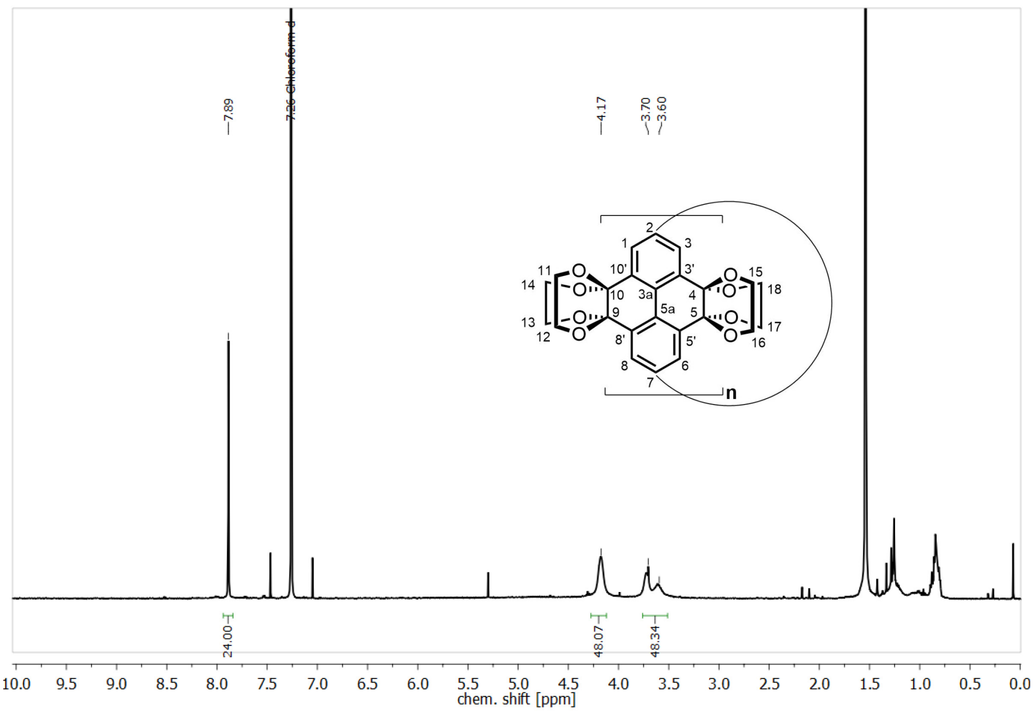

Figure A. 77. ^{1}H NMR spectrum (500 MHz, 298 K) of [6]cyclo-2,7-pyren-(4,5,9,10-tetra(ethyleneglycol)ketal)ylene (**4[6]**) in CDCl$_3$. (solvent residues 5.32 CH_2Cl_2, 1.56 H_2O, and impurities (grease) 0.8 and 1.3 ppm).

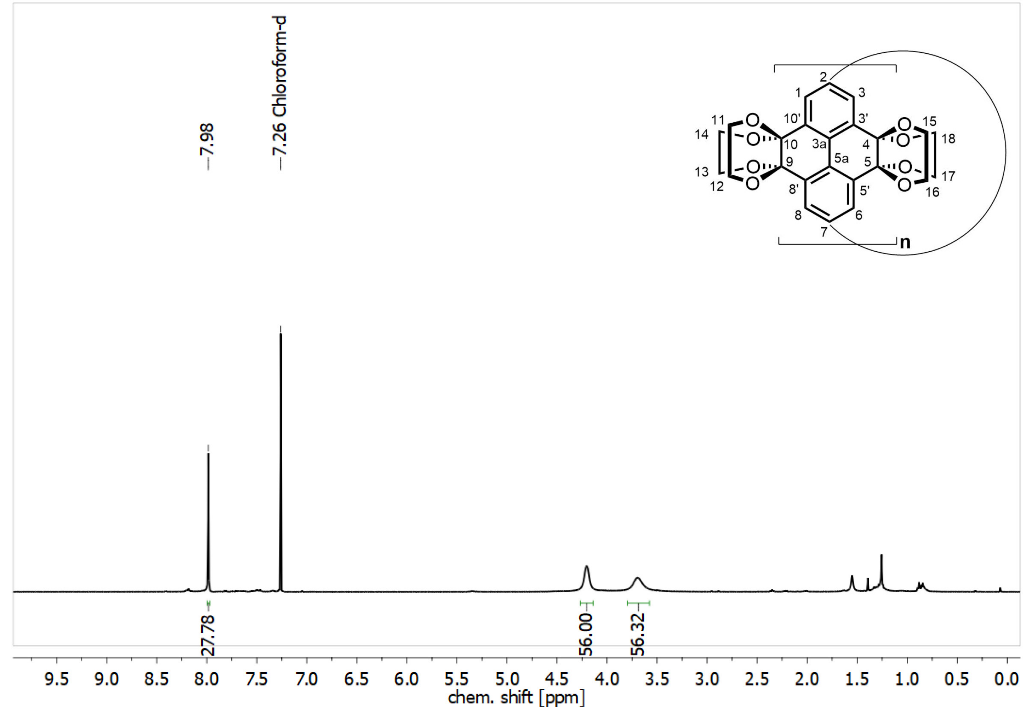

Figure A. 78. ^{1}H NMR spectrum (500 MHz, 298 K) of [7]cyclo-2,7-pyren-(4,5,9,10-tetra(ethyleneglycol)ketal)ylene (**4[7]**) in CDCl$_3$.

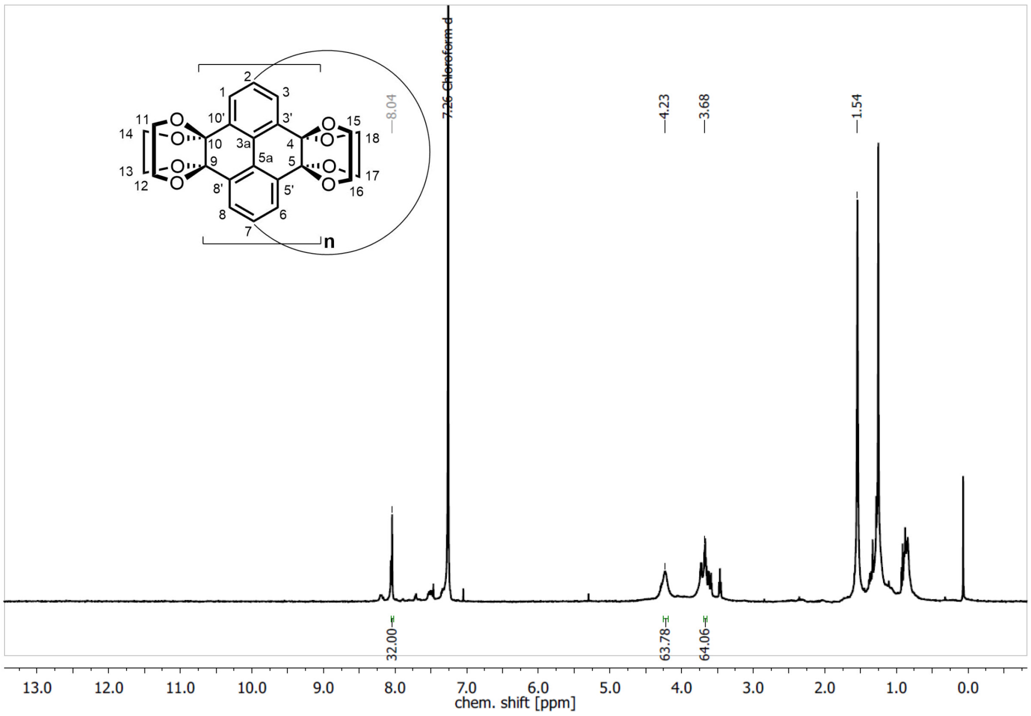

Figure A. 79. ^{1}H NMR spectrum (500 MHz, 298 K) of [8]-2,7-pyren-(4,5,9,10-tetra(ethyleneglycol)ketal)ylene (**4[8]**) in $CDCl_3$.

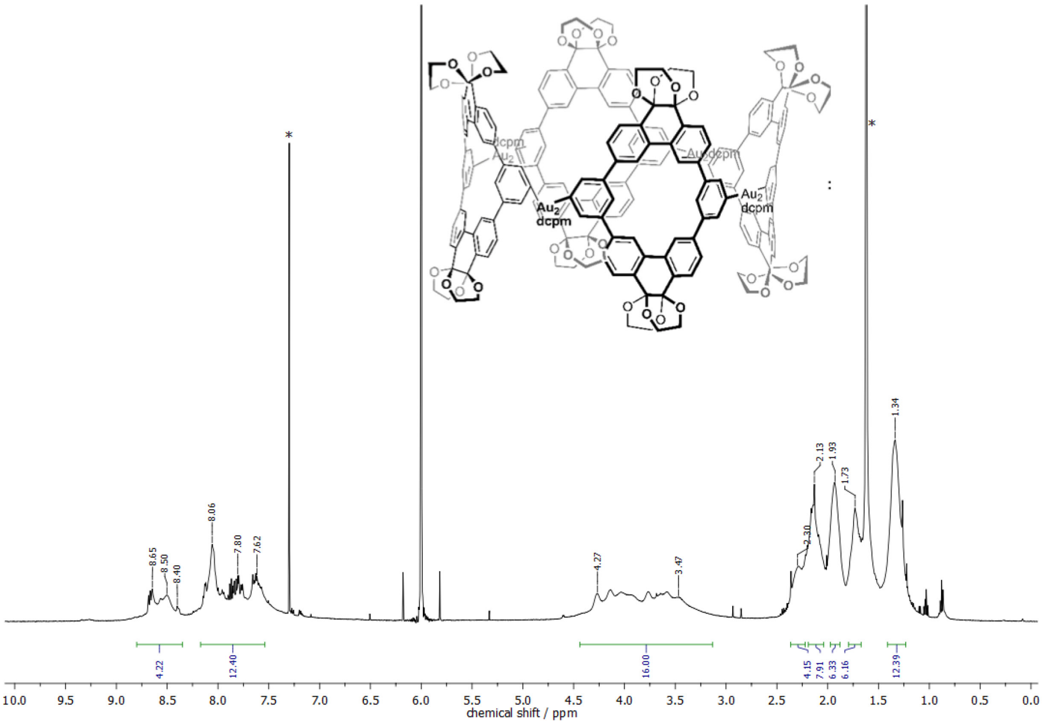

Figure A. 80. ^{1}H NMR spectrum (500 MHz, $C_2D_2Cl_4$, 25 °C) of Au-macrocycle **26[4]**. Residual solvent resonances are assigned with (*).

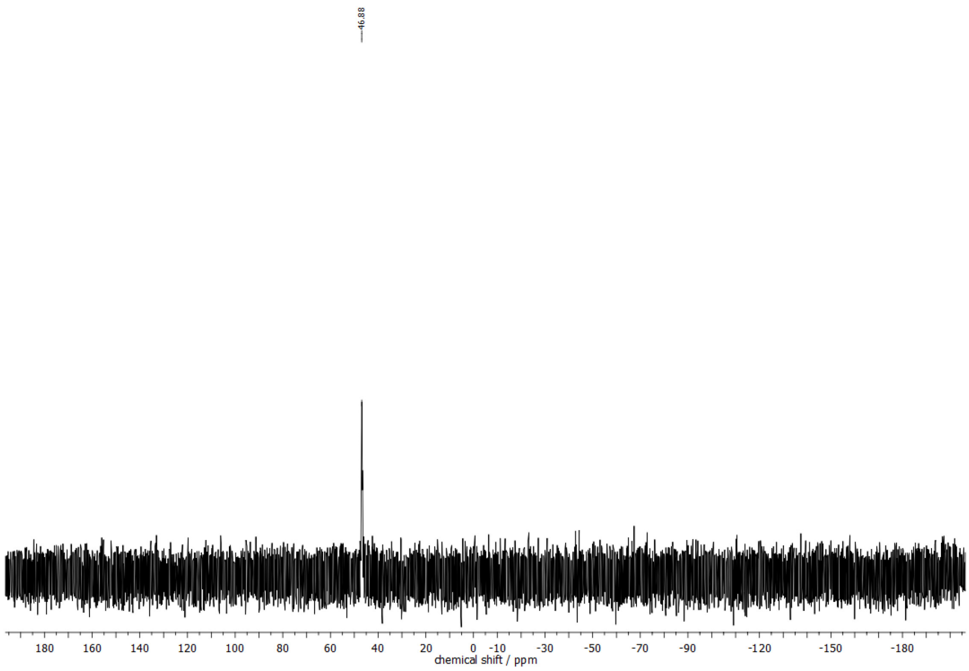

Figure A. 81. ^{31}P spectrum (500 MHz, 126 MHz, $C_2D_2Cl_4$, 25 °C) of Au-macrocycle **26[4]**.

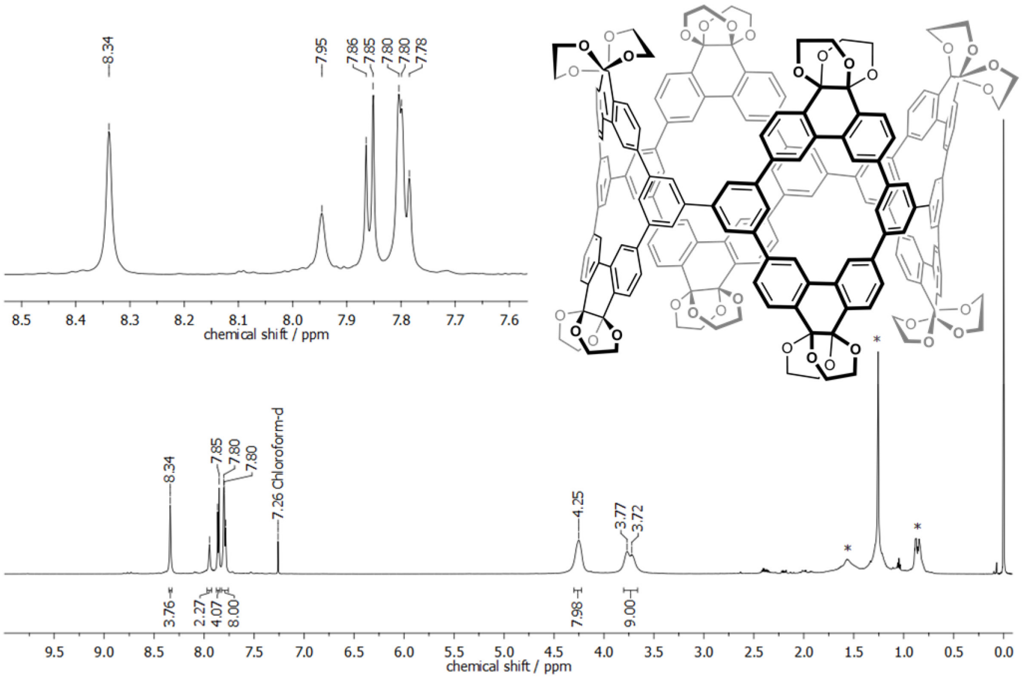

Figure A. 82. ^1H NMR spectrum (600 MHz, $CDCl_3$, 25 °C) of the tetramer **12[4]**. All residual solvent resonances are assigned with (*).

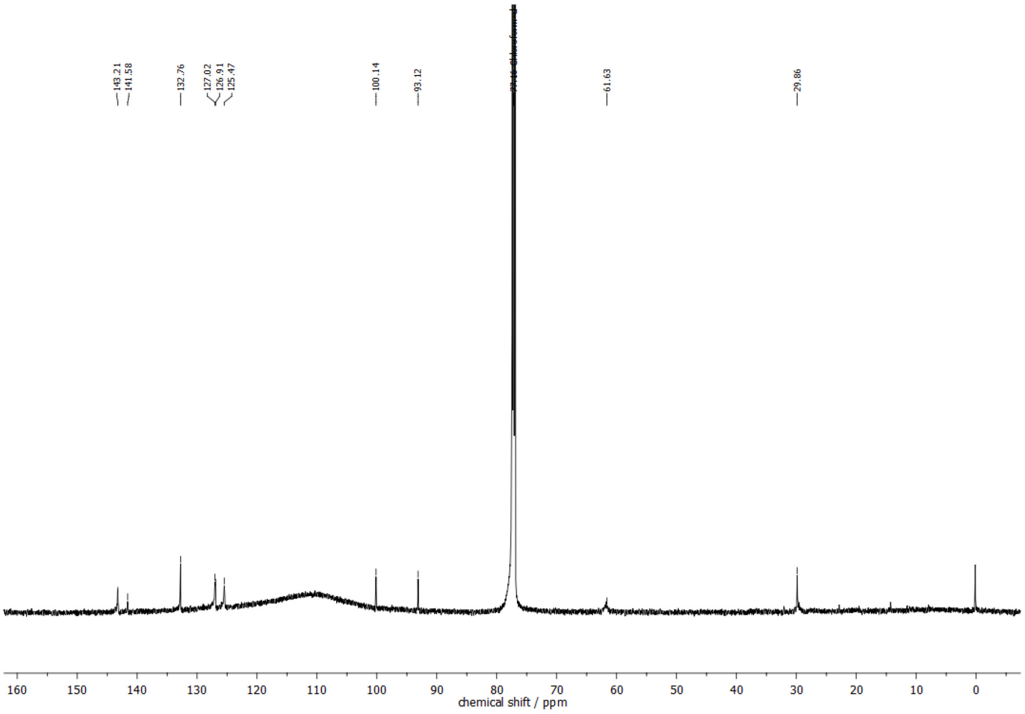

Figure A. 83. ^{13}C spectrum (151 MHz, CDCl$_3$, 25 °C) of the tetramer **12[4]**.

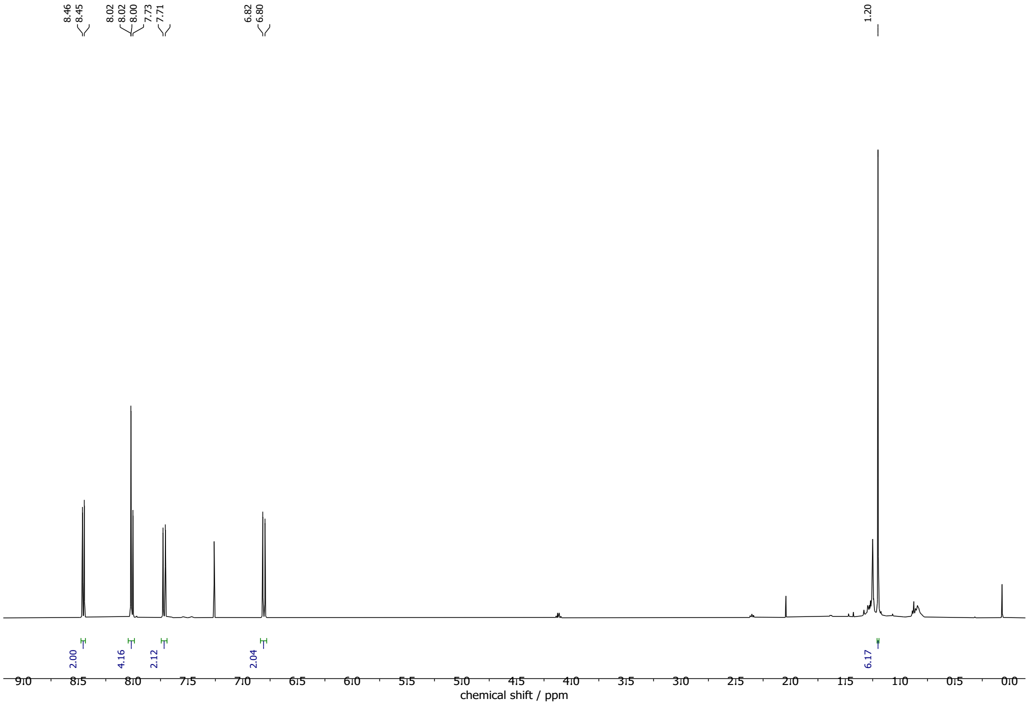

Figure A. 84. ^{1}H NMR spectrum (500 MHz, 298 K) of (±)-7a,7b-dimethyl-7a,7b-dihydrobenzo[*ghi*]perylene-5,10-dione ((±)-**31-C**) in CDCl$_3$.

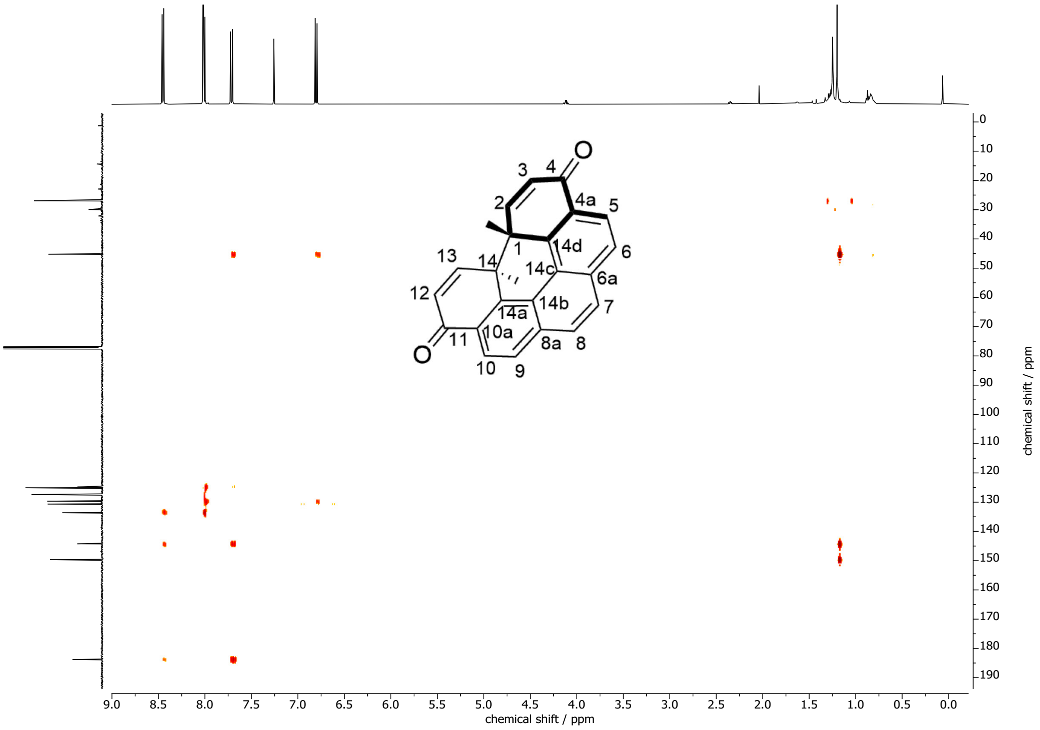

Figure A. 85. $^1H,^{13}C$-HMBC NMR spectrum (500 MHz, 126 MHz, 298 K) of (±)-7a,7b-dimethyl-7a,7b-dihydrobenzo[*ghi*]perylene-5,10-dione ((±)-**31-C**) in $CDCl_3$.

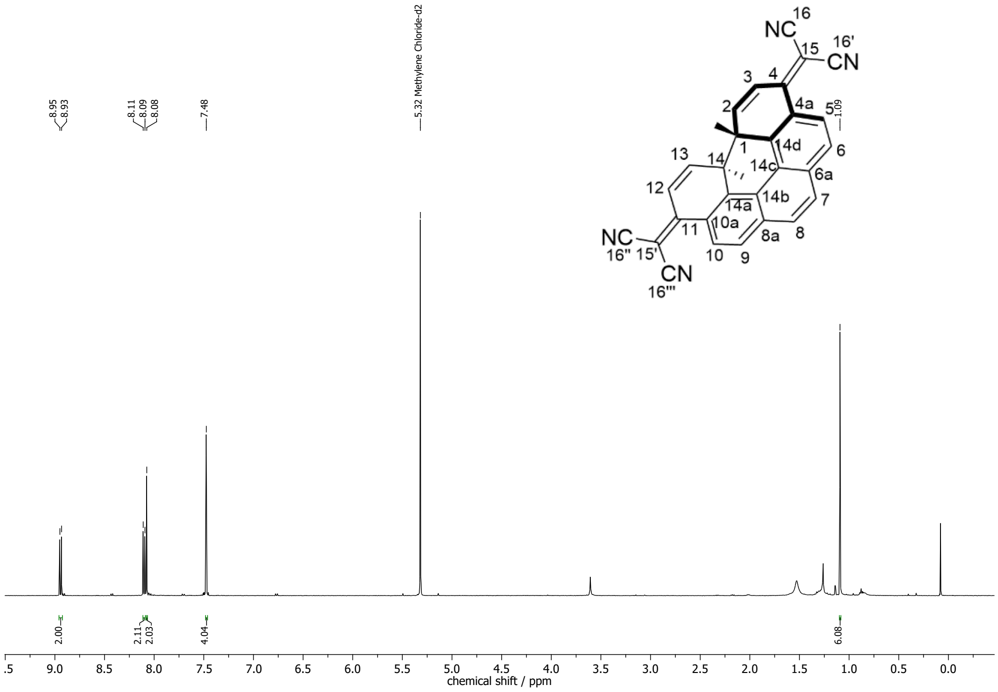

Figure A. 86. ^1H NMR spectrum (500 MHz, 298 K) of (±)-2,2'-(7a,7b-dimethyl-7a,7b-dihydrobenzo[*ghi*]perylene-5,10-diylidene)dimalononitrile ((±)-**34-C**) in CD_2Cl_2.

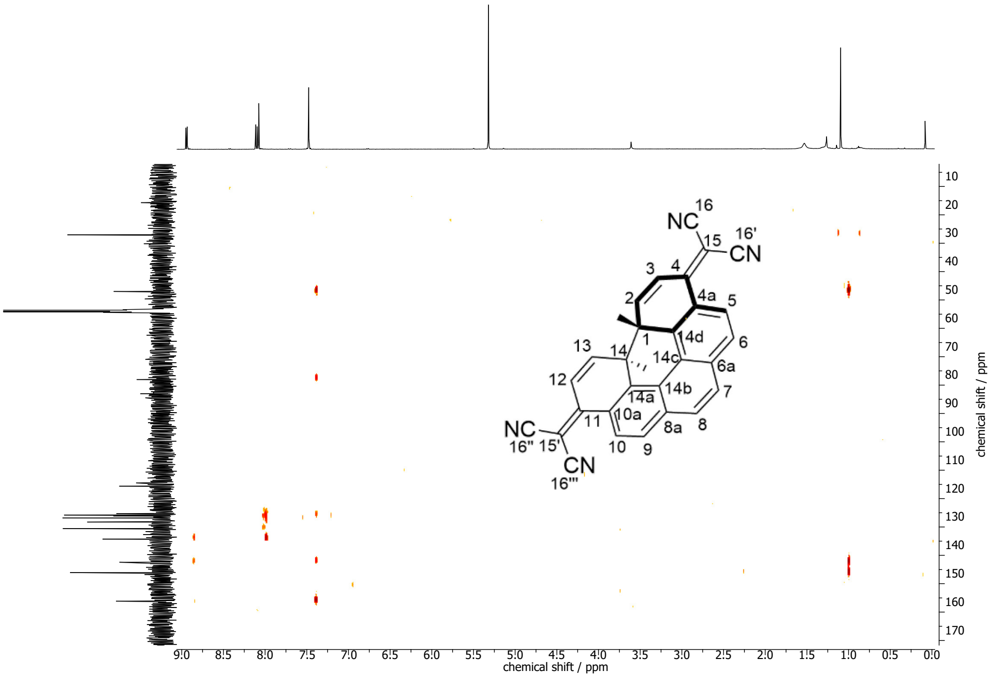

Figure A. 87. ^{1}H,^{13}C-HMBC NMR spectrum (500 MHz, 126 MHz, 298 K) of (±)-2,2'-(7a,7b-dimethyl-7a,7b-dihydrobenzo[*ghi*]perylene-5,10-diylidene)dimalononitrile ((±)-**34-C**) in CD$_2$Cl$_2$.

References

[1] K. S. Novoselov, A. K. Geim, S. V Morozov, D. Jiang, Y. Zhang, S. V Dubonos, I. V Grigorieva, A. A. Firsov, *Science* **2004**, *306*, 666–669.

[2] H. W. Kroto, J. R. Heath, S. C. O'Brien, R. F. Curl, R. E. Smalley, *Nature* **1985**, *318*, 162–163.

[3] S. Iijima, *Nature* **1991**, *354*, 56–58.

[4] K. Kaiser, L. M. Scriven, F. Schulz, P. Gawel, L. Gross, H. L. Anderson, *Science* **2019**, *365*, 1299–1301.

[5] Y. Hu, C. Wu, Q. Pan, Y. Jin, R. Lyu, V. Martinez, S. Huang, J. Wu, L. J. Wayment, N. A. Clark, M. B. Raschke, Y. Zhao, W. Zhang, *Nat. Synth.* **2022**, *1*, 449–454.

[6] S. Ferro, *J. Mater. Chem.* **2002**, *12*, 2843–2855.

[7] T. W. Ebbesen, P. M. Ajayan, *Nature* **1992**, *358*, 220–222.

[8] R. M. Koenig, H.-R. Tian, T. L. Seeler, K. R. Tepper, H. M. Franklin, Z.-C. Chen, S.-Y. Xie, S. Stevenson, *J. Am. Chem. Soc.* **2020**, *142*, 15614–15623.

[9] J. Cai, P. Ruffieux, R. Jaafar, M. Bieri, T. Braun, S. Blankenburg, M. Muoth, A. P. Seitsonen, M. Saleh, X. Feng, K. Müllen, R. Fasel, *Nature* **2010**, *466*, 470–473.

[10] J. W. G. Wilder, L. C. Venema, A. G. Rinzler, R. E. Smalley, C. Dekker, *Nature* **1998**, *391*, 59–62.

[11] T. W. Odom, J.-L. Huang, P. Kim, C. M. Lieber, *Nature* **1998**, *391*, 62–64.

[12] A. K. Geim, K. S. Novoselov, *Nat. Mater.* **2007**, *6*, 183–191.

[13] G. Dennler, M. C. Scharber, C. J. Brabec, *Adv. Mater.* **2009**, *21*, 1323–1338.

[14] D. S. Hecht, L. Hu, G. Irvin, *Adv. Mater.* **2011**, *23*, 1482–1513.

[15] L. T. Scott, *Angew. Chem. Int. Ed.* **2004**, *43*, 4994–5007.

[16] D. Lungerich, H. Hoelzel, K. Harano, N. Jux, K. Y. Amsharov, E. Nakamura, *ACS Nano* **2021**, *15*, 12804–12814.

[17] M. Naguib, M. Kurtoglu, V. Presser, J. Lu, J. Niu, M. Heon, L. Hultman, Y. Gogotsi, M. W. Barsoum, *Adv. Mater.* **2011**, *23*, 4248–4253.

[18] A. P. Côté, A. I. Benin, N. W. Ockwig, M. O'Keeffe, A. J. Matzger, O. M. Yaghi, *Science* **2005**, *310*, 1166–1170.

[19] A. Brown, S. Rundqvist, *Acta Crystallogr.* **1965**, *19*, 684–685.

[20] B. Radisavljevic, A. Radenovic, J. Brivio, V. Giacometti, A. Kis, *Nat. Nanotechnol.* **2011**, *6*, 147–150.

[21] C. S. Diercks, O. M. Yaghi, *Science* **2017**, *355*, eaal1585.

[22] A. M. Evans, L. R. Parent, N. C. Flanders, R. P. Bisbey, E. Vitaku, M. S. Kirschner, R. D. Schaller, L. X. Chen, N. C. Gianneschi, W. R. Dichtel, *Science* **2018**, *361*, 52–57.

[23] S. J. Rowan, S. J. Cantrill, G. R. L. Cousins, J. K. M. Sanders, J. F. Stoddart, *Angew. Chem. Int. Ed.* **2002**, *41*, 898–952.

[24] K. Geng, T. He, R. Liu, S. Dalapati, K. T. Tan, Z. Li, S. Tao, Y. Gong, Q. Jiang, D. Jiang, *Chem. Rev.* **2020**, *120*, 8814–8933.

[25] P. J. Waller, F. Gándara, O. M. Yaghi, *Acc. Chem. Res.* **2015**, *48*, 3053–3063.

[26] H. Schiff, *Liebigs Ann. Chem.* **1864**, *131*, 118–119.

[27] E. H. Cordes, W. P. Jencks, *J. Am. Chem. Soc.* **1962**, *84*, 832–837.

[28] E. G. Sander, W. P. Jencks, *J. Am. Chem. Soc.* **1968**, *90*, 6154–6162.

[29] M. Ciaccia, R. Cacciapaglia, P. Mencarelli, L. Mandolini, S. Di Stefano, *Chem. Sci.* **2013**, *4*, 2253–2261.

[30] M. Ciaccia, S. Di Stefano, *Org. Biomol. Chem.* **2015**, *13*, 646–654.

[31] M. E. Belowich, J. F. Stoddart, *Chem. Soc. Rev.* **2012**, *41*, 2003–2024.

[32] E. Jin, M. Asada, Q. Xu, S. Dalapati, M. A. Addicoat, M. A. Brady, H. Xu, T. Nakamura, T. Heine, Q. Chen, D. Jiang, *Science* **2017**, *357*, 673–676.

[33] S. Bi, C. Yang, W. Zhang, J. Xu, L. Liu, D. Wu, X. Wang, Y. Han, Q. Liang, F. Zhang, *Nat. Commun.* **2019**, *10*, 2467.

[34] P. Kuhn, M. Antonietti, A. Thomas, *Angew. Chem. Int. Ed.* **2008**, *47*, 3450–3453.

[35] J. Guo, Y. Xu, S. Jin, L. Chen, T. Kaji, Y. Honsho, M. A. Addicoat, J. Kim, A. Saeki, H. Ihee, S. Seki, S. Irle, M. Hiramoto, J. Gao, D. Jiang, *Nat. Commun.* **2013**, *4*, 1–8.

[36] H. Li, A. M. Evans, W. R. Dichtel, J.-L. Bredas, *ACS Mater. Lett.* **2021**, *3*, 398–405.

[37] K. Koner, S. Karak, S. Kandambeth, S. Karak, N. Thomas, L. Leanza, C. Perego, L. Pesce, R. Capelli, M. Moun, M. Bhakar, T. G. Ajithkumar, G. M. Pavan, R. Banerjee, *Nat. Chem.* **2022**, *14*, 507–514.

[38] T. Kobayashi, T. Kubota, K. Ezumi, *J. Am. Chem. Soc.* **1983**, *105*, 2172–2174.

[39] M. He, S. Zhang, J. Zhang, *Chem. Rev.* **2020**, *120*, 12592–12684.

[40] M. Ouyang, J.-L. Huang, C. L. Cheung, C. M. Lieber, *Science* **2001**, *292*, 702–705.

[41] M. M. Shulaker, G. Hills, N. Patil, H. Wei, H.-Y. Chen, H.-S. P. Wong, S. Mitra, *Nature* **2013**, *501*, 526–530.

[42] L. Liu, J. Han, L. Xu, J. Zhou, C. Zhao, S. Ding, H. Shi, M. Xiao, L. Ding, Z. Ma, C. Jin, Z. Zhang, L.-M. Peng, *Science* **2020**, *368*, 850–856.

[43] S. E. Lewis, *Chem. Soc. Rev.* **2015**, *44*, 2221–2304.

[44] E. Heilbronner, *Helv. Chim. Acta* **1954**, *37*, 921–935.

[45] E. Heilbronner, *Helv. Chim. Acta* **1954**, *37*, 913–921.

[46] Z. Chen, D. Jiang, X. Lu, H. F. Bettinger, S. Dai, P. von R. Schleyer, K. N. Houk, *Org. Lett.* **2007**, *9*, 5449–5452.

[47] Z. Xia, S. H. Pun, H. Chen, Q. Miao, *Angew. Chem. Int. Ed.* **2021**, *60*, 10311–10318.

[48] K. Y. Cheung, K. Watanabe, Y. Segawa, K. Itami, *Nat. Chem.* **2021**, *13*, 255–259.

[49] Y. Han, S. Dong, J. Shao, W. Fan, C. Chi, *Angew. Chem. Int. Ed.* **2021**, *60*, 2658–2662.

[50] K. Y. Cheung, S. Gui, C. Deng, H. Liang, Z. Xia, Z. Liu, L. Chi, Q. Miao, *Chem* **2019**, *5*, 838–847.

[51] R. Jasti, J. Bhattacharjee, J. B. Neaton, C. R. Bertozzi, *J. Am. Chem. Soc.* **2008**, *130*, 17646–17647.

[52] S. Yamago, Y. Watanabe, T. Iwamoto, *Angew. Chem. Int. Ed.* **2010**, *49*, 757–759.

[53] H. Takaba, H. Omachi, Y. Yamamoto, J. Bouffard, K. Itami, *Angew. Chem. Int. Ed.* **2009**, *48*, 6112–6116.

[54] Y. Tsuchido, R. Abe, T. Ide, K. Osakada, *Angew. Chem. Int. Ed.* **2020**, *59*, 22928–22932.

[55] M. S. Dresselhaus, G. Dresselhaus, R. Saito, *Carbon* **1995**, *33*, 883–891.

[56] F. Yang, M. Wang, D. Zhang, J. Yang, M. Zheng, Y. Li, *Chem. Rev.* **2020**, *120*, 2693–2758.

[57] V. C. Parekh, P. C. Guha, *J. Indian Chem. Soc* **1934**, *11*, 95–100.

[58] R. Friederich, M. Nieger, F. Vögtle, *Chem. Ber.* **1993**, *126*, 1723–1732.

[59] R. Jasti, J. Bhattacharjee, J. B. Neaton, C. R. Bertozzi, *J. Am. Chem. Soc.* **2008**, *130*, 17646–17647.

[60] F. Alonso, M. Yus, *Tetrahedron* **1991**, *47*, 7471–7476.

[61] H.-J. Liu, J. Yip, K.-S. Shia, *Tetrahedron Lett.* **1997**, *38*, 2253–2256.

[62] Y. Ishii, Y. Nakanishi, H. Omachi, S. Matsuura, K. Matsui, H. Shinohara, Y. Segawa, K. Itami, *Chem. Sci.* **2012**, *3*, 2340–2345.

[63] J. Xia, R. Jasti, *Angew. Chem. Int. Ed.* **2012**, *51*, 2474–2476.

[64] P. J. Evans, E. R. Darzi, R. Jasti, *Nat. Chem.* **2014**, *6*, 404–408.

[65] T. Iwamoto, Y. Watanabe, Y. Sakamoto, T. Suzuki, S. Yamago, *J. Am. Chem. Soc.* **2011**, *133*, 8354–8361.

[66] G. Fuhrmann, T. Debaerdemaeker, P. Bäuerle, *Chem. Commun.* **2003**, *3*, 948–949.

[67] T. Iwamoto, E. Kayahara, N. Yasuda, T. Suzuki, S. Yamago, *Angew. Chem. Int. Ed.* **2014**, *53*, 6430–6434.

[68] S. Hitosugi, W. Nakanishi, T. Yamasaki, H. Isobe, *Nat. Commun.* **2011**, *2*, 492.

[69] H. W. Jiang, T. Tanaka, T. Kim, Y. M. Sung, H. Mori, D. Kim, A. Osuka, *Angew. Chem. Int. Ed.* **2015**, *54*, 15197–15201.

[70] J. S. Wössner, D. Wassy, A. Weber, M. Bovenkerk, M. Hermann, M. Schmidt, B. Esser, *J. Am. Chem. Soc.* **2021**, *143*, 12244–12252.

[71] H. Jia, G. Zhuang, Q. Huang, J. Wang, Y. Wu, S. Cui, S. Yang, P. Du, *Chem. – Eur. J.* **2020**, *26*, 2159 –2163.

[72] M. Ball, B. Fowler, P. Li, L. A. Joyce, F. Li, T. Liu, D. Paley, Y. Zhong, H. Li, S. Xiao, F. Ng, M. L. Steigerwald, C. Nuckolls, *J. Am. Chem. Soc.* **2015**, *137*, 9982–9987.

[73] L. Sicard, F. Lucas, O. Jeannin, P. A. Bouit, J. Rault-Berthelot, C. Quinton, C. Poriel, *Angew. Chem. Int. Ed.* **2020**, *59*, 11066–11072.

[74] H. Jia, Y. Gao, Q. Huang, S. Cui, P. Du, *Chem. Commun.* **2018**, *54*, 988–991.

[75] E. Kayahara, T. Hayashi, K. Takeuchi, F. Ozawa, K. Ashida, S. Ogoshi, S. Yamago, *Angew. Chem. Int. Ed.* **2018**, *57*, 11418–11421.

[76] Y. Yoshigoe, Y. Suzaki, K. Osakada, *Chem. Lett.* **2014**, *43*, 1337–1339.

[77] Y. Suzaki, T. Yagyu, K. Osakada, *J. Organomet. Chem.* **2007**, *692*, 326–342.

[78] S. P. Dent, C. Eaborn, A. Pidcock, *J. Organomet. Chem.* **1975**, *97*, 307–311.

[79] N. Grabicki, K. T. D. Nguyen, S. Weidner, O. Dumele, *Angew. Chem. Int. Ed.* **2021**, *60*, 14909–14914.

[80] W. J. Wolf, M. S. Winston, F. D. Toste, *Nat. Chem.* **2014**, *6*, 159–164.

[81] Y. Yoshigoe, Y. Tanji, Y. Hata, K. Osakada, S. Saito, E. Kayahara, S. Yamago, Y. Tsuchido, H. Kawai, *JACS Au* **2022**, *2*, 1857–1868.

[82] V. Martí-Centelles, M. D. Pandey, M. I. Burguete, S. V Luis, *Chem. Rev.* **2015**, *115*, 8736–8834.

[83] V. Hensel, K. Lützow, A.-D. Schlüter, J. Jacob, K. Gessler, W. Saenger, *Angew. Chem. Int. Ed.* **1997**, *36*, 2654–2656.

[84] P. Ruggli, *Liebigs Ann. Chem.* **1912**, *392*, 92–100.

[85] W. Zhang, J. S. Moore, *Angew. Chem. Int. Ed.* **2006**, *45*, 4416–4439.

[86] H. A. Staab, F. Binnig, *Tetrahedron Lett.* **1964**, *5*, 319–321.

[87] Y. Li, A. Yagi, K. Itami, *J. Am. Chem. Soc.* **2020**, *142*, 3246–3253.

[88] W. Pisula, M. Kastler, C. Yang, V. Enkelmann, K. Müllen, *Chem. – Asian J.* **2007**, *2*, 51–56.

[89] O. M. Behr, G. Eglinton, A. R. Galbraith, R. A. Raphael, *J. Chem. Soc.* **1960**, 3614–3625.

[90] J. Y. Xue, K. Ikemoto, N. Takahashi, T. Izumi, H. Taka, H. Kita, S. Sato, H. Isobe, *J. Org. Chem.* **2014**, *79*, 9735–9739.

[91] W. Nakanishi, T. Yoshioka, H. Taka, J. Y. Xue, H. Kita, H. Isobe, *Angew. Chem. Int. Ed.* **2011**, *50*, 5323–5326.

[92] J. S. Moore, J. Zhang, *Angew. Chem. Int. Ed.* **1992**, *31*, 922–924.

[93] Y. Segawa, T. Kuwabara, K. Matsui, S. Kawai, K. Itami, *Tetrahedron* **2015**, *71*, 4500–4503.

[94] S. Yang, A. Miyachi, T. Matsuno, H. Muto, H. Sasakawa, K. Ikemoto, H. Isobe, *J. Am. Chem. Soc.* **2021**, *143*, 15017–15021.

[95] S. Höger, A.-D. Meckenstock, H. Pellen, *J. Org. Chem.* **1997**, *62*, 4556–4557.

[96] M. J. Marsella, Z.-Q. Wang, R. J. Reid, K. Yoon, *Org. Lett.* **2001**, *3*, 885–887.

[97] D. Myśliwiec, M. Kondratowicz, T. Lis, P. J. Chmielewski, M. Stępień, *J. Am. Chem. Soc.* **2015**, *137*, 1643–1649.

[98] S. Santra, I. S. Kovalev, D. S. Kopchuk, G. V Zyryanov, A. Majee, V. N. Charushin, O. N. Chupakhin, *RSC Adv.* **2015**, *5*, 104284–104288.

[99] P.-H. Ge, W. Fu, W. A. Herrmann, E. Herdtweck, C. Campana, R. D. Adams, U. H. F. Bunz, *Angew. Chem. Int. Ed.* **2000**, *39*, 3607–3610.

[100] Y. Jin, Q. Wang, P. Taynton, W. Zhang, *Acc. Chem. Res.* **2014**, *47*, 1575–1586.

[101] D. Zhao, J. S. Moore, *J. Org. Chem.* **2002**, *67*, 3548–3554.

[102] S. P. Black, J. K. M. Sanders, A. R. Stefankiewicz, *Chem. Soc. Rev.* **2014**, *43*, 1861–1872.

[103] A. D. Chavez, A. M. Evans, N. C. Flanders, R. P. Bisbey, E. Vitaku, L. X. Chen, W. R. Dichtel, *Chem. – Eur. J.* **2018**, *24*, 3989–3993.

[104] A. Baeyer, *Ber. Dtsch. Chem. Ges.* **1885**, *18*, 2269–2281.

[105] K. B. Wiberg, *Angew. Chemie* **1986**, *98*, 312–322.

[106] J. D. Kemp, K. S. Pitzer, *J. Chem. Phys.* **1936**, *4*, 749.

[107] F. Weinhold, *Nature* **2001**, *411*, 539–541.

[108] A. Almenningen, O. Bastiansen, L. Fernholt, B. N. Cyvin, S. J. Cyvin, S. Samdal, *J. Mol. Struct.* **1985**, *128*, 59–76.

[109] W. C. McKee, P. von R. Schleyer, *J. Am. Chem. Soc.* **2013**, *135*, 13008–13014.

[110] S. E. Wheeler, K. N. Houk, P. v. R. Schleyer, W. D. Allen, *J. Am. Chem. Soc.* **2009**, *131*, 2547–2560.

[111] Y. Segawa, H. Omachi, K. Itami, *Org. Lett.* **2010**, *12*, 2262–2265.

[112] C. E. Colwell, T. W. Price, T. Stauch, R. Jasti, *Chem. Sci.* **2020**, *11*, 3923–3930.

[113] S. M. Bachrach, D. Stück, *J. Org. Chem.* **2010**, *75*, 6595–6604.

[114] J. M. Baskin, J. A. Prescher, S. T. Laughlin, N. J. Agard, P. V Chang, I. A. Miller, A. Lo, J. A. Codelli, C. R. Bertozzi, *Proc. Natl. Acad. Sci.* **2007**, *104*, 16793–16797.

[115] R. Walker, R. M. Conrad, R. H. Grubbs, *Macromolecules* **2009**, *42*, 599–605.

[116] C. W. Bielawski, R. H. Grubbs, *Prog. Polym. Sci.* **2007**, *32*, 1–29.

[117] S. Kammermeier, P. G. Jones, R. Herges, *Angew. Chem. Int. Ed.* **1996**, *35*, 2669–2671.

[118] K. Tahara, Y. Tobe, *Chem. Rev.* **2006**, *106*, 5274–5290.

[119] J. Xia, J. W. Bacon, R. Jasti, *Chem. Sci.* **2012**, *3*, 3018–3021.

[120] T. J. Sisto, M. R. Golder, E. S. Hirst, R. Jasti, *J. Am. Chem. Soc.* **2011**, *133*, 15800–15802.

[121] R. Jasti, C. R. Bertozzi, *Chem. Phys. Lett.* **2010**, *494*, 1–7.

[122] E. R. Darzi, T. J. Sisto, R. Jasti, *J. Org. Chem.* **2012**, *77*, 6624–6628.

[123] E. R. Darzi, R. Jasti, *Chem. Soc. Rev.* **2015**, *44*, 6401–6410.

[124] B. M. White, Y. Zhao, T. E. Kawashima, B. P. Branchaud, M. D. Pluth, R. Jasti, *ACS Cent. Sci.* **2018**, *4*, 1173–1178.

[125] J. P. Hill, W. Jin, A. Kosaka, T. Fukushima, H. Ichihara, T. Shimomura, K. Ito, T.

Hashizume, N. Ishii, T. Aida, *Science* **2004**, *304*, 1481–1483.

[126] F. Würthner, C. R. Saha-Möller, B. Fimmel, S. Ogi, P. Leowanawat, D. Schmidt, *Chem. Rev.* **2016**, *116*, 962–1052.

[127] Y. Xu, M. von Delius, *Angew. Chem. Int. Ed.* **2020**, *59*, 559–573.

[128] T. Iwamoto, Y. Watanabe, T. Sadahiro, T. Haino, S. Yamago, *Angew. Chem. Int. Ed.* **2011**, *50*, 8342–8344.

[129] Y. Xu, R. Kaur, B. Wang, M. B. Minameyer, S. Gsänger, B. Meyer, T. Drewello, D. M. Guldi, M. Von Delius, *J. Am. Chem. Soc.* **2018**, *140*, 13413–13420.

[130] Y. Kodama, K. Nishihata, M. Nishio, N. Nakagawa, *Tetrahedron Lett.* **1977**, *18*, 2105–2108.

[131] S. Tsuzuki, A. Fujii, *Phys. Chem. Chem. Phys.* **2008**, *10*, 2584–2594.

[132] T. Matsuno, M. Fujita, K. Fukunaga, S. Sato, H. Isobe, *Nat. Commun.* **2018**, *9*, 3779.

[133] T. Matsuno, K. Fukunaga, S. Sato, H. Isobe, *Angew. Chem. Int. Ed.* **2019**, *58*, 12170–12174.

[134] S. Hashimoto, T. Iwamoto, D. Kurachi, E. Kayahara, S. Yamago, *ChemPlusChem* **2017**, *82*, 1015–1020.

[135] T. Matsuno, Y. Ohtomo, M. Someya, H. Isobe, *Nat. Commun.* **2021**, *12*, 1–8.

[136] H. Kwon, C. J. Bruns, *Nano Res.* **2022**, *15*, 5545–5555.

[137] S. Adachi, M. Shibasaki, N. Kumagai, *Nat. Commun.* **2019**, *10*, 3820.

[138] P. Della Sala, C. Talotta, M. De Rosa, A. Soriente, S. Geremia, N. Hickey, P. Neri, C. Gaeta, *J. Org. Chem.* **2019**, *84*, 9489–9496.

[139] T. Matsuno, S. Terasaki, K. Kogashi, R. Katsuno, H. Isobe, *Nat. Commun.* **2021**, *12*, 5062.

[140] P. Della Sala, C. Talotta, T. Caruso, M. De Rosa, A. Soriente, P. Neri, C. Gaeta, *J. Org. Chem.* **2017**, *82*, 9885–9889.

[141] N. Grabicki, O. Dumele, *Synlett* **2022**, *33*, 1–7.

[142] S. Hitosugi, W. Nakanishi, T. Yamasaki, H. Isobe, *Nat. Commun.* **2011**, *2*, 492.

[143] T. Matsuno, S. Kamata, S. Hitosugi, H. Isobe, *Chem. Sci.* **2013**, *4*, 3179–3183.

[144] P. Sarkar, Z. Sun, T. Tokuhira, M. Kotani, S. Sato, H. Isobe, *ACS Cent. Sci.* **2016**, *2*, 740–747.

[145] J. Wang, G. Zhuang, M. Chen, D. Lu, Z. Li, Q. Huang, H. Jia, S. Cui, X. Shao, S. Yang, P. Du, *Angew. Chem. Int. Ed.* **2020**, *59*, 1619–1626.

[146] M. Hermann, D. Wassy, J. Kohn, P. Seitz, M. U. Betschart, S. Grimme, B. Esser, *Angew. Chem. Int. Ed.* **2021**, *60*, 10680–10689.

[147] J. Malinčík, S. Gaikwad, J. P. Mora-Fuentes, M.-A. Boillat, A. Prescimone, D. Häussinger, A. G. Campaña, T. Šolomek, *Angew. Chem. Int. Ed.* **2022**, *61*, e202208591.

[148] C. Grave, A. D. Schlüter, *Eur. J. Org. Chem.* **2002**, *2002*, 3075–3098.

[149] H. Omachi, Y. Segawa, K. Itami, *Org. Lett.* **2011**, *13*, 2480–2483.

[150] G. R. Schaller, F. Topić, K. Rissanen, Y. Okamoto, J. Shen, R. Herges, *Nat. Chem.* **2014**, *6*, 608–613.

[151] E. Heilbronner, *Tetrahedron Lett.* **1964**, 1923–1928.

[152] W. Xu, X.-D. Yang, X.-B. Fan, X. Wang, C.-H. Tung, L.-Z. Wu, H. Cong, *Angew. Chem. Int. Ed.* **2019**, *58*, 3943–3947.

[153] H. Tanaka, Y. Inoue, T. Mori, *ChemPhotoChem* **2018**, *2*, 386–402.

[154] J. P. Riehl, F. S. Richardson, *Chem. Rev.* **1986**, *86*, 1–16.

[155] J. Kumar, T. Nakashima, T. Kawai, *J. Phys. Chem. Lett.* **2015**, *6*, 3445–3452.

[156] M. Schadt, *Annu. Rev. Mater. Sci.* **1997**, *27*, 305–379.

[157] J. F. Sherson, H. Krauter, R. K. Olsson, B. Julsgaard, K. Hammerer, I. Cirac, E. S. Polzik, *Nature* **2006**, *443*, 557–560.

[158] L. Rosenfeld, *Zeitschrift für Phys.* **1929**, *52*, 161–174.

[159] M. Wakabayashi, S. Yokojima, T. Fukaminato, K. Shiino, M. Irie, S. Nakamura, *J. Phys. Chem. A* **2014**, *118*, 5046–5057.

[160] A. E. Hansen, J. S. Avery, *Chem. Phys. Lett.* **1972**, *17*, 561–564.

[161] J. A. Schellman, *Chem. Rev.* **1975**, *75*, 323–331.

[162] E. M. Sánchez-Carnerero, A. R. Agarrabeitia, F. Moreno, B. L. Maroto, G. Muller, M. J. Ortiz, S. de la Moya, *Chem. – Eur. J.* **2015**, *21*, 13488–13500.

[163] P. V Demekhin, *J. Phys. B At. Mol. Opt. Phys.* **2014**, *47*, 025602.

[164] M. Krupová, J. Kessler, P. Bouř, *ChemPlusChem* **2020**, *85*, 561–575.

[165] J. L. Greenfield, F. J. Rizzuto, I. Goldberga, J. R. Nitschke, *Angew. Chem. Int. Ed.* **2017**, *56*, 7541–7545.

[166] E. Samu, P. Huszthy, L. Somogyi, M. Hollósi, *Tetrahedron: Asymmetry* **1999**, *10*, 2775–2795.

[167] D. Aranda, N. J. Schuster, X. Xiao, F. J. Ávila Ferrer, F. Santoro, C. Nuckolls, *J. Phys. Chem. C* **2021**, *125*, 2554–2564.

[168] L. Arrico, L. Di Bari, F. Zinna, *Chem. – Eur. J.* **2021**, *27*, 2920–2934.

[169] C. A. Emeis, L. J. Oosterhoff, *Chem. Phys. Lett.* **1967**, *1*, 129–132.

[170] P. S. Bols, H. L. Anderson, *Acc. Chem. Res.* **2018**, *51*, 2083–2092.

[171] M. Iyoda, J. Yamakawa, M. J. Rahman, *Angew. Chem. Int. Ed.* **2011**, *50*, 10522–10553.

[172] M. Ball, B. Zhang, Y. Zhong, B. Fowler, S. Xiao, F. Ng, M. Steigerwald, C. Nuckolls, *Acc. Chem. Res.* **2019**, *52*, 1068–1078.

[173] Y. Segawa, A. Fukazawa, S. Matsuura, H. Omachi, S. Yamaguchi, S. Irle, K. Itami, *Org. Biomol. Chem.* **2012**, *10*, 5979–5984.

[174] S. Yamago, E. Kayahara, T. Iwamoto, *Chem. Rec.* **2014**, *14*, 84–100.

[175] M. Hermann, D. Wassy, B. Esser, *Angew. Chem. Int. Ed.* **2021**, *60*, 15743–15766.

[176] F. Haase, B. V Lotsch, *Chem. Soc. Rev.* **2020**, *49*, 8469–8500.

[177] A. Mateo-Alonso, *Chem. Soc. Rev.* **2014**, *43*, 6311–6324.

[178] J. Hu, D. Zhang, F. W. Harris, *J. Org. Chem.* **2005**, *70*, 707–708.

[179] J. Guo, Y. Xu, S. Jin, L. Chen, T. Kaji, Y. Honsho, M. A. Addicoat, J. Kim, A. Saeki, H. Ihee, S. Seki, S. Irle, M. Hiramoto, J. Gao, D. Jiang, *Nat. Commun.* **2013**, *4*, 2736.

[180] A. S. R. Bati, L. Yu, M. Batmunkh, J. G. Shapter, *Nanoscale* **2018**, *10*, 22087–22139.

[181] Z. Liu, Y. Wang, Y. Chen, J. Liu, Q. Fang, C. Kleeberg, T. B. Marder, *J. Org. Chem.* **2012**, *77*, 7124–7128.

[182] J. Merz, M. Dietz, Y. Vonhausen, F. Wöber, A. Friedrich, D. Sieh, I. Krummenacher, H. Braunschweig, M. Moos, M. Holzapfel, C. Lambert, T. B. Marder, *Chem. – Eur. J.* **2020**, *26*, 438–453.

[183] S. I. Kawano, M. Baumgarten, D. Chercka, V. Enkelmann, K. Müllen, *Chem. Commun.* **2013**, *49*, 5058–5060.

[184] A. B. Marco, D. Cortizo-Lacalle, C. Gozalvez, M. Olano, A. Atxabal, X. Sun, M. Melle-Franco, L. E. Hueso, A. Mateo-Alonso, *Chem. Commun.* **2015**, *51*, 10754–10757.

[185] L. Ueberricke, D. Mizioch, F. Ghalami, F. Rominger, T. Oeser, M. Elstner, M. Mastalerz, F. Mildner, *Eur. J. Org. Chem.* **2021**, 4816–4823.

[186] B. L. Hu, K. Zhang, C. An, D. Schollmeyer, W. Pisula, M. Baumgarten, *Angew. Chem. Int. Ed.* **2018**, *57*, 12375–12379.

[187] N. Wang, X. Bao, Y. Yan, D. Ouyang, M. Sun, V. A. L. Roy, C. S. Lee, R. Yang, *J. Polym. Sci. Part A Polym. Chem.* **2014**, *52*, 3198–3204.

[188] Z. Sun, T. Mio, K. Ikemoto, S. Sato, H. Isobe, *J. Org. Chem.* **2019**, *84*, 3500–3507.

[189] E. Kayahara, R. Qu, M. Kojima, T. Iwamoto, T. Suzuki, S. Yamago, *Chem. – Eur. J.* **2015**, *21*, 18939–18943.

[190] C. Eaborn, K. J. Odell, A. Pidcock, *J. Chem. Soc. Dalt. Trans.* **1978**, 357–368.

[191] Y. Tsuchido, R. Abe, T. Ide, K. Osakada, *Angew. Chem. Int. Ed.* **2020**, *59*, 22928–22932.

[192] F. Lucas, N. McIntosh, E. Jacques, C. Lebreton, B. Heinrich, B. Donnio, O. Jeannin, J. Rault-Berthelot, C. Quinton, J. Cornil, C. Poriel, *J. Am. Chem. Soc.* **2021**, *143*, 8804–8820.

[193] P. Neuhaus, A. Cnossen, J. Q. Gong, L. M. Herz, H. L. Anderson, *Angew. Chem. Int. Ed.* **2015**, *54*, 7344–7348.

[194] M. Fujitsuka, D. W. Cho, T. Iwamoto, S. Yamago, T. Majima, *Phys. Chem. Chem. Phys.* **2012**, *14*, 14585–14588.

[195] S. E. Wheeler, K. N. Houk, P. V. R. Schleyer, W. D. Allen, *J. Am. Chem. Soc.* **2009**, *131*, 2547–2560.

[196] V. Maslak, Z. Yan, S. Xia, J. Gallucci, C. M. Hadad, J. D. Badjić, *J. Am. Chem. Soc.* **2006**, *128*, 5887–5894.

[197] K. Hermann, Y. Ruan, A. M. Hardin, C. M. Hadad, J. D. Badjić, *Chem. Soc. Rev.* **2015**, *44*, 500–514.

[198] K. N. Houk, K. Nakamura, C. Sheu, A. E. Keating, *Science* **1996**, *273*, 627–629.

[199] D. P. van Heerden, L. J. Barbour, *Chem. Soc. Rev.* **2021**, *50*, 735–749.

[200] L. J. Barbour, *J. Appl. Crystallogr.* **2020**, *53*, 1141–1146.

[201] D. Zhang, T. K. Ronson, J. L. Greenfield, T. Brotin, P. Berthault, E. Leónce, J. L. Zhu, L. Xu, J. R. Nitschke, *J. Am. Chem. Soc.* **2020**, *141*, 8339–8345.

[202] S. A. L. Rousseaux, J. Q. Gong, R. Haver, B. Odell, T. D. W. Claridge, L. M. Herz, H. L. Anderson, *J. Am. Chem. Soc.* **2015**, *137*, 12713–12718.

[203] H. Wu, Y. Wang, L. O. Jones, W. Liu, B. Song, Y. Cui, K. Cai, L. Zhang, D. Shen, X. Y. Chen, Y. Jiao, C. L. Stern, X. Li, G. C. Schatz, J. Fraser Stoddart, *J. Am. Chem. Soc.* **2020**, *142*, 16849–16860.

[204] B. F. Vögtle, W. M. Müller, *Angew. Chem. Int. Ed.* **1979**, *18*, 623–624.

[205] K. Kim, S. Y. Kim, I. S. Jung, E. Lee, J. Kim, S. Sakamoto, K. Yamaguchi, *Angew. Chem. Int. Ed.* **2001**, *40*, 2119–2121.

[206] S. J. Dalgarno, J. L. Atwood, C. L. Raston, *Chem. Commun.* **2006**, 4567–4574.

[207] T. N. Parac, M. Scherer, K. N. Raymond, *Angew. Chem. Int. Ed.* **2000**, *39*, 1239–1242.

[208] A. Lützen, A. R. Renslo, C. A. Schalley, B. M. O'Leary, J. Rebek, *J. Am. Chem. Soc.* **1999**, *121*, 7455–7456.

[209] J. R. Long, R. S. Drago, *J. Chem. Educ.* **1982**, *59*, 1037.

[210] P. Thordarson, *Chem. Soc. Rev.* **2011**, *40*, 1305–1323.

[211] M. O. Banikhaled, J. D. Mottishaw, H. Sun, *Cryst. Growth Des.* **2015**, *15*, 2235–2242.

[212] A. S. Weingarten, R. V. Kazantsev, L. C. Palmer, M. McClendon, A. R. Koltonow, A. P. S. Samuel, D. J. Kiebala, M. R. Wasielewski, S. I. Stupp, *Nat. Chem.* **2014**, *6*, 964–970.

[213] Z. Sun, K. Ikemoto, T. M. Fukunaga, T. Koretsune, R. Arita, S. Sato, H. Isobe, *Science* **2019**, *155*, 151–155.

[214] W. J. Wolf, M. S. Winston, F. D. Toste, *Nat. Chem.* **2014**, *6*, 159–164.

[215] D. Lu, G. Zhuang, H. Wu, S. Wang, S. Yang, P. Du, *Angew. Chem. Int. Ed.* **2017**, *56*, 158–162.

[216] H. A. Staab, F. Binnig, *Chem. Ber.* **1967**, *100*, 293–305.

[217] K. Ikemoto, R. Kobayashi, S. Sato, H. Isobe, *Angew. Chem. Int. Ed.* **2017**, *56*, 6511–6514.

[218] R. Laplaza, R. A. Boto, J. Contreras-García, M. M. Montero-Campillo, *Phys. Chem. Chem. Phys.* **2020**, *22*, 21251–21256.

[219] F. A. L. Anet, A. J. R. Bourn, *J. Am. Chem. Soc.* **1967**, *89*, 760–768.

[220] W. Pisula, M. Kastler, C. Yang, V. Enkelmann, K. Müllen, *Chem. – Asian J.* **2006**, *2*, 51–56.

[221] K. Ikemoto, T. Tokuhira, A. Uetani, Y. Harabuchi, S. Sato, S. Maeda, H. Isobe, *J. Org. Chem.* **2020**, *85*, 150–157.

[222] W. Huang, M. Wang, C. Du, Y. Chen, R. Qin, L. Su, C. Zhang, Z. Liu, C. Li, Z. Bo, *Chem. – Eur. J.* **2011**, *17*, 440–444.

[223] J. Wang, Y.-Y. Ju, K.-H. Low, Y.-Z. Tan, J. Liu, *Angew. Chem. Int. Ed.* **2021**, *60*, 11814–11818.

[224] S. M. Kim, M. H. Kim, S. Y. Choi, J. G. Lee, J. Jang, J. B. Lee, J. H. Ryu, S. S. Hwang, J. H. Park, K. Shin, Y. G. Kim, S. M. Oh, *Energy Environ. Sci.* **2015**, *8*, 1538–1543.

[225] N. Grabicki, K. T. D. Nguyen, S. Weidner, O. Dumele, *Angew. Chem. Int. Ed.* **2021**, *60*, 14909–14914.

[226] U. Mueller, R. Förster, M. Hellmig, F. U. Huschmann, A. Kastner, P. Malecki, S. Pühringer, M. Röwer, K. Sparta, M. Steffien, M. Ühlein, P. Wilk, M. S. Weiss, *Eur. Phys. J. Plus* **2015**, *130*, 141.

[227] U. Mueller, N. Darowski, M. R. Fuchs, R. Förster, M. Hellmig, K. S. Paithankar, S. Pühringer, M. Steffien, G. Zocher, M. S. Weiss, *J. Synchrotron Radiat.* **2012**, *19*, 442–449.

[228] Y. Segawa, S. Miyamoto, H. Omachi, S. Matsuura, P. Šenel, T. Sasamori, N. Tokitoh, K. Itami, *Angew. Chem. Int. Ed.* **2011**, *50*, 3244–3248.

[229] T. Nishihara, Y. Segawa, K. Itami, Y. Kanemitsu, *J. Phys. Chem. Lett.* **2012**, *3*, 3125–3128.

[230] T. C. Lovell, C. E. Colwell, L. N. Zakharov, R. Jasti, *Chem. Sci.* **2019**, *10*, 3786–3790.

[231] E. Kayahara, R. Qu, S. Yamago, *Angew. Chem. Int. Ed.* **2017**, *56*, 10428–10432.

[232] N. Grabicki, O. Dumele, *Synlett* **2022**, *33*, 1–7.

[233] D. Brynn Hibbert, P. Thordarson, *Chem. Commun.* **2016**, *52*, 12792–12805.

[234] F. Ulatowski, K. Dabrowa, T. Bałakier, J. Jurczak, *J. Org. Chem.* **2016**, *81*, 1746–1756.

[235] Y. Yamamoto, E. Tsurumaki, K. Wakamatsu, S. Toyota, *Angew. Chem. Int. Ed.* **2018**, *57*, 8199–8202.

[236] M. Nishio, *Phys. Chem. Chem. Phys.* **2011**, *13*, 13873–13900.

[237] D. J. Hill, M. J. Mio, R. B. Prince, T. S. Hughes, J. S. Moore, *Chem. Rev.* **2001**, *101*, 3893–4011.

[238] T. R. Cook, P. J. Stang, *Chem. Rev.* **2015**, *115*, 7001–7045.

[239] Z. J. Kinney, C. S. Hartley, *J. Am. Chem. Soc.* **2017**, *139*, 4821–4827.

[240] J. L. Alonso-Gómez, P. Rivera-Fuentes, N. Harada, N. Berova, F. Diederich, *Angew. Chem. Int. Ed.* **2009**, *48*, 5545–5548.

[241] P. Rivera-Fuentes, J. L. Alonso-Gómez, A. G. Petrovic, F. Santoro, N. Harada, N. Berova, F. Diederich, *Angew. Chem. Int. Ed.* **2010**, *49*, 2247–2250.

[242] S. Castro-Fernández, R. Yang, A. P. García, I. L. Garzón, H. Xu, A. G. Petrovic, J. L. Alonso-Gómez, *Chem. – Eur. J.* **2017**, *23*, 11747–11751.

[243] M. Hasegawa, Y. Nojima, Y. Mazaki, *ChemPhotoChem* **2021**, *5*, 1042–1058.

[244] P. Ravat, R. Hinkelmann, D. Steinebrunner, A. Prescimone, I. Bodoky, M. Juríček, *Org.*

Lett. **2017**, *19*, 3707–3710.

[245] M. Rickhaus, M. Mayor, M. Juríček, *Chem. Soc. Rev.* **2016**, *45*, 1542–1556.

[246] M. Sapir, E. V. Donckt, *Chem. Phys. Lett.* **1975**, *36*, 108–110.

[247] Y. Hu, X.-Y. Wang, P.-X. Peng, X.-C. Wang, X.-Y. Cao, X. Feng, K. Müllen, A. Narita, *Angew. Chem. Int. Ed.* **2017**, *56*, 3374–3378.

[248] T. Fujikawa, D. V Preda, Y. Segawa, K. Itami, L. T. Scott, *Org. Lett.* **2016**, *18*, 3992–3995.

[249] P. Ravat, P. Ribar, M. Rickhaus, D. Häussinger, M. Neuburger, M. Juríček, *J. Org. Chem.* **2016**, *81*, 12303–12317.

[250] R. B. Woodward, R. Hoffmann, *Angew. Chem. Int. Ed.* **1969**, *8*, 781–853.

[251] S. Venkataramani, U. Jana, M. Dommaschk, F. D. Sönnichsen, F. Tuczek, R. Herges, *Science* **2011**, *331*, 445–448.

[252] O. Sato, J. Tao, Y.-Z. Zhang, *Angew. Chem. Int. Ed.* **2007**, *46*, 2152–2187.

[253] J. Larionova, L. Salmon, Y. Guari, A. Tokarev, K. Molvinger, G. Molnár, A. Bousseksou, *Angew. Chem. Int. Ed.* **2008**, *47*, 8236–8240.

[254] S. Thies, H. Sell, C. Schütt, C. Bornholdt, C. Näther, F. Tuczek, R. Herges, *J. Am. Chem. Soc.* **2011**, *133*, 16243–16250.

[255] V. Wellm, C. Näther, R. Herges, *J. Org. Chem.* **2021**, *86*, 9503–9514.

[256] G. D. Harzmann, R. Frisenda, H. S. J. van der Zant, M. Mayor, *Angew. Chem. Int. Ed.* **2015**, *54*, 13425–13430.

[257] M. Milek, F. W. Heinemann, M. M. Khusniyarov, *Inorg. Chem.* **2013**, *52*, 11585–11592.

[258] S. Hayami, S. M. Holmes, M. A. Halcrow, *J. Mater. Chem. C* **2015**, *3*, 7775–7778.

[259] T. Nishiuchi, R. Ito, E. Stratmann, T. Kubo, *J. Org. Chem.* **2020**, *85*, 179–186.

[260] H. Kurata, S. Kim, K. Matsumoto, T. Kawase, M. Oda, *Chem. Lett.* **2007**, *36*, 386–387.

[261] M. B. S. Wonink, B. P. Corbet, A. A. Kulago, G. B. Boursalian, B. de Bruin, E. Otten, W. R. Browne, B. L. Feringa, *J. Am. Chem. Soc.* **2021**, *143*, 18020–18028.

[262] S. Nakatsuji, *Chem. Soc. Rev.* **2004**, *33*, 348–353.

[263] K. Tanaka, F. Toda, *J. Chem. Soc. Perkin Trans. 1* **2000**, 873–874.

[264] Y. Kishimoto, J. Abe, *J. Am. Chem. Soc.* **2009**, *131*, 4227–4229.

[265] K. Fujita, S. Hatano, D. Kato, J. Abe, *Org. Lett.* **2008**, *10*, 3105–3108.

[266] R. Kurata, K. Tanaka, A. Ito, *J. Org. Chem.* **2016**, *81*, 137–145.

[267] T. Hayashi, K. Maeda, *Bull. Chem. Soc. Jpn.* **1960**, *33*, 565–566.

[268] P. Ravat, T. Šolomek, D. Häussinger, O. Blacque, M. Juríček, *J. Am. Chem. Soc.* **2018**, *140*, 10839–10847.

[269] Y. Nakakuki, T. Hirose, H. Sotome, M. Gao, D. Shimizu, R. Li, J. Hasegawa, H. Miyasaka, K. Matsuda, *Nat. Commun.* **2022**, *13*, 1475.

[270] D. S. Acker, W. R. Hertler, *J. Am. Chem. Soc.* **1962**, *84*, 3370–3374.

[271] M. Maxfield, A. N. Bloch, D. O. Cowan, *J. Org. Chem.* **1985**, *50*, 1789–1796.

[272] Z. Zeng, M. Ishida, J. L. Zafra, X. Zhu, Y. M. Sung, N. Bao, R. D. Webster, B. S. Lee, R.-W. Li, W. Zeng, Y. Li, C. Chi, J. T. L. Navarrete, J. Ding, J. Casado, D. Kim, J. Wu, *J. Am. Chem. Soc.* **2013**, *135*, 6363–6371.

[273] T. Ishiyama, M. Murata, N. Miyaura, *J. Org. Chem.* **1995**, *60*, 7508–7510.

[274] Y. Shen, H.-Y. Lu, C.-F. Chen, *Angew. Chem. Int. Ed.* **2014**, *53*, 4648–4651.

[275] P. Ravat, T. Šolomek, M. Rickhaus, D. Häussinger, M. Neuburger, M. Baumgarten, M. Juríček, *Angew. Chem. Int. Ed.* **2016**, *55*, 1183–1186.

[276] M. Uno, K. Seto, S. Takahashi, *J. Chem. Soc. Chem. Commun.* **1984**, 932–933.

[277] Y. Shen, C.-F. Chen, *Chem. Rev.* **2012**, *112*, 1463–1535.

[278] S. H. Chen, D. Katsis, A. W. Schmid, J. C. Mastrangelo, T. Tsutsui, T. N. Blanton, *Nature* **1999**, *397*, 506–508.

[279] D. B. Amabilino, *Chem. Soc. Rev.* **2009**, *38*, 669–670.

[280] P. Ravat, T. Šolomek, M. Juríček, *ChemPhotoChem* **2019**, *3*, 180–186.

[281] G. Berkovic, V. Krongauz, V. Weiss, *Chem. Rev.* **2000**, *100*, 1741–1754.

[282] L. Kortekaas, W. R. Browne, *Chem. Soc. Rev.* **2019**, *48*, 3406–3424.

[283] M. Irie, *Chem. Rev.* **2000**, *100*, 1685–1716.

[284] K. Dyrek, M. Che, *Chem. Rev.* **1997**, *97*, 305–332.

[285] M. Chiesa, E. Giamello, M. Che, *Chem. Rev.* **2010**, *110*, 1320–1347.

[286] L. Salem, C. Rowland, *Angew. Chem. Int. Ed.* **1972**, *11*, 92–111.

[287] J. Michl, V. Bonačić-Koutecký, *Tetrahedron* **1988**, *44*, 7559–7585.

[288] A. Schweiger, G. Jeschke, *Principles of Pulse Electron Paramagnetic Resonance*, Oxford University Press, **2001**.

[289] T. Šolomek, P. Ravat, Z. Mou, M. Kertesz, M. Juríček, *J. Org. Chem.* **2018**, *83*, 4769–4774.

[290] M. Solà, *Front. Chem.* **2013**, *1*.

[291] E. Clar, W. Kemp, D. G. Stewart, *Tetrahedron* **1958**, *3*, 325–333.

[292] E. Clar, I. A. Macpherson, *Tetrahedron* **1962**, *18*, 1411–1416.

[293] Z. Sun, S. Lee, K. H. Park, X. Zhu, W. Zhang, B. Zheng, P. Hu, Z. Zeng, S. Das, Y. Li, C. Chi, R.-W. Li, K.-W. Huang, J. Ding, D. Kim, J. Wu, *J. Am. Chem. Soc.* **2013**, *135*, 18229–18236.

[294] K. Yamaguchi, *Chem. Phys. Lett.* **1975**, *33*, 330–335.

[295] M. Abe, *Chem. Rev.* **2013**, *113*, 7011–7088.

[296] J. J. Dressler, Z. Zhou, J. L. Marshall, R. Kishi, S. Takamuku, Z. Wei, S. N. Spisak, M. Nakano, M. A. Petrukhina, M. M. Haley, *Angew. Chem. Int. Ed.* **2017**, *56*, 15363–15367.

[297] Z. Zeng, Y. M. Sung, N. Bao, D. Tan, R. Lee, J. L. Zafra, B. S. Lee, M. Ishida, J. Ding, J. T. López Navarrete, Y. Li, W. Zeng, D. Kim, K.-W. Huang, R. D. Webster, J. Casado, J. Wu, *J. Am. Chem. Soc.* **2012**, *134*, 14513–14525.

[298] N. Gallagher, H. Zhang, T. Junghoefer, E. Giangrisostomi, R. Ovsyannikov, M. Pink, S. Rajca, M. B. Casu, A. Rajca, *J. Am. Chem. Soc.* **2019**, *141*, 4764–4774.

[299] Z.-Y. Wang, Y.-Z. Dai, L. Ding, B.-W. Dong, S.-D. Jiang, J.-Y. Wang, J. Pei, *Angew. Chem. Int. Ed.* **2021**, *60*, 4594–4598.

[300] Y.-C. Hsieh, C.-F. Wu, Y.-T. Chen, C.-T. Fang, C.-S. Wang, C.-H. Li, L.-Y. Chen, M.-J. Cheng, C.-C. Chueh, P.-T. Chou, Y.-T. Wu, *J. Am. Chem. Soc.* **2018**, *140*, 14357–14366.

[301] L. Valenta, M. Mayländer, P. Kappeler, O. Blacque, T. Šolomek, S. Richert, M. Juríček, *Chem. Commun.* **2022**, *58*, 3019–3022.

[302] T. Koshido, T. Kawai, K. Yoshino, *J. Phys. Chem.* **1995**, *99*, 6110–6114.

[303] A. Peters, N. R. Branda, *J. Am. Chem. Soc.* **2003**, *125*, 3404–3405.

[304] W. R. Browne, J. J. D. de Jong, T. Kudernac, M. Walko, L. N. Lucas, K. Uchida, J. H. van Esch, B. L. Feringa, *Chem. – Eur. J.* **2005**, *11*, 6430–6441.

[305] Y. Moriyama, K. Matsuda, N. Tanifuji, S. Irie, M. Irie, *Org. Lett.* **2005**, *7*, 3315–3318.

[306] W. R. Browne, J. J. D. de Jong, T. Kudernac, M. Walko, L. N. Lucas, K. Uchida, J. H. van Esch, B. L. Feringa, *Chem. – Eur. J.* **2005**, *11*, 6414–6429.

[307] D. H. Evans, K. Hu, *J. Chem. Soc. Faraday Trans.* **1996**, *92*, 3983–3990.

[308] H. Lund, M. M. Baizer, *Organic Electrochemistry: An Introduction and a Guide*, M. Dekker, **1991**.

[309] C. P. Andrieux, *Terminology and Notations for Multistep Electrochemical Reaction Mechanisms*, **1994**.

[310] F. Troiani, M. Affronte, *Chem. Soc. Rev.* **2011**, *40*, 3119–3129.

[311] K. Sato, S. Nakazawa, R. Rahimi, T. Ise, S. Nishida, T. Yoshino, N. Mori, K. Toyota, D. Shiomi, Y. Yakiyama, Y. Morita, M. Kitagawa, K. Nakasuji, M. Nakahara, H. Hara, P. Carl, P. Höfer, T. Takui, *J. Mater. Chem.* **2009**, *19*, 3739–3754.

[312] M. N. Leuenberger, D. Loss, *Nature* **2001**, *410*, 789–793.

[313] S. Takahashi, I. S. Tupitsyn, J. van Tol, C. C. Beedle, D. N. Hendrickson, P. C. E. Stamp, *Nature* **2011**, *476*, 76–79.

[314] E. Moreno-Pineda, C. Godfrin, F. Balestro, W. Wernsdorfer, M. Ruben, *Chem. Soc. Rev.* **2018**, *47*, 501–513.

[315] C. M. Agapakis, P. M. Boyle, P. A. Silver, *Nat. Chem. Biol.* **2012**, *8*, 527–535.

[316] M. Marguet, C. Bonduelle, S. Lecommandoux, *Chem. Soc. Rev.* **2013**, *42*, 512–529.

[317] Y. Itoh, S. Chen, R. Hirahara, T. Konda, T. Aoki, T. Ueda, I. Shimada, J. J. Cannon, C. Shao, J. Shiomi, K. V Tabata, H. Noji, K. Sato, T. Aida, *Science* **2022**, *376*, 738–743.

[318] Y. Zhang, Y. Zheng, H. Zhou, M.-S. Miao, F. Wudl, T.-Q. Nguyen, *Adv. Mater.* **2015**, *27*, 7412–7419.

[319] X. Hu, W. Wang, D. Wang, Y. Zheng, *J. Mater. Chem. C* **2018**, *6*, 11232–11242.

[320] F. Evers, A. Aharony, N. Bar-Gill, O. Entin-Wohlman, P. Hedegård, O. Hod, P. Jelinek, G. Kamieniarz, M. Lemeshko, K. Michaeli, V. Mujica, R. Naaman, Y. Paltiel, S. Refaely-Abramson, O. Tal, J. Thijssen, M. Thoss, J. M. van Ruitenbeek, L. Venkataraman, D. H. Waldeck, B. Yan, L. Kronik, *Adv. Mater.* **2022**, *34*, 2106629.

[321] L. Venkataraman, J. E. Klare, C. Nuckolls, M. S. Hybertsen, M. L. Steigerwald, *Nature* **2006**, *442*, 904–907.

[322] G. M. Sheldrick, *Sadabs*, **1996**.

[323] G. M. Sheldrick, *Acta Crystallogr. Sect. A* **2015**, *71*, 3–8.

[324] G. M. Sheldrick, *Acta Crystallogr. Sect. C* **2015**, *71*, 3–8.

[325] O. V. Dolomanov, L. J. Bourhis, R. J. Gildea, J. A. K. Howard, H. Puschmann, *J. Appl. Crystallogr.* **2009**, *42*, 339–341.

[326] B. Rees, L. Jenner, M. Yusupov, *Acta Crystallogr. Sect. D Biol. Crystallogr.* **2005**, *61*, 1299–1301.

[327] P. van der Sluis, A. L. Spek, *Acta Crystallogr. Sect. A* **1990**, *46*, 194–201.

[328] A. L. Spek, *J. Appl. Crystallogr.* **2003**, *36*, 7–13.

[329] D. N. Coventry, A. S. Batsanov, A. E. Goeta, J. A. K. Howard, T. B. Marder, R. N. Perutz, *Chem. Commun.* **2005**, 2172–2174.

[330] W. H. Powell, R. Panico, J. G. Traynham, W. Coordinator, *Pure Appl. Chem.* **1998**, *70*, 1513–1545.

[331] H. A. Favre, D. Hellwinkel, W. H. Powell, H. A. Smith, *Chem. Int.* **2002**, *24*, 25–26.

[332] G. J. Chen, C. Tamborski, *J. Organomet. Chem.* **1983**, *251*, 149–158.

[333] L. Z. Gong, Q. S. Hu, L. Pu, *J. Org. Chem.* **2001**, *66*, 2358–2367.

[334] D. C. Harrowven, M. I. T. Nunn, D. R. Fenwick, *Tetrahedron Lett.* **2002**, *43*, 7345–7347.

[335] T. Bruhn, A. Schaumlöffel, Y. Hemberger, G. Bringmann, *Chirality* **2013**, *25*, 243–249.

[336] S. Grimme, J. Antony, S. Ehrlich, H. Krieg, *J. Chem. Phys.* **2010**, *132*, 154104.

[337] A. D. Becke, *Phys. Rev. A* **1988**, *38*, 3098–3100.

[338] R. Lee, Cheng, Yang, Weitao, Parr, *Phys. Rev. B* **1988**, *37*, 785–789.

[339] W. J. Hehre, R. Ditchfield, J. A. Pople, *J. Chem. Phys.* **1972**, *56*, 2257–2261.

[340] D. G. A. Smith, L. A. Burns, K. Patkowski, C. D. Sherrill, *J. Phys. Chem. Lett.* **2016**, *7*, 2197–2203.

[341] F. Weigend, R. Ahlrichs, *Phys. Chem. Chem. Phys.* **2005**, *7*, 3297–3305.

[342] T. H. Dunning, *J. Chem. Phys.* **1989**, *90*, 1007–1023.

[343] V. Barone, M. Cossi, *J. Phys. Chem. A* **1998**, *102*, 1995–2001.

Selbständigkeitserklärung

„Ich erkläre, dass ich die Dissertation selbständig und nur unter Verwendung der von mir gemäß § 7 Abs. 3 der Promotionsordnung der Mathematisch-Naturwissenschaftlichen Fakultät, veröffentlicht im Amtlichen Mitteilungsblatt der Humboldt-Universität zu Berlin Nr. 42/2018 am 11.07.2018 angegebenen Hilfsmittel angefertigt habe.“

Berlin, den 09.03.2023

(Niklas Jan Grabicki)